The Processing and Characterisation of Novel Self-Assembled DNA Platinum Electrocatalysts for the Hydrogen Evolution Reaction (HER)

By

Ruba Hendi

A thesis submitted to the

University of Birmingham

for the degree of

DOCTOR OF PHILOSOPHY

School of Chemical Engineering

College of Engineering and Physical Science

University of Birmingham

September 2020

Abstract

Fuel cell technology is a sustainable and green means of power generation and can help to tackle the global demands of energy and power. Fuel cells can have a wide range of applications, from use in small portable devices such as mobile phones or laptops to more energy demanding applications like electric vehicles or industrially for heat and power generation. However, their high expense has hindered their commercialization and widespread adoption. The major contribution to these high costs arises from the use of expensive raw materials, in particular platinum metal which is commonly used as a catalyst however is highly prone to poisoning from impurities in the fuel.

With the aim of reducing platinum metal loadings further in catalytic materials associated with clean fuel and energy production, a novel synthetic biology approach to platinum nanostructure design involving the use of DNA as a scaffold for the accurate placement of metal atoms is suggested. The design of the material considers the spacing of the individual platinum metal atoms along the backbone of DNA, in order to reduce and control undesirable metal clustering and consequently expose more of the metal active sites, thereby raising the catalytic efficiency of the resultant material. The use of DNA as a versatile tool for self-assembly is emerging in the field of DNA nanotechnology and particularly methods such as DNA origami, where the fabrication of two-dimensional nanostructures is possible. These methods will be employed to achieve the catalyst nanostructure design of well distributed platinum metal on a DNA scaffold. The platinating agent in this study involves the use of the anticancer drug cisplatin (cisPt), [Pt $(NH_3)_2Cl_2$], due to its extensively studied and well understood covalent interactions with the DNA nucleobases. The ability of this platinum metal complex to form such strong interactions with the DNA is pivotal in ensuring the formation of a robust catalyst precursor material. Lastly, through the combination of the well understood Watson-Crick specific base pairings of the DNA and the interactions between cisPt and DNA nucleobases reported in the literature, the aim is to specifically control the assembly of the platinum on the DNA template to produce localised and highly distributed platinum active sites suited for catalysing fuel cell reactions like the hydrogen evolution reaction (HER).

In this study, the novel DNA-cisPt based nano-material (synthesised in-house) is characterised to measure its electrochemical properties in order to assess its feasibility for its use as an electrocatalyst for fuel cell applications. The initial work, involving the complex formation between salmon milt DNA and cisPt, focuses on investigating the ideal and optimum platinum metal loading on the DNA scaffold for the HER in an acidic environment (pH 3). The studies reveal interesting trends in catalytic behaviour as a function of platinum loading for the HER and the influence of this on the resultant surface morphology of the material via STEM imaging characterisation. This includes increased electrocatalytic performance with increased metal loadings although simultaneously we observed increased clustering of the metal atoms and poorer distribution of it on the DNA support.

However, the non-conductive nature of the DNA material greatly hindered the attainable electrocatalytic performance at all loadings of the platinum metal. Thus, an integral study focusing on different processing treatments of the DNA was carried out to improve the conductive and electronic properties of the DNA material as an electrocatalyst support, which would both improve the electrochemical activity and durability of the nanomaterial. The resulting effect of three different methods has been detailed throughout the thesis including the method of: functionalization of single walled carbon nanotubes (SWCNT's) with the DNA-cisPt material, the graphitization of the DNA through the evacuation of the hydrogen and oxygen atoms upon high dose exposure to an electron beam, and finally carbonisation of the DNA via a low temperature pseudo pyrolysis process (255 °C, 30 minutes).

Experimental work presented in this thesis focuses on assessing the surface morphology of the nanomaterial using Scanning Transmission Electron Microscopy (STEM) and the electrocatalytic performance for the HER via electrochemical studies. X-ray Photoelectron Spectroscopy (XPS) is used to identify the chemical composition of the material, while Atomic Force Microscopy (AFM) is occasionally used to observe the surface topography of the DNA.

The experimental results reveal that interesting trends in catalytic behaviour as a function of platinum loading in the DNA-cisPt nanomaterial can be attained for the HER reaction (pH 3). It is clear from the experimental findings that the functionalisation of the SWCNTs with cisPt gives rise to exceptional improvements in the electrocatalytic performance of the nanotubes towards the HER (pH 3), compared to the unmodified SWCNT's. Insights into the mechanism of the HER reaction, as revealed by the Tafel slopes, show that the Volmer-Heyrovsky reaction mechanism dominates for the HER over the surface of the fabricated SWCNT-DNA-cisPt structures and that the cisPt loading correlates strongly with the calculated transfer coefficient (α) and the Tafel slope.

On the other hand, the treatment process of the DNA via its projection to a flood electron beam (e-beam) led to significant improvements in the electrochemical performance of the material for the electrocatalysis of the HER (pH 3) compared to the untreated counterpart. This supports the hypothesis made to suggest that the conductive properties of the DNA can be improved through this processing technique. The electrocatalytic performance of the e-beam treated DNA-cisPt material could be correlated with the platinum (Pt) loading. An optimum loading was found, which was intermediate of all the Pt loadings studied. Lastly, carbonisation of the DNA/glassy carbon (GC) and DNA-cisPt /GC modified electrode via a heat treatment process at the optimum experimental pseudo pyrolysis conditions found (255 °C for a duration of 30 minutes) was also proven to be successful in significantly improving the electrocatalytic performance of the material for the HER (pH 3), compared to the untreated counterpart. Carbonization of the virgin DNA via a pseudo pyrolysis process can significantly improve the electrochemical performance for the catalysis of the HER (pH 3) and the performance attained is equivalent to that measured in the presence of the platinum metal i.e. carbonised DNA-cisPt. It can be proposed that the carbonised DNA is best described as being equivalent to a nitrogen, phosphorus doped (N, P-doped) (graphitic) carbon, which justifies the improved electrocatalytic response measured.

The experimental results have shown that cisPt is an effective source of platinum metal and its combination with DNA is ideal for establishing controlled placement of the platinum metal atoms on the scaffold, at an atomic precision level via covalent bonding. This enables improved distribution of the platinum metal on the DNA catalyst support, thus increasing the utilisation of the expensive metal and consequently reducing its costs.

To achieve this distribution, self-assembled nanostructures such as triangular DNA origami structures and Holliday Junction (HJ) arrays have been employed in the final part of this work. The experimental results have shown that electrocatalysts of reduced platinum metal loadings can be fabricated without compromising the fuel cell performance as demonstrated through the electrochemical studies of the HER (pH 3). The surface morphological studies via STEM imaging have shown how highly distributed platinum metal atoms on the DNA nanostructures can be achieved as opposed to the non-assembled DNA scaffold i.e. salmon milt DNA. As a result of this, there is increased availability and exposure of the catalyst active sites. This is a stepping stone towards improving the utilisation of the 'true' available surface area, consequently leading to more effective and efficient use of the platinum metal and consequently reducing costs.

Dedication

This thesis is dedicated to my beloved father, Ahmed Hendi, since without his support, this thesis and PhD journey would have never had happened.

Acknowledgements

First of all, I begin by expressing my gratitude to Almighty Allah for the successful completion of this work. Secondly, I thank the best supervisor anyone could ask for, Dr. Neil V. Rees, for his continued support and guidance throughout this research work. I would also like to thank Dr. Alex Robinson for supporting my ideas and providing me with access to a range of facilities in his labs, and most importantly the help of his supportive research group (Carmen, Karolis and Alan), where I developed a range of technical skills because of them. I thank Professor James Tucker, from the School of Chemistry, for supervising this collaborative project from his side and showing appreciation to my contribution to the work. Major thanks go to Klaudia Englert for her hard work and provision of all the materials used in this research work, and her continued friendship and support till this day.

I also thank Dr. Wolfgang Theis, from the School of Physics and Astronomy, for the training he delivered on using the scanning transmission electron microscope (STEM), and having a key role in the expert that I have become today with operating this instrumentation. I also sincerely appreciate the support of Alex Pattinson from Wolfgang's research group, for being a life-saver and helping me out after falling into trouble (many troubles too), whilst operating the STEM instrumentation.

I also thank the School of Chemical Engineering and acknowledge their role in funding my award of a PhD studentship.

Finally, I thank every member of my beloved family, my amazing parents and proud siblings, for their unconditional love and support throughout my PhD. I forever appreciate our gatherings every evening after a long day in the lab and know this was key to what kept me going the past 3 years. Lastly, but by no means least, I thank my dear husband, who stood by me all the way ever since we met, supporting my career dreams and ambitions every step of the way. I am grateful to every one of you.

Publications

Publications that arose from this thesis:

[1] *Klaudia Englert, Ruba Hendi, Peter H. Robbs,Neil V. Rees, Alex P. G. Robinson, James H. R.Tucker. Cisplatin adducts of DNA as pre-cursors for nanostructured catalyst materials. Nanoscale Adv, Royal Society of Chemistry (2020).*

Other Publications:

[2] *Ruba Hendi, Peter H.Robbs, Beatrice Sampson, Ryan Pearce, Neil V.Rees. The electrochemical reduction kinetics of oxygen in dimethyl-sulfoxide. Journal of Electroanalytical Chemistry. (2018), 829; 16-19.*

[3] *Azrul Azhar, Tshiamo Manyepedza, Abiola V.Oladeji, Ruba Hendi, Neil V.Rees. The electroreduction of oxygen in aprotic solvents. Journal of Electroanalytical Chemistry (2020).*

Other publications under editing

[4] *Ruba Hendi, Klaudia Englert, Neil V. Rees, Alex P. G. Robinson, James H. R.Tucker. DNA-cisplatin modified single-walled carbon nanotubes as electrocatalyst for the hydrogen evolution reaction (HER).*

[5] *Ruba Hendi, Klaudia Englert, Neil V. Rees, Alex P. G. Robinson, James H. R.Tucker. Processing DNA-cisPt electrocatalyst material for hydrogen evolution reaction (HER): Pyrolysis processing of the material compared with its electron beam irradiation.*

[6] *Ruba Hendi, Klaudia Englert, Neil V. Rees, Alex P. G. Robinson, James H. Tucker. Processing self-assembled DNA nanostructures as an electrocatalyst for the hydrogen evolution reaction (HER): Platinum Holliday Junction arrays and triangular DNA origami nanostructures.*

Table of contents

List of Abbreviations

2D	Two-dimensional
3D	Three-dimensional
3LL	Three-Layer Logpile
AFM	Atomic Force Microscopy
BF	Bright field
B-V	Butler-Volmer
CD	Circular Dichroism
CE	Counter Electrode
cisPt	Cisplatin
CV	Cyclic Voltammetry
DNA	Deoxyribose Nucleic Acid
Ds	Double stranded
E1/2	Half-wave Potential
E	Potential
EBL	Electron Beam Lithography
EDL	Electrical Double Layer
e-beam	Electron beam
EDX	Energy Dispersive X-ray Spectroscopy
FC	Fuel Cell
GC	Glassy Carbon
HER	Hydrogen Evolution Reaction
HAADF-STEM	High angle annular Dark Field - Scanning Transmission Electron Microscopy
J	Measured Current Density based on geometric surface area
N7	Nitrogen 7

N-P-doped	Nitrogen- phosphorous doped
O6	Oxygen 6
ORR	Oxygen Reduction reaction
PEMFC/PEM	Polymer Electrolyte Membrane Fuel Cell
Pt	Platinum
RE	Reference Electrode
SAM	Self-assembled Monolayer
SCE	Saturated Calomel Electrode
SHE	Standard Hydrogen Electrode
sm-DNA	Salmon milt-DNA
ss-DNA	Single stranded DNA
STEM	Scanning Transmission Electron Microscopy
STM	Scanning tunnelling microscopy
SWCNTs	Single walled carbon nanotubes
WE	Working Electrode
V-H	Volmer-Heyrovsky reaction mechanism
XPS	X-ray Photoelectron Spectroscopy
1:1 or 1 to 1 or 1-1	Ratio of DNA to cisPt in the material of 1 to 1

DNA Bases

A	Adenine
C	Cytosine
G	Guanine
T	Thymine

Chapter 1- Introduction

Chapter 1: Introduction

1.1 Background

The global energy demand reported its highest increase of 2.3 % in 2018, primarily due to the strong global economic growth (3.7 %) (1). As both global development and population continue to rise, an increased demand equating to a growth from 16 Terawatt (TW) (in 2010) to 23 and 30 TW is expected by the year 2030 and 2050 respectively (2). Currently these energy demands are being met primarily by conventional fossil fuel resources such as petroleum oil, natural gas and coal, which is highly undesirable given that they are non-renewable and greenhouse gas emitting. Meanwhile, as of 2017, renewable energy accounted for an estimated 18.1 % of total final energy consumption (TFEC), which includes renewable energy source such as hydropower, bio-power, wind and solar photovoltaics (1). This leads to a serious energy challenge which must address the balance between energy demand and supply, whilst considering sustainable development. This includes the production, transmission, distribution, and energy conversion of the fuel (3). In particular, renewable fuels are favourable energy sources for power generation, and there has been an increased demand for renewable electricity, of around 25 % between the years of 2013 and 2017 (1).

An efficient means of power generation, addressing the issues of both sustainability and net zero carbon emissions is one based on fuel cell technology (4). Fuel cell technology converts the chemical energy in a fuel to electrical energy by reacting it with oxygen or air. A commonly used fuel is hydrogen which is a "green" means of power generation, since its combustion by-product is water (H_2O) thus contributing favourably to the realization of low carbon-energy systems in Europe by 2030 (5). However, common methods for the generation of hydrogen have entailed inefficient production routes that use fossil fuels. Alternative methods, such as the electrolysis of water to form hydrogen via the hydrogen evolution reaction (HER) and oxygen via the oxygen evolution reaction (OER), is a more environmentally friendly and sustainable way of generating the chemical fuel (6). Through their recombination, chemical energy can then be converted into electricity, which is the fundamental operating principle behind the Polymer Electrolyte Membrane Fuel Cell (PEMFC) technology, involving the hydrogen oxidation reaction (HOR) and oxygen reduction reaction (ORR).

Fuel cells can have a wide range of applications, from use in small portable devices such as mobile phones or laptops to more energy demanding applications like electric vehicles or industrially for heat and power generation (4). In addition, the thermodynamic efficiencies of fuel cells is higher i.e. 40-60 % compared to the 35 and 20 % efficiencies of conventional power plants and gasoline engines respectively (7). Fuel cell technology has an additional favourable advantage of high electrical efficiency, which is maintained even at the very small scale units with negligible emissions (7).

However, this technology has had limited applications due to its high expense, which has hindered its global popularity and commercialization. The major contribution to these high costs arises from the use of expensive raw materials as catalysts, which are prone to poisoning from impurities in the fuel and so have wide-ranging stabilities (5). Other challenges faced with fuel cells is their short durability (useful lifetime of 5-6 years) compared to the lifetime of energy generated from coal and gas. Moreover, more popular challenges are associated with the production, transportation and storage of hydrogen which is more commonly referred to as an issue of infrastructure (7). Nevertheless despite these challenges, the interest in the development of fuel cell technology and specifically for use in portable devices received great attention as it is an efficient means of generating power.

In particular, to support the integration of fuel cell technology in a low-carbon economy by 2050, several targets have been set (7). This includes:

- Reducing the production cost of fuel cell systems by a factor of 10.
- Increasing the electrical efficiency of fuel cells for power production by 10 % from the current level (40-50 %) (7).

1.1.1 Polymer Electrolyte Membrane Fuel Cells (PEMFC)

Brief historical overview of fuel cells

The origin behind the operating principles of fuel cell technology can be credited to the work of Christian Friedrich Schönbein (1799-1868), where in 1839 Schönbein was the first person to report the generation of current from the combination of hydrogen and oxygen i.e. hydrogen fuel cell. However, the invention of fuel cells and their development as an energy generating technology was accredited to Sir William Robert Grove (1811-1896), who demonstrated a means for producing electricity through the combination of hydrogen and oxygen in 1845 (8). Following these two remarkable scientific discoveries, other scientists began to explore the development of this technology as a means of generating power. In particular, in 1894, Friedrich Wilhelm Ostwald emphasised the great potential of storing and generating energy via an electrochemical process, encouraging mankind to replace the conventional heat engines with fuel cells which offered higher efficiencies. This has since been the ambition in the field of energy generation, with many research interests focusing on the development and commercialisation of fuel cell technology as a renewable and efficient means of power generation (8).

A fuel cell can simply be described by its three components, including a fuel electrode (anode), an oxidant electrode (cathode) and an electrolyte medium (a proton conducting membrane). The catalytic oxidation of the fuel (at the anode) results in the generation of electrons and ions. The electrons are diverted to an external circuit, generating electricity, while the ions are transported through the electrolyte to the cathode. The ions recombine with the oxidant at the cathode electrode generating the reaction by-product i.e. exhaust as shown in figure 1.

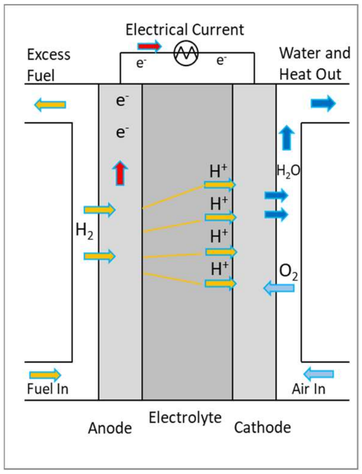

Figure 1- *Schematic diagram of Polymer Electrolyte Membrane (PEM) fuel cell compartment. Adapted from (8).*

A range of fuel cells have been developed over the years based on this operating principle, and have been differentiated by the type of electrolyte medium used in the fuel cell e.g. alkaline fuel cells (AFC), solid oxide fuel cells (SOFC), phosphoric acid fuel cells (PAFC), molten carbonate fuel cells (MCFC), and proton-exchange (or polyelectrolyte) membrane fuel cells (PEMFCs). The latter class is the primary focus of this research project and we focus our attention to the reactions that occur in this type of fuel cell.

1.1.2 Electrochemical Reactions in a PEMFC

The PEMFC is highly attractive as it operates at low temperatures, typically between 60 to 80 °C, which enables both quick warm-up and start-up times, and it also responds to load changes rapidly. Compared to other types of fuel cells, the PEMFC has a high efficiency which makes its application for transport and portable fuel cell-applications appropriate (9). However, like the majority of fuel cells, this technology uses a precious metal platinum catalyst which contributes to around 55 % of the total expense (3). Two common electrolyte media in the PEMFC operating in acidic environments include either: phosphoric acid (high temperatures) or Nafion^{TM}, a sulfonated tetrafluoroethylene-based membrane (low temperatures), both producing power densities greater than 500 mW cm^{-2} (5). The main redox reactions that occur simultaneously at the electrodes to generate electrical energy and water (by-product) are shown:

$$Anode: Pt\ \frac{1}{2}H_2\ (g)\ \rightleftharpoons\ H^+(aq) + e^-(m)\ Eq.(1)$$

$$Cathode: Pt\ \frac{1}{2}O_2 + 2H^+ + 2e^- \rightleftharpoons H_2O\ Eq.(2)$$

$$Overall: \frac{1}{2}O_2\ + H_2 \rightarrow\ H_2O\ \ E^0 = 1.23\ V\ Eq.(3)$$

Where E^0 is the standard potential of the reaction.

Recently, more efficient membranes, electrodes, and catalyst materials have been explored to reduce the associated expenses and prolong durability (5). The commonly employed catalyst material at both electrodes is made up of platinum nanoparticles supported on a porous carbon structure. This enables sufficient electrical contact between the electrode and electrolyte and provides high surface areas to establish fast rates of electron transfer and consequently a desirable fuel cell performance (10). However, the hydrogen oxidation reaction (HOR) at the anode is extremely fast, requiring much lower Pt loadings (< 0.05 mg cm^{-2}) compared to the sluggish reaction kinetics of the oxygen reduction reaction (ORR) at the cathode, requiring much higher Pt loadings (0.4 mg cm^{-2}) (11).

However, despite the scarcity of the platinum metal, it remains the optimum catalyst for both of these electrochemical reactions. As a result, research interests have focused on the reducing the fuel cell costs by developing platinum electrocatalysts of reduced metal loadings, without compromising the fuel cell performance. A rational approach in the development process of electrocatalysts has been to focus on controlling the platinum particle size, catalyst shape/dendritic morphology and the catalyst architectural structure (platinum skin, core-shell, or platinum monolayer) (2)&(3). In general, this has ranged from depositing platinum onto a carbon-based catalyst support to alloying of the platinum metal with other transition metals. However, each method gives rise to its own complications when used as the electrocatalyst material. For example, this can entail agglomeration and sintering issues of the platinum nanoparticles after some period of operation on the carbon-based support, or alternatively issues of instability and dissolution effects with time for platinum-metal based alloy material (2). Some methods have developed platinum alloys using noble metals like gold or palladium (9) to overcome the latter problem. Meanwhile, alternative supports to the commonly used furnace black and acetylene black carbon are being developed for supporting the platinum metal such as single walled carbon nanotubes for the HER (12).

1.2 Research aims and objectives

With the aim of reducing platinum metal loadings further in catalytic materials associated with clean fuel and energy production, a novel synthetic biology approach to the platinum nanostructure design involving the use of DNA as a scaffold for the accurate placement of metal atoms is suggested. The design of the material considers the spacing of the individual platinum metal atoms along the backbone of DNA, in order to reduce and control undesirable metal clustering and consequently expose more of the metal active sites, thereby raising the catalytic efficiency of the resultant material. The use of DNA as a versatile tool for self-assembly is emerging in the field of DNA nanotechnology and particularly methods such as DNA origami, where the fabrication of two-dimensional nanostructures is possible. These methods will be employed to achieve the catalyst nanostructure design of well distributed platinum metal on a DNA scaffold. The platinating agent in this study involves the use of the anticancer drug cisplatin, $[Pt\,(NH_3)_2Cl_2]$, due to its extensively studied and well understood covalent interactions with the DNA nucleobases. The ability of this platinum metal complex to form such strong interactions with the DNA is pivotal in ensuring the formation of a robust catalyst precursor material. Lastly, through the combination of the well understood Watson-Crick specific base pairings of the DNA and reported cisPt DNA interactions in the literature, we can specifically control the assembly of the platinum on the DNA template to produce localised and highly distributed platinum active sites suited for catalysing fuel cell reactions like the HER.

1.2.1 Thesis

Experimental work will first investigate and characterise the complex formation between salmon milt DNA and cisplatin in water and the resultant STEM microscopy and electrochemical studies of the resulting dry films formed from these metal-DNA complexes. The studies reveal interesting trends in catalytic behaviour as a function of platinum loading in the HER reaction.

In order to achieve improved conductive and electronic properties of the DNA material as a catalyst support, the non-conductive nature of the DNA molecule needs to be changed such that both improved electrochemical activity and durability is achieved. Chapters 4 to 6 focus on three different methods of addressing this, including:

- Functionalization of single walled carbon nanotubes (SWCNT's) with the DNA-cisplatin material;
- Graphitization of the DNA through the evacuation of the hydrogen and oxygen atoms upon high dose exposure to an electron beam i.e. graphitization;
- Carbonisation of the DNA via a low temperature pseudo pyrolysis process i.e. 255 °C.

Finally, chapter 7 addresses the need to precisely control the metal placement on the DNA via self-assembled nanostructures including DNA origami triangles and Holliday Junction arrays. The advantage of this approach is to achieve electrocatalysts of reduced platinum metal loadings without compromising the fuel cell performance as demonstrated through electrochemical testing for the HER and surface morphology studies, where highly distributed platinum atoms on the DNA nanostructures as opposed to the non-assembled DNA scaffold could be observed. Finally, carbonisation of the DNA in the Holliday junction arrays is achieved as means of overcoming the highly restive nature of the DNA, making the fabricated material more suited for fuel cell technology applications.

In addition, besides the content of this thesis, preliminary research work, involving the study of the complex oxygen reduction reaction (ORR) have been made. Initially, this was explored at different electrode surfaces (platinum (Pt), pallidum (Pd), gold (Au) and glassy carbon (GC)) in dimethyl-sulfoxide and aprotic solvents*,* resulting in publications (13) and (14) respectively. Although experimental studies for the ORR at the surface of DNA/DNA-cisPt/DNA-cisPt-SWCNT modified glassy carbon electrodes have been made, due to the project capacity and the current situation imposed by *Covid-19*, data collection was limited and remarkable conclusions from the data collected could not be included in this thesis. However, suggestions for future work is made.

References

1. Kusch-Brandt. Urban Renewable Energy on the Upswing: A Spotlight on Renewable Energy in Cities in REN21's "Renewables 2019 Global Status Report." Vol. 8, Resources. 2019. 139 p.

2. Zhu J, Hu L, Zhao P, Lee LYS, Wong KY. Recent Advances in Electrocatalytic Hydrogen Evolution Using Nanoparticles. Chem Rev. 2020;120(2):851–918.

3. Wang YJ, Zhao N, Fang B, Li H, Bi XT, Wang H. Carbon-Supported Pt-Based Alloy Electrocatalysts for the Oxygen Reduction Reaction in Polymer Electrolyte Membrane Fuel Cells: Particle Size, Shape, and Composition Manipulation and Their Impact to Activity. Chem Rev. 2015;115(9):3433–67.

4. European Commission. Hydrogen Energy and Fuel Cells. Directorate-General for Research 2003 Directorate-General for Energy and Transport. 2003. EUR 20719 EN.

5. Gasik M. Materials for Fuel Cells. Woodhead Publishing; 2008.

6. Shiva Kumar S, Himabindu V. Hydrogen production by PEM water electrolysis – A review. Mater Sci Energy Technol. 2019;2(3):442–54.

7. Niakolas DK, Daletou M, Neophytides SG, Vayenas CG. Fuel cells are a commercially viable alternative for the production of "clean" energy. Ambio. 2016;45(1):32–7.

8. Page KA, Rowe BW. An overview of polymer electrolyte membranes for fuel cell applications. ACS Symp Ser. 2012;1096:147–64.

9. Selvarani G, Selvaganesh SV, Sridhar P, Pitchumani S, Shukla AK. Pt-Au/C cathode with enhanced oxygen-reduction activity in PEFCs. Bull Mater Sci. 2011;34(2):337–46.

10. A C, S T, Ould SId E C, M C, M M, A K. Development of Graphite-DNA Polymer Composites as Electrode for Methanol Fuel Cells. J Mater Sci Eng. 2017;6(2):6–9.

11. Shao M, Chang Q, Dodelet J-P, Chenitz R. Recent Advances in Electrocatalysts for Oxygen Reduction Reaction. Chem Rev. 2016;116(6):3594–657.

12. Tavakkoli M, Holmberg N, Kronberg R, Jiang H, Sainio J, Kauppinen EI, et al. Electrochemical Activation of Single-Walled Carbon Nanotubes with Pseudo-Atomic-Scale Platinum for the Hydrogen Evolution Reaction. ACS Catal. 2017;7(5):3121–30.

13. Hendi R, Robbs PH, Sampson B, Pearce R, Rees N V. The electrochemical reduction kinetics of oxygen in dimethylsulfoxide. J Electroanal Chem. 2018;829(July):16–9.

14. Azhar A, Manyepedza T, Oladeji A V., Hendi R, Rees N V. The electroreduction of oxygen in aprotic solvents. J Electroanal Chem. 2020;(xxxx):113989.

Chapter 2- Theory and Literature Survey

Chapter 2: Theory and Literature Survey

2.1 Introduction

In this chapter the key principles behind electrochemical processes are reviewed and the mechanism for the hydrogen evolution reaction (HER) is outlined. The aim is to support the understanding behind the experimental methods employed in this work, to assess the feasibility of the fabricated electrocatalyst material for its intended application in fuel cell technology. A thorough literature review is made to highlight the relevant and recent research around the synthesis of electrocatalyst materials for the HER. Furthermore, the emerging field of using DNA as a versatile tool for nano-construction is discussed to reflect on how this can aid the synthesis of a self-assembled heterogeneous electrocatalyst material. Specifically, this is done by focusing on how DNA origami has been used to fabricate two-dimensional (2D) nanostructures using DNA templates. Subsequently, considerations on how the metal atoms can be incorporated into the DNA scaffold is made by outlining the common approaches taken in the literature. Finally, a literature survey is conducted to portray the feasibility of using the common anti-cancer drug, cisplatin (cisPt), as a platinating agent for the DNA. Particular attention is paid to experimental reports on the employment of DNA as a support for common electrocatalyst materials such as platinum, palladium, or nickel, for electrochemical reactions including the HER.

2.1.1 Thermodynamics

Electrochemistry is concerned with the generation of electrical energy from a chemical reaction when the transfer of electrons occurs during a series of reduction and oxidation (redox) processes.

The transfer of electrons in a redox process is governed by three significant phenomena including thermodynamics, mass transport and kinetics. The transfer occurs at the surface interface of the electrode and molecule. The electrical potential difference between the electrode and the analyte only develops when an equilibrium is set-up between the metal (electrode) and the solution (analyte). Previously, we established that at dynamic equilibrium no charge transfer takes place across the interface. A typical electrochemical process is described by equation (1) and will form the basis for the considerations made for the phenomena discussed in the following section.

$$A + e^{-} \underset{k_a}{\overset{k_c}{\rightleftharpoons}} B \; Eq.(1)$$

Where A and B refer to the oxidised and reduced species respectively. The cathodic and anodic rate constants (k_c) and (k_a) are a function of the applied potential. At dynamic equilibrium, this process is best described by a fundamental relationship known as the Nernst equation, shown below:

$$E = E_f^0 + \frac{RT}{nF} ln\left(\frac{[A]_{bulk}}{[B]_{bulk}}\right) Eq.(2)$$

Where E refers to the potential of the electrode versus a standard reference at which no current flow is observed. E_f^0 is the formal reduction potential of the redox couple and $[A]_{bulk}/[B]_{bulk}$ are the bulk concentrations of the reduced and oxidised species. R is the universal gas constant (8.314 J K^{-1} mol^{-1}), T is the absolute temperature (K), n is the number of electrons transferred and F is Faraday's constant (96485 C mol^{-1}).

2.1.2 Reaction rates

The redox reactions that occur in electrochemical processes involve both a change in the Gibbs energy and a transfer of electrical charge. The reaction rate at which the electrochemical reactions occur at the surface are determined by an activation energy barrier that the charge must overcome to move the electrolyte to the electrode surface. This is dependent on the rate at which the electrons are released (or consumed) leading to the flow of electrical current.

The current flow (I) can be measured as a function of charge transferred and consumption of reactant per unit area i.e. mass flux (J) as shown:

$$I = nFAJ_A \; Eq. (3a)$$

Where n is the number of electrons transferred, F is Faraday's constant, A is the electrode area and J_A is the mass flux of species A (mol cm^{-2} s^{-1}). The '*nF*' term is the charge transferred component (C mol^{-1}). A positive current value is indicative of oxidation whilst negative current implies reduction. This convention refers to anodic and cathodic current flow respectively (1). As a result, the reaction rate can be easily measured through a current measuring device (2), which is reflective of the net current of the reaction i.e. the difference in the anodic and cathodic currents on the electrode.

For an electrochemical process such as that shown by equation (1), the net current is the resulting difference between the electrons released and those consumed in the redox reactions. Expression (3a) takes the following form for measuring the net current density output, (i, A cm^{-2}), of the process:

$$i = nF[J_a - J_c] = nF\big[k_c[A] - k_a[B]\big] \; Eq. (3b)$$

Where k_c and k_a are the cathodic and anodic reaction rate coefficients respectively (s^{-1}) and [A] and [B] are the surface concentration of the reacting species (mol cm^{-2}).

Under equilibrium conditions, the net current is equal to zero, which means the forward reaction rate (reduction) is equal to the backward reaction rate (oxidation). The rate at which this occurs (i.e. at equilibrium) is known as the exchange current density [i_0].

2.1.3 Exchange current density

The exchange current density (i_0) is a measure of the current output per unit of electrode geometrical area i.e. A cm^{-2}. For an electrochemical process, i_0 is equivalent to the rate constant in chemical reactions. However, i_0 is a function of concentration as well as temperature. Furthermore, parameters such as electrode catalyst loading, catalyst specific surface area and surface roughness also influence the effective exchange current density. A high exchange current density is indicative of a highly active electrode surface and consequently a lower energy barrier for the electrical charge transfer to occur (2).

2.2 Electrode kinetics

2.2.1 The Butler-Volmer (BV) equation

The transfer of electrons from the electroactive species to the working electrode surface and vice versa, can be quantitatively described using phenomenological and theoretical principles. This is achieved using the Butler-Volmer (BV) formulation describing the kinetics at the electrode. The electrochemical rate constants based on the BV theory of electron transfer is given below by expressions (4) and (5) for an anodic and cathodic process respectively.

$$k_a = \ k_0 exp\left[\frac{\beta F(E - \ {E_f}^0)}{RT}\right] \ Eq.(4)$$

$$k_c = k_0 \ exp\left[\frac{-\alpha F(E - \ {E_f}^0)}{RT}\right] \ Eq.(5)$$

Where k_0 is the standard heterogeneous electrochemical rate constant (cm s^{-1}) at the formal potential, ${E_f}^0$of the (A/B) redox couple, α is the charge transfer coefficient (β= 1 - α) and E is the potential of the electrode (1). These equations are applicable under the following conditions:

- The solution species are within a distance of less than 10-20 Å from the electrode surface.
- The drop-in potential between the electrode and the bulk solution must also occur within a similar distance i.e. < 10-20 Å from electrode surface.

These conditions have normally been acquired using an appropriate supporting electrolyte, for example for aqueous environments this would be potassium chloride (KCl) or tetra-*n*-butylammonium salts (e.g. ClO_4^-, BF_4^-, PF_6^-) in non-aqueous environments such as acetonitrile solutions (1).

Overpotential

The relative value of the half-cell potential at equilibrium is significant and can be used to predict the electrochemical behaviour of the cell. When the electrode is polarized to a potential greater than the equilibrium value (E_e), also known as the formal potential (${E_f}^0$), the overpotential (η) is positive leading to oxidation. However at smaller polarization values, a negative overpotential is observed leading to a reduction process (3). The overpotential has been defined in the literature (4) as:

$$\eta = E - {E_f}^0 \ Eq.(6)$$

A different form of the BV formulation can be used to express current as a function of overpotential, thereby describing the charge transfer across an electrified interface for a range of electrochemical potentials. Therefore, the overpotential measured at a given current is reflective of the activation energy required to drive the heterogeneous process. By introducing equations (4-6) into equation (3b), the net current density (i) for an electrochemical process can be described by:

$$i = i_f - i_b \ = -nF \ \left\{k_0[A] \ exp\left[\frac{-\alpha F\eta}{RT}\right] - k_0[B] exp\left[\frac{\beta F\eta}{RT}\right]\right\} \ Eq.(7)$$

where i_f and i_b are the forward and backward current densities respectively, α is the transfer coefficient and η is the overpotential (in V) (2).

At equilibrium , the net current density (*i*) is zero, therefore the current density becomes the exchange current density (i_0) such that:

$$i_0 = nFk_0[A]\ exp\left[\frac{-\alpha F\eta}{RT}\right] = -nFk_0[B]exp\left[\frac{\beta F\eta}{RT}\right]\ Eq.(8)$$

Therefore by combining expressions (7) and (8), a theoretical relationship between the current density and potential can be derived, which also measures the net rate of reaction for a single electron transfer process. This is known as the 'Butler-Volmer' (BV) equation:

$$i = -i_0\left\{exp\left(\frac{-\alpha\eta F}{RT}\right) - exp\left(\frac{(1-\alpha)\eta F}{RT}\right)\right\}\ Eq.(9)$$

This form of the BV expression is applicable for a one electron transfer process and reactions in which the electron transfer process is the rate determining step. This means mass transport limitations are negligible.

The transfer coefficient α is commonly between 0.3 - 0.7, and is a measure of the proportion of the applied overpotential exerted to the forward reaction. These expressions are valid for describing the electrode kinetics provided that mass transfer effects are negligible in the process. The exchange current density (i_0) serves as a good indicator for assessing the feasibility of an electrochemical process. For example, when a small exchange current is measured, it implies the need for a high overpotential to achieve high current flow, meanwhile a large exchange current value implies that a low overpotential is required to establish current flow.

However, this method becomes limited when the forward and backward reactions have different overpotential requirements, such as the reactions of the H_2/O_2 PEMFC. In this case, the exchange current density for the oxidation of hydrogen on the surface of platinum is around 5-6 times greater than that for the reduction of oxygen (5). This results in high voltage losses and low efficiency, which can be overcome by using a platinum electrocatalyst at the cathode side to increase the reaction kinetics (5).

2.2.2 The Tafel Law

For a simple process like that described by equation (1), the relationship between an arbitrary potential *(E)* imposed on the working electrode and the net flux is made up of the contribution due to the reduction current as a result of species *A* gaining an electron and the oxidation current due to the removal of an electron from species *B*. The net flux, *J*, (mol cm^{-2} s^{-1}) i.e. current output is given by:

$$j = -k_0 exp\left[\frac{-\alpha F(E - E_f{}^0)}{RT}\right][A]_0 + k_0 exp\left[\frac{+\beta F(E - E_f{}^0)}{RT}\right][B]_0\ Eq.(10)$$

Where the symbols and constants have their usual meanings.

The voltage difference at equilibrium drives the electrochemical reaction and is referred to as the activation polarization or overpotential (η). This is normally associated with sluggish electrode kinetics and so the higher the exchange current density, the lower the activation polarization losses. These losses can be described by the Tafel equation, which takes the following form:

$$\eta = a + b\ log(i)\ Eq.(11)$$

Where the coefficients 'a' and 'b' are defined by:

$$a = -2.3\frac{RT}{\alpha F}\log(i_0)\ Eq. (12)\ \ and\ b = -2.3\frac{RT}{\alpha F}\ Eq. (13)$$

Where the symbols have their usual meanings. The logarithmic plot of the voltage and current relationship enables the derivation of three parameters i.e. the coefficients '*a*' and '*b*', and the exchange current density i_0. This is known as the Tafel plot, from which we can follow and understand the reaction mechanism of the electrochemical process and consequently identify the rate determining step. However, it is the magnitude of the Tafel slope that reveals this information and is highly dependent on the value of the transfer coefficient, (α), see equation (13).

2.2.3 Tafel Plots

Under extreme potentials i.e. $E \gg {E_f}^0$ or $E \ll {E_f}^0$, expression (10) can be simplified down to one term or another, depending on whether we are studying the reduction or oxidation of the electroactive species. For example, considering a reductive electrochemical process, (see forward reaction of equation (1)), this becomes:

$$j = -k_0 exp\left[\frac{-\alpha F(E - {E_f}^0)}{RT}\right][A]_0\ Eq. (14)$$

Provided that the concentration terms i.e. $[A]_0$ and $[B]_0$ are constant over the range of potential values tested and that they are not substantially changed from their bulk values. The expressions for the reduction and oxidation currents take the following forms respectively:

$$\ln|I_{red}| = \frac{-\alpha FE}{RT} + constant\ Eq. (15)$$

$$\ln|I_{ox}| = \frac{\beta FE}{RT} + constant\ Eq. (16)$$

Where I_{red} and I_{ox} are the reduction and oxidation currents respectively. Through the plot of ln[I_{red}] against *E* (or ln[I_{ox}] against *E*) , we construct the Tafel plot from which the value of the transfer coefficients, α and β can be obtained (1). Expressions (15) and (16) are restrictive forms of the Tafel analysis and are applicable for electrochemical systems where depletion of the reactants does not take place and hence mass transport limitations are negligible.

However, if the current response is limited by mass transport, such as attaining a sigmoidal voltammetry response (common at reactions over the surface of microelectrodes or hydrodynamic electrodes), then instead, mass transport corrected forms of the Tafel law are used. This accounts for mass transport limitations as shown in the following expression:

$$\eta = \frac{2.303RT}{\alpha nF}log i_0 + \frac{-2.303RT}{\alpha nF}\log\left[\frac{i_d i}{i_d - i}\right]\ Eq. (17)$$

Where the overpotential (η) equals $E - {E_f}^0$, *R* is the gas constant, *T* is the absolute temperature, α is the transfer coefficient, n is the number of electrons involved, i_0 is the exchange current density, i_d is the limiting current density, and i is the current density (6). The second component in the expression i.e. $\frac{i_d i}{i_d - i}$ refers to the measured component of the current, also known as 'i_K'. This expression is fundamental in gaining a true perspective of the reaction mechanism, as reflected by the magnitude of the Tafel slope attained which can be compared and contrasted with literature reportings.

2.3 Hydrogen Evolution Reaction (HER)

In the former part of this report we mentioned the significance of using the Tafel law and Tafel plots to identity the reaction mechanism based on the electrode kinetics. We turn our attention to the use of Tafel plots for revealing the reaction mechanism for the hydrogen evolution reaction (HER).

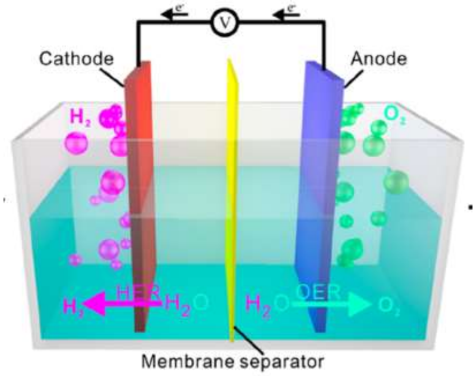

Figure 1- *Hydrogen evolution reaction and oxygen evolution reaction of electrocatalytic water splitting adapted from Zhu et al.* (19).

The HER commonly occurs on a platinum surface, at the cathode, see figure 1, and several mechanisms have been proposed to describe the resulting intermediate products. This entails an electrochemical hydrogen adsorption step (Volmer reaction), an electrochemical desorption step (Heyrovsky reaction) or a chemical desorption step (Tafel reaction).

Under alkaline conditions, this reaction takes place via two of the three elementary steps proposed:

$$H_2O + e^- \rightleftharpoons H_{ads} + OH^- \; (Volmer) \; Eq. (18)$$

$$H_2O + H_{ads} + e^- \rightleftharpoons H_2(g) + OH^- \; (Heyrovsky) \; Eq. (19)$$

$$2H_{ads} \rightleftharpoons H_2(g) \; (Tafel) \; Eq. (20)$$

This includes either a Volmer-Heyrovsky (V-H) or a Volmer-Tafel (V-T) route (7). On the other hand, in acidic conditions the proposed reaction mechanism can entail two of the three reaction steps:

$$H^+ + e^- \rightleftharpoons H_{ads} \; (Volmer) \; Eq. (21)$$

$$H_{ads} + H^+ + e^- \rightleftharpoons H_2 \; (Heyrovsky) \; Eq. (22)$$

$$2H_{ads} \rightleftharpoons H_2 \; (Tafel\ ) \; Eq. (23)$$

This also includes either a Volmer-Heyrovsky (V-H) mechanism or a Volmer-Tafel (V-T) route. The reaction mechanism can be revealed by the slope of the Tafel plots, as shown in figure 2.

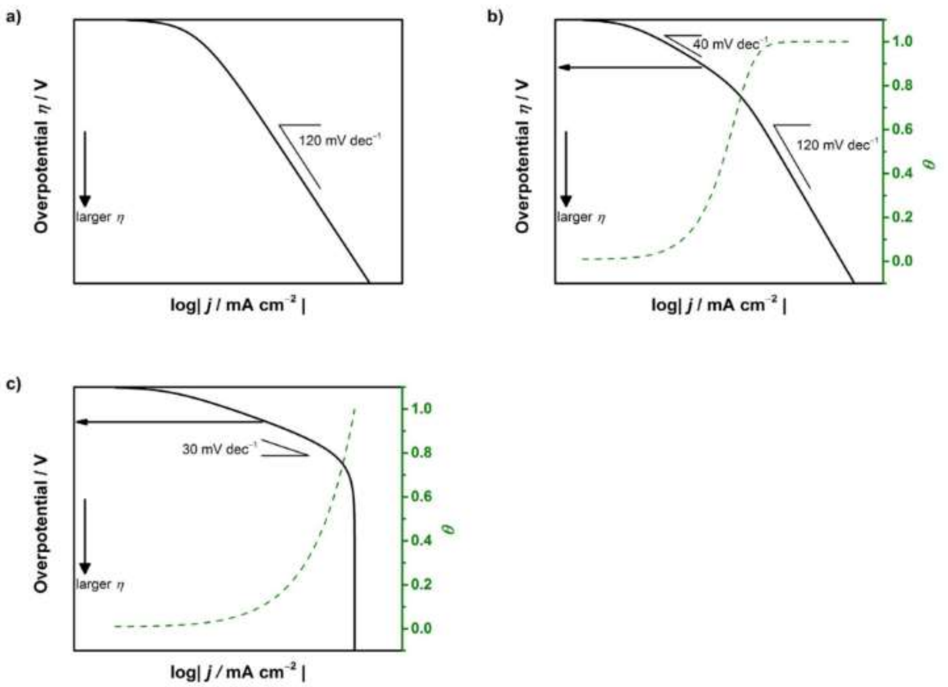

Figure 2*- Simulated behaviour of the Tafel relation for the hydrogen evolution reaction assuming (a) Volmer reaction, Equation 21 (or 18), (b) Heyrovsky reaction, Equation 22 (or 19) and (c) Tafel reaction , Equation 23 (or 20) as the rate-determining adapted from Shinagawa et al.* (63).

Therefore by comparing the experimental Tafel slopes to the reported theoretical limits for the Volmer, Heyrovsky and Tafel steps i.e. 120, 40 and 30 mV dec^{-1} respectively, the rate determining reactions can be identified. In the work of Zalitis et al. (8), a poor performance of platinum in alkaline environments was shown whilst they showed that platinum is an ideal catalyst for the hydrogen oxidation reaction (HOR) or the HER under acidic conditions (8). Commonly, platinum disks and high surface area catalysts have shown a Tafel limiting step (slope of -30 mV dec^{-1}), where a more detailed analysis of this is discussed in the literature (9), (10) and (11).

2.4 Voltammetry at a heterogonous electrocatalyst surface

The main difficulty in modelling heterogeneous catalytic processes is the true representation of the texture of the porous catalyst material. The employed experimental methods for assessing the electrocatalytic performance of the fabricated material will inevitably result in film variation across the electrode surface, giving rise to different and random distributions of active and inactive regions. This means the electrochemical activity will vary across the electrode surface. In this section, we show how the diffusion profile of the electrode surface can be identified by drawing correlations between the experimental measures of the electrocatalysis compared with the theoretical predictions we expect. For example, by relating the timescale of the voltammetry process to the distance diffused by the electroactive species, we can understand the voltammetry attained using methods commonly employed in the literature (12). In the following section, the surface profile of the electrode-electrolyte interface will firstly be reviewed to gain a better understanding of the concept of the diffusion layer thickness.

2.4.1 Electrical double layer

The fundamental principles behind electron transfer can be understood by firstly appreciating the variation in the distribution of charge at the electrode-electrolyte interface. The distribution can influence the kinetic rate of the electrochemical process and can be controlled by the addition of excess electrolyte. Various models of the electrical double layer have been developed. The Stern and Grahame model provide a good representation of the electrical double layer (EDL) at the electrode-electrolyte interface, see figure 3. The electron transfer process begins with the electroactive species entering the electrical double layer, most commonly via diffusion. Once it is within a distance of approximately 10 Å, it reaches the plane of electron transfer (PET) where there is a reasonable probability of electron tunnelling. The molecule may need to undergo structural reorganisation, and/or reorientation to consequently give up (or take) electrons in the least activation energy requirements. This is best described by the Marcus Theory, where a parameter known as the reorganisation energy (λ) describes the energy needs for the reorganisation of the reactant bonds and surrounding solvents to match those found in the product (13).

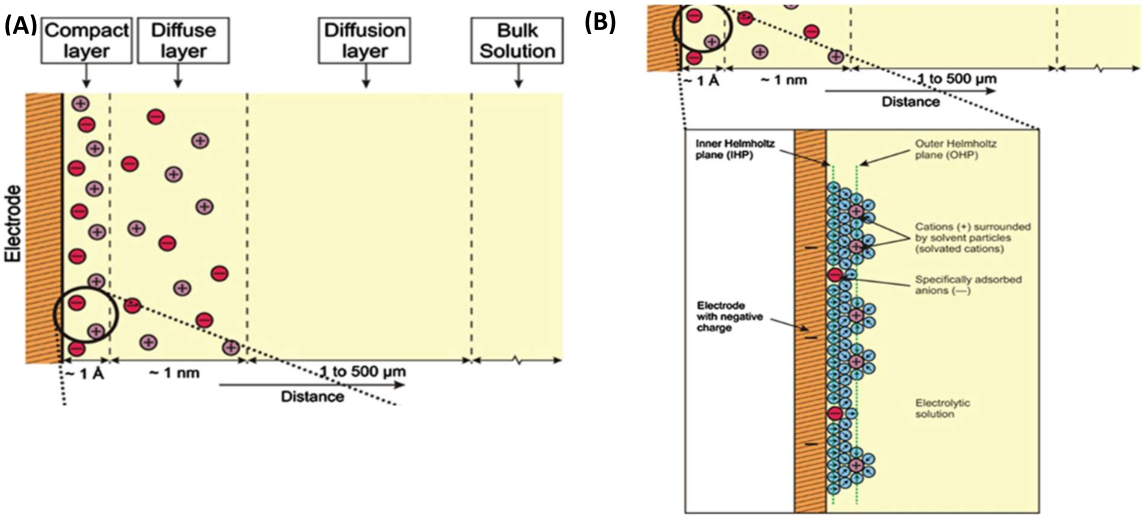

Figure 3 *- Schematic diagram of the electrical double layer with distance from electrode surface adapted from Brownson et al.* (14).

The interface is made up of three key regions, including a metal layer (the electrode), a diffuse layer and an inner layer. The compact layer which is also known as the Inner Helmholtz Plane (IHP), describes the closest region in which the solvated ions can reside. In this layer, the change in potential is linear with distance from the electrode surface. On the other hand, in the diffuse layer the changes observed are exponential (14). The diffuse layer refers to the region that is between the bulk and Outer Helmholtz Plane (OHP) i.e. the closest plane of non-specifically adsorbed species see figure 3(B) (4).

The diffusion layer thickness (δ) is a function of the diffusion coefficient of the electroactive species, as described by the Nernst diffusion layer model:

$$\delta = \sqrt{2Dt}\ Eq.(24)$$

Normally the size of the diffusion layer is an order of magnitude larger than the diffuse layer. The Nernst diffusion layer (linear diffusion layer) is useful since from this thickness, we can infer the efficiency of the diffusion process taking place and extent of the region in the solution where the concentration of electroactive species begins to change, as presented in the following section. Furthermore, from the diffusion layer thickness (δ), we can predict both the contribution of convective mass transport to the process and the diffusion profiles over the heterogeneous catalyst surface (15,16). In the following section, the correlations drawn between the diffusion layer thickness (δ) and the diffusion processes that occur over the different electrode surface morphologies are presented.

2.5 Semi-infinite diffusion

For uniformly accessible active sites on the electrode surface, e.g. (hemi)-spheres and cylinders, mass transport occurs predominantly by diffusion. The driving force for the transport process is concentration gradient, described by a single spatial co-ordinate reflective of the direction normal to the electrode surface (15). Near the electrode surface, there is a special region commonly referred to as the boundary layer (10^{-2} cm thick) in which the concentration of both the oxidised and reduced species is a function of their distance from the electrode surface (4). However, at distances further away from the electrode surface, natural convection can occur, which establishes a well-mixed region (14).

The linear diffusion layer thickness (δ) is defined as the distance to the electrode surface where the linear concentration profile takes the bulk value c_{bulk}, as shown in figure 4.

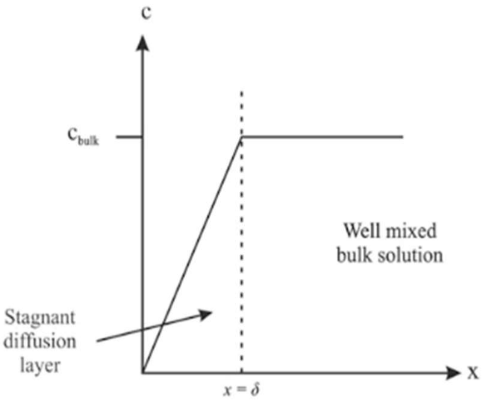

Figure 4 - *The concentration profile of the electroactive species with distance from the electrode surface adapted from Brownson et al.* (14).

The process of diffusion is best described mathematically by Fick's first law of diffusion:

$$J_A = -D_A\left(\frac{d[A]}{dx}\right)\ Eq.(25)$$

where J_A is the molar flux of species A (mol cm^{-2} s^{-1}) , D_A is the diffusion coefficient of A (cm^2 s^{-1}) and $\frac{d[A]}{dx}$ is the concentration gradient of A (1). Diffusion coefficients are a function of temperature and can be described in a similar form to Arrhenius equation using:

$$D = D_\infty exp\left(\frac{-E_a}{RT}\right)\ Eq.(26)$$

Where E_a is the activation energy for diffusion and $D_\infty$is the hypothetical diffusion coefficient at an infinite temperature. This thermo-sensitive dependence suggests the need for thermostatically controlled experiments in voltammetry. The activation energy can be determined from an Arrhenius plot of ln D vs T^{-1}.

2.6 Diffusion in rough nano-porous surfaces

The process of mass transport becomes more complex when we move from an electrochemical process involving a uniform electrode surface to that involving heterogeneous catalysts. This is because the diffusional processes that occur when heterogeneous catalyst surfaces are employed is a function of the surface morphology and topology of the catalyst material, thereby resulting in additional forms of mass transport. This entails the transition from semi-infinite diffusion to thin-layer diffusion or even the mixed combination of the two. In addition, the diffusion of molecules through the porous network, gives rise to collisions of the molecules with the pore walls as opposed to their intermolecular collision i.e. Brownian motion. As a result of these collisions, the molecules interact with the active sites on the wall resulting in a reaction (17). This is known as the Knudsen diffusion, a predominant mechanism of transport for the reactions of gases in mesoporous materials (2 - 50 nm). This means the surface roughness of the wall should be accounted for when modelling the reactions over heterogeneous surfaces as reported in the literature (17).

2.6.1 Semi-infinite diffusion vs thin layer diffusion

Understanding the transition from semi-infinite diffusion to thin-layer diffusion is important for understanding the charge transport processes that occur in porous media. In the context of electrochemical processes, it is important to distinguish between enhanced transport effects resulting from the nano-confinement of the catalyst material (thin layer diffusion) to that occurring from the diffusion of solute in bulk solution onto the porous layer on the electrode surface (Fickian diffusion) giving rise to thin-layer diffusion (18).

To best describe the difference between semi-infinite and thin layer diffusion, we focus the discussion on a macro-electrode surface modified with a conductive porous layer such as carbon nanotubes (CNTs).

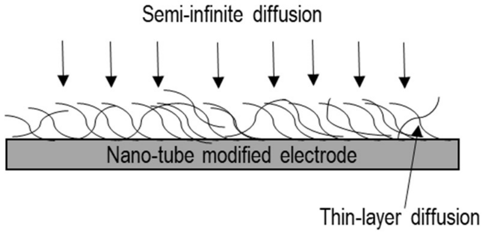

Figure 5 *- Schematic of the two types of diffusion that contribute to the current output at the surface of the carbon nanotube modified electrode reproduced from Batchelor-McAuley et al.* (15).

In this case, the mass transport of solute to the conductive surface (the macro-electrode and CNTs) takes place by two components. Firstly, via semi-infinite diffusion from the bulk solution to the surface of the porous layer and secondly via thin layer diffusion due to diffusion transport within the porous layer, as illustrated in figure 5.

Alternatively, provided that the packing density and thickness of the porous layer is high, the diffusion process can be modelled as ‘thin layer’ since the distance that needs to be diffused by the solute is shorter than that for semi-infinite diffusion conditions (15).

Moreover, Batcheor-McAuley et al. demonstrated that the transition in the predominant diffusion process is reflected in the voltammetry response, as shown in figure 6 (14).

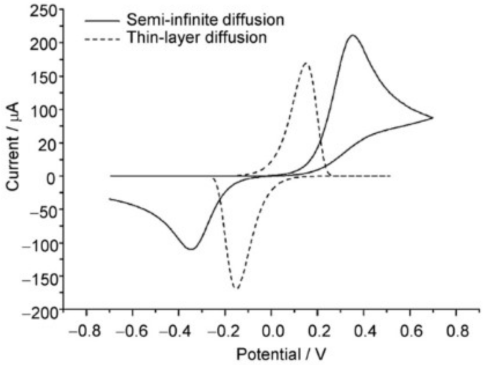

Figure 6- *Comparison of linear sweep voltammetry using a semi-infinite and thin layer planar diffusion models, adapted from Batchelor-McAuley et al.* (15).

Where for both diffusion models, the voltammetry response was modelled using the following parameters: a rate constant (k_0) of 10^{-4} cm s^{-1}, D of 10^{-5} cm^2s^{-1}, υ of 0.1 V s^{-1} and a concentration of 10^{-6} $molcm^{-3}$. At the electrode surface, for the semi-infinite diffusion model, an area of 1 cm^2 was used while for the thin layer model an area of 30 cm^2 and a layer thickness of 1 µm was assumed (15).

It is evident from figure 6, that for the thin layer diffusion model, the peak-to-peak separation is lower than that in a semi-infinite process, due to the changes in mass transport. The shift in peak potential to a lower value in a thin layer model arises because of the reduced distances needed for the diffusion process. Eventually as the diffusion is reduced, the peak potential will tend to a limiting value equivalent to the formal potential of the redox couple in the electrochemical process. This explains why heterogeneous catalyst surfaces can result in overlapping voltammetry peaks i.e. changes in mass transport induce a change in the electron transfer kinetics (15).

Lastly, in extreme cases, a mixed contribution of the two diffusion processes can be observed. This is reflected in the voltammetry with the appearance of two peaks in the electrochemical process (a single A/B redox couple), one attributed to a thin-layer process and the other to a semi-infinite diffusion (15). This mixed contribution of thin layer and semi-infinite diffusion in principle is useful in identifying the heterogeneous rate constants for quasi-reversible and irreversible electron transfer processes (17).

2.7 Knudsen self-diffusion

Self-diffusion refers to the translational mobility of individual molecules under conditions of thermodynamic equilibrium. The diffusion of an individual molecule can be described by Einstein's equation , which shows that the squared displacement of the molecule from its original position will eventually increase in a linear fashion with time (17), as expressed below:

$$x = \sqrt{2Dt} \quad Eq. (27)$$

Where *x* is the distance diffused, *D* is the diffusion coefficient and *t* is time. This equation implies that the movement of a diffusing species is reduced greatly with the distance from its source i.e. region of high concentration, or electrode generating the species of interest in context of electrochemistry.

As a result of the complexity that can arise from the different diffusional transport processes in heterogeneous catalysis, the shape and magnitude of the voltammetry response are dependent on a range of factors. This includes the size of the individual electrodes, the size of the diffusion zones (δ), and the size of the diffusion zones compared with the size of the insulating material which separates neighbouring active spots (the centre-to-centre separation, (d)) (12). For example , the voltammetry of a microelectrode array can be described by one (or a combination) of four cases, depending on the size of the individual microelectrode and diffusion zone (δ), as shown by Davies et al. (12) and detailed in chapter 4.

2.8 Randles-Ševčík equation

The important parameters of a cyclic voltammogram, (see figure 2, chapter 3), include the magnitudes of the cathodic and anodic peak currents ($i_{p,c}$ and $i_{p,a}$ respectively) and the potentials at which these currents are observed ($E_{p,c}$ and $E_{p,a}$ respectively). These electrochemical parameters can consequently be used to calculate the formal reduction potential (E_f^0), which is located half-way between $E_{p,\,a}$ and $E_{p,\,c}$ and the number of electrons (n) transferred in the charge transfer reaction. The ratio of the anodic and cathodic current should ideally be near unity for a reversible (fast) electrochemical process. The diffusion coefficient value (D) can be found from the peak current value (i_p) (1). For a one-electron reversible process, the Randles-Ševčík equation is given by:

$$i_p = 0.446FA\,C_{bulk}\sqrt{\frac{FDv}{RT}}\ Eq.(28\ a)$$

Which can be simplified to

$$i_p = (2.69\ \times\ 10^5)AC_{Bulk}D^{\frac{1}{2}}v^{\frac{1}{2}}\ Eq.(28\ b)$$

where i_p refers to the peak current, A is the electrode area (cm^2), C_{Bulk} refers to the concentration of the analyte in the bulk, n is the number of electrons transferred, v is the scan rate ($V\ s^{-1}$) and D is the diffusion coefficient ($cm^{-2}\ s^{-1}$). On the other hand for (one electron) irreversible processes, a different correlation applies, see equation (29).

$$i_p = 0.496\sqrt{\alpha}FA\,C_{bulk}\sqrt{\frac{FDv}{RT}}\ Eq\ (29\ a)$$

$$i_p = (2.99\ \times\ 10^5)\sqrt{\alpha}AC_{Bulk}D^{\frac{1}{2}}v^{\frac{1}{2}}\ Eq.(29\ b)$$

Where α is the transfer coefficient and can be found theoretically using an appropriate correlation. Under irreversible conditions, the transfer coefficient takes a value between 0 and 1, but is commonly reported to be 0.5 ± 0.2 for a one-electron process (15).

The following section is a literature survey focusing on reviewing the recent literature reporting's for the development of electrocatalyst material for the hydrogen evolution reaction (HER).

2.9 Literature review on HER catalyst materials

Platinum-group metal (PGM)-based catalysts have been reported as the most favourable candidates as the electrode surface for the HER (19), (20). This is due to their high efficiency, resulting from optimum Gibbs energy for atomic hydrogen adsorption (ΔG_{H*}) and low activation energies for H desorption from the surface (19), see figure 7. The Gibbs free energy ($\Delta G°$) of a reaction refers to the free energy available to do useful work. At equilibrium for an electrochemical cell reaction this is given by:

$$\Delta G° = -nFE°_{cell} \; Eq. (30)$$

Where $\Delta G°$ is measured in joules (J), n refers to the number of electrons transferred in the reaction, F is Faraday's constant (96485 C mol^{-1}) and $E°_{cell}$ is the cell potential (V).

An ideal HER electrocatalyst will have an intermediate hydrogen binding energy (HBE) therefore neither a weak nor strong affinity. If the HBE is weak, a low concentration of protons will be adsorbed onto the electrocatalyst surface. However, if the HBE is too strong, the active sites of catalysts will remain occupied by the adsorbed proton (H*) resulting in catalytic poisoning effects. A spontaneous reaction Alternatively, the Gibbs energy for the atomic hydrogen adsorption (ΔG_{H*}) should ideally be zero (or infinitely close to zero) for an ideal HER electrocatalyst, since the standard hydrogen electrode potential is defined as zero (19).

As a result platinum-based nanomaterials can enable high exchange current densities (i_0) to be established close to the thermodynamic potential of a small Tafel slope, yielding ~100 % Faradaic efficiency (19). Specifically, for the HER, Faradaic efficiency refers to the ratio of the experimental to theoretical amount of hydrogen generation (19).

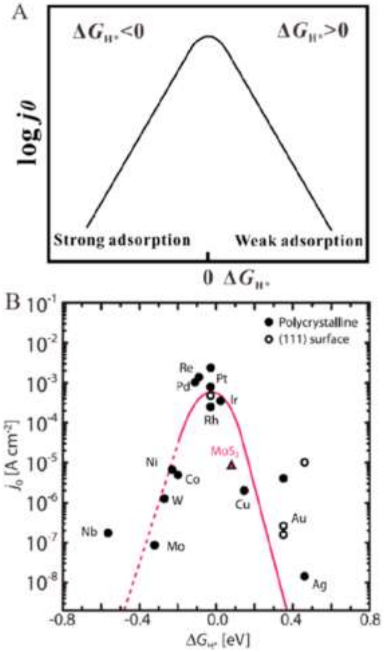

Figure 7- *(A) Relationship between j_0 and ΔG_{H*} under the assumption of a Langmuir adsorption model. Adapted from Zhu et al.* (19) *(B) dependence of j_0 on ΔG_{H*} for HER on the surface of various metals, alloy compounds, and non-metallic materials in acidic medium.*

However, both the high cost and limited availability of the platinum (Pt) has initiated the search for alternative materials/ improved utilization of the noble Pt metal as an electrocatalyst for the HER. This has ranged from reduced platinum metal loadings to metal-free electrocatalysts (21),(22) and (23), to compromise between catalytic activity, durability and costs.

More recently, research aims to fabricate HER electrocatalysts have focused on the use of advanced nanomaterials. The catalytic activity of platinum at the nanoscale varies from that at higher scales given that the electronic properties and surface topography (both a function of particle size) are changed at the nanoscale (1). This enables increased utilisation efficiency of the platinum metal, given that an optimum particle size and improved distributions can be attained, working at the atomic level (19).

Moreover, a popular approach has involved preparing highly stable single atoms of platinum onto an electrically conducting support. However, because of the high surface energy of single metal atoms, the catalyst is more likely to become unstable. To overcome this issue, metal oxide supports have been employed to immobilise single atoms of the Pt catalyst material (24). Alternatively, other methods have designed and prepared catalysts by combining noble and non-noble metals, as alloys or core-shell particles, with improved stabilities (24). However, the electronic interactions between the core materials and the outer layer influence the durability (24). To overcome issues of instability, research interests focusing on achieving good interactions of the Pt atoms with the carbon support have been explored, such as the use of SWCNT’s (24).

Most research aims have focused on reducing the cost of the electrocatalyst material by reducing the platinum content. The catalyst performance is improved by modifying the crystalline and electronic structures. A popular approach for achieving increased mass activities entails dispersing the platinum metal on a high surface area support material such as carbon black, carbon nanofibers or single walled carbon nanotubes. Alternatively, alloying the platinum with other metals like Fe, V, Co or Ti can improve the catalysis since alloying results in a change to the Pt-Pt interatomic distance, which can improve chemisorption of the electroactive species. In addition, it causes lattice strain and consequently a downshift of the d-band centre i.e. the ligand effect (25).

2.9.1 Properties of the Electrocatalyst

The platinum particle size, shape, composition and spatial distribution of the active component are indicative measures of the catalytic performance of the material (26). To reduce the expenses associated with the platinum use, methods to control the size and shape of the platinum nanoparticles have been adopted to maximize its utilisation efficiency.

The catalytic activities are dominated by the size of nanoparticles, for example for the HER , cluster and single-atom catalysts have received great interest since minimal Pt metal loadings can be employed, whilst simultaneously high activities and stabilities can be attained, thus increasing the utilization of surface catalytic atoms (19). Fabrication and control of the material down to an atomic level is attainable using nanotechnology, which will be discussed in more detail in the coming section. Alternatively, a more simple approach focuses on the use of a support material to establish the desired attributes of the catalyst, enabling improved electrocatalytic performance, as discussed below.

2.9.2 Distribution of the active component on support

The employment of a catalyst support material, is another method for achieving improved electrocatalytic performance for the HER. This is primarily due to the attainable distribution of the platinum metal on the support, whereby single-atom catalysts can be produced, increasing the utilisation efficiency (19).

In addition to reduced Pt metal loadings and improved particle size, the support material can enable increased durability of the catalyst, through its interactions with the active component of the catalyst which improve the electronic properties (27).

Carbon materials are commonly used as the platinum catalyst support for PEMFC (28), providing desirable attributes including high electrical conductivity, high specific surface area, high porosity and also good interactions with the platinum (26). In addition, carbon support makes the recycling of used platinum electrocatalyst possible which supports the efficient use of the precious metal (26).

Improved distributions of the platinum particles can lead to enhanced rates of reaction as the catalytic surface area is increased with the metal distribution. This was shown theoretically by Jacob and Goddard (29) using the Density Functional Theory (DFT) for the heterogeneous catalysis of water production on the surface of platinum. The model was conducted for the reactions of H_2 and O_2 over the catalyst surface (29).

However although 'carbon-based support' materials have been the main material of choice for the platinum electrocatalyst there are several concerns with its use including the presence of micro/nano-pores within material such as carbon black, which lead to the entrapment of platinum particles and consequently reduce the PEMFC performance (28). Alternatively, single-walled carbon nanotubes (SWCNTs) are also promising support materials for platinum metal electrocatalysts for the HER, where stable pseudo-atomic-scale metallic Pt (i.e. individual atoms or sub-nanometer clusters) could be fabricated on the carbon network of pristine SWCNTs (30). Through DFT calculations, they suggest that SWCNTs have greater potential than graphene as a catalyst support for Pt atoms, enabling atomic dispersion. Furthermore, they were able to compare the HER activity of the SWCNTs functionalised with Pt atoms to suggest that it was similar to that of bulk Pt (30).

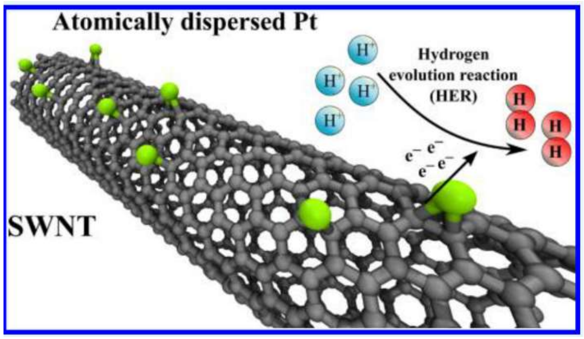

Figure 8- *Atomic distribution of platinum metal on SWCNT support material, copied from Tavakkoli et al.* (30).

2.10 Nanotechnology

Nanotechnology can simply be defined as the ability to work at the molecular level, atom-by-atom, to create large structures with essentially a new molecular organization (31). Nanotechnology has had increased popularity over the years, due to the desirable characteristics that can be achieved at the nanoscale. In the context of catalysis, this evolves from the changes to the atomic and molecular levels with size reduction including increased surface activity and consequently increased kinetic rates.

In order to fabricate structures at the nanoscale, nanolithography has been used for a range of sectors involving semiconductors, medicine and energy harvesting to synthesise material of at least one dimension smaller than 100 nm (32). There are a range of nanolithography methods, for example electron-beam lithography (EBL) (33), however each have had their own limitations, giving rise to process complexity issues during the fabrication process (32). A new emerging field over the years has focused on the utilisation of DNA as a versatile tool for the nanofabrication of structures of defined arbitrary patterns and shapes (34) and (35). The success of this has primarily been attributed to the favourable programmability of the DNA molecule where DNA nano-construction has been more thoroughly reviewed in the literature (36).

2.10.1 DNA Nanofabrication

The nucleic acid (DNA) possesses highly desirable mechanical and chemical properties which makes its use favourable as a construction material in nanotechnology. In particular, its molecular recognition and its unique ability to self-assemble, are two key contributors behind the successful use of DNA in nanofabrication, see Table 1. The employment of DNA in nanotechnology is highly supported by the nanoscale dimensions of the polynucleotide including its double helix diameter of about 2 nm, helical pitch of around 3 to 3.5 nm and a 3.4 nm distance between the base pairs (34).

Moreover, precision at the atomic scale can be attained using the DNA molecule, and its specific and well understood Watson–Crick base pairing, enabling programmability via self-assembly (36). This is discussed and reviewed in greater detail below.

Table 1- *How the DNA molecule features support its application for producing self-assembled structures* (34)**.**

DNA attribute	***Suitability for DNA Origami***
Rigid, well defined non-linear double helix form	Folding of single strands with helpers or self-interactions is possible at defined location targets
Well defined molecular conformation	Accurate predictions can be assumed about the molecule behaviour
Rapid synthesis of oligo's is possible (hours to days)	Simpler processing methods and thus lower expenses
Can incorporate enzymatic manipulations	Reduces the costs associated with DNA synthesis

2.10.2 DNA structure

The DNA molecule is a long polypeptide (polymer) chain normally found in a double helix form. The molecule is made up of three key units including a deoxyribose sugar, a phosphorous group and a nucleotide base. There are four main types of nucleotide bases classified into two categories namely purines (adenine (A) and guanine (G)) and pyrimidines (cytosine (C) and thymine (T)). The base pair interactions occur via Watson-Crick hydrogen bonds where A forms two hydrogen bonds with T and C forms three hydrogen bonds with G. Phosphodiester linkages connect the nucleotides within each strand forming a sugar phosphate backbone which acts as a structural support. This complementary base pairing leads to the distinctive double helix structure (37).

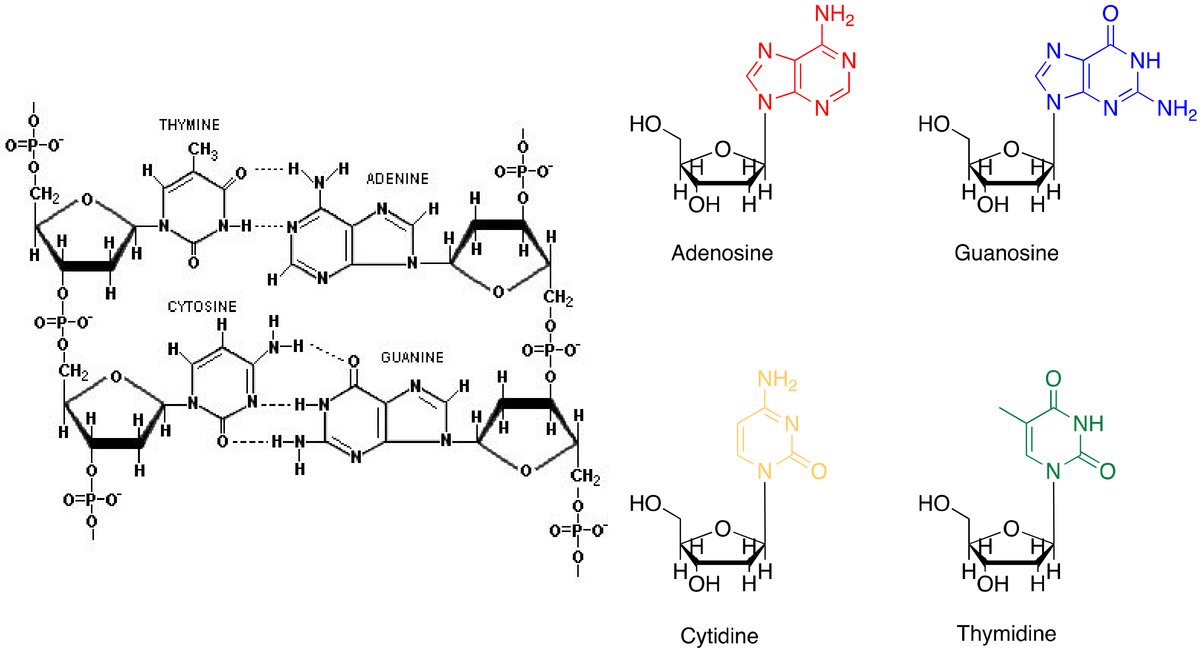

Figure 9*- Chemical Structure of DNA molecule copied from Kortaberria et al.* (64)**.**

2.10.3 DNA origami

DNA origami is the process of nanofabrication involving the folding of a single long strand of DNA to synthesise the desired nanostructure, with the support of smaller oligonucleotides or 'staple' strands in the folding. This method was first introduced by Paul Rothemund in 2006, where he reported the self-assembly of DNA as a method for establishing two dimensional (2D) nanostructures of high precision, (commonly attained using top-down fabrication methods) via a simple bottom-up approach (34). The usefulness of DNA origami templates became recognized and received greater interest in the field of nanotechnology since then.

However, although the DNA origami is primarily based on the ability of the readily engineered molecule to undergo self-assembly to form the desired final complex structure, the 'staple strands' equally have a significant role in accomplishing this, given that these oligonucleotides enable the folding of the DNA into that final shape (38). A range of nanomaterials such as metal nanoparticles, quantum dots and carbon nanotubes could be organized into the desired shapes using DNA origami templates (39). In the interest of this work, 2D nanostructures based on a DNA Holliday Junction (HJ) array are highlighted as a potential scaffold and support material for the platinum metal electrocatalyst.

2.10.4 DNA Holliday Junction arrays

More ordered DNA nanostructures avoiding distortion have been achieved through assemblies based on a of four arm Holliday Junction array. For example, in the work of Tuberfield et.al (40), a three-layer logpile (3LL) that is successfully synthesised from four double-stranded DNA arms. The arms consisted of sticky ends which included 6 unpaired bases, which enabled the formation of the extended array. This is of particular interest in this project, since the DNA can be assembled as a 2D scaffold whereby the platinum distribution can be controlled on the support. This is consequently predicted to result in an improved electrocatalyst performance and efficiency. The theoretical principles behind this controlled covalent interactions between the DNA and the cisplatin are discussed later in the thesis.

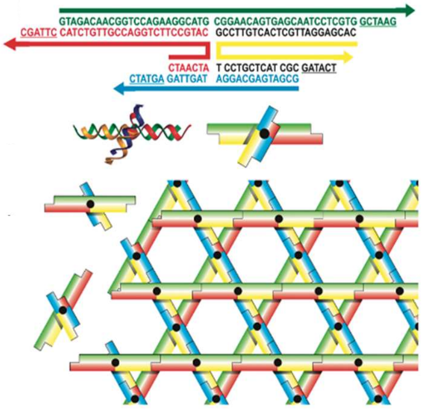

Figure 10 – *Three-layer logpile design showing the structural unit, arrangement of sticky ends and a schematic representation of the lattice, copied from Malo et.al* (40).

The self-assembled structures have had a range of applications from electronics, photonics to artificial enzymatic networks (41).

2.10.5 DNA Metallisation

The metallisation of DNA with metal nanoparticles gives rise to various interesting and useful applications ranging from photonics, therapeutics to electronics and sensing. This process is simple and can be achieved by several ways as reviewed by (42). The principles behind the modification of the DNA with the metal involves one of three methods:

- The binding of the metal to the unmodified DNA
- The attachment of the metal to ligand-modified DNA
- Pre-synthesis of the metal complex and subsequent attachment to the DNA during or after DNA synthesis (43), as illustrated in figure 11.

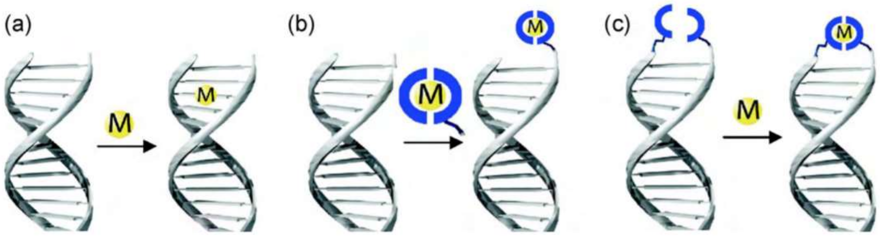

Figure 11*- Methods to site-specifically incorporate metals onto DNA. (a) Metal binding to unmodified DNA. (b) Attachment of metal complexes to DNA (c) metal binding to ligand-modified DNA. Copied from Yang et al.* (43).

The first method (figure 11 (a)) is straightforward, without the need for DNA modification, however results in a low specificity. Alternatively, the other two approaches allow for a more controlled placement of the metal onto the DNA template (43). The metal cations interact directly with the nitrogen atoms and phosphate oxygen atoms of the DNA bases through electrostatic or co-ordination (covalent) interactions. Specifically the main co-ordination sites include the N1 and N7 atoms of the Adenine base, N7 and O6 of the Guanine and the N3 of the Thymine and Cytosine bases (42). The precise positioning of the metal can be achieved by placing the reducing agents/groups at the specific target site of the DNA base(s) (42).

The first reported work on metallised DNA template architectures was made by Yan et al. where gold nanoparticles were successfully synthesized into triangular DNA origami templates. The role of the DNA origami templates was to precisely arrange gold (Au) nanoparticles in a way to prepare linear chains with gap sizes of less than 10 nm (44). Similarly, the association of DNA origami structures with silver nanoparticles and carbon nanotubes (CNTs) has also been achieved. For example, Ding et al. (44) developed triangular structures of DNA origami assembled with silver nanoparticles. Alternatively, Maune et al. (45) proved the ability to arrange CNTs onto a DNA origami complex. These methods illustrate the versatility of the DNA origami technique as a tool for developing structures for a wide range of applications.

Zero-dimensional (0D) metal nanomaterials can be synthesised from the deposition of the metal atoms on a scaffold of DNA by controlling the ratios of the metal ions to the bases, reaction kinetics or parameters, the DNA sequence or conformation (46). In this study, the metallisation of platinum on the DNA will be controlled through the synthesis of a specific base sequence, to precisely place the platinum along the DNA under controlled and desired ratios.

2.11 The interactions of cisplatin with DNA

Cisplatin (cisPt) or cis-diamminedichloro-platinum(II) has been widely used as an anticancer drug since its discovery and approval in 1979, to treat a range of tumours from small cell lung tumours to ovarian, head and neck tumours (47). The mode of action of the drug has been well studied and understood over the years, where it has been reported to work by inhibiting the cellular mechanisms of the DNA molecule by binding directly to the nucleobases.

2.11.1 Reactions of cisPt with DNA

Initially, an active electrophilic species of the cisPt drug is formed through the hydrolysis process of the drug (see figure 12(B)). The chloride ion (Cl^-) co-ordinated to the Pt ion is labile whereas the ammonia group (NH_3) is non-labile. Both chloride ions are therefore potential leaving groups and the electrophiles formed can therefore interact with the DNA molecule through the interaction of the Pt^{2+} ion with the G-G and G-A base pairs of DNA (48). This interaction is favoured due to the electrostatic force of attraction between the positive metal centres and the negative DNA molecule (49).

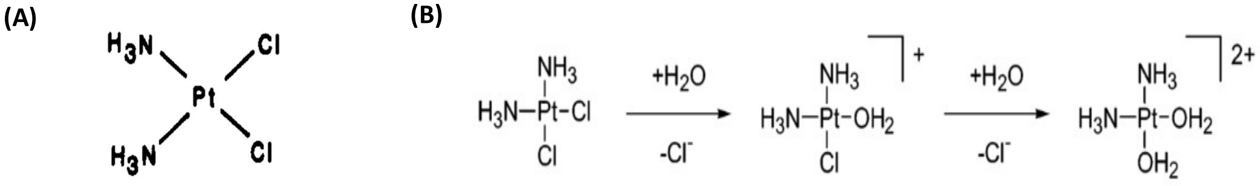

Figure 12- *(A) Chemical structure of cisplatin copied from Lippard et.al* (65) *(B) scheme of the hydrolysis process of cisplatin reproduced from Baik et al.* (47).

Specifically, the primary binding site of the cisPt is the N7 position of the guanine bases, followed by the N7 position of adenine (50). This point of attack first generates monofunctional adducts, which subsequently closes by coordination to the N7 position of an adjacent purine (guanine or adenine) to afford an intrastrand cross-link (51), as shown in figure 13. The co-ordination of platinum to the N7 results from the high electron density and accessible sites on the N7 purines via an electrophilic mechanism. These sites are not involved in base-pair hydrogen-bonding and are found in the major groove of the double helix (48).

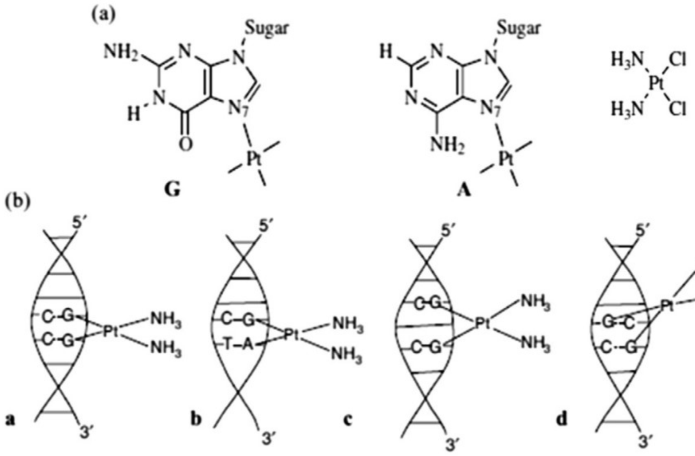

Figure 13 - *(a) Modes of binding of cisplatin to guanine (G) and adenine (A); (b) 1,2-intrastrand GpG (structure a), 1,2-intrastrand ApG (structure b), 1,3-intrastrand GpNpG (structure c), and 1,2-interstrand GpG (structure d) copied from Sirajuddin et al.* (37).

In-vitro experiments conducted by Reedijk et al. found that for the identified DNA-Pt adducts, approximately 90 % of the total entailed a Pt linked to the N7 atoms of the nucleobases guanine and adenine. However, only about 50 % of the Pt were found in the cross-links on d(pGpG) (52).

Similarly, Eastman (53) had also shown that the major adduct was a cross-link between two deoxyguanosines joined by a phosphodiester bond. The next major adduct was a cross-link between deoxyguanosine and deoxyadenosine, also joined by a phosphodiester linkage. The minor adduct was a cross-link between two deoxyguanosines but lacking any phosphate. The proportion of the formed adducts was expressed as a function of incubation time between the cisPt drug and the DNA and also as function of a ‘double stranded’ or ‘single stranded’ DNA (53). Furthermore, it was reported that upon interaction, the cisPt complex can bend the DNA molecule (by 35 - 40˚), which inhibits the long-range electron transfer through DNA (54).

2.11.2 DNA-cisPt adducts assessed for electrochemical applications

In this work, cisplatin (cisPt) is employed as a platinating agent as opposed to the conventional reported methods that have organized the platinum metal nanoparticles directly onto the DNA template (50),(55), (55),(56) and (57). The DNA functionalization with cisPt was first reported by Ford et al. (48), demonstrating the feasibility of the use of platinum metal complexes to achieve metallisation of the DNA (48). In their work, two platinum metal complexes were used, cisPt and Pt(terpy)Cl_2 ((dichloro(2,2’:6’,2”-terpyridine)platinum(II)) to generate a colloidal Pt/DNA composite through the chemical reduction of the platinated DNA enabling the fabrication of a nanometre-sized platinum particle of improved stability towards aggregation and particle growth by its interaction with the DNA (48). Several authors (58),(49),(59) and (60) have reported the use of electrochemical methods for studying the interactions in the formed platinum(II)-DNA adducts.

The interest in the electrochemical properties of the nucleic acid has received great attention due to its development for use in applications such as electrochemical biosensors. The oxidation and reduction of the nucleotide bases can be studied by cyclic voltammetry or stripping techniques. It must be emphasized that the type of electrode material employed can greatly influence the redox processes of the nucleic acid. For example, for oxidation processes, carbon electrodes are commonly employed (61). It is the observed changes in the oxidation signals of the purine bases (G and A) that are of particular interest since they are the primary binding targets of the platinum (II) ion (54). Upon binding, the guanine imidazole ring is chemically damaged resulting in the absence of the G^{ox} peak (guanine oxidation) in the electrochemical response as shown by (54). The reported mechanisms of electron transfer of guanine and adenine in DNA undergoing an oxidation process involves the transfer of 4 and 6 electrons respectively (61). Furthermore, various process parameters such as the influence of the ratio of drug to DNA on the electrochemical behaviour of the adducts can be also be studied as Erdogan and Yaman (59) have demonstrated.

2.12 Literature Review on the DNA based support templates for metal electrocatalysts

The utilization of platinum electrocatalysts, based on a DNA template, has previously been reported in the literature, and is reviewed and detailed below.

2.12.1 Pt Nanoparticle Anchored Molecular Self-Assemblies of DNA

Anantharaj et al. (57) have demonstrated the efficiency of using platinum nanoparticles embedded onto self-assembled structures of DNA as an electrocatalyst for the hydrogen evolution reaction (HER). The authors report the successful development of a colloidal solution of platinum-DNA monolayer using Pt nanoparticles of an average size of 3.5 ± 0.3 nm. The electrochemical behaviour of the prepared colloidal solution was then assessed in a 0.5 M H_2SO_4 electrolyte solution using 5 µL of Pt@DNA colloidal solution which equates to a loading of 15 µg cm^{-2} of platinum (57). From their findings they report that the interactions between DNA and glassy carbon can provide an efficient and stable electrocatalyst material. It was found that a commercial Pt/C 10 wt.% catalyst with Nafion binder could not compete with the fabricated colloidal Pt on DNA, suggesting that the electrocatalyst-loaded DNA molecular self-assemblies have great potential for the HER (57).

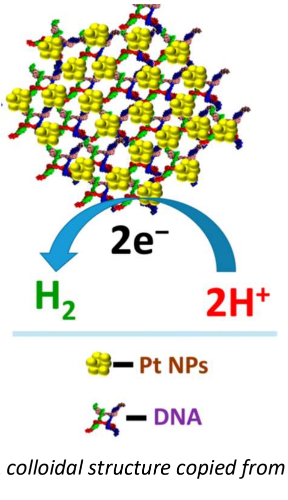

Figure 14- *Pt@DNA colloidal structure copied from Anantharaj et al.* (57).

2.12.2 Stable platinum nanoclusters on genomic DNA–graphene oxide

In the work of Tiwari et al. they demonstrated the success of depositing platinum clusters of a radius of approximately 1.4 nm onto genomic double stranded DNA-graphene oxide (GO) composites for achieving the catalysis of the oxygen reduction reaction (ORR). The reported experimental findings of (55) found that the prepared Pt/DNA–GO composite had an increased ORR onset potential, half-wave potential, mass activity and specific activity. The authors ascribed these results to changes in the active surface area of Pt and chemical interactions between Pt and GO where the electron density in the d-orbitals of Pt is changed in favour of the ORR. Furthermore, the transfer of the reduced species is supported by the strong interaction between the DNA and GO. This gives rise to increased electronic conductivity and resistance to corrosion (55).

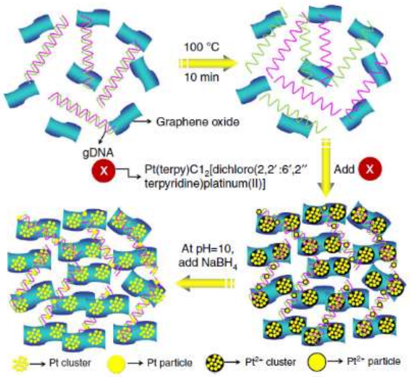

Figure 15- *Schematic diagram of the synthesis of the Pt/DNA-GO composites copied from Tiwari et al.*(55).

2.12.3 Deoxyribonucleic acid-directed growth of well dispersed nickel palladium platinum nanoclusters on graphene

The use of DNA templates for fabricating electrocatalysts from an alloy of metals was reported by Ma et al. (56). In particular they deposited nanoclusters of nickel-palladium and platinum alloys onto a DNA-Graphene Oxide (GO) composite. The prepared electrocatalysts of about 10 nm were then employed for the catalysis of the ethanol electro-oxidation reaction under alkaline conditions. This NiPdPt/DNA-GO material demonstrated both great electrocatalysis with an activity reaching a mass current density of 3.4 A mg^{-1}_{metal} and stability (56).

2.13 Conclusion

The employment of the DNA template as a catalyst support, can enable the production of an electrocatalyst of an increased surface area, improved electrochemical performance and structural stability i.e. catalyst durability. However, the main drawback with its use for electronic based applications have been associated with its poor electrical conductivity, i.e. highly resistive nature of the DNA. There is therefore a need to increase the electrical conductivity of the polyanion, which is essential as far as this study is concerned for maximizing the attainable catalyst activity (62). In the long term, when the fabricated electrocatalyst is used in a fuel cell compartment, desirable characteristics of the DNA catalyst support material includes: high electrical conductivity, good reactant gas contact with the electrocatalyst , a high specific surface area, good water handling ability, and good resistance to corrosion. A known material which satisfies this criteria is graphene or carbon with a large graphitic composition. These materials can improve the durability of the electrocatalyst and can enhance electrochemical reactions (55). In this study, different processing techniques will be employed to achieve the conversion of the DNA material into a favourable conductive material, more suited for fuel cell technology applications.

References

1. Compton RG, Banks CE. Understanding Voltammetry. Imperial College Press; 2011.
2. Barbir F. PEM Fuel Cells: Theory and Practice. Elsevier Science; 2005.
3. Hibbert DB. Introduction to electrochemistry / D. Brynn Hibbert. Basingstoke: Macmillan Press; 1993.
4. Southampton Electrochemistry G. Instrumental methods in electrochemistry / Southampton Electrochemistry Group. Chichester: Horwood Publishing; 2001.
5. Yuan XZ, Song C, Wang H, Zhang J. Electrochemical Impedance Spectroscopy in PEM Fuel Cells: Fundamentals and Applications. Springer London; 2009.
6. Zhang L, Ma C, Mukerjee S. Oxygen reduction and transport characteristics at a platinum and alternative proton conducting membrane interface. J Electroanal Chem. 2004;568(1–2):273–91.
7. Gennero M, Nacional U, Chialvo AC, Nacional U. Hydrogen evolution reaction : Analysis of the Volmer-Heyrovsky-Tafel mechanism with a generalized adsorption ... Hydrogen evolution reaction : analysis of the Volmer-Heyrovsky-Tafel. 2014;372(February):209–23.
8. Zalitis CM, Kucernak AR, Sharman J, Wright E. Design principles for platinum nanoparticles catalysing electrochemical hydrogen evolution and oxidation reactions: edges are much more active than facets. J Mater Chem A. 2017;5(110):23328–38.
9. Tavares M., Machado SA., Mazo L. Study of hydrogen evolution reaction in acid medium on Pt microelectrodes. Electrochim Acta. 2001;46(28):4359–69.
10. Shinagawa T, Garcia-esparza AT, Takanabe K. Insight on Tafel slopes from a microkinetic analysis of aqueous electrocatalysis for energy conversion. Nat Publ Gr. 2015;(May):1–21.
11. Marković NM, Grgur BN, Ross PN. Temperature-dependent hydrogen electrochemistry on platinum low-index single-crystal surfaces in acid solutions. J Phys Chem B. 1997;101(27):5405–13.
12. Davies TJ, Compton RG. The cyclic and linear sweep voltammetry of regular and random arrays of microdisc electrodes: Theory. J Electroanal Chem. 2005;585(1):63–82.
13. Silverstein TP. Marcus theory: Thermodynamics CAN control the kinetics of electron transfer reactions. J Chem Educ. 2012;89(9):1159–67.
14. Brownson DAC, Banks CE. The Handbook of Graphene Electrochemistry. Springer London; 2014.
15. Batchelor-Mcauley C, Kätelhön E, Barnes EO, Compton RG, Laborda E, Molina A. Recent Advances in Voltammetry. ChemistryOpen. 2015;4(3):224–60.
16. Davies TJ, Ward-Jones S, Banks CE, Del Campo J, Mas R, Muñoz FX, et al. The cyclic and linear sweep voltammetry of regular arrays of microdisc electrodes: Fitting of experimental data. J Electroanal Chem. 2005;585(1):51–62.
17. Malek K, Coppens MO. Knudsen self- and Fickian diffusion in rough nanoporous media. J Chem Phys. 2003;119(5):2801–11.
18. Ward KR, Xiong L, Lawrence NS, Hartshorne RS, Compton RG. Thin-layer vs. semi-infinite diffusion in cylindrical pores: A basis for delineating Fickian transport to identify nano-confinement effects in voltammetry. J Electroanal Chem. 2013;702:15–24.

19. Zhu J, Hu L, Zhao P, Lee LYS, Wong KY. Recent Advances in Electrocatalytic Hydrogen Evolution Using Nanoparticles. Chem Rev. 2020;120(2):851–918.

20. Gehrke H, Pelka J, Hartinger CG, Blank H, Bleimund F, Schneider R, et al. Platinum nanoparticles and their cellular uptake and DNA platination at non-cytotoxic concentrations. Arch Toxicol. 2011 Jul;85(7):799–812.

21. Gao Q, Zhang W, Shi Z, Yang L, Tang Y. Structural Design and Electronic Modulation of Transition-Metal-Carbide Electrocatalysts toward Efficient Hydrogen Evolution. Adv Mater. 2019;31(2):1–35.

22. Hou J, Wu Y, Zhang B, Cao S, Li Z, Sun L. Rational Design of Nanoarray Architectures for Electrocatalytic Water Splitting. Adv Funct Mater. 2019;29(20):1–39.

23. Morales-Guio CG, Stern LA, Hu X. Nanostructured hydrotreating catalysts for electrochemical hydrogen evolution. Chem Soc Rev. 2014;43(18):6555–69.

24. Zhang C, Shen X, Pan Y, Peng Z. A review of Pt-based electrocatalysts for oxygen reduction reaction. Front Energy. 2017;11(3):268–85.

25. Wu J, Yang H. Platinum-based oxygen reduction electrocatalysts. Acc Chem Res. 2013;46(8):1848–57.

26. Wang YJ, Zhao N, Fang B, Li H, Bi XT, Wang H. Carbon-Supported Pt-Based Alloy Electrocatalysts for the Oxygen Reduction Reaction in Polymer Electrolyte Membrane Fuel Cells: Particle Size, Shape, and Composition Manipulation and Their Impact to Activity. Chem Rev. 2015;115(9):3433–67.

27. Balgis R, Anilkumar GM, Sago S, Ogi T, Okuyama K. Nanostructured design of electrocatalyst support materials for high-performance PEM fuel cell application. J Power Sources. 2012;203:26–33.

28. Ma J, Sahai Y. Effect of electrode fabrication method and substrate material on performance of alkaline fuel cells. Electrochem commun. 2013;30:63–6.

29. Jacob T, Goddard WA. Water formation on Pt and Pt-based alloys: A theoretical description of a catalytic reaction. ChemPhysChem. 2006;7(5):992–1005.

30. Tavakkoli M, Holmberg N, Kronberg R, Jiang H, Sainio J, Kauppinen EI, et al. Electrochemical Activation of Single-Walled Carbon Nanotubes with Pseudo-Atomic-Scale Platinum for the Hydrogen Evolution Reaction. ACS Catal. 2017;7(5):3121–30.

31. Ramsden JJ. What is nanotechnology? Nanotechnology. 2016;1–18.

32. Du K, Park M, Ding J, Hu H, Zhang Z. Sub-10 nm patterning with DNA nanostructures: A short perspective. Nanotechnology. 2017;28(44).

33. Duan H, Winston D, Yang JKW, Cord BM, Manfrinato VR, Berggren KK. Sub-10-nm half-pitch electron-beam lithography by using poly(methyl methacrylate) as a negative resist. J Vac Sci Technol B, Nanotechnol Microelectron Mater Process Meas Phenom. 2010;28(6):C6C58-C6C62.

34. Rothemund PWK. Design of DNA origami. IEEE/ACM Int Conf Comput Des Dig Tech Pap ICCAD. 2005;2005(December 2005):470–7.

35. Malo J, Mitchell JC, Turberfield AJ. A Two-Dimensional DNA Array : The Three-Layer Logpile. 2009;13574–5.

36. Xavier PL, Chandrasekaran AR. DNA-based construction at the nanoscale: Emerging trends and applications. Nanotechnology. 2018;29(6).

37. Sirajuddin M, Ali S, Badshah A. Drug-DNA interactions and their study by UV-Visible, fluorescence spectroscopies and cyclic voltametry. J Photochem Photobiol B Biol. 2013;124:1–19.

38. Hong F, Zhang F, Liu Y, Yan H. DNA Origami: Scaffolds for Creating Higher Order Structures. Chemical Reviews. 2017. acs. chemrev.6b00825.

39. Seeman NC. Nanomaterials Based on DNA. Annu Rev Biochem. 2010;79(1):65–87.

40. Malo J, Mitchell JC, Turberfield AJ. A two-dimensional DNA array: The three-layer logpile. J Am Chem Soc. 2009;131(38):13574–5.

41. Taniguchi M, Kawai T. DNA electronics. Phys E Low-Dimensional Syst Nanostructures. 2006;33(1):1–12.

42. Chen Z, Liu C, Cao F, Ren J, Qu X. DNA metallization: Principles, methods, structures, and applications. Chem Soc Rev. 2018;47(11):4017–72.

43. Yang H, Metera KL, Sleiman HF. DNA modified with metal complexes: Applications in the construction of higher order metal-DNA nanostructures. Coord Chem Rev. 2010;254(19–20):2403–15.

44. Ding B, Deng Z, Yan H, Cabrini S, Zuckermann RN. Supporting Online Information Gold Nanoparticles Self-similar Chain Structure Organized by DNA Origami. J Am Chem Soc. 2010;132(10):1–16.

45. Maune HT, Han S, Barish RD, Bockrath M, III WAG, Rothemund PWK, et al. Self-assembly of carbon nanotubes into two-dimensional geometries using DNA origami templates. Nat Nanotechnol. 2010;5(1):61–6.

46. Tiwari JN, Tiwari RN, Kim KS. Zero-dimensional, one-dimensional, two-dimensional and three-dimensional nanostructured materials for advanced electrochemical energy devices. Prog Mater Sci. 2012;57(4):724–803.

47. Baik MH, Friesner RA, Lippard SJ. Theoretical Study of Cisplatin Binding to Purine Bases: Why Does Cisplatin Prefer Guanine over Adenine? J Am Chem Soc. 2003;125(46):14082–92.

48. Ford WE, Harnack O, Yasuda A, Wessels JM. Platinated DNA as precursors to templated chains of metal nanoparticles. Adv Mater. 2001;13(23):1793–7.

49. Mello LD, Ribeiro ES, Kubota LT, Elmroth SKC, Pereira RMS. Electrochemical and spectroscopic evidences of the interaction between DNA and Pt(II)(dppf)-complex. BioMetals. 2009;22(2):385–92.

50. Seidel R, Ciacchi LC, Weigel M, Pompe W, Mertig M. Synthesis of platinum cluster chains on DNA templates: Conditions for a template-controlled cluster growth. J Phys Chem B. 2004;108(30):10801–11.

51. Park J-S, Kim SH, Lee N-K, Lee KJ, Hong S-C. In situ analysis of cisplatin binding to DNA: the effects of physiological ionic conditions. Phys Chem Chem Phys. 2012;14(9):3128–33.

52. Fichtinger-Schepman AMJ, Lohman PHM, van der Veer JL, den Hartog JHJ, Reedijk J. Adducts of the Antitumor Drug cis-Diamminedichloroplatinum(II) with DNA: Formation, Identification, and Quantitation. Biochemistry. 1985;24(3):707–13.

53. Eastman A. The formation, isolation and characterization of DNA adducts produced by anticancer platinum complexes. Pharmacol Ther. 1987;34(2):155–66.

54. Horáková P, Těsnohlídková L, Havran L, Vidláková P, Pivoňková H, Fojta M. Determination of the level of DNA modification with cisplatin by catalytic hydrogen evolution at mercury-based electrodes. Anal Chem. 2010;82(7):2969–76.

55. Tiwari JN, Nath K, Kumar S, Tiwari RN, Kemp KC, Le NH, et al. Stable platinum nanoclusters on genomic DNA-graphene oxide with a high oxygen reduction reaction activity. Nat Commun. 2013;4:1–7.

56. Ma J, Wang J, Zhang G, Fan X, Zhang G, Zhang F, et al. Deoxyribonucleic acid-directed growth of well dispersed nickel-palladium-platinum nanoclusters on graphene as an efficient catalyst for ethanol electrooxidation. J Power Sources. 2015;278:43–9.

57. Anantharaj S, Karthik PE, Subramanian B, Kundu S. Pt Nanoparticle Anchored Molecular Self-Assemblies of DNA: An Extremely Stable and Efficient HER Electrocatalyst with Ultralow Pt Content. ACS Catal. 2016;6(7):4660–72.

58. Ravera M, Gabano E, Sardi M, Alessio M, Osella D. Electrochemical Biosensor Assay of the Interaction between [PtCln(NH3)4–n](2–n) (n = 0–4) Complexes and ds-DNA. Vol. 2011. 2011.

59. Erdogan DA, Özalp-Yaman Ş. Novel Pt(II) complexes containing pyrrole oxime; Synthesis, characterization and DNA binding studies. J Mol Struct. 2014;1064(1):50–7.

60. Krizkova S, Adam V, Petrlova J, Zitka O, Steiskal K, Zehnalek J, et al. A suggestion of electrochemical biosensor for study of platinum(II)-DNA interactions. Electroanalysis. 2007;19(2–3):331–8.

61. Paleček E, Bartošík M. Electrochemistry of nucleic acids. Chem Rev. 2012;112(6):3427–81.

62. Braun E, Eichen Y, Sivan U, Ben-Yoseph G. DNA-templated assembly and electrode attachment of a conducting silver wire. Nature. 1998;391(6669):775–8.

63. Shinagawa T, Garcia-Esparza AT, Takanabe K. Insight on Tafel slopes from a microkinetic analysis of aqueous electrocatalysis for energy conversion. Sci Rep. 2015;5(August):1–21.

64. Kortaberria G, Arruti P. 1 Dynamics of deoxyribonucleic acid as studied by dielectric spectroscopy. Transw Res Netw. 2009;(January).

65. Pinto AL, Lippard SJ. Binding of the antitumor drug cis diamminedichloroplatinum(II) (cisplatin) to DNA. BBA - Rev Cancer. 1985;780(3):167–80.

Chapter 3- Materials, Experimental Methods and Techniques

Chapter 3- Materials, Experimental Methods and Techniques

3.1 Introduction

An overview of the key methods employed to characterize the fabricated DNA-cisPt nanostructures and assess the material feasibility for electrocatalytic applications is provided. The operating principles behind each characterisation technique is described and an experimental method where relevant is included. Table 1 summarises these methods.

***Table 1-** The key methods for studying the properties, morphology and dispersion of the platinum metal on the DNA catalyst support material.*

Characterization Technique	**Relevance of this method to this work**
Scanning Transmission Electron Microscopy (STEM) and *STEM-EDX (Energy Dispersive X-ray) spectroscopy studies*	For studying the morphology of the produced nanostructures and observing the dispersion of the platinum metal atoms on the DNA scaffold. The size of the platinum nanoclusters can be measured from these images using the tools provided in image processing programs such as 'Image J'. STEM EDX imaging enables elemental mapping to be made.
Atomic Force Microscopy (AFM)	To gain an insight into the topographical features of the material and confirm that there is interaction between the DNA and the cisplatin under the incubation conditions employed. DNA is easily visible in AFM compared to STEM and is useful for characterizing DNA nanostructures like the DNA triangle origami assemblies in this work.
X-ray Photoelectron Spectroscopy (XPS)	This method determines the elemental composition and speciation of matter by studying the electronic structure of the atoms located at the surface of the sample under study. Information such as the chemical bonding and binding energies between the DNA and cisplatin can determine if covalent interaction has been successfully achieved. Moreover, XPS studies can reveal the sp^2 and sp^3 content of the material, enabling us to determine if the process treatment methods used i.e. electron beam irradiation and pseudo pyrolysis, have achieved the graphitization of the DNA.
Electrochemical testing (3 working electrode cell)	The electrocatalytic properties of the material are explored for the hydrogen evolution reaction (HER) in acidic conditions. This is the main intended application of the fabricated DNA-cisPt material i.e. electrocatalyst for a fundamental reaction in the polymer electrolyte fuel cell (PEMFC).

3.2 Synthesis of the DNA-Platinum material

All the materials employed in this project, were synthesised by Klaudia Englert, in the School of Chemistry, University of Birmingham. Confirmation of successful interaction of the synthesized adduct samples were made using spectroscopic means. In particular the use of UV-vis spectroscopy and Circular Dichroism (CD) has enabled the evaluation of the mode and strength of binding. This characterization and analysis was completed and presented by Klaudia Englert (1) as part of the collaborative project between the School of Chemistry and Chemical Engineering at the University of Birmingham. The findings show that successful interaction is achieved between the DNA and cisplatin adducts at the incubation reaction conditions of 37 °C for around 10-12 hours (1).

3.3 Electrochemical methods

Various voltammetry techniques are available for studying the electrochemical behaviour of a particular process and a detailed description of each method can be found in the literature (2). Cyclic voltammetry methods will be the main technique employed in this work, to gain a better understanding of the electrochemical behaviour of the DNA-cisplatin adducts for the electrocatalysis of the HER in acidic conditions.

The Electrochemical cell

Most electrochemical cells are made up of three electrodes, namely a reference electrode (RE), a working electrode (WE) and a counter electrode (CE), forming a three working electrode cell, see figure 1(A). The electrochemical cell can operate in two different modes either a galvanostatic or potentiostatic mode. These operational modes are achieved by controlling either the current or voltage respectively and consequently measuring the response of the uncontrolled variable. These electrochemical measurements are achieved using an instrumental device known as a potentiostat, see figure 1(B).

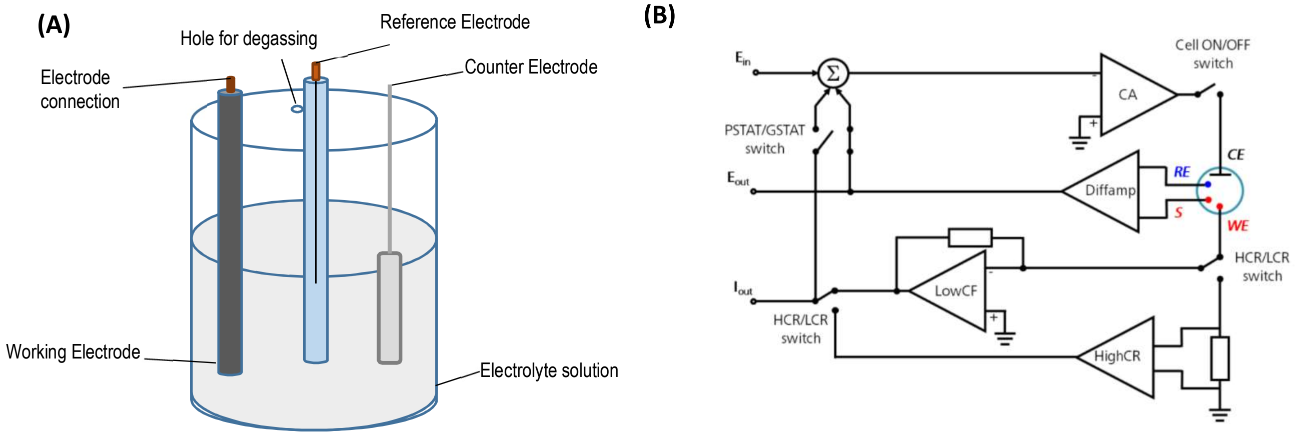

Figure 1 *- (A) Schematic diagram of a three-working electrode electrochemical cell (B) Basic diagram of a potentiostat/galvanostat (figure 1(B) copied from Autolab* (3)*).*

The set-up employed will be in the potentiostatic mode, where the potentiostat (an Autolab PGSTAT302, supplied by Metrohm-Autolab (Utrecht, NL) controls the potential of the CE against the WE. This ensures that the potential difference between the WE and RE is well defined and corresponds to the set value. The control amplifier (CA), which connects to the CE, forces the current to flow through the cell (3).

The absolute measurement of single potentials at the working electrode cannot be achieved and alternatively measurements relative to a known standard are made. Different types of reference electrodes (RE) are available however they all have a common characteristic which includes stability and a well-defined reversible electrochemical behaviour. A stable electrode is non-polarizable, therefore upon the flow of a small current, the electrode potential remains unchanged. In this study, all the measured potentials are reported against a saturated calomel reference electrode (SCE).

The calomel electrode is made up of mercury (Hg) immersed into a saturated potassium chloride solution (KCl) and has an electrode potential of 0.241 V vs. Standard Hydrogen electrode (SHE) at 298 K. The behaviour of this electrochemical system is described by the following:

$$\frac{1}{2}Hg_2Cl_2(s) + e^- \rightleftharpoons Hg_{(l)} + Cl^-_{(aq)}\ E^0 = +0.268\ V\ Eq.(1)$$

The purpose of the counter electrode (CE) also known as the auxiliary electrode, is to complete the electrical circuit in the three working electrode cell. As the redox reaction of the electroactive species e.g. its oxidation (or its reduction) takes place over the WE surface, current begins to flow and is recorded as the electrons flowing between the CE and WE. The CE passes all the current needed to balance the current measured at the working electrode, permitting the potential of the working electrode to be measured against a known reference electrode, without compromising the stability of the RE, by passing a current over it. High surface areas are required by the CE i.e. greater than that of the WE, to ensure that the kinetics of the reactions at the CE do not supress those at WE. Other key requirements needed by a CE include: high electrical conductivity and electrochemical inertness to the electrochemical reaction being studied. In the experiments carried out in this work, a platinum mesh is used due to its inertness, stability, large surface area and high electrical conductivity.

The electrochemical reactions take place at the surface of the working electrode. The applied potential to the WE is controlled by the potentiostat as a function of the reference electrode potential. The WE consists of an inert and catalytically active metal, such as platinum, gold or silver, or non-metals, such as glassy carbon. In this work, a glassy carbon (GC) electrode of a diameter equivalent to 3 or 5 mm (BASi) is used as the working surface. The reactive surface of the GC electrode was activated and polished on micro-cloth pads using motions of a figure of eight in a water alumina slurry in order of decreasing alumina slurry size (1.0, 0.3, 0.05 µm, Buehler Inc.). This was followed by cleaning for 60 seconds in an ultrasonic bath and drying under a gentle flow of nitrogen. Once dry, the electrodes were modified by casting an aliquot of the DNA-cisPt (25 or 42 µL, for a 3 and 5 mm electrode area respectively) and drying under a lamp. The modified GC electrodes with the DNA-cisPt films were cycled at 50 mV s^{-1}, with the exception to the Randles-Ševčík study, where a range of different scan rates were employed.

3.3.1 Cyclic Voltammetry

Cyclic voltammetry is a potential sweep technique used for the electrochemical analysis of a particular system of interest and the kinetics of the process of electron transfer. As highlighted above, a potentiostat can control the voltage at a set value between the WE and CE. The corresponding current is then measured and is an indication of the electron flow which is necessary for enabling the establishment of an active electrochemical process with rates equal to the applied potential. Different wave forms can be followed for the application of potential. In particular, cyclic voltammetry uses a triangular waveform and measures the corresponding current response (i) (4), see figure 2.

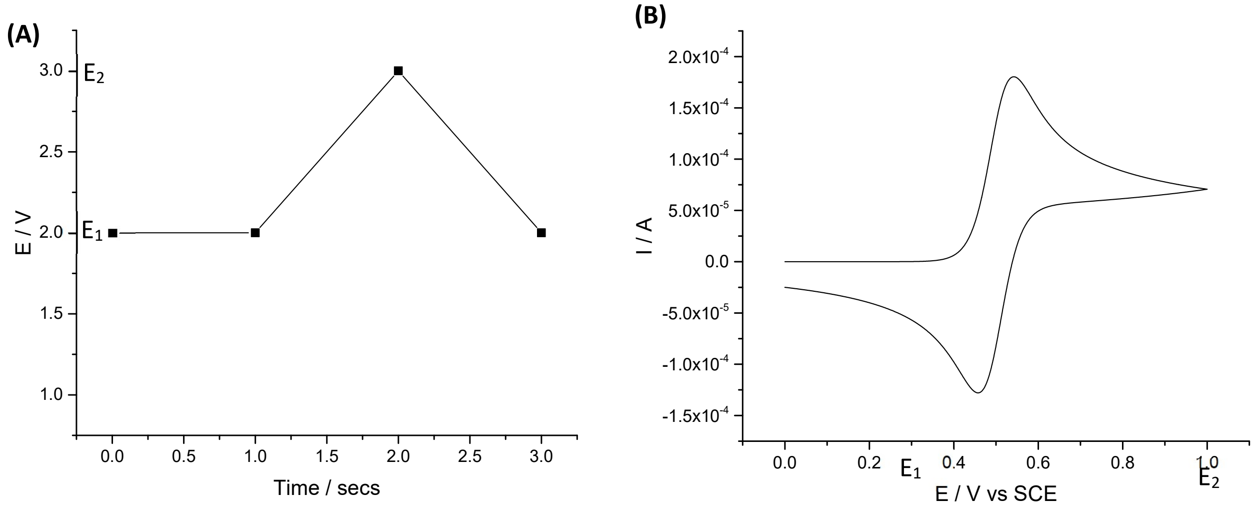

Figure 2*- (A) Triangular waveform for a cyclic voltammetry experiment (B) Cyclic voltammogram due to triangular wave-form.*

Initially a potential, E_1, is chosen and applied to ensure that the analyte would be electrochemically inactive at that value. The potential is then swept, at a chosen voltage scan rate (*v*), to a second potential, E_2, where the species of interest is known to have electrochemical activity. The applied potential should be sufficient to initiate an electron transfer process and consequently lead to the depletion of reactant near the electrode surface. This prevents the electrode kinetics from being rate limiting and instead at this point we observe mass transport limitations. The potential sweep is then reversed and scanned to the initial value E_1. The outcome is a voltammogram, see figure 2(B), from which two significant electrochemical parameters can be determined. That includes the ratio of the current peaks ($I_{p,a}/I_{p,c}$) and the separation peak potentials ($E_{p,a}$ - $E_{p,c}$) (where subscript a and c refer to the anodic (+) and cathodic (-) parameters respectively, which can be found from figure 2(B).

3.4 Scanning Transmission Electron Microscopy (STEM)

Electron microscopy is a powerful tool enabling atomic-resolution imaging and nanoscale analysis. This provides detailed information on the surface morphology of the catalyst material fabricated in this work. It is the properties of the electrons that enable this imaging characterisation to be useful, as explained below.

3.4.1 Properties of the electrons

Electrons are charged particles with interesting characteristics since they possess both wave like and particle like properties. The wave like properties of the electrons enable image formation and diffraction patterns to be made, hence providing detail on the internal structure of the material. The wavelength of the electron beam can be quantified by the De Broglie expression below:

$$\lambda = {}^{h}/_{p} \quad Eq.(2)$$

Where λ is the wavelength (m), *h* is Planck's constant (kg m^2 s^{-1}) and *p* is momentum of the electrons (kg m s^{-1}). The wavelength of the electron can be tuned using the magnitude of the acceleration voltage of the electron beam, (V). For example, at 200 kV, the wavelength is equivalent to 2.75 pm. On the other hand, the charged particle like properties of the electrons enable chemical analysis to be made since it is these properties that affect the interaction of the specimen with the electron beam.

3.4.2 Principles of STEM

Overview

The operating principle behind STEM imaging characterization involves focusing a beam of electrons by electron optics to form a small illuminating probe that is rastered across a sample. Thin samples are used to ensure that the vast majority of electrons are transmitted and the scattered electrons are detected. Thin sample preparation is normally achieved by distributing the material of interest onto a commercial carbon support TEM grid. The highly focused beam of electrons can be scanned over the sample material whilst collecting desired signals from the electron scattering to form an image i.e. signal intensity as a function of probe position. This can be achieved at a high level of resolution. These images are a reflection of the morphology of the sample i.e. chemical composition and surface roughness. The opportunity of being able to use a range of detectors makes STEM instrumentation a versatile tool compared to other electron microscopy imaging methods such as TEM or SEM.

Operating principles

Similar to SEM, STEM also operates under high vacuum conditions, i.e. a vacuum pressure of around 10^{-10} mbar, which is maintained by liquid nitrogen cooling. The source of electrons is a Field Emission Gun (FEG), either a cold field-emission gun (CFEG) or a Schottky thermally-assisted field-emission gun. The commonly used gun for generating electrons is the CFEG, which generates more monochromatic electrons upon the application of an intense electric field. On the other hand, the Schottky thermionic source combines both heating and field emission to generate electrons. The material normally used for the tip to generate electrons is tungsten (W) or lanthanum hexaboride (LaB_6), which have a high melting point and a low work function. A high electric field at the apex of the tip is applied for electron emission of around 10^6 Vcm^{-1} (5). This generates an intense beam of electrons that escapes into the vacuum. It is the accelerating voltage that determines the resolution of the image attained. Commonly, the electron gun is located at the bottom of the column, with the electrons traveling upwards as shown in figure 3.

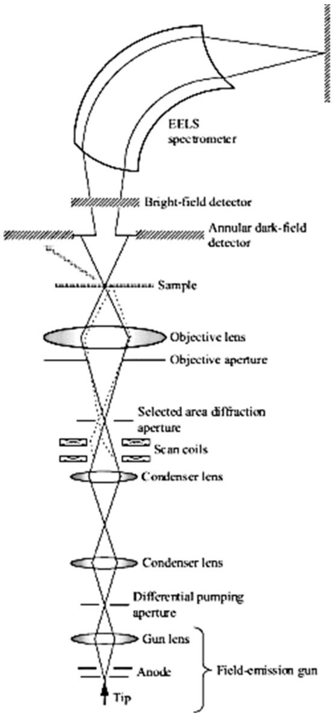

Figure 3- Schematic of the essential elements of a dedicated STEM instrument showing the most common detectors. Adapted from Nellist (7).

The electrons are focused by a series of lenses, enabling the build-up of an image of the electron source at the specimen to be made. The electron spot, also called 'probe' is scanned across the sample in a 'raster' fashion by excited scanning deflection coils. Finally, the scattered electrons are detected and their intensity is measured as function of probe position, leading to the image formation.

The objective lens focuses the beam to form the probe, while the condenser lenses are placed before the objective lens to control the degree of demagnification of the electron source that will form the probe. Probe sizes that are below the interatomic spacing's in many materials are often possible, making STEM imaging a powerful analysis tool. However, the electron lenses can suffer from inherent aberrations, such as spherical and chromatic aberrations, thus can result in loss of spatial resolution. To overcome this issue, an objective aperture is used in the column. However, this can be problematic as it gives rise to a diffraction limit, limiting the smallest probe that can be formed and this diffraction limit may even be larger than the source image. The other issue is limitations in the current that can pass through the aperture and consequently a limited availability of current in the probe.

Normally, a spherical corrector compensates for the fact that the lenses result in the loss of the focus of the rays, which pass through at different points. This improves the quality of the image by eliminating the Frensel fringes and delocalization effects, allowing for a more representative surface structure analysis of the material to be made. The STEM detectors are placed after the sample to detect the transmitted electrons, where each detector has its own unique properties. For example, a

High Angle Annular Dark Field (HAADF) detector enables both elemental and structural information to be obtained whilst Secondary Electron (SE) detectors provide images of high resolution (6).

3.4.3 STEM Energy Dispersive X-ray spectroscopy (EDX)

STEM can use an energy-dispersive X-ray (EDX) spectrometer to enable STEM-EDX spectroscopy analysis of the sample to be made. This provides information on the chemical composition and analysis on the distribution of each element present in the sample via a process of elemental mapping (7). The principles behind STEM-EDX characterisation are simple and involve the excitation of a core electron in the sample by the fast-traversing electron in the sample. The ejected electron on the inner shell, creates a hole, which is refilled by an electron of a higher energy (in the outer shell). As a result of this, the excited system decays releasing energy in the form of an X-ray photon (or Auger electron). The analysis of the emitted X-ray photons is known as EDX analysis, since the energy of the particle released is a characteristic of the core electron energy level and is unique for each element therefore allowing elemental compositional analysis to be made (7).

3.4.4 Nanoparticle size and lattice space measurements

The STEM images produced can be combined with an appropriate image processing program to enable qualitative analysis to be made. This includes using the functions and tools to directly measure the particle size and lattice spacing. In this work, the image processing program called Image J is used. Specifically, in-built tools using the Fast Fourier Transform (FFT) function and d-plot tools are used for measuring the lattice spacing. To ensure the measurements were accurate, comparisons with literature reporting was made.

3.5 X-ray Photoelectron Spectroscopy (XPS)

In the field of heterogeneous catalysis, XPS can enable the determination of both chemical and physical changes in the catalyst upon exposures to different environmental conditions. Given the importance of the surface properties of a catalyst (where the adsorption of the reactant and reactions takes place) it is highly important to determine the properties of the catalyst material with accuracy. Both qualitative and quantitative information can be provided by XPS, including the elemental composition and binding energies (8).

XPS characterization was conducted at Harwell XPS (UK) facilities to obtain the binding energies (BE) and survey spectra of the material synthesized in this work, using α-Kl as the X-ray source. The α-Kl has a characteristic energy of 1486.68 eV.

Overview

The operating principle behind XPS characterisation entails derivation of the surface chemical properties by directing an energetic photon beam (X-ray) at a sample, which consequently results in the emission of the core-level electrons. The measured energy of electrons is specific to the type of atoms/ ions in the element. In addition, the amount or ratios of the respective atoms/ions i.e. composition of the volume analysed and also the form of interactions that have occurred can be determined using XPS analysis.

Operating principles

The operating method involves radiating the specimen with an X-ray beam (commonly MgKα and AlKα) or UV photons under vacuum conditions. The energy of the radiated photon is transferred to the core electrons (k-shells or valent shells) and once sufficient energy is absorbed by the electrons, they are removed from the atoms through the surface region of the sample.

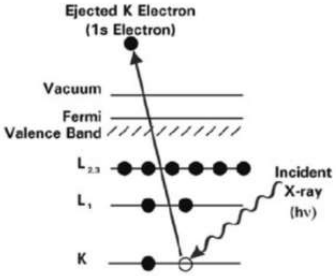

Figure 4*- The photoemission process involved for XPS surface analysis, where the spheres represent electrons and the bars represent energy levels within the material being analysed. Adapted from XPS simplified* (13).

The photoelectrons emitted by the photons are unique since they are from the inner orbits thus their energy characteristics are reflective of the atoms they originate from. The excited electrons can leave the hole and travel to the surface from which they can escape out of the molecule into the vacuum. It is these electrons that are detected and a linear relationship exists between the photoelectron count and electron binding energy.

In addition to the photoelectron emission, Auger and fluorescent electrons can also be emitted from the surface of the molecule into the vacuum. The dispersion of the ejected electrons takes place according to binding energy of the element, which is a function of the kinetic energy of the electron and the radiated photon energy source, which are related as shown by the following expression:

$$BE = h\nu - KE - \phi \; Eq. (3)$$

Where ϕ is the work function, KE refers to the kinetic energy, BE is the binding energy and $h\nu$ is the photon energy.

XPS measures the kinetic energy (E_{ke}) of the photoelectrons, whilst electrons contained within atoms are characterized by an internally referenced binding energy value (E_{be}) determined by the chemical environment for an atom. An X-ray photoelectron spectrum is constructed from the measurement of the number of electrons of a given energy for a specific time interval emitted from the atoms in the surface material. This is quantified as 'counts per second' (CPS) and is a function of kinetic energy (eV).

The surface properties attainable with this characterization technique includes surface composition and atomic percentage (%).The relative area of the peak occupied by each element is reflective of the elemental composition whilst the binding energy portrays information like the nature of the chemical environment of the element involved in the bond (6).

3.6 Atomic Force Microscopy (AFM)

Atomic force microscopy (AFM) is one of two forms of scanning probe microscopy (SPM) techniques which works by scanning a sharp probe tip in a raster fashion over the surface and measuring the interaction upon contact with the surface. This technique involves scanning the sample surface using a sharp tip attached to the end of a cantilever of a defined spring constant. The tip is pressed against the sample by the cantilever, allowing for its interaction and consequently accurate surface profiling to be made. The relative motion is performed to a sub-angstrom level of accuracy using a piezoelectric actuator (usually a tube/tripod).

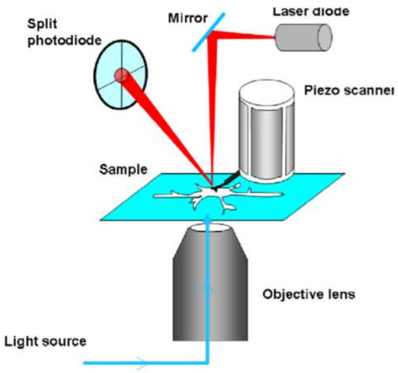

Figure 5- *Schematic of an AFM coupled with an inverted optical microscope. Adapted from Alessandrini and Facci* (9).

The measured feedback signal at each scanning point on a 2D matrix, results in the build-up of a 3D image, which is a reconstruction of the surface topography of the sample. This is primarily formed from the cantilever deflections due to the attractive or repulsive forces between the tip and surface. The detection system that is employed uses a laser light to convert the cantilever deflection into an electrical signal. A split photo-detector amplifies the cantilever deflections.

For most operating modes of the AFM, a feedback circuit, connected to the cantilever deflection sensor, maintains the tip and sample interaction at a fixed distance. This imaging method has enabled imaging of non-conducting samples and has received great interest for biological applications (9), see figure 5.

Cantilever selection

Several parameters can be chosen to optimize the imaging process. This includes the stiffness and type of cantilever used, the imaging phase and the operating mode employed. Key properties of the cantilever that can influence the imaging include: stiffness, size and shape. These can influence the applied force and disturbance to the surface and consequently the interaction of the tip and sample. The laser beam is focused onto the back of the cantilever thus any changes in the cantilever angle lead to a change in the laser spot position on the four-quadrant photodiode (PD). This highlights how the cantilever properties can affect the imaging process. The primary operating mode of AFM for biological material includes Tapping Mode (TM) (9).

Unlike contact mode where the tip scans in close contact with the surface of the sample, TM involves excitation of the cantilever into oscillations near its resonance frequency of an amplitude of up to 100 nm, resulting in the tapping of the cantilever along the surface which is maintained by a constant feedback loop as opposed to the pushing of the cantilever against the sample surface with a piezoelectric positioning element in contact mode. Finally, the TM image is constructed from the contact of the tip with the surface (10).

3.7 Raman spectroscopy

Raman is a light scattering technique, enabling the detection of structural patterns of the molecule based on the resulting interactions of the light source e.g. laser light with the chemical bonds in the molecule. Rayleigh scattering refers to scattered light at the same wavelength (or colour) as the laser source, see figure 6. On the other hand, Raman scattering is more useful for analysis since it refers to light that is scattered at a different wavelength to the laser light and is characteristic of the chemical bond in the molecule of the analyte.

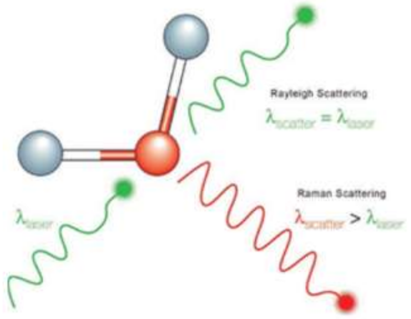

Figure 6*- Principle of Raman spectroscopy adapted from Horiba* (11).

The Raman spectrum produced includes a number of peaks, reflective of the intensity and wavelength position of the Raman scattered light. More specifically, each peak is a fingerprint of a particular molecular bond vibration, including individual bonds such as C-C, C=C, N-O and/or C-H (11). The purpose of using this characterisation method for this work is to identify whether a graphene or graphitic based material is formed following the processing of the DNA via pseudo pyrolysis.

3.8 Graphitization methods

3.8.1 Flood gun electron beam tool for electron beam irradiation

The graphitisation of the DNA in the fabricated catalyst material was achieved using electron beam irradiation. A flood gun electron source was used made up of a column, a chamber and an electron gun. The pump is initially started to set the vacuum conditions required from which then the beam of electrons can be generated from a tungsten tip and consequently accelerated at the set acceleration voltage.

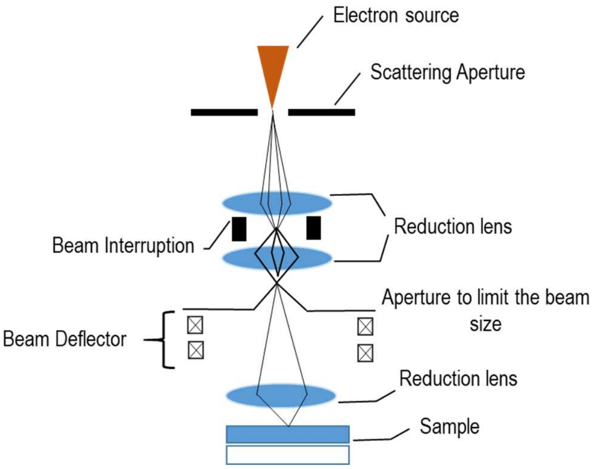

Figure 7*- Schematic diagram of the electron beam column in the flood electron beam tool.*

Inside the column (figure 7) beam blanking also takes place enabling the beam to be simply switched on and off. Typically, the samples are loaded into the chambers interferometric stage, which is controlled by an accurate positioning handled manually using X, Y and Z coordinates.

3.8.2 Tubular Furnace for the pseudo pyrolysis process

Carbonisation of the DNA in the fabricated catalyst material was achieved using a low temperature pseudo pyrolysis process. A tube furnace (Carbolite MTF 12/38/400) with a quartz tube (35 mm outer diameter x 32 mm inner diameter and a 600 mm long main body) was used for the heat processing treatment of the material, under an inert atmosphere. The furnace was purged with nitrogen before loading the sample and for the duration of the pseudo pyrolysis process. The furnace was controlled by a temperature program, based on a feedback controlled process, where built-in thermocouples were used to adjust the furnace temperature to the desired set-point. The mechanism of heat transfer to the sample is described.

3.8.2.1 Brief background on mechanisms of heat transfer

There are three mechanisms of heat transfer including conduction, convection, and radiation. These take place in solids, fluids (liquids and gases) and between any radiant energy emitting bodies (at a different temperature from its surroundings) respectively. The predominant forms of heat transfer in the pseudo pyrolysis reaction are convection and some radiation, given that outer wall of the furnace is insulated and there is no direct contact between the sample and the walls, thus conduction is negligible. Convection is governed by Newton's Law of Cooling:

$$\mathrm{q} = \mathrm{hA}(\mathrm{T_s} - \mathrm{T_\infty})\ Eq.(4)$$

Where q is heat flux (Wm^{-2}), A is the area of heat transfer body (m^2), h is the local heat transfer coefficient ($Wm^{-2}K^{-1}$), $\mathrm{T_s}$ is the temperature of the surface and $\mathrm{T_\infty}$ is the temperature of the bulk fluid (K).

On the other hand, radiation is governed by the Stefan-Boltzmann law:

$$\mathrm{q} = \varepsilon \mathrm{A}\sigma\left(\mathrm{T_s}^4 - \mathrm{T_{surr}}^4\right)\ Eq.(5)$$

Where q is heat flux (Wm^{-2}), A is the area of heat transfer body (m^2), σ is Stefan-Boltzmann constant ($5.67\ x10^{-8}$ W $(m^2K^4)^{-1}$), ε is the emissivity of the material, $\mathrm{T_s}$ is the temperature of the surface and T_{surr} is the temperature of the surrounding (K).

The same surface may transfer heat by convection and radiation simultaneously, thus a total contribution for each can be defined.

3.8.2.2 Temperature profile in a tubular furnace

The temperature profile in a tubular furnace reaches its peak point at the centre position of the tube, see figure 8. This means the sample would need to be placed centrally each time to ensure that the same temperature exposure is achieved for each sampling run.

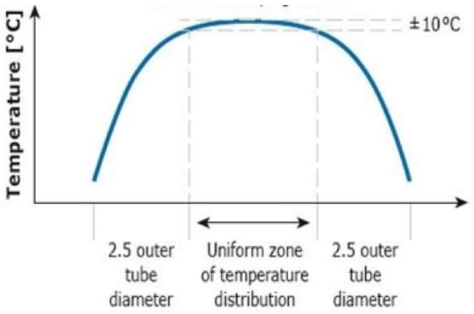

Figure 8*- Temperature distribution for a single zone furnace adapted from Carbolite Gero* (14).

3.9 Materials, experimental instrumentation and procedures

3.9.1 Material Synthesis

All the material detailed and used in this work was synthesized and provided by Klaudia Englert (1), School of Chemistry, University of Birmingham. Deoxyribonucleic Acid (DNA), sodium salt from salmon testes, cisplatin (99.99 % purity (based on trace metal analysis)) were purchased from Sigma Aldrich. DNA-cisPt adducts were synthesized by dissolving the salmon milt DNA (sm-DNA) in Milli-Q water (resistivity ≥ 18.2 MΩ.cm) and sonicating to prepare a stock solution. Cisplatin in aqueous form was mixed with the salmon-milt (sm)-DNA and incubated at 37 °C overnight for 10 hours. Confirmation of the adduct formation was achieved using spectrophotometric techniques using Shimadzu UV-1800 spectrophotometer, Jasco J-810 spectropolarimeter and Cary 5000 UV-Vis-NIR Spectrophotometer by Klaudia Englert (1). The range of loadings prepared and tested in this work (chapters 4-7) are displayed in Table 2. A detailed method outlining the calculations of the concentration of the cisPt and the sm-DNA in a 1000 µL solution is provided in appendix 1.

Table 2- *Ratio and concentrations of the contents of the DNA-cisPt samples synthesized and characterized.*

[1]

Ratio of sm-DNA: cisPt	***Concentration of cisPt in a 1000 µL solution /µM***	***Concentration of sm-DNA in a 1000 µL solution /mM***
1:0	0	1
$1:10^{-4}$	0.1	1
$1: 10^{-3}$	1	1
$1: 10^{-2}$	10	1
1: 0.1	100	1
1:1	1000	1
cisPt	1000	0

Experimental work

The material received was experimentally tested and characterized by the author of this thesis in the experimental methods described below.

3.8.2 Electrochemical testing

The samples prepared (see Table 2) were electrochemically tested using a 3 electrode cell, involving a glassy carbon electrode (GC, 3 or 5 mm, BASi) as the working, a saturated calomel reference (SCE, BASi) and a bright platinum mesh counter electrode. The cell was controlled by an Autolab 128N potentiostat running Nova 2.1 software (Metrohm-Autolab BV, Netherlands). All potentials are reported against SCE. All chemicals involved were used in their analytical grade and used without any purification. Perchloric acid (70 %, 99.99 % trace metals) (1 mM, pH 3) and sodium perchlorate (≥ 98 %) as the supporting electrolyte (0.1 M) supplied by Sigma Aldrich. All electrolytes were made up with MilliQ water of a resistivity not less than 18.2 MΩ.cm (MilliQ, Millipore) and thoroughly degassed with dry nitrogen (oxygen-free, BOC Gases plc) prior to experimentation.

3.8.3 Dry film preparation on Glassy Carbon (GC) stubs

A series of glassy carbon (GC) stubs (d=5 mm) were polished on micro cloth pads with decreasing size alumina slurries (1.0, 0.3, 0.05 µm, Buehler Inc., IL, USA), followed by rinsing with ultrapure water and drying under a gentle flow of nitrogen. Once dry, the electrodes were modified by drop casting an aliquot of 42 µL of the prepared DNA-cisPt onto the 5 mm GC stub and drying under a lamp.

---

[1] Synthesis by Klaudia Englert, School of Chemistry, University of Birmingham.

Once the stubs were prepared they were loaded into the furnace to achieve carbonisation of the material. For the 3 mm GC electrodes, the same method was followed except a smaller aliquot of 25 µL of the prepared DNA-cisPt was drop cast.

3.9.4 Electron Microscopy

The microscope is set up to a CESCOR aberration correction system and can operate in both TEM and STEM modes at an acceleration voltage of 200 keV. It is equipped with a number of detectors ranging from Gatan bright field and dark field detectors, Gatan TEM charge coupled device (CCD), electron energy loss spectrometer (EELS) to Bruker energy dispersive X-ray (EDX) detector. The Gatan DF detector is also used for high angle annular dark field (HAADF) STEM imaging. Both the Dark Field (DF) and Bright Field (BF) detectors are physically located above one another allowing for their simultaneous use.

The surface morphology of the material in this work was attained using STEM imaging in both DF and BF imaging modes using a JEOL 2100F instrument. The samples were prepared for imaging by casting 3 µL of the sample onto a 300 Cu mesh holey carbon TEM grid and drying under a lamp. The STEM was operated in Z-contrast mode using a HAADF detector at 200 keV acceleration voltage. STEM EDX imaging was employed to observe the distribution of the platinum atoms in the DNA-cisPt nanomaterial.

3.9.5 Surface Topography

AFM imaging was used to observe the morphology of the fabricated DNA origami triangles with evidence of platinum metal atoms on the nanostructure. This validates the success of the material fabrication under the reaction conditions employed. The surface topography was assessed via AFM imaging using a 'Dimension 3100' Atomic Force Microscope (AFM) (Veeco Digital Instruments**,** Bruker), equipped with a NanoScope IIIa controller. 5 µl of the DNA origami sample was dropped onto a cleaved mica surface (cleaved with cellotape) and was left to dry in air for 10 minutes before blowing away the remaining solution using a stream of nitrogen gas. The microscope was operated in tapping mode. Cantilevers provided by Apex Probes Ltd (Bracknell, UK) (length: 225 µm, frequency: 75 kHz and a force constant: 2.8 N m^{-1}) (FM-10) in air were employed.

An aliquot of 20 µL of the sm-DNA-cisPt sample was drop cast onto a Highly Ordered Pyrolytic Graphite (HOPG) surface and was left to dry in air followed by drying off the remaining solution using a stream of nitrogen gas. The microscope was operated in tapping mode.

3.9.6 Surface chemical properties

3.9.6.1 XPS

XPS characterization was conducted at Harwell XPS, UK facilities to obtain the binding energies (BE) and survey spectra of the materials synthesized using α-Kl as the X-ray source (characteristic energy of 1486.68 eV). The BE is reflective of the oxidation states of the elements in the DNA-cisPt adducts including Pt, Cl, C, P, N and O. The surface chemical properties of the 1:10^{-4} DNA-cisPt loading and the 1 mM virgin DNA films following pseudo pyrolysis and the 1:10^{-3} DNA-cisPt loading and the 1 mM virgin DNA films following electron beam irradiation of the material were explored to assess for any changes in the elemental composition following these processing treatments. Moreover, through XPS characterisation any graphitic content could be detected using this analysis.

3.9.6.2 Raman characterization

Raman was carried out with Renishaw system (RL633) with a 532 nm source and a laser power of 1 mW. The integration time for each scan was set at 10 seconds and the instrumentation was controlled using a WIRE software. The surface chemical properties of the 1 mM unmodified DNA films following pseudo pyrolysis of the material were explored to assess for any changes in the elemental composition following treatment and more importantly see if any graphitic content could be detected.

3.9.7 Graphitization methods

3.9.7.1 Electron beam irradiation

In this work an aliquot of the desired DNA: cisPt sample was drop cast onto a GC electrode stub and dried under a lamp. The prepared electrode was loaded onto the sample chamber. The material was exposed using an electron beam of acceleration voltage of 5 kev for 24 minutes i.e. the optimum reaction time found (see chapter 6). The tool was set such that the electron beam elevation consisted of the following coordinates Z: 102 X: 60 and Y: 25, ideally central coordinates of where the beam falls.

3.9.7.2 Low temperature pseudo pyrolysis process

The quartz tubes for the furnace were supplied by MultiLab Ltd supplier (Newcastle upon Tyne, UK) and consisted of a furnace tube of a 35 mm outer diameter and a 32 mm inner diameter. The main body was 600 mm long. A furnace cap of an outer diameter of 8 mm was used.

The sm-DNA-cisPt films prepared by casting onto a GC stub were loaded into a corundum boat which was then placed in a tubular furnace under an inert nitrogen atmosphere purging at 50 mL min^{-1}. The optimum reaction temperature was investigated within a temperature range of 160-350 °C for a duration of 30 minutes (12). All the samples were carbonised at the optimised reaction conditions found of 255 °C for 30 minutes (see chapter 7).

References

1. Englert K. DNA Origami Catalysts. [PhD thesis]. Birmingham (UK): University of Birmingham; 2019.
2. Brownson DAC, Banks CE. The Handbook of Graphene Electrochemistry. Springer London; 2014.
3. Autolab Application Note EC08. Basic overview of the working principle of a potentiostat/galvanostat (PGSTAT) – Electrochemical cell setup. Metrohm AutolabBV. 2011;1–3.
4. Bard AJ, Faulkner LR. Electrochemical Methods: Fundamentals and Applications. Wiley; 2000.
5. Allard T, Balan E, Calas G. Handbook of Clay Science. Dev Clay Sci. 2013;5:127–38.
6. Smith DJ. Chapter 1. Characterization of Nanomaterials Using Transmission Electron Microscopy. (37):1–29.
7. Nellist PD. Scanning Transmission electron microscopy. In 2019. p. 49–99.
8. Smith RAP. Surface characterisation of heterogeneous catalysts by XPS: Part I. Platin Met Rev. 2009;53(1):55–6.
9. Alessandrini A, Facci P. AFM: A versatile tool in biophysics. Meas Sci Technol. 2005;16(6).
10. Etzler FM, Drelich J, Frequency R, Surface S, Microscopy AF, Microscope AF. Their Interactions terization of Surfaces , Particles , and Atomic Force Microscopy for Charac- Tapping Mode.
11. Horiba. No Title [Internet]. What is Raman Spectroscopy? 2020. Available from: https://www.horiba.com/en_en/raman-imaging-and-spectroscopy/
12. Nakao H, Tokonami S, Yamamoto Y, Shiigi H, Takeda Y. Fluorescent carbon nanowires made by pyrolysis of DNA nanofibers and plasmon-assisted emission enhancement of their fluorescence. Chem Commun. 2014;50(80):11887–90.
13. Scientific TX. No Title [Internet]. What is X-Ray Photoelectron Spectroscopy (XPS)? 2020 [cited 2020 Apr 21]. Available from: https://xpssimplified.com/whatisxps.php
14. GERO C. Graphitisation at up to 3000 °C. 2017;E42–6.

Chapter 4-

Electrochemical Testing and Characterization of (Salmon Milt) DNA-Cisplatin Adducts for the Electrocatalysis of the Hydrogen Evolution Reaction (HER)

Chapter 4: Electrochemical Testing and Characterization of (Salmon Milt) DNA-Cisplatin Adducts for the Electrocatalysis of the Hydrogen Evolution Reaction (HER)

4.1 Introduction

The electrolysis of water to form hydrogen via the Hydrogen Evolution Reaction (HER) and oxygen via the Oxygen Evolution Reaction (OER), is an environmentally friendly and sustainable way of generating chemical fuel (1). Through their recombination, chemical energy can then be converted into electricity, which is the fundamental operating principle behind Polymer Electrolyte Membrane Fuel Cell (PEMFC) technology, involving the hydrogen oxidation reaction (HOR) and oxygen reduction reaction (ORR) (2). These occur at the anodic and cathodic compartments respectively and are shown by equations (1, 2).

$$H_2 \rightarrow 2H^+ + 2e^- \; Eq.(1)$$

$$\frac{1}{2}O_2 + 2H^+ + 2e^- \rightarrow H_2O \; Eq.(2)$$

Platinum metal outperforms many electrocatalysts for both the HER (in acidic conditions) and ORR. However, given the concerns involved over its cost and availability, there is ongoing research into how catalytic performance can be maintained with lower platinum loadings (3), (4) (5), since at least one study has found that lower loadings led to an improvement in the efficiency (6). This was explained by an increase in the platinum particle size, which is a function of increased loadings, having an adverse effect on electrocatalysis. In fact metal nanostructures and size are both important considerations in the catalyst design, as only certain metal sites on the surface of the catalyst are actually active, with the majority typically being inactive (7).

With the aim of reducing platinum metal loadings further in catalytic materials associated with clean fuel and energy production, herein a synthetic biology approach is employed to create a nanostructure design that uses DNA as a scaffold for the accurate placement of the platinum metal atoms (see figure 1). In the design the spacing of the individual platinum atoms along the backbone of DNA is considered and is a means of reducing undesirable clustering and instead exposing more of the metal atoms as 'active sites', thereby raising the catalytic efficiency of the resultant material. In fact the use of DNA as a scaffold for metal complexes is not unprecedented, (8) and (9) , with it previously being used for attaching, or directing the growth of platinum nanoclusters as catalysts for either the HER or ORR (10), (11) and (12).

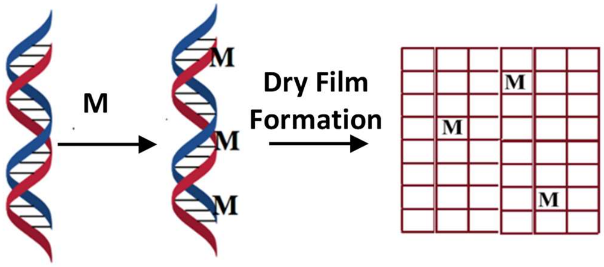

***Figure 1**- Schematic representation of the fabrication process of the catalytic material used and assessed in this work, where M = Pt.*

However, in this approach, the anticancer drug cisplatin [Pt $(NH_3)_2Cl_2$] is used as the source of platinum atoms. The binding mode of cisPt to DNA is well understood, with the major interaction being the formation of two intrastrand Pt-N bonds that link adjacent guanine nucleobases at the N7 position, although interactions with other mono- and bi-dentate purine adducts is possible (13),(14),(15),(16). This is illustrated in figure 13 in chapter 2. The ability of cisPt to form strong monomeric complexes with DNA is an important factor in ensuring that robust catalyst precursor materials are formed, containing individually and regularly spaced platinum atoms.

The electrochemical behaviour of DNA-cisPt material for the HER has been reported in the literature at a mercury electrode which shows that the presence of the platinum metal had an influence on the electrochemical peak signals commonly associated with the guanine and cytosine bases (17). It has also been reported that the catalytic evolution of hydrogen at the surface of hanging mercury drop electrodes by platinum contained in DNA-cisPt adducts can result in chemical conversions of the guanine base in the DNA into 7,8-dihydroguanine (18).

However, in the interest of this work, it is the findings reported by (19), that are more remarkable, showing that decreasing the concentration of free cisPt by the addition of DNA led to a delay in the deposition of platinum at the working electrode surface which consequently reduced the appearance of the peak currents for the proton/hydrogen-system. This is explained simply by the suppression of the electroreduction of cisPt following the molecules interactions with DNA. The author (19) also reports this being due to steric hindrance hence the electrolytic current for proton reduction is decreased as the number of free cisPt is reduced and consequently there is a reduced loading of platinum deposited on the surface of the glassy carbon electrode (19).

Similar observations to this have also been reported to support these findings i.e. the presence of DNA has an influence on electroreduction of cisPt and consequently catalysis of HER by the platinum nanoparticles as reported in the literature (20), (21) and (22).

The aims of the work produced in this chapter are to assess the feasibility of the use of DNA-cisPt adducts for the catalysis of HER at different loadings of cisPt. The objectives include characterization of the material to assess the co-ordination of the platinum and DNA and the ideal loading of platinum as a catalyst for electrochemical reactions. This entails experimental techniques like Scanning Transmission Electron Microscopy (STEM) imaging, Atomic Force Microscopy (AFM) imaging, X-ray Photoelectron Spectroscopy (XPS) of the material and finally electrochemical testing of the resulting dry films for HER under acidic conditions. The results demonstrate interesting trends in catalytic behaviour as a function of platinum loading in the HER reaction. The work in this chapter focuses on finding the optimum reaction parameters for electrochemical testing of the material by firstly finding the electrochemical window for the HER in the electrolyte and solvent conditions employed at the working electrode, made up of a DNA-cisPt modified glassy carbon surface. In addition, the optimum loading of the volume of the DNA-cisPt adducts casted onto the glassy carbon surface is explored as a function of the change in the voltammetry response. The electrochemical behaviour for the HER can then be investigated and the effects observed with different loadings of the cisPt to the DNA.

4.2 Materials and Experiments

4.2.1 Material Synthesis

All the material detailed and used in this work was synthesized and provided by Klaudia Englert (23), School of Chemistry, University of Birmingham.

Deoxyribonucleic Acid (DNA), sodium salt from salmon testes, cisplatin (99.99 % purity (based on trace metal analysis)) were purchased from Sigma Aldrich. DNA-cisPt adducts were synthesized by dissolving the salmon milt DNA (sm-DNA) in Milli-Q water (resistivity ≥ 18.2 MΩ.cm) and sonicating to prepare a stock solution. Cisplatin in aqueous form was mixed with the sm-DNA and incubated at 37 °C overnight for 10 hours. Confirmation of the adduct formation was achieved using spectrophotometric techniques using Shimadzu UV-1800 spectrophotometer, Jasco J-810 spectropolarimeter and Cary 5000 UV-Vis-NIR Spectrophotometer. The platinum metal loadings employed in the initial work of this study were much higher than the initial targets of the project; going up to ratios with twice as much platinum metal as DNA , for example a ratio loading of 1:2 DNA-cisPt.

The findings from the initial work (24) suggest that at higher metal loadings we start to re-aggregate the metal on the DNA, resulting in unfavourable changes to the surface morphology i.e. agglomeration of platinum nanoclusters instead of the localized platinum atoms that are better distributed on the DNA. This justifies the employment of much lower cisPt loadings in the material synthesized, processed and characterized in this thesis. The ultimate goal of this project is to synthesise a pre-cursor catalyst material with optimum electrocatalytic activity at the lowest platinum (i.e. cisplatin) loading attainable. The range of loadings prepared and tested in this work are displayed in Table 1.

***Table 1**- Ratio and concentrations of the DNA-cisPt samples synthesized and characterized.*

Ratio of sm-DNA to cisPt	*Concentration of cisPt in a 1000 µL solution /µM*	*Concentration of sm-DNA in a 1000 µL solution /mM*
1:0	0	1
$1:10^{-4}$	0.1	1
1: 10^{-3}	1	1
1: 10^{-2}	10	1
1: 0.1	100	1
1:1	1000	1
cisPt	1000	0

[2]

Experimental work

The material received was experimentally tested and characterized by the author of this thesis in the experimental methods described below.

4.2.2 Electrochemical testing

4.2.2.1 Film formation on a glassy carbon macroelectrode

Glassy Carbon (GC) electrode surfaces modified with nucleic acids have been employed for a range of voltammetry techniques ranging from differential pulse voltammetry to linear sweep voltammetry. Pang et al. (25) reported the existence of strong adsorption on GC electrode provided the DNA was evaporated to dryness on the electrode surface. The interaction of DNA and GC is a combination of both hydrophobic and electrostatic forces, leading to the adsorption of the nucleic acids onto the surface. Observations have been made to show that the quantities of modification of double stranded DNA (dsDNA) were greater when the DNA was cast on a metal (gold and platinum) compared to a GC

---

[2] Synthesis by Klaudia Englert, School of Chemistry, University of Birmingham.

surface (25). This difference is likely from the differences in the surface structures of each of these materials, affecting the stability of the DNA. For example on platinum, DNA demonstrates no resistance to acids and bases while on glassy carbon and gold, DNA is unstable to bases.

A 3 mm GC macroelectrode was polished on micro-cloth pads with decreasing size alumina slurries (1.0, 0.3, 0.05 µm, Buehler IL), followed by rinsing with de-ionised water (DIW) and drying under a gentle flow of nitrogen. Once dry, the electrodes were modified by drop casting an aliquot of the prepared DNA-cisPt sample (optimum volume of 25 µL onto the 3 mm GC electrode surface) and drying under a lamp.

4.2.2.2 Method of electrochemical testing

The samples prepared (see Table 1) were electrochemically tested using a 3 electrode cell, involving a glassy carbon electrode (GC, 3 mm, BASi) as the working, a saturated calomel (SCE) (BASi) reference and a bright platinum mesh counter electrode. The cell was controlled by an Autolab 128N potentiostat running Nova 2.1 software (Metrohm-Autolab BV, Netherlands). All potentials are reported against a SCE. All chemicals involved were used in their analytical grade and used without any purification. Perchloric acid (70 %, 99.99 % trace metals) (1 mM, pH 3) and sodium perchlorate (≥ 98 %) as the supporting electrolyte (0.1 M) supplied by Sigma Aldrich. All electrolytes were made up with DIW of a resistivity $\leq$ 18.2 MΩ.cm (MilliQ, Millipore) and thoroughly degassed with dry nitrogen (oxygen-free, BOC Gases plc) prior to experimentation.

4.2.2.3 Electron Microscopy

The surface morphology of the material was attained using High Angle Annular Dark Field Scanning Transmission Electron Microscopy (HAADF-STEM) operated in both dark field and bright field imaging using a JEOL2100F instrument. The samples were prepared for imaging by casting 3 µL of the sample onto a 300 Cu mesh holey carbon TEM grid and drying under a lamp. The STEM was operated in Z-contrast mode using a HAADF detector at 200 kV acceleration voltage.

4.2.2.4 Surface Topography

The change in the surface topography as a result of the interactions of the cisplatin with DNA were observed using 'Dimension 3100' Atomic Force Microscope (AFM) (Veeco Digital Instruments, Bruker), equipped with a NanoScope IIIa controller. 20 µL of the DNA-cisPt solution was drop cast onto a HOPG surface and was left to dry in air before using a stream of nitrogen gas to achieve complete drying. The microscope was operated in tapping mode.

4.2.2.5 Surface chemical properties

XPS characterization was conducted at Harwell XPS, UK facilities to obtain the binding energies (BE) and survey spectra of the samples synthesized, using α-Kl as the X-ray source (characteristic energy of 1486.68 eV). The BE is reflective of the oxidation states of the elements in the DNA-cisplatin adducts including Pt, Cl, C, P, N and O. The changes in the BE confirms whether the covalent interaction of the platinum occurs on the expected oligonucleotide base site.

4.3 Results and Discussions

4.3.1 Electrocatalysis of the hydrogen evolution reaction (HER)

Electrochemical testing using the 1:1 DNA-cisPt were conducted to explore the limits of the electrical voltage applied, the volume of the DNA-cisPt material casted onto the GC surface and the influence of washing off unbound cisPt molecules from the casted films using water, prior to assessing the effects of platinum loading in the DNA-cisPt on the electrocatalytic performance.

4.3.1.1 Electrochemical voltage window

The limits of the electrical voltage window change with the solvent used and the working electrode surface employed (26). Therefore the electrochemical window was explored for the electrocatalysis of the HER by DNA-cisPt/GC in perchloric acid ($HClO_4$) and sodium perchlorate ($NaClO_4$) electrolyte solution, starting the scan by applying 0 V vs SCE and ceasing until solvent breakdown was observed i.e. point at which the applied voltage results in an infinite increase in the current density output.

In addition, being aware of the electrochemical voltage window is important since in acidic environments, DNA can dissociate from the surface of the GC electrode and the electrochemical reductions of Adenine and Cytosine bases can subsequently take place in the aqueous solution. For example, this has been reported in the literature to occur at a half-wave potential ($E_{1/2}$) of -1.33 V vs. SCE for Adenine and -1.44 V vs SCE for Cytosine at a pH of 4.2 (27). This can help to distinguish between the electrochemical peaks being associated with the electrochemical reactions of the electroactive species of interest i.e. proton reduction or instead with the electrochemical reactions of the DNA bases.

4.3.1.2 Optimum volume

Defining an optimum volume of the DNA-cisPt material to cast onto the GC surface is key since in principle, there will be a volume in which the loading of the catalyst will no longer be the limiting factor to the catalysis and the geometric surface area of the GC electrode will be insufficient for complete and effective coverage. This would result in uneven films of the material and poor adsorption to the surface.

In this work, the optimum volume for the 1:1 DNA-cisPt and 1000 µM cisPt samples was explored by casting and drying volumes in the range of 5-35 µL of the material onto the GC electrode surface (d=3 mm) and testing electrochemically in the aforementioned ways at 3 scan rates including 10, 25 and 50 mV s^{-1} in 1 mM $HClO_4$, 0.1 M $NaClO_4$. The voltammetry response for the 50 mV s^{-1} is displayed in figure 3(B) and repeats were found to obtain an average value for the measured peak potential (E_p) and peak current (I_P) values.

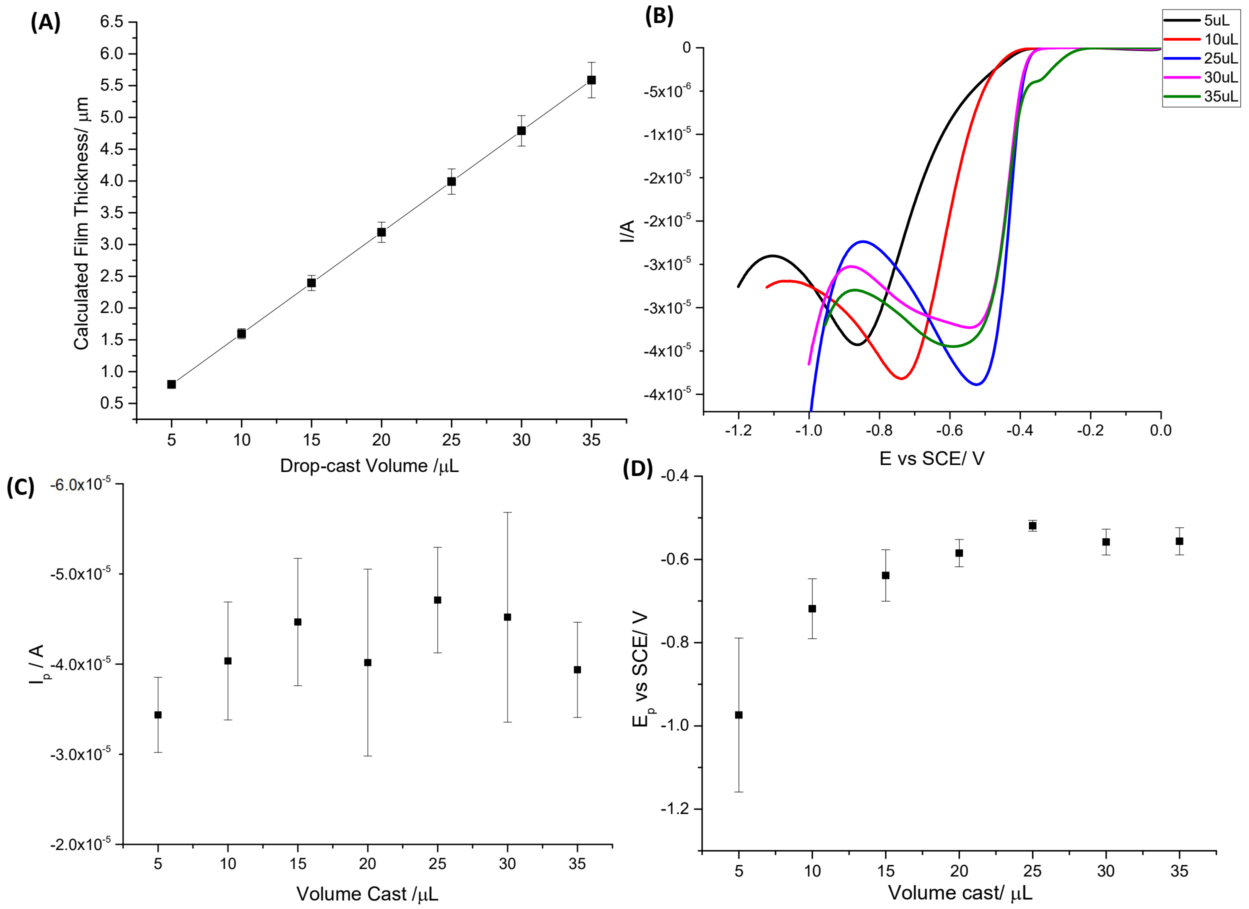

Figure 3- *(A) How the modelled film thickness varies with drop cast volume of 1 to 1 DNA-cisPt on 3 mm GC surface (B) The voltammetry response for the HER (1 mM $HClO_4$, 0.1 M $NaClO_4$) 50 mVs^{-1} at different volumes of 1:1 DNA-cisPt cast on GC (d= 3 mm) (C) The change in the peak current value with volume cast (D) The change in peak potential with volume cast (3rd cycle). Error bars are based on a calculated standard deviation.*

We observe a significant shift in the wave peak potential as the drop cast volume is increased from 5 to 20 µL where it reaches a constant value, as illustrated in figure 3(D). This is predominantly due to the resistive nature of the DNA. As the amount of Pt deposited increases, the resistance of the modifying layer decreases and the size and number of Pt clusters increase. In addition, there may be changes to the diffusion profiles as the thickness of the DNA-cisPt material is changed with drop-cast volume.

4.3.2 Changes to the diffusion profile

As the volume of the catalyst material increases, the platinum mass loading also increases and simultaneously the drop cast film thickness also increases as demonstrated in figure 3(A). This is based on the measurement of film thickness being modelled as a function of both the mass of DNA in the drop cast volume and the density of DNA films reported in the literature of 1.41 ± 0.03 g cm^{-3} (28). The modelling method has been detailed in appendix 1, see figure A1.1. Thus the model follows the theoretical expectations i.e. that as we increase the volume of the material drop cast, there is an increased thickness of the dry film, which would reduce the rate of diffusional transport, giving rise to changes in the diffusion profile.

This also gives rise to changes to the thickness and number of porous layers, with the drop cast volume, whereby there will also be inaccessible pores which can change the diffusion profile, from bulk to thin layer diffusion. The presence of pores also implies an increased likelihood for Knudsen diffusion, see chapter 2. This highlights the under-lying issue of drop-cast techniques, where we observe electrocatalytic profiles due to a mixed diffusion regime i.e. Fickian vs Knudsen vs thin layer, leading to shifts in the half wave potential resulting from the heterogeneous surface, see chapter 2. Hence the shifts in both the E_p and I_p do not necessarily associate with electrocatalytic effects , but instead may be due to changes in the profile of thin-layer diffusion effects (29). Thus, changing the thickness of the DNA-cisPt layer, will change the CV response too.

4.3.3 Electrocatalytic effect

On the other hand, from an electrochemical standpoint, there is a threshold for the mass loading of platinum onto the surface of GC. For example literature reporting's (30) found that beyond 28 µg cm^{-2} of platinum, there tends to be aggregation of the platinum particles, thus hindering the performance of the catalysis for the Oxygen Reduction Reaction (ORR). They noted that the specific activity (SA) increased at reduced Pt loadings, whilst increased agglomeration in the active layer was observed for higher Pt loadings. This hypothesis could correlate with the experimental findings shown in figures 3 (C &D), whereby beyond 25 µL, the magnitude of the peak current (I_p) declines and the peak potential (E_P) does not significantly change. However, to further explore this statement for the HER, STEM imaging characterisation is used to study the changes in the platinum nanocluster size with cisPt loading on the DNA scaffold. This is discussed later in this chapter.

4.3.4 Changing the scan rate

The same testing and analysis was applied for the results attained at a scan rate of 10 and 25 mV s^{-1}, see appendix 1, figures A1.3-A1.4. Anomalous results were omitted and it can be concluded that at a loading of 25 µL of 1:1 DNA-cisPt, we attained the lowest peak potential (E_P) and maximum peak current (I_P), for all the scan rates investigated, see appendix 1, figure A1.5.

In summary, there will be a small shift in peak potential with the drop cast volume as the voltammogram changes from being down to electrocatalytic effects to instead, the changes resulting from mass transport and specifically thin-layer voltammetry (29). To further elaborate, this means by increasing the thickness of the DNA-cisPt deposit, the CV response will become more like a thin-layer response. However, after a volume deposit of 25 µL, the shift in E_p is insignificant suggesting that Fickian diffusion to the surface of the deposit dominates and that there are mass transport limitations. Meanwhile, below 25 µL, there is incomplete coverage of the electrode surface, in addition to few metal aggregates.

The dependence of the peak current on the drop cast volume, figure 3(C), can be explained by a suppression to the interaction of the DNA with the GC surface as the volume drop cast is increased. Similar observations involving DNA-metal complexes have been reported in the literature (31), where it was demonstrated using their work on DNA-Cu^{2+} complexes that there would be a maximum concentration of copper that would be reached to achieve maximum current output, in their work involving the DNA-Cu^{2+} complex as a hydrogen peroxide sensor (31). Although their work involved a more controlled means of determining film thickness, they explained that the cation would start to prevent the electrostatic interaction between the DNA and the electrode, resulting in a reduced amount of electrodeposited material onto the glassy carbon surface. A similar hypothesis is made by Lin et al. who reported that during an electrodeposition process, the localisation of DNA onto the surface of GC was highly influenced by the electrostatic force of attraction between the negative phosphate backbone of the DNA chain and carbon substrate (32).

To provide a comparison, analogous experiments were conducted on drop-cast cisPt only. In this case, the electrochemical behaviour is expected to greatly improve in the absence of DNA, since it can be proposed that the unbound cisPt could form platinum nanoclusters and thus should demonstrate electrocatalytic response more equivalent to that of a bulk platinum metal.

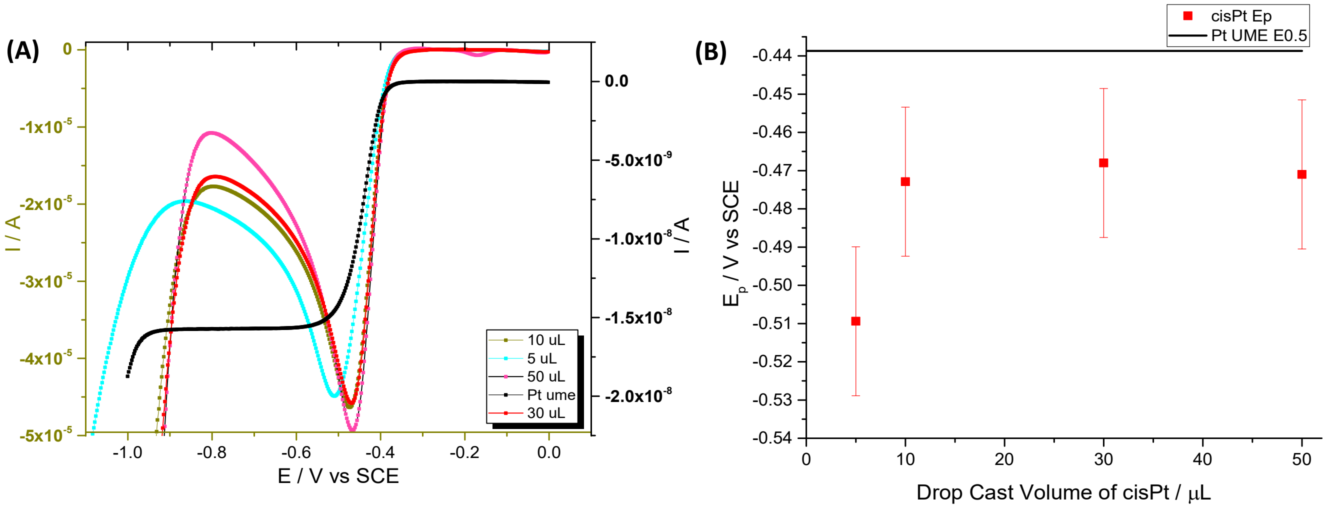

Figure 4- *(A) The voltammetry response for the HER (1 mM $HClO_4$, 0.1 M $NaClO_4$) 50 mVs^{-1} at different volumes of 1 mM cisPt cast on GC (d= 3 mm) at 50 mVs^{-1} (B) The change in the peak potential with volume cast (1st cycle) and how it compares to the half wave potential ($E_{1/2}$) of Pt UME.*

It is evident from figure 4, that beyond a loading of 10 µL, the shift in the peak potential towards that of Pt UME becomes insignificant. It was reported in the literature (30), that the specific activity is higher when the platinum loading is reduced. This is discussed by Chaiburi & Hacker (30) , where at higher platinum loadings, larger and more aggregated platinum particles are formed. This increases the surface roughness, leading to changes in the distribution of the active sites on the GC electrode.

The criticism of the casting method employed to prepare the modified GC electrode is that it can lead to irreproducibility in the results obtained, since there is no means of controlling the film thickness upon drying. However despite this, we can conclude that the magnitude of the current density is improved and a maximum output is measured at the maximum drop cast volume employed i.e. 50 µL.

4.3.5 Hydrogen Evolution vs. Platinum reduction reaction

In order to be confident that the electrochemical reduction peak is due to the electroactive species i.e. $H^{+,}$ instead of the platinum contained in the cisPt film cast on the surface of the GC electrode, the Nernst equation (equation (3)) was applied.

For the HER, the electrochemical reaction is summarised by equation (1) presented at the beginning of this chapter. This takes place at a formal potential of 0 V vs Normal Hydrogen Electrode (NHE), while the reduction of Pt^{2+} to Pt^0 occurs at a formal potential of 1.18 V vs NHE (33).

$$E_f{}^0{}_{eff}(H^+/H_2) = E_f{}^0(\,H^+/H_2) - 0.059\,pH\ Eq.(3)$$

The effective formal potential vs. NHE can be converted to SCE by shifting the value (negatively) by 0.244 V. Thus we find by using equation (3) that we expect the reduction of platinum to shift by 0.1772 V vs NHE under a pH 3 condition (34). This is equivalent to an effective potential of 1.11 V vs. SCE. The proton (H^+) reduction reaction is expected to occur at - 0.4187 V vs SCE. This value corresponds with the overpotential observed for the HER at the surface of the Pt UME for the reaction conditions employed in this work (1 mM $HClO_4$, pH 3), see figure 4.

4.3.6 Purification of the DNA-cisPt

The influence of purification of the prepared samples of DNA-cisPt adducts on the voltammetry response for the HER is explored since the prepared material is made up of a mixture of unbound cisPt and DNA strands in addition to the DNA-cisPt adducts. Since the DNA is likely to demonstrate little or no significant activity to the electrocatalysis of the HER, it is more important to remove unbound cisPt molecules from the cast film to ensure the observed behaviour is due to the platinum covalently bound to the DNA (i.e. on the DNA scaffold). Thus to remove free cisPt from the deposited film on the surface of GC, the modified electrode (DNA-cisPt/GC) was rinsed with water, since cisPt is soluble in water but DNA is insoluble. To explore the effect of rinsing, following casting and drying of the material onto the GC surface, the film is rinsed with deionised water prior to electrochemical testing. The results are displayed in figure 5.

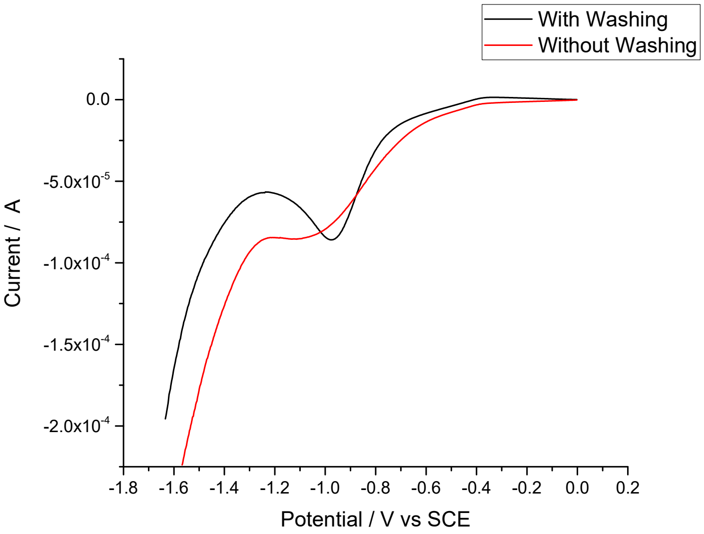

Figure 5- *The influence of washing unbound cisPt from the drop cast film on GC electrode using water on the electrocatalysis of the HER (1 mM $HClO_4$, 0.1 M $NaClO_4$) at 25 mV s^{-1} (1st cycle).*

It is evident that by rinsing the unbound cisPt with water, the voltammetry response is improved. Several theories can be proposed to explain this observation. One evident explanation is that complexation of cisPt with DNA contributes to steric hindrance as previously observed in the work of Yoshimoto et al. (19). This implies that the steric hindrance influences the available platinum / surface area of the platinum active sites exposed to the electroactive species. By removing the unbound cisPt, the inhibition to the electrocatalysis is prevented. This is because steric hindrance arises from the non-chemical interactions of the cisPt with the DNA-cisPt adducts which could slow down chemical reactions. Future work could investigate if cisPt adsorbs onto the GC working electrode surface by dispersing a bare GC electrode in a solution of cisPt and consequently immersing into a perchloric acid solution, followed by CV testing. This then enables comparisons to be made between the voltammetry of the casted DNA-cisPt films and that of the bare GC immersed in the cisPt solution to investigate whether the peak potential (E_p) of the platinum falls at the same voltage as the DNA-cisPt, under the same experimental conditions.

4.3.7 Shift in E_p with the scan number

It is clear from figure 5 that the peak potential is shifted from that measured at the first scan compared to at the third cycle. That is a shift from -1 V vs SCE (figure 5) to -0.65 V vs. SCE after the third scan (see figure 12) for 25 µL of the 1 to 1 DNA-cisPt film on GC at 50 mV s^{-1}. The hypothesis is that as we scan the surface of the drop-cast material, the size of the platinum nanoclusters is increased with cycling, shifting the voltammetry towards the response of bulk cisPt.

This follows the observations reported in the literature for cisPt (19), where the Scanning Transmission Electron Microscopy (STEM) images revealed that the density of the nanoparticles was increased with the number of scans. This is explained as both the growth of the nanoparticles and reduction of cisPt simultaneously (19).

4.3.8 Randles –Sěvcík plot at bare GC and diffusion coefficient

The cyclic voltammetry experiments of the HER, at different scan rates were explored at a bare GC electrode surface to explore the effect of scan rate on the reduction peak current for proton reduction by cyclic voltammetry testing and consequently confirm that the electrocatalytic response of the drop cast films is due to mass transport in one dimensional form. This is important, since the drop cast method employed to prepare the working electrode, could lead to the production of thick layers with voids, which behaves as a “thin-layer diffusion” system and doesn’t vary with the square root of the scan rate applied, see chapter 2. Furthermore, the corresponding diffusion coefficient for H^+ in aqueous environments can also be found from the R-S slope.

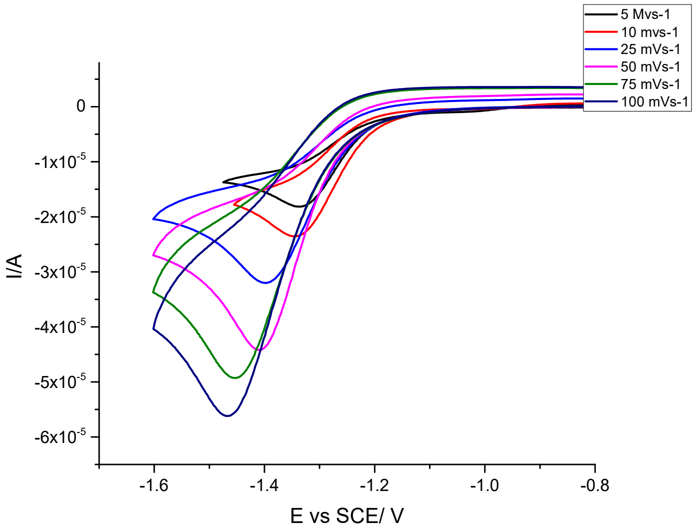

Figure 6-*CV’s for HER at GC (d=3 mm) in 1 mM $HClO_4$, 0.1 M $NaClO_4$ at different scan rates.*

The electrochemical reduction of protons (H^+) at the surface of the electrode can be described using the Randles- Sěvcík equations for an irreversible process Eq.(4) or reversible process Eq.(5), displayed below:

$$I_p = (2.99 \times 10^5)\sqrt{\alpha}\mathrm{A}\mathrm{C}_{\mathrm{Bulk}}\mathrm{D}^{\frac{1}{2}}\nu^{\frac{1}{2}}\,Eq.(4)$$

$$I_p = (2.69 \times 10^5)AD^{\frac{1}{2}}C_{Bulk}\nu^{\frac{1}{2}}\,Eq.(5)$$

where I_p is the peak current (A), A is the electrode surface area (cm^2), C_{Bulk} refers to the bulk concentration of the analyte, ν is the scan rate ($V\ s^{-1}$),D is the diffusion coefficient ($cm^2\ s^{-1}$) and α is the transfer coefficient value (assumed to be 0.5) (35). The resulting plot is shown in figure 7 and indicates a one-dimensional diffusional process (as opposed to any adsorbed behaviour).

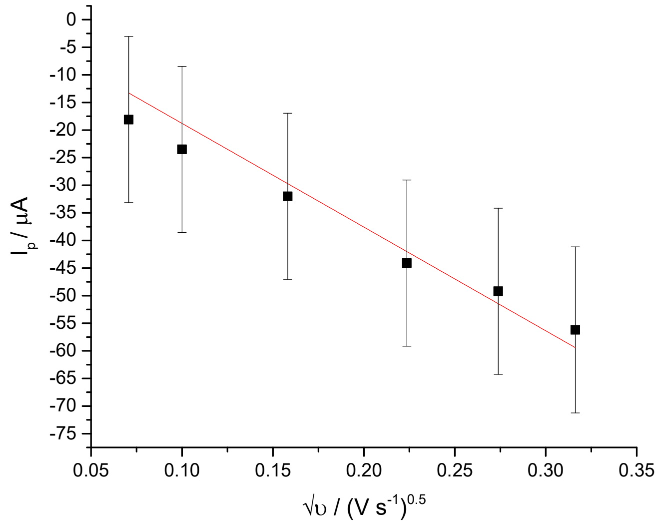

Figure 7*- Plot of Eq. (4) for the reductive current peak for the HER at GC (d=3 mm) in 1 mM $HClO_4$, 0.1 M $NaClO_4$, Gradient = -1.879 x 10^{-4} / A $(Vs^{-1})^{-0.5}$. $R^2=0.9378$.*

The diffusion coefficient can be found from the slope of the R-S plot, figure 7 and Eq. (4). Hence at a transfer coefficient (α) of 0.5, the diffusion coefficient can be calculated via Eq. (4) to be 9.78 × 10^{-5} cm^2 s^{-1}. For comparison, using the reversible R-S equation i.e. Eq. (5), a diffusion coefficient output of 1.58 x 10^{-4} $cm^2 s^{-1}$ is calculated. This value is higher than the reported diffusion coefficients of protons (D_{H^+}) in strong acids like sulphuric acid of 2.31 x 10^{-5} cm^2 s^{-1} (36) , for a 1 mM acid concentration. The irreversible equation outputs a diffusion coefficient (9.78 x 10^{-5} $cm^2 s^{-1}$) which is close to the value reported in the literature for protons in aqueous environments of 8.6 x 10^{-5} cm^2 s^{-1} (36).

4.3.9 DNA-cisPt modified GC surface

Following drop-casting of the DNA-cisPt material, the assumption that the geometric area of the electrode is fully electroactive is validated by modelling the number of cisPt molecules and surface area occupied by one cisPt molecule , based on a square planar geometry, see figure 8. This is found to exceed the geometric surface area of the working electrode i.e. 49.26 cm^2 vs. a geometric surface area of 0.0707 cm^2, see appendix 2 for the detailed method and calculations.

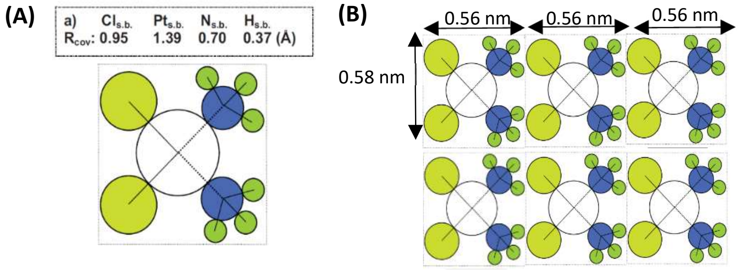

Figure 8*- cisPt molecule (A) distribution of atoms and molecular radii (B) Square planar geometry , perfectly distributed model of cisPt complexes on surface reproduced from (37).*

Based on the reports made on the interactions of DNA and cisPt at the atomic scale (37), the atomic spacing between the platinum atoms in the cisPt molecules can be modelled as illustrated in figure 8(B), to follow that of a perfectly distributed material deposit based on a square planar geometry. This means the inter-spacing between the platinum atoms can be taken as 0.56 nm.

As the loading of platinum in the material is increased, the spacing between the Pt active centres is reduced, resulting in a cyclic voltammetry (CV) profile of that of a macroelectrode (38). This results from the changes to the diffusion profile, as the diffusion zones begin to overlap (38) as shown in figure 9, where we start to move towards profiles like those presented in category 3 and 4.

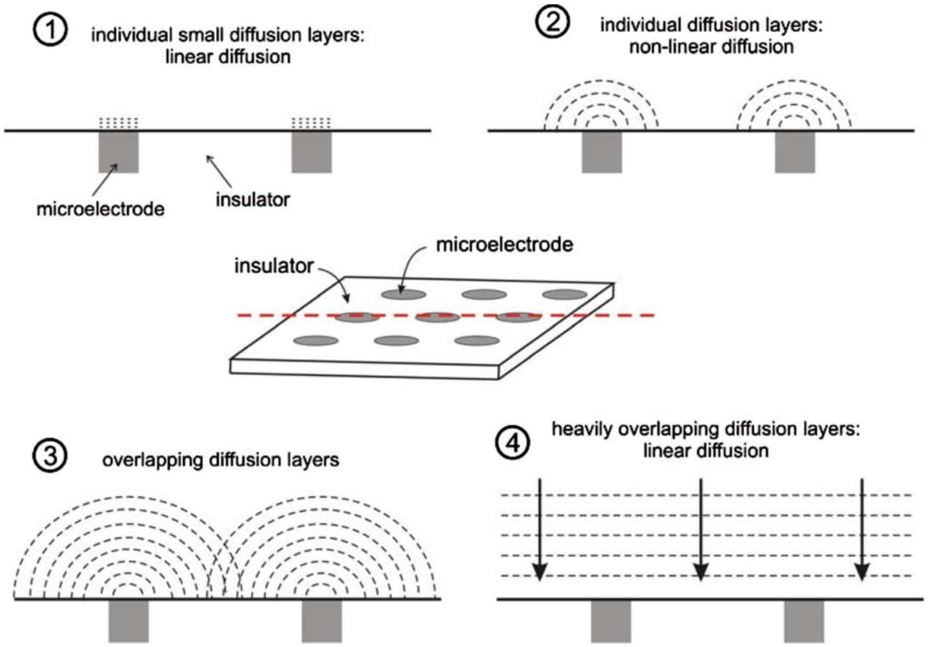

Figure 9 *- Schematic diagram of the four categories a diffusion profile may belong to for an array of microelectrodes* (38).

However to validate which category, the voltammetry response of the DNA-cisPt / cisPt / GC material falls into, an estimation of the diffusion layer thickness must be made. The diffusion layer thickness can be estimated using the following expression:

$$\delta = \sqrt{2D\frac{\Delta E}{\nu}}\ Eq.(6)$$

where δ is the diffusion thickness, ν is the scan rate (V s^{-1}), D is the diffusion coefficient (cm^2 s^{-1}) and ΔE is the difference in the potential of the electrochemically active region of the scan (V), which can be found by taking a closer insight at the region of the electrochemical peak, as demonstrated in figure 10.

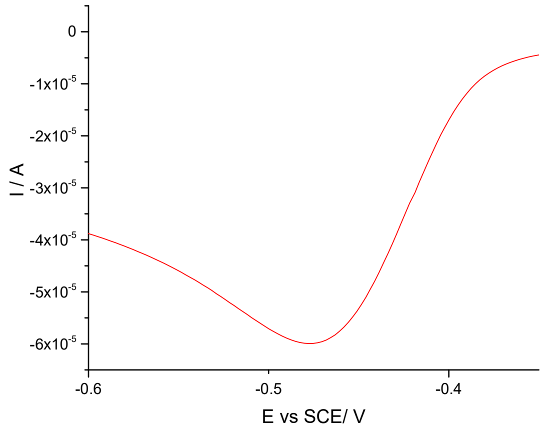

Figure 10- *Finding the size of the electrochemical potential window (ΔE) for the voltammetry response of 25 μL of 1 mM cisPt cast on a 3 mm GC surface for the HER at 50 mV s^{-1} (1 mM $HClO_4$, 0.1 M $NaClO_4$).*

Thus we find that the electrochemical potential difference is 0.25 V vs SCE, according to figure 10. By using the diffusion coefficient found from before (9.78 x 10^{-5} cm^2 s^{-1}) and a ΔE of 0.25 V for a scan rate of 50 mV s^{-1}, the diffusion layer thickness is expected to be 0.03919 cm. This implies that $\delta \gg d$ which suggests that we fall into category 4 (as shown in figure 9).

One-dimensional diffusion profile in drop casted material

The construction of the plot of log scan rate (v) vs. log current (I) can be used as a tool to evaluate whether we have a diffusion or an adsorption controlled response. A gradient of 0.5 or 1 equates to a diffusion or adsorption controlled process respectively. This is explored for the range of drop-cast volumes employed in this study i.e. from 5 to 35 μL. To illustrate how the magnitude of the slope was found, figure 11(A) shows the data points measured at the drop cast volume of 35 μL. This analysis was applied to the other volumes employed, and the logarithmic plot of scan rate (υ) vs peak current (I_p) was constructed to find that the gradient varied from 0.48 to 0.54 (within experimental error) as the drop cast volume was increased. This is an indication of a purely diffusional (semi-infinite) electrode response.

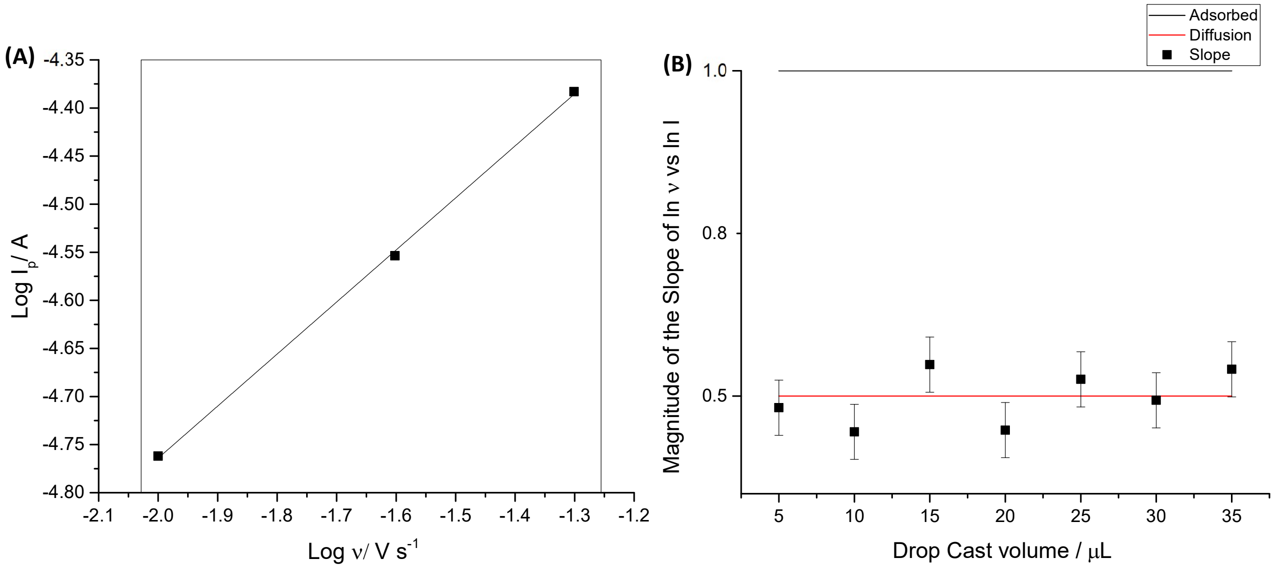

__Figure 11__- (A) Plot of Log ν vs Log I_p for 35 µL of 1:1 DNA-cisPt cast on GC (d= 3 mm), y= 0.5412x – 3.6817 (R^2= 0.9995) at 50 mVs^{-1} (B) How the magnitude of the slope of the plot of log scan rate (ν) vs. log current (I) changes with the drop cast volume of 1:1 DNA-cisPt on GC at 50 mVs^{-1} for HER (1 mM $HClO_4$, 0.1 M $NaClO_4$).

4.3.10 Electrocatalysis of HER: Different loadings of cisPt

The electrochemical behaviour of the different fabricated samples was then investigated for the HER in acidic environment (pH 3). Despite the largely resistive nature of polymeric DNA (39), additional redox-active centres retain their electrochemical activity (40),(41).DNA saturated with transition metal cations can be electrochemically reduced to metallic nanowires (9),(42) and (43). The activity of the DNA-cisPt adducts was assessed using cyclic voltammetry in 1 mM $HClO_4$, 0.1 M $NaClO_4$ at a voltage scan rate of 50 mV s^{-1}. Initially a total of 25 µL of the DNA-cisPt solution was drop cast onto the GC electrode and dried under a lamp, before rinsing with water.

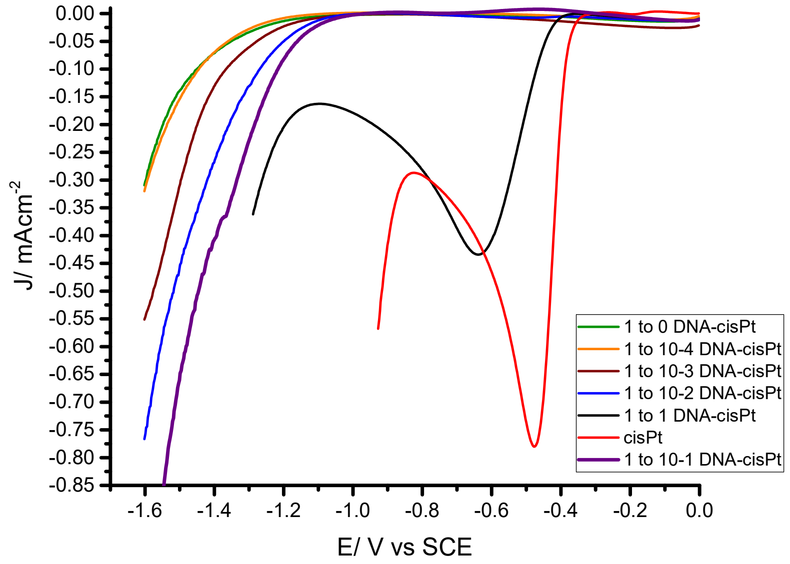

__Figure 12__- Electrocatalysis of the HER In 1 mM $HClO_4$, 0.1 M $NaClO_4$ at 50 mVs^{-1} at different loadings of cisPt in DNA-cisPt material casted on a GC (d= 3 mm) (3rd Cycle).

The DNA-modified electrodes show a clear correlation between the nominal Pt content and voltammetry response and figure 12 shows that the electrocatalysis is improved with increased cisPt loading, since a higher current density output is measured and a shift in the peak potential towards a lower overpotential i.e. towards that of the bulk cisPt is observed. The current densities achieved for the DNA-cisPt/GC are lower than the cisPt/GC surface, which indicates that the interaction of the DNA with the cisPt does indeed suppress the electrocatalysis of the reduction of protons by the Pt, which has previously been reported in the literature (20).

First, the highly resistive nature of the DNA-modified electrode will cause a considerable shift to more negative potentials. This prevents good electron transfer kinetics across the surface of the material, thus suppressing the attainable electrocatalytic activity.

As Pt is added to the DNA, these atoms are not all in electrical contact with the substrate electrode and their contact resistances are not the same. As Pt loading is increased, the mean contact resistance might be expected to decrease, causing an ohmic shift in the wave towards lower overpotentials (24). Secondly, as the Pt loading increases, the spatial distance between Pt atoms/clusters decreases and the diffusional characteristics may change from Case 1 (at ultra-low loadings) via Cases 2 & 3 to Case 4 at moderate loadings (38), see figure 9.

This leads to a gradual change in the shape of the voltammetry from sigmoidal to peak-shaped. At the loadings used here, and based on the STEM imaging characterisation below, the diffusional behaviour is expected to be within Class 4, see figure 9. Similarly, this change in shape may also reflect the mechanistic changes occurring as Pt loading increases which is discussed in the next section of this chapter, see ‘mechanistic analysis: Tafel plots’.

Optimum Faradaic current is achieved when the centre-centre separation between the arrays is large enough to avoid diffusion zone overlap, which would increase planar diffusion (44). Thus, good dispersion of the platinum atoms on the DNA is required. Previous observations reported in the literature (45) found that a cluster containing a minimum of 5 Pt metal atoms is required to electrolyse acidic solutions. Hence at lower loadings, only small clusters form, which is insufficient for the catalysis of the proton reduction (45). Furthermore, there is steric hindrance resulting from the DNA-cisPt interactions, leading to much lower current densities being observed for proton (H^+) reduction, since the majority of the platinum is bound to the DNA purine bases i.e. mostly guanine and some to adenine, thus reducing the catalysis of the HER by bulk platinum (19).

At these low loadings, nucleobase coordination dominates, thus the absence of the peak current density is explained by the DNA: cisPt films not reducing to form large enough clusters, due to the increased interparticle distance between the fewer platinum catalyst sites. Additionally, at the low metal loadings, the Pt atoms and few-atom clusters experience a high resistance, and the potential on these nanoclusters will be less negative than the potential on the underlying electrode. The resistivity of the DNA connection to the substrate electrode is therefore likely to be a significant controlling factor in the HER kinetics (24).

However, as the cisPt loading is increased, the cisPt species coordinates to the DNA non-specifically (46), (47) & (48), therefore the metal sites would become both more numerous and more mobile than covalently bound moieties, bringing them in to a close enough proximity to form catalytic centres in irregular arrays of metallic particles. As the size and number of the Pt clusters increase, the electrical contact to the substrate electrode will be lower, thus the potential (ohmic) drop across it is reduced.

4.3.11 Mechanistic Analysis: Tafel Plots

To further compare the electrocatalytic behaviour at the different DNA-cisPt loadings explored, Tafel analysis can be employed to reveal the reaction mechanism of the HER. It should be noted that a Tafel treatment of these modified electrodes is approximate due to the likelihood that the voltammetry is influenced by the kinetic, mass transport and ohmic (resistance) factors.

The mechanism for the HER in acidic conditions has been well studied and reported in the literature (2), (49) ,(50) and (51), and entails 2 of 3 possible steps shown:

$$Volmer\ H_3O^+ + e^- + * \rightleftharpoons\ H^* +\ H_2O\ \ Eq.(7)$$

$$Heyrovsky\ H^* +\ H_3O^+ +\ e^-\ \rightleftharpoons\ H_2 +\ H_2O\ \ Eq.(8)$$

$$Tafel\ 2H^*\ \rightleftharpoons\ H_2\ \ Eq.(9)$$

Where * denotes a vacant active site on the surface of the catalyst and H* is a hydrogen atom adsorbed on an active site.

The first step involves the reduction of a proton on an active site of the catalyst surface Eq. (7), followed by a second proton/ electron transfer leading to the evolution of molecular H_2, , Eq. (8), or consequently through the recombination of two adsorbed protons at the surface, Eq. (9). Other authors (2) have discussed the assignment of the Tafel slope with the mechanism of reaction in more detail.

Tafel plots (see figure 13) were constructed from the electrochemical data obtained (figure 12) and the Tafel slope was consequently found from the gradient of the plot, for the different DNA-cisPt loadings employed. The ratio of the DNA-cisPt and the relevant concentrations (see Table 1) were used to calculate the mass loadings of the cisPt i.e. platinum metal and sm-DNA (unmodified) in each of the material cast on the GC electrode. This is summarized in Table 2. Detailed calculations of the mass loadings can be found in appendix 2.

Table 2- *Mass loadings of prepared DNA-cisPt samples in an aliquot of 25 µL.*

sm-DNA: cisPt loading	Mass of cisPt in 25 µL/ g	Mass of DNA in 25 µL/ g
1:0	0	0.0319
1:10^{-4} (0.1 µM)	7.50×10^{-10}	0.0319
1:10^{-3} (1 µM)	7.50×10^{-9}	0.0319
1:10^{-2} (10 µM)	7.50×10^{-8}	0.0319
1:10^{-1} (100 µM)	7.50×10^{-7}	0.0319
1:1 (1000 µM)	7.50×10^{-6}	0.0319
0:1 (1000 µM)	7.50×10^{-6}	0.0319

The Tafel slopes found were compared to the widely accepted and reported theoretical limits for the Volmer, Heyrovsky and Tafel steps of 120, 40 and 30 mV dec^{-1} respectively in being the rate determining reactions. Commonly platinum disks and high surface area catalysts have shown a Tafel limiting step (slope of around 30 mVdec^{-1}), where detailed analysis of this is discussed in the literature by (2), (49) and (50). This observation holds for the experimental findings in this work, for the HER at the surface of a platinum ultra-micro electrode (UME) (grey line) in figure 13 (B).

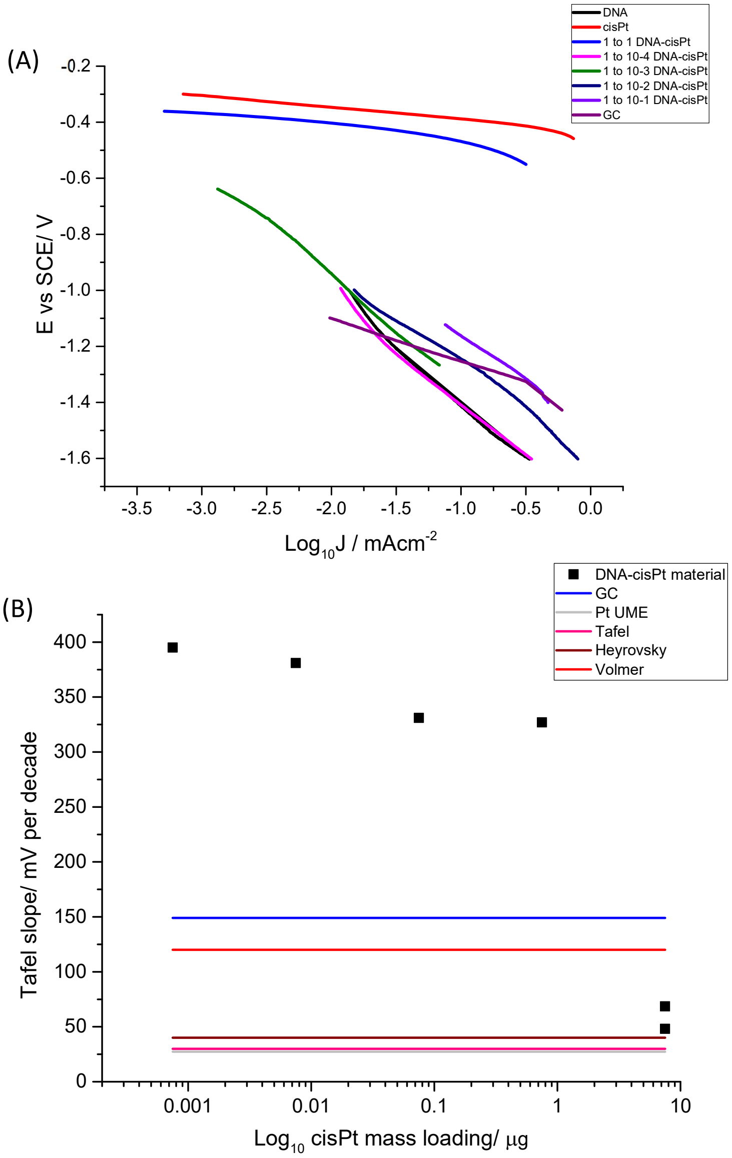

Figure 13- *(A) Tafel plot constructs for HER in 1 mM $HClO_4$ 0.1 M $NaClO_4$ at 50 mV s^{-1} for different DNA-cisPt loadings cast on GC (d=3 mm) (B) Tafel slope variation with the logarithmic scale of the mass loading of cisPt in the material.*

It is evident from figure 13(B) that as the cisPt loading is increased in the DNA-cisPt material, the Tafel slope is reduced as we move from the unmodified sm-DNA (425 mV per decade) to bulk cisPt (48 mV per decade). This change is thus reflective of the change in the mechanism of HER i.e. from the Volmer limit (DNA or DNA-cisPt/GC modified electrode) to the Heyrovsky limit (cisPt/GC modified electrode). The rate limiting step for proton reduction therefore changes from being Eq. (7) to Eq. (8).

4.3.12 XPS Analysis

Studying the interaction of DNA with cisPt using X-ray photoelectron spectroscopy (XPS) has previously been reported by (52) and (53). Both authors report the strength of XPS for gaining an insight into the specific binding that occurs between the N_7,O^6 and the Pt atom. This can be identified from the observable changes in the binding energies i.e. the chemical shift. The XPS results have revealed that the DNA-cisPt complexation results in a chemical shift not only to the atoms directly involved in the interaction, (nitrogen), but also to those surrounding them (oxygen and carbon).

The XPS survey spectra for 1 to 10^{-4} and 1 to 10^{-3} DNA-cisPt loadings (see figure 14) show no observable Pt 4f and Cl 2p peaks. This implies that XPS is not feasible for detecting low concentrations of cisPt thus alternative methods like inductively coupled plasma mass spectrometry can be suggested for future work.

At the very low platinum metal loadings in the material i.e. low ratios of $1:10^{-4}$ and $1:10^{-3}$ DNA-cisPt, the Pt 4f signal is difficult to detect by XPS. However as the metal loading is increased, the signal is improved, see figures 14 (C-D) & (F) and the binding energy of the Pt 4f peak can be found to be between 72 and 73 eV. This corresponds to the presence of a Pt (II) species as expected for the complexation of cisPt with DNA (54). The binding of the platinum with oxygen and nitrogen influences the binding energies of the surrounding atoms including carbon and phosphorus, see appendix 1, Table A1.3-A1.4 for raw binding energies data. Furthermore, Xiao et al.(54) reported that the stability of the chemical bond could be further increased with incubation time which can be explored as part of future work of this project.

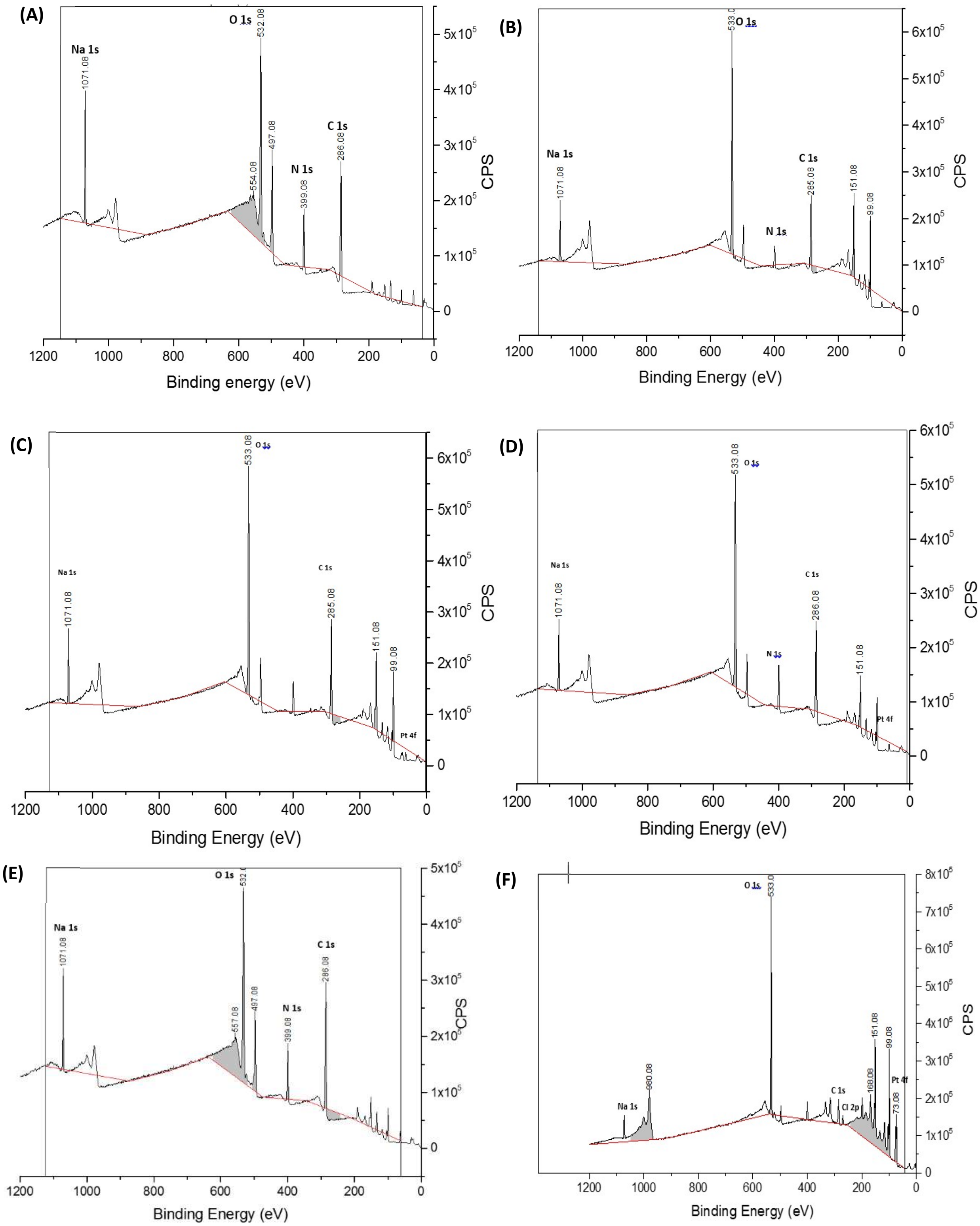

Figure 14- *XPS Survey Spectra of: (A) 1 to 10^{-4} DNA-cisPt (B) 1 to 10^{-3} DNA-cisPt (C) 1 to 10^{-1} DNA-cisPt (D) 1 to 10^{-2} DNA-cisPt (E) 1 to 0 DNA-cisPt and (F) 1 to 1 DNA-cisPt.*

The binding energy (BE) of each of the chemical elements found in the samples can be found from figure 15. To explore the effect of the cisPt complexation to the DNA, the change in the BE is defined according to the following expression:

$$\Delta BE = BE_{1:x\,DNA-cisPt} - BE_{1:0\,DNA-cisPt}\ Eq.(8)$$

Where x denotes the ratio of cisPt in the sample.

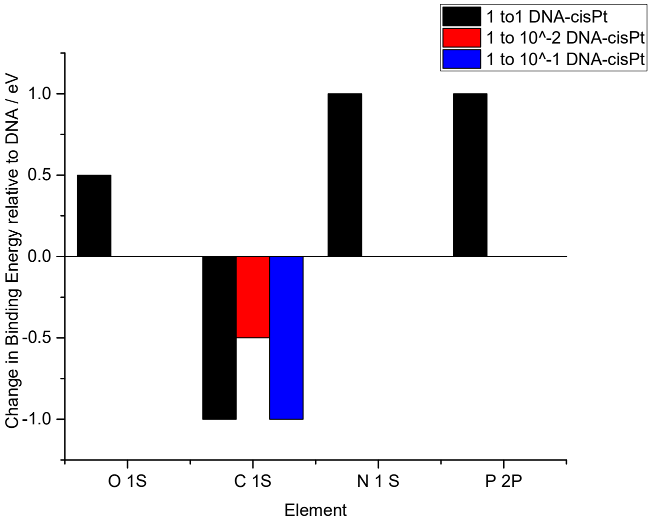

Figure 15*- Change in the binding energy values for low cisPt loadings following complexation with DNA.*

The effect of the complexation of DNA with cisPt is reflected by the increased energy values of the binding energy of the P 2p, O 1s and N 1s atoms, as illustrated in figure 15. However, the changes in all of these element is only detectable for the 1 to 1 DNA-cisPt loading, while no observable change at the lower cisPt loadings are noted with the exception to the C 1s element signal (see figure 15).

The binding energy (BE) of the P 2p atom increases by 1 eV, suggesting that the chemical interactions of platinum with oxygen and nitrogen influences the phosphate backbone. In the work of Xiao et al. (54), similar finding were made with the exclusion of the platinum to backbone interactions. The BE of the O 1s and N 1s peaks also increases as a result of the interaction of the Pt^{2+} ion with the lone pair of electrons on the nitrogen and oxygen atoms. The chemical shift in the O 1s spectra implies that the neighbouring O^6 and N_7 sites are also involved in the binding, see figure 16. This observation was previously reported by (52) and (53) where they concluded that a specific chelate is formed through the interaction of platinum with the N_7 (Gua).O^6(Gua). The change in the O 1s spectra is the result of the platinum interaction with the carbonyl group near the N_7 sites of guanine (54), as illustrated in figure 16 below. Following this interaction, the electronegative oxygen and nitrogen atoms withdraw electrons in the carbon bond, which increases the Dirac delta positive (δ^+) on the carbon atom. This consequently reduces the binding energy of C 1s atom as illustrated in figure 15.

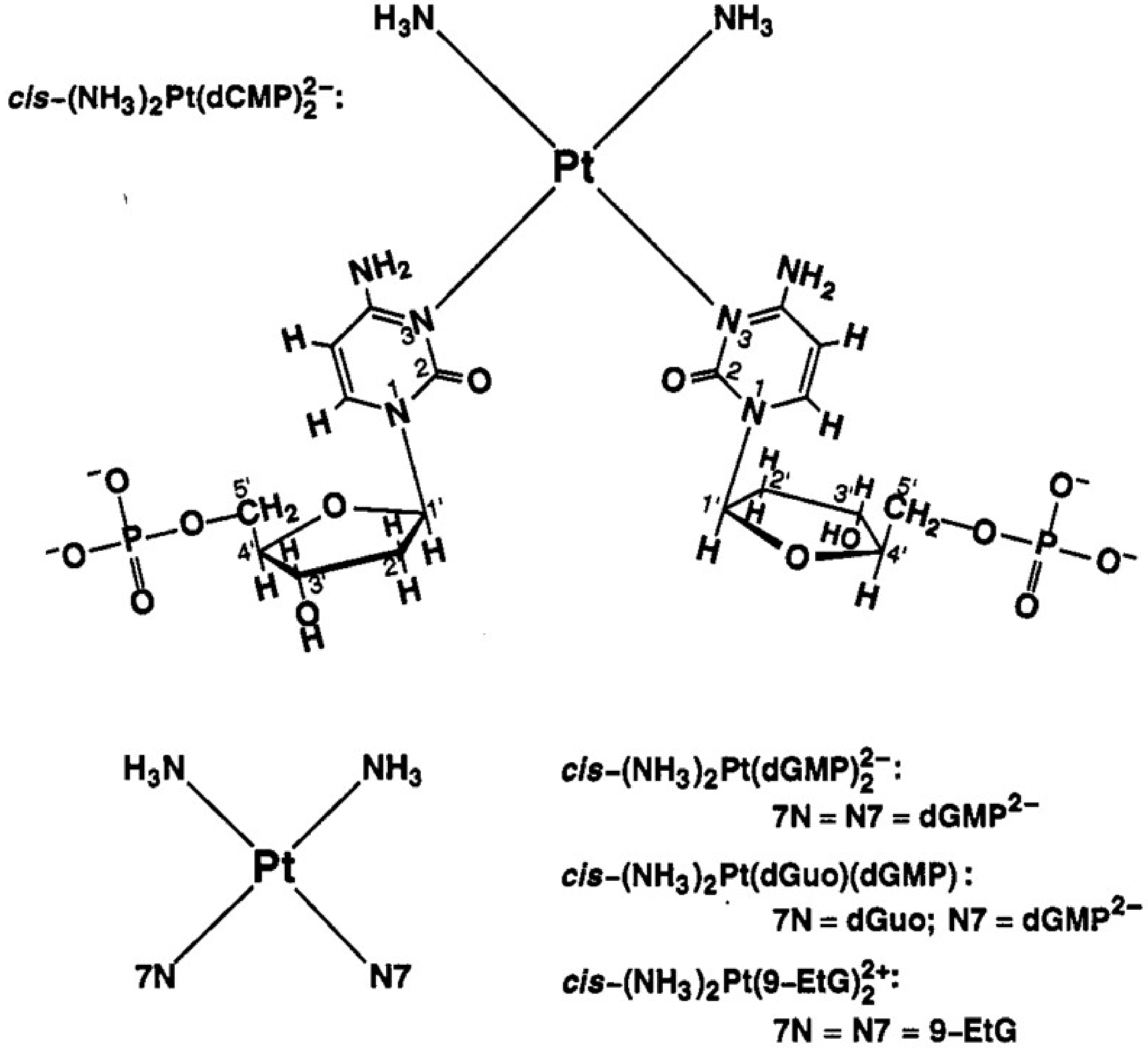

cis-$(NH_3)_2Pt(dCMP)_2^{2-}$:

cis-$(NH_3)_2Pt(dGMP)_2^{2-}$:
7N = N7 = $dGMP^{2-}$

cis-$(NH_3)_2Pt(dGuo)(dGMP)$:
7N = dGuo; N7 = $dGMP^{2-}$

cis-$(NH_3)_2Pt(9\text{-}EtG)_2^{2+}$:
7N = N7 = 9-EtG

Figure 16*- Chemical interactions between oligonucleotide and cisPt molecule copied from Lippert &Sigel* (59).

4.3.13 AFM Imaging

Initially, AFM imaging was used to confirm that interactions between the DNA and cisPt molecules had been achieved under the incubation conditions employed. This is evident from the resulting changes to the surface topography of the material following complexation of the DNA and cisPt. This is reported in the literature by Liu et al. (55) as being the resulting change in the transition of the extended DNA chains to more compact globular structures following its binding to cisPt. This observation was reported for their work on the interactions of a 1134 base pair DNA molecule with cisPt on a mica surface. The resulting change is reflective of the coordination and electrostatic interaction of the drug with the purine bases of the DNA (55).

The AFM imaging of the sm-DNA-cisPt, see figure 17, produced the same result as the literature reporting's (55), where we see a change from the extended DNA chains in the unmodified sm-DNA material (figure 17(A)) to more compact, globular structures in the presence of cisPt (figures 17(C-E)). This holds even when a lower loading of cisPt is employed i.e. 1 to 10^{-1} sm-DNA-cisPt, as shown in figure 17(E).

The observable changes in the materials topographical features are attributed to the bending of the DNA chain upon complexation with cisPt. Experimental factors such as incubation time of the cisPt with the DNA can also influence the extent of bending towards the major groove as Liu et al. (55) demonstrated.

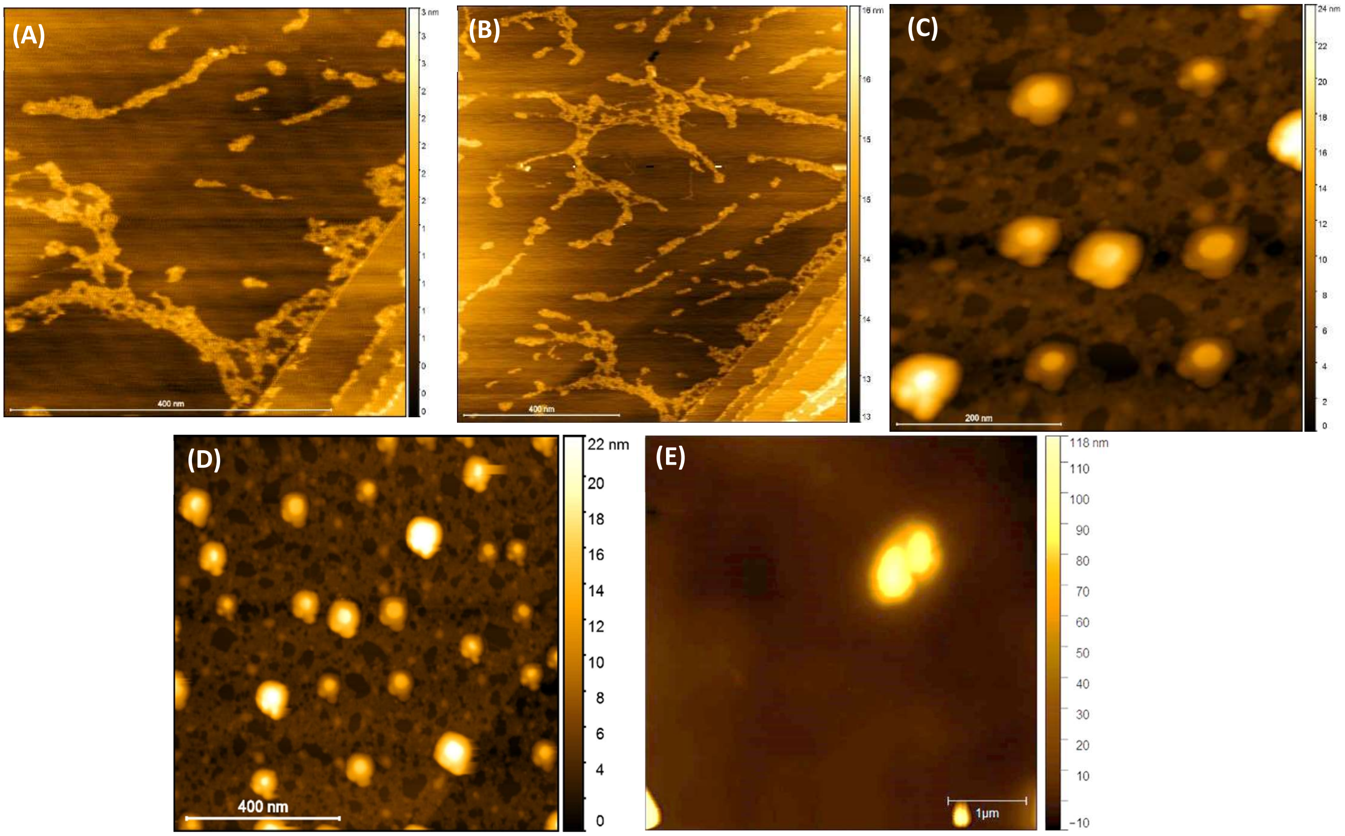

Figure 17- *AFM Imaging (Tapping mode) of (A, B) 1000 μM DNA (C, D) 1 to 1 DNA-cisPt and (E) 1 to 10^{-3} DNA-cisPt on Highly Ordered Pyrolytic Graphite (HOPG).*

In addition, the imaging surface employed can influence the true topographical features of the molecules been observed depending on the imaging conditions employed, such as in air or aqueous conditions and also the properties of the cantilever (56). It is reported by Klinov et al. that mica surfaces tend to flatten out the DNA molecules more than on a HOPG surface, as demonstrated in figure 18 (56).

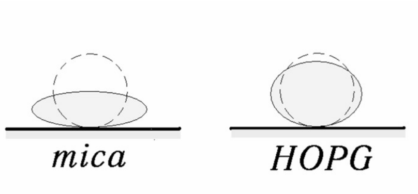

Figure 18- *The proposed scheme of DNA deposition on mica and HOPG. Cross-section of the molecules are shown. Dashed circles demonstrate natural size of the molecule in solution, copied from Klinov et al.* (56).

The main aim of this imaging technique was to observe the DNA chains in the material and confirm that complexation was achieved under the incubation conditions employed. For this research work, we are more interested in the surface morphology of the platinum metal on the DNA and being able to measure the platinum nanoparticle size. This can be achieved using high resolution imaging methods such as electron microscopy, as detailed below.

4.3.14 STEM Imaging

To study the morphology of the material and explore how the distribution of the platinum changes in the presence and absence of DNA, Scanning Transmission Electron Microscopy (STEM) imaging was employed to achieve high resolution imaging to an atomic scale.

Initially, the stage alignment on the STEM instrument was achieved using gold nanoparticles on a copper (Cu) based holey carbon Transmission Electron Microscopy (TEM) grid. Once the ronchigram is attained images of high resolution can be recorded, as presented in figure 19.

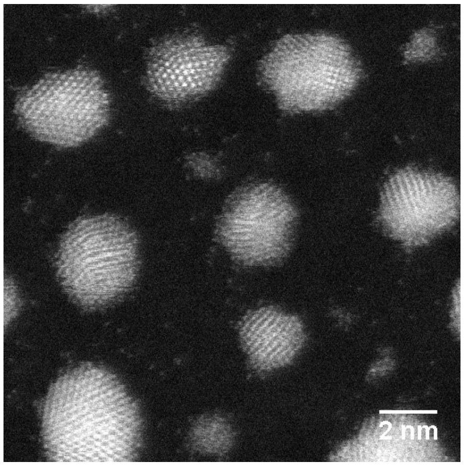

Figure 19- *HAADF STEM imaging of Gold (Au) nanoparticles casted on 300 mesh Cu based holey carbon TEM grid at x10 million magnification.*

The ultimate goal is to produce a hybrid material which consists of well dispersed and anchored platinum metal atoms on a DNA scaffold, to allow for increased efficiency and catalytic activity. Each sample was prepared separately for STEM imaging by casting 3 µL onto a holey carbon on a 300 mesh copper (Cu) TEM grid and drying under a lamp.

It must be highlighted that as evident from the STEM characterization, agglomerated platinum nanoclusters are observed when cisPt was deposited directly from solution (i.e. without reaction with DNA first) (see figures 20 (A & B)). This could be down to the nature of the material of being bulky, which is influenced by the storage time, the concentration of the cisPt and furthermore the casting methods employed. The clusters were found to have a diameter size of 1.81 ± 0.26 nm and 1.80 ± 0.27 nm for the 1000 µM and 0.1 µM cisPt, based on a standard deviation error of 27 and 29 measurements respectively, see appendix 1,Table A1.7. This agrees with the measurements reported in the literature for cisPt of 1.84 nm (57). In the absence of cisPt, as expected, DNA appears as an amorphous carbon film (figure 20(C)), without the bright spots shown in figures 20 (A &B). Figure 20(C) shows that when virgin sm-DNA solution is casted on the holey carbon film, in addition to the complex extended structures of the DNA (see figures 17 (A,B)), in some regions we observe ordered and amorphous films, which are only revealed by the electron microscopy imaging. This suggest that the films can provide large surface areas, supporting the materials use as a scaffold for the platinum catalyst.

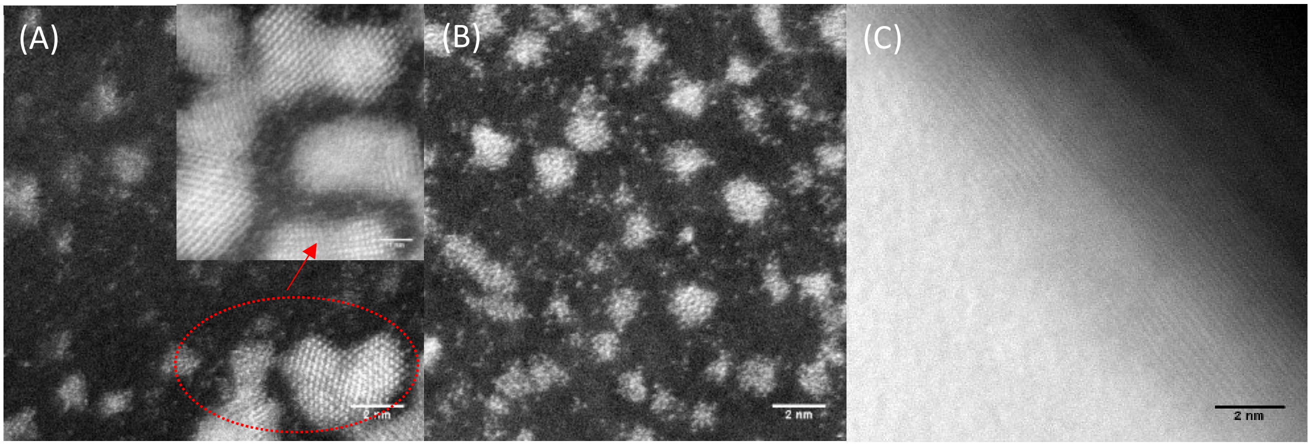

Figure 20- *Scanning Transmission Electron Microscopy imaging of drop cast films from 1000 µM solutions of (A, B) cisPt solution at magnification x10 million (x20 million inset); (B): cisPt at magnification x8 million; (C): sm- DNA at magnification x8 million. All films cast from 3 µL solutions on holey carbon TEM grid.*

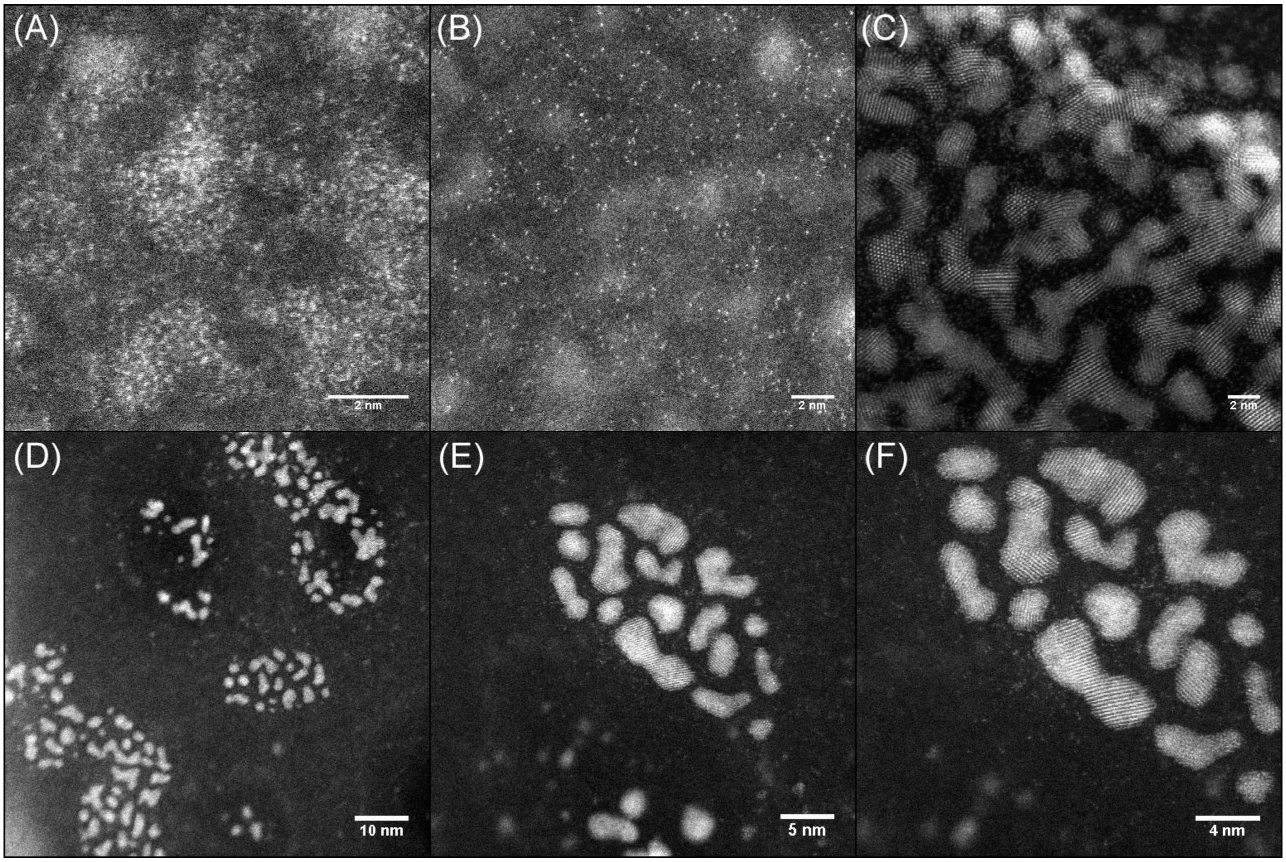

Figure 21- *HAADF STEM images of drop cast films of (A) 1 : 0.1 sm-DNA : cisPt (equivalent to 100 µM cisPt) x 15 million; (B) 1 : 0.1 sm-DNA : cisPt (equivalent to 100 µM cisPt) x 8 million; (C) cisPt (from 100 µM solution, no DNA), x 6 million and (D-F) 1 : 1 sm- DNA : cisPt (equivalent to 1000 µM cisPt) at magnifications of 200k, 400k and 600k respectively. All films cast from 3 µL solutions on holey carbon TEM grid.*

Reacting the cisPt with DNA improves the distribution of platinum when the ratio of platinum is lower than DNA in the sample. This is reflected by the changes in the size of the platinum nanoclusters measured at a higher metal loading (1:1 DNA-cisPt) compared to that at a lower metal loading (1:0.1 DNA-cisPt).

This is evident given that in figures 21 (A & B), we observe bright spots reflective of smaller platinum atoms, as opposed to the agglomerated nanoclusters seen for an equivalent bulk cisPt concentration i.e. 100 µM, figure 21 (C). However, as the cisPt loading is increased in the DNA-cisPt sample i.e. 1:1 loading, the effect is reversed and much larger nanoclusters are observed (3.83 ± 1.85 nm, see appendix 2, Table A2.9) compared to bulk cisPt of the same concentration, (figures 21 (D-F) vs. figures 20 (A&B), at increasing magnifications).

Furthermore, the platinum is more distributed at the lower metal loading compared to agglomerated nanoclusters at the higher metal ratios, (figures 21 (A & B) vs. figure 21(F)), which implies the presence of distributed individual platinum atoms as opposed to the agglomerated nanoclusters seen for cisPt deposited on its own at the same concentration. Whilst it is not clear why the nanocluster size is larger in the case of highly loaded Pt-DNA complexes, it is apparent that this occurs once the metal loading has exceeded the available nucleobase binding sites on the DNA, and non-specific binding to the DNA backbone has occurred as indicated by the spectroscopic studies displayed in our group publication (24).

4.3.15 Low loading of platinum DNA-cisPt containing material: 1 to 10^{-4} DNA-cisPt

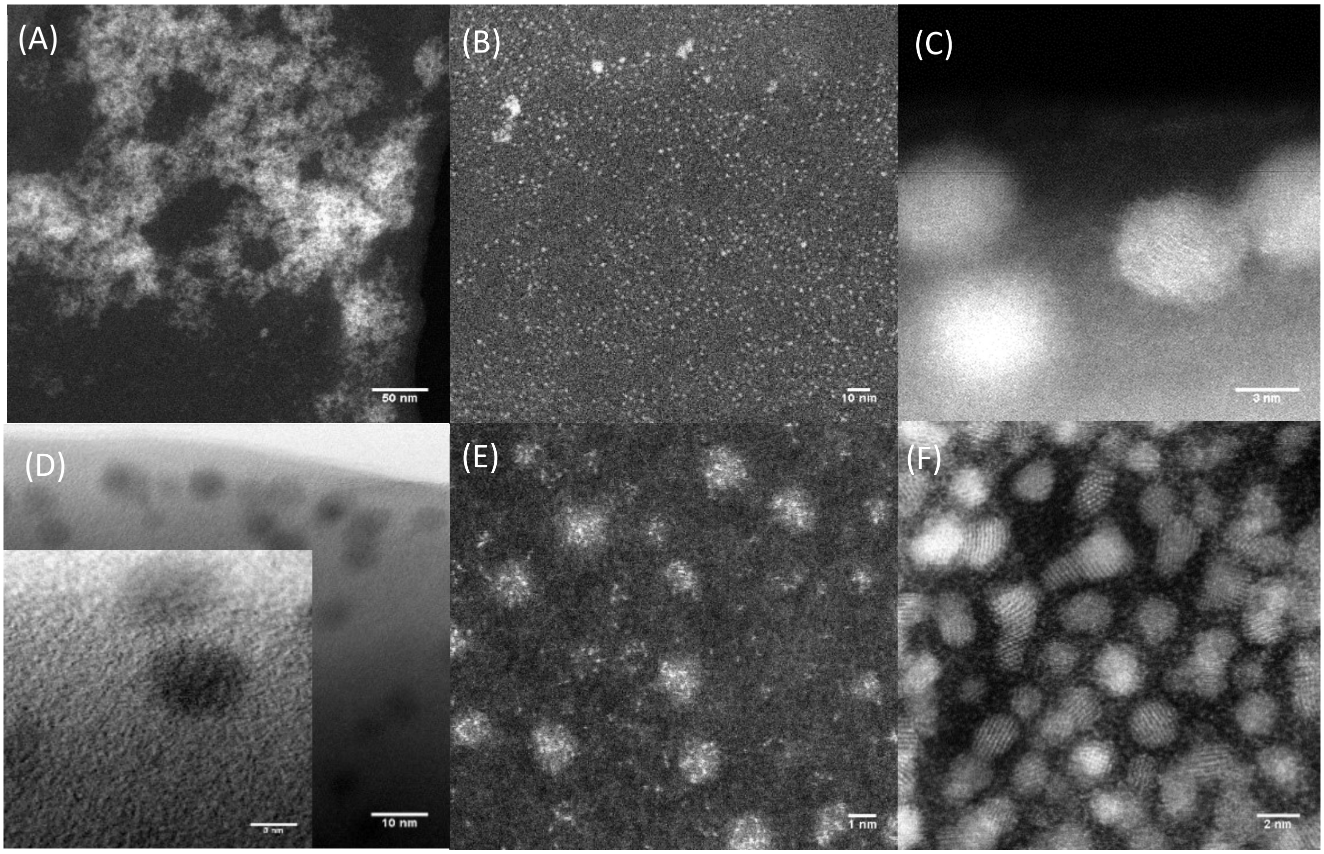

Figure 22- *HAADF STEM imaging of (A-D) 1:10^{-4} DNA-cisPt (E, F) 0.1 µM cisPt, 3 µL cast on holey carbon TEM grid.*

The changes in the surface morphology of the DNA-cisPt material was explored for the material synthesised with the lowest loading of cisPt, equivalent to 0.75 ng, see Table 2. The observations made from figure 22 are similar to those made above for the 1:10^{-1} DNA-cisPt and the 1:1 DNA-cisPt material, which are that as the ratio of the cisPt to the DNA is reduced, there is a reduced clustering of the platinum, as reflected in the morphologies we observe in figures 22(B-D) compared with figures 21(D-F).

In addition, at the low loadings in some regions of the TEM grid, it was found that that the platinum is more distributed (see figure 22 (D)) than in the absence of DNA for the same concentration of cisPt (figure 22 (F)).

It is evident that at the low metal loadings, on some regions of the TEM grid surface, we observe regions of bulky deposits of the material, see figure 22 (A). It could be proposed that these films are salt deposits from the sodium buffer that the DNA–cisPt aqueous solutions are contained in. However, this hypothesis would need confirmation and testing using STEM Energy Dispersive X-ray (EDX) mapping, thus could be suggested as part of future work.

4.3.15.1 STEM imaging limitations

To conclude, it is evident that nano-clustering of the platinum atoms occurs, hence measuring the Pt-Pt interatomic distance at this stage would be difficult given the nature of the sm-DNA i.e. large, but also the clumpy state of the bulk cisPt. In addition, the material being imaged consists of both DNA-cisPt adducts and unbound cisPt, making the surface morphology more challenging to characterise accurately.

In addition, the interactions of the material are not controlled, thus we have steric interactions in addition to covalent bindings to the DNA bases (guanine and adenine). Both of these issues are overcome using self-assembled DNA nanostructures with precise interactions of the platinum metal as presented in the work in chapter 8 of this thesis.

Lastly, imaging with high resolution at increased ratios of DNA to cisPt becomes more challenging, most probably due to the higher ratio content of salt deposits (sodium and phosphate from the buffer solution) being introduced onto the surface of the TEM grid, as noted above in figure 22(A). This is understandable from an electron microscopy point since both sodium and phosphate have a lower Z atomic number, thus have a lower imaging resolution because of the nature of their interactions with the irradiated electron beam. On the other hand, when a higher metal ratio is present in the material, the imaging resolution is improved due to the higher Z atomic number of the platinum metal leading to better interactions with the electron beam.

4.3.16 Electrical conductivity of DNA

Based on a number of charge transport studies of DNA, it was found that the resistance of DNA ranged from 1 to 10^7 MΩ (39). This wide range is primarily because of the sensitive nature of the charge transport process, which is particularly sensitive to the integrity of the base pair stack, the absence of damage within the duplex, and the electrical connections to the duplex (39). Despite the highly resistive nature of the DNA polymer (39), the redox-active centres demonstrate electrochemical activity (40),(41). Through the process of graphitisation the electrical resistance can be greatly reduced as reported for carbon nanofibers (58) where the resistivity dropped by a factor of 10^3 (58). Methods of reducing this resistivity and improving the electrical conductivity of the DNA are explored via a range of methods, as presented in the work in chapters 5-7 of this thesis.

4.4 Conclusion

In conclusion, we have synthesised a novel DNA-cisPt catalytic nano-material, characterised and assessed its electrocatalytic behaviour to assess it feasibility for its use in fuel cell applications. From this, we found that DNA can act successfully as a scaffold to disperse the platinum atoms along its backbone.

It was found through STEM imaging of the DNA-cisPt solutions that the surface morphology of the cisPt was changed with the addition of DNA as a function of platinum content. For example, at ultra-low loadings, the clustering effects were reduced and distributed individual platinum atoms could be observed.

However, for solutions of a higher platinum metal loading such as the 1 to 1 DNA-cisPt, the effect was reversed and agglomeration was increased. Larger nanoclusters were measured in the presence of DNA compared to its absence, which suggest that there is an optimum ratio of platinum metal loading to DNA for studying electrocatalysis. This new approach of using DNA as a scaffold shows promising results for fabricating fine-tuned loadings and distributions of individual platinum metal atoms, using a support other than the commercially available carbon.

In the next set of chapters, we move towards having more control over the covalent interactions of the platinum with the DNA bases, in order to achieve more localized distributions of the platinum atoms on the DNA scaffold. This will reduce the loading of the platinum metal whilst maximizing its utilisation. In addition, we focus on how we can overcome the highly resistive nature of the DNA to improve the performance of the electrochemical response measured for the HER to that of the attainable response.

References

1. Shiva Kumar S, Himabindu V. Hydrogen production by PEM water electrolysis – A review. Mater Sci Energy Technol. 2019;2(3):442–54.

2. Shinagawa T, Garcia-esparza AT, Takanabe K. Insight on Tafel slopes from a microkinetic analysis of aqueous electrocatalysis for energy conversion. Nat Publ Gr. 2015;(May):1–21.

3. Ozdemir OK. Effect of Sputtering Power on the Electrochemical Properties of Low Loaded Pt Catalysts for PEM Fuel cell. Electrochem Soc Japan. 2015;83(2):76–9.

4. Fofana D, Natarajan SK, Hamelin J, Benard P. Low platinum, high limiting current density of the PEMFC (proton exchange membrane fuel cell) based on multilayer cathode catalyst approach. Energy. 2014;64:398–403.

5. Billy E, Maillard F, Morin A, Guetaz L, Emieux F, Thurier C, et al. Impact of ultra-low Pt loadings on the performance of anode/cathode in a proton-exchange membrane fuel cell. J Power Sources. 2010;195(9):2737–46.

6. Mukerjee S, Srinivasan S, Appleby AJ. Effect of sputtered film of platinum on low platinum loading electrodes on electrode kinetics of oxygen reduction in proton exchange membrane fuel cells. Electrochim Acta. 1993;38(12):1661–9.

7. Mizuno N, Misono M. Heterogeneous catalysis. Chem Rev. 1998;97(1):199–217.

8. Duchemin N, Heath-Apostolopoulos I, Smietana M, Arseniyadis S. A decade of DNA-hybrid catalysis: From innovation to comprehension. Org Biomol Chem. 2017;15(34):7072–87.

9. Mohamed HDA, Watson SMD, Horrocks BR, Houlton A. Chemical and electrochemical routes to DNA-templated rhodium nanowires. J Mater Chem C. 2015;3(2):438–46.

10. Anantharaj S, Karthik PE, Subramanian B, Kundu S. Pt Nanoparticle Anchored Molecular Self-Assemblies of DNA: An Extremely Stable and Efficient HER Electrocatalyst with Ultralow Pt Content. ACS Catal. 2016;6(7):4660–72.

11. Tiwari JN, Nath K, Kumar S, Tiwari RN, Kemp KC, Le NH, et al. Stable platinum nanoclusters on genomic DNA-graphene oxide with a high oxygen reduction reaction activity. Nat Commun. 2013;4:1–7.

12. Ma J, Wang J, Zhang G, Fan X, Zhang G, Zhang F, et al. Deoxyribonucleic acid-directed growth of well dispersed nickel-palladium-platinum nanoclusters on graphene as an efficient catalyst for ethanol electrooxidation. J Power Sources. 2015;278:43–9.

13. Sirajuddin M, Ali S, Badshah A. Drug-DNA interactions and their study by UV-Visible, fluorescence spectroscopies and cyclic voltametry. J Photochem Photobiol B Biol. 2013;124:1–19.

14. Pages BJ, Ang DL, Wright EP, Aldrich-Wright JR. Metal complex interactions with DNA. Dalt Trans. 2015;44(8):3505–26.

15. Pinto AL, Lippard SJ. Binding of the antitumor drug cis diamminedichloroplatinum(II) (cisplatin) to DNA. BBA - Rev Cancer. 1985;780(3):167–80.

16. Jamieson ER, Lippard SJ. Structure , Recognition , and Processing of Cisplatin − DNA Adducts. 1999;

17. Horáková P, Těsnohlídková L, Havran L, Vidláková P, Pivoňková H, Fojta M. Determination of the level of DNA modification with cisplatin by catalytic hydrogen evolution at mercury-based

electrodes. Anal Chem. 2010;82(7):2969–76.

18. Daňhel A, Havran L, Trnková L, Fojta M. Hydrogen Evolution Facilitates Reduction of DNA Guanine Residues at the Hanging Mercury Drop Electrode: Evidence for a Chemical Mechanism. Electroanalysis. 2016;28(11):2785–90.

19. Yoshimoto Y, Yasukawa T, Mizutani F. Cisplatin-based DNA sensing with enhanced current response. Analyst. 2009;134(10):2113.

20. Yoshimoto Y, Yasukawa T, Mizutani F. Cisplatin-based DNA sensing with enhanced current response. Analyst. 2009;134(10):2113–7.

21. Yasukawa T, Yamashita Y, Moede R, Nakayama D, Iijima S, Mizutani F. A DNA hybridization sensor based on catalytic response by platinum deposition. Analyst. 2015;140(4):1014–8.

22. Zabost E, Liwinska W, Kowalczyk A, Glowinska A, Tomczyszyn A, Misicka A, et al. Complexes of DNA with peptide derivatives of cisPt. Electroanalytical examination. Electrochim Acta. 2016;219:568–76.

23. Englert K. DNA Origami Catalysts. [PhD thesis]. Birmingham (UK): University of Birmingham; 2019.

24. Englert K, Hendi R, Robbs PH, Rees N V., Robinson APG, Tucker JHR. Cisplatin adducts of DNA as precursors for nanostructured catalyst materials. Nanoscale Adv. 2020;

25. Zhao Y, Pang D, Wang Z, Cheng J, Qi Y. DNA-modified electrodes . Part 2 . Electrochemical characterization of gold electrodes modified with DNA. 1997;431:203–9.

26. Elgrishi N, Rountree KJ, McCarthy BD, Rountree ES, Eisenhart TT, Dempsey JL. A Practical Beginner’s Guide to Cyclic Voltammetry. J Chem Educ. 2018;95(2):197–206.

27. Paleček E, Bartošík M. Electrochemistry of nucleic acids. Chem Rev. 2012;112(6):3427–81.

28. Śmiałek MA, Jones NC, Hoffmann SV, Mason NJ. Measuring the density of DNA films using ultraviolet-visible interferometry. Phys Rev E - Stat Nonlinear, Soft Matter Phys. 2013;87(6):1–4.

29. Sims MJ, Rees N V., Dickinson EJF, Compton RG. Effects of thin-layer diffusion in the electrochemical detection of nicotine on basal plane pyrolytic graphite (BPPG) electrodes modified with layers of multi-walled carbon nanotubes (MWCNT-BPPG). Sensors Actuators, B Chem. 2010;144(1):153–8.

30. Chaiburi C, Hacker V. ScienceDirect ScienceDirect Catalytic activity of various platinum loading in acid electrolyte at K the heat demand-outdoor Assessing the feasibility of using temperature function for a long-term district heat demand forecast. Energy Procedia. 2017;138:229–34.

31. Zeng X, Liu X, Kong B, Wang Y, Wei W. A sensitive nonenzymatic hydrogen peroxide sensor based on DNA-Cu 2+ complex electrodeposition onto glassy carbon electrode. Sensors Actuators, B Chem. 2008;133(2):381–6.

32. Lin X, Jiang X, Lu L. DNA deposition on carbon electrodes under controlled dc potentials. Biosens Bioelectron. 2005;20(9):1709–17.

33. Vanýsek P. Electrochemical Series. Corros Mater. 2018;665–71.

34. Daubinger P, Kieninger J, Unmüssig T, Urban GA. Electrochemical characteristics of nanostructured platinum electrodes-A cyclic voltammetry study. Phys Chem Chem Phys.

2014;16(18):8392–9.

35. Compton RG, Banks CE. Understanding Voltammetry. Imperial College Press; 2011.

36. Leaist DG. Diffusion in aqueous solutions of sulfuric acid. Can J Chem. 1984;62(9):1692–7.

37. Heyrovska R. New insight into DNA damage by cisplatin at the atomic scale. Nat Preced. 2012;33.

38. Davies TJ, Ward-Jones S, Banks CE, Del Campo J, Mas R, Muñoz FX, et al. The cyclic and linear sweep voltammetry of regular arrays of microdisc electrodes: Fitting of experimental data. J Electroanal Chem. 2005;585(1):51–62.

39. Guo X, Gorodetsky AA, Hone J, K. BJ, Nuckolls, Colin. Conductivity of a single DNA duplex bridging a carbon nanotube gap. nat nanotechnol. 2008;3(3):163–7.

40. Slinker JD, Muren NB, Renfrew SE, Barton JK. DNA Charge Transport over 34 nm. Natl Chem. 2011;3(3):230–5.

41. Duprey JLHA, Carr-Smith J, Horswell SL, Kowalski J, Tucker JHR. Macrocyclic Metal Complex-DNA Conjugates for Electrochemical Sensing of Single Nucleobase Changes in DNA. J Am Chem Soc. 2016;138(3):746–9.

42. Yang H, Metera KL, Sleiman HF. DNA modified with metal complexes: Applications in the construction of higher order metal-DNA nanostructures. Coord Chem Rev. 2010;254(19–20):2403–15.

43. Fang C, Fan Y, Kong JM, Zhang GJ, Linn L, Rafeah S. DNA-templated preparation of palladium nanoparticles and their application. Sensors Actuators, B Chem. 2007;126(2):684–90.

44. Davies TJ, Compton RG. The cyclic and linear sweep voltammetry of regular and random arrays of microdisc electrodes: Theory. J Electroanal Chem. 2005;585(1):63–82.

45. Dickinson EJF, Limon-Petersen JG, Rees N V., Compton RG. How much supporting electrolyte is required to make a cyclic voltammetry experiment quantitatively “diffusional”? A theoretical and experimental investigation. J Phys Chem C. 2009;113(25):11157–71.

46. Jangir DK, Mehrotra R. Raman spectroscopic evaluation of DNA adducts of a platinum containing anticancer drug. Spectrochim Acta - Part A Mol Biomol Spectrosc. 2014;130:386–9.

47. Shamsi MH, Kraatz HB. Interactions of Metal Ions with DNA and Some Applications. J Inorg Organomet Polym Mater. 2013;23(1):4–23.

48. Duguid J, Bloomfield VA, Benevides J, Thomas GJ. Raman spectroscopy of DNA-metal complexes. I. Interactions and conformational effects of the divalent cations: Mg, Ca, Sr, Ba, Mn, Co, Ni, Cu, Pd, and Cd. Biophys J. 1993;65(5):1916–28.

49. Tavares M., Machado SA., Mazo L. Study of hydrogen evolution reaction in acid medium on Pt microelectrodes. Electrochim Acta. 2001;46(28):4359–69.

50. Marković NM, Grgur BN, Ross PN. Temperature-dependent hydrogen electrochemistry on platinum low-index single-crystal surfaces in acid solutions. J Phys Chem B. 1997;101(27):5405–13.

51. Dubouis N, Grimaud AJL. The Hydrogen Evolution Reaction: From Material to Interfacial Descriptors. Chem Sci. 2019;

52. Millard, M.M, Macquet , J.P and Theophanides, T. X-Ray Photoelectron Spectroscopy of DNA-

Pt Complexes. Evidence Of 06 (Gua) - N~(Gua) chelation with DNA. 1975;2:166–70.

53. Xiao F, Yao X, Bao Q, Li D, Zheng Y. Sensitive marker of the cisplatin-DNA interaction: X-ray photoelectron spectroscopy of CL. Bioinorg Chem Appl. 2012;2012.

54. Xiao F, Yao X, Bao Q, Li D, Zheng Y. Sensitive Marker of the Cisplatin-DNA Interaction : X-Ray Photoelectron Spectroscopy of CL. 2012;2012.

55. Liu Z, Tan S, Zu Y, Fu Y, Meng R, Xing Z. The interactions of cisplatin and DNA studied by atomic force microscopy. Micron. 2010;41(7):833–9.

56. Klinov D V, Dubrovin E V, Yaminsky I V. Scanning P robe M icroscopy of DNA on M ica and G raphite. :452–6.

57. Sheader AA, Varambhia AM, Fleck RA, Flatters SJL, Nellist P. Observation of metal nanoparticles at atomic resolution in Pt-based cancer chemotherapeutics. 1865;1–16.

58. Wang B, Wolfe DE, Terrones M, Haque MA, Ganguly S, Roy AK. Electro-graphitization and exfoliation of graphene on carbon nanofibers. Carbon N Y. 2017;117:201–7.

59. Sigel H, Lippert B. The effects of N7-coordinated cis-diammine-platinum(II) on the acid-base properties of guanine derivatives. Pure Appl Chem. 1998;70(4):845–54.

Chapter 5-

Functionalization of DNA-Cisplatin with Single Walled Carbon Nano-tubes (SWCNTs)

Chapter 5: Functionalisation of DNA-Cisplatin with Single Walled Carbon Nanotubes (SWCNT)

5.1 Introduction

The discovery of carbon nanotubes was first made in 1991 by Iijima , who reported the synthesis of a new type of finite carbon structure, made up of multi-walled carbon nanotubes (MWCNTs), synthesised using an arc-discharge evaporation method (1). Alternatives to MWCNTs are single walled carbon nanotubes (SWCNTs), where the CNTs form a one atom thick sheet cylindrical tube. They have a high aspect ratio (length to diameter) and are made up of a single layer of graphene (2). The size of the SWCNT can range from 0.5 to 1 nm (2). Although some report that the typical diameter range for SWCNTs can vary from 0.4 to 3 nm. SWCNTs with a diameter smaller than 0.4 nm are thermodynamically unstable due to the strain induced by the curvature onto the carbon to carbon bonds. There is attraction between the opposing ends of the graphene cylinder, thus increasing the cylinder diameter (to greater than 3 nm) and consequently overcoming the radial stiffness as the cylinder begins to flatten (3). On the other hand, MWCNTs are made up of two concentric cylindrical shells of graphene coaxially arranged around a central hollow core held by Van der Waals forces between the adjacent layers (4) as illustrated in figure 1.

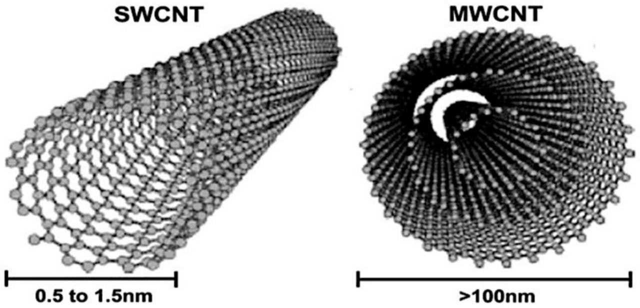

Figure 1- *Schematic representation of single walled carbon nanotube (SWCNT) and multi walled carbon nanotubes (MWCNT) , copied from* (4).

The employment of carbon based support material for platinum nanoparticles has ranged from methods looking at increasing the number of active sites on bulk Pt to methods reducing the thickness of the active layer ($\leq$ 25 µm) to developing smaller Pt nanoparticles (< 10 nm) on a carbon-support (5).

Several methods have been employed in the literature to disperse platinum metal nanoparticles onto carbon nanotubes such as a polyol procedure (6) to a microwave assisted process (7). The employment of nano-carbon as a support material for Pt, has been claimed to enable both better utilisation of the Pt metal and relatively low Pt metal loadings to be used for the polymer electrolyte membrane fuel cell (PEMFC). The main drawbacks were however, the expense of using nano-carbons as a support material (5).

In addition, the effectiveness of this depends on the method employed to load the metal onto the support (5). The advantages of the employment of carbon nanotubes as a catalyst support is reviewed in the literature (6), whereby their use as a support is justified by enabling reduced Pt loadings for the PEMFC. In addition, the review (6) also outlines how the use of SWCNTs enables improved stability and corrosion resistance of the catalyst material. The use of SWCNTs improves the performance of catalyst since platinum can be localized in both the inner and outer walls of SWCNTs, leading to good electrocatalytic properties (6).

A thorough review by Luo et al. (6) has shown the impact of carbon nanotubes (CNTs) as a support material for the dispersion of noble metal(s). Their work explored how the durability and stability of the electrocatalyst changes with the CNT diameter, and that the shape of the Pt nanoparticles influence their interaction with the support i.e. tetrahedral nanoparticles provide the greatest adhesion (6).

The functionalization of SWCNT with platinum results in an improved electrocatalytic performance compared with a commercial Pt/C material when assessed in an ex-situ electrochemical cell (8). In their work, Tavokkali et al. (8) rely on an electrochemical deposition method to deposit Pt atoms from a Pt foil onto the SWCNTs. The developed pseudo-atomic scale structures showed a promising electrocatalytic performance for the hydrogen evolution reaction (HER) which is comparable to that of a commercial Pt/C electrocatalyst. In their work, the performance of the catalyst material was defined using a range of electrochemical parameters including onset potential, overpotential and current density (8). For example, the onset potential was found to be 0 V vs normal hydrogen electrode (NHE) for the 200 and 400 SWCNT/Pt samples, thus close to the thermodynamic potential of the HER (i.e. 0 V) and significantly lower than that of the pristine SWCNT (approximately -0.3 V), where 200 and 400 represent the number of times the material has been cycled.

On the other hand, for the overpotential parameter, the 400-SWCNT/Pt electrode requires lower overpotentials of 27, 130, and 210 mV to achieve current densities of 10, 100, and 180 mA cm^{-2} respectively, which is similar to those of a Pt/C material (8).

In addition, Density Functional Theory (DFT) calculations showed that the SWCNT establishes higher performances as a catalyst support for platinum than graphene for the HER. This is because it enabled efficient dispersion of the metal atoms to be achieved and the performance of the single Pt atoms was equivalent to bulk Pt (8). This observation was also made by Sharma et al. (9) in their work involving the functionalization of SWCNT with hexachloroplatinic acid. In particular, the employment of SWCNT support for metal nanoparticles for the electrocatalysis of water splitting or HER was found to provide a large specific area and optimum overpotentials towards the HER. In addition, water reduction near the thermodynamic limit is achieved, despite the low mass loading of the catalytic material (10^{-2} mg cm^{-2}) (10).

Furthermore , metal catalysts including Pt, Ru, and Pt/Ru nanoparticles supported on CNTs show promising results in terms of activity and selectivity in a large variety of reactions when compared to classical supports (11). For example, it is reported that CNTs as a heterogeneous catalyst support for platinum can provide a higher voltage than the traditional carbon black support, where a CNT with 12 wt.% Pt deposition can give 10 % higher voltages than carbon black with 29 wt.% Pt deposition in a PEMFC (12). The maximum power density attainable for a cathode catalyst is increased upon the dispersion of platinum onto MWCNTs (doped with nitrogen) to 0.78 mWcm^{-2} compared to a commercial carbon supported Pt catalyst (of 0.72 mW cm^{-2}) (6). Similarly for SWCNT, the current densities achievable for the catalysis of HER in acidic environments can be enhanced by increasing the number of activation cycles, for example, after 200 and 400 activation cycles, the current density value ,(j_0), of 0.06 mA cm^{-2} for SWCNT is significantly improved to 1.15 and 1.94 mA cm^{-2} respectively, which means a reaction rate equivalent to and higher than that on Pt/C (1.22 mA cm^{-2}) can be attained (8).

5.2 DNA functionalized with SWCNTs

The functionalization reaction between carbon nanotubes and DNA is favourable since there is a rich electron density available on the DNA bases (i.e. π electrons) and SWCNTs have delocalised electrons at their surface. The electrons can move via a hopping mechanism along the DNA (13). Computational studies demonstrate that non-covalent bonding can occur between the DNA and SWCNTs resulting in stacking interactions. These non-covalent bonds refer to Van der Waals (VDW) and electrostatic forces of attraction. These also occur between the π-orbitals of the aromatic rings of a complementary base pair, which stabilizes the molecule. A conductive path is also enabled through these delocalized π electrons (13).

The resulting composite of DNA-SWCNTs has poor mechanical properties, however it can form good conductive films, depending on what DNA nucleotide base is available for the interaction (13). Guanine is reported to have the highest surface area and can thus interact more strongly with the SWCNTs (13). The SWCNTs are electrochemically active since there is a rich electron conjugation and high surface area.

The DNA nucleoside base is placed 3.3 Å away from the wall of the CNT and the N- and C-atoms in adenine are arranged in positions that maximize the VDW forces of attraction between the N, O, and C atoms of the nucleotide base and the C atom of SWCNT. The bases adsorb perpendicularly to the SWCNT tube axis or at a tilted angle. The interaction is primarily based on VDW forces and interactions arising from mutual polarization of molecules in close proximity to each other. Theoretically, it has been shown through Density Functional based Tight Binding (DFTB) calculations by (13) that the interaction involves a couple of mixed states that appear below the Fermi level in addition to VDW forces. The π orbital overlapping between the DNA and the CNT enables interactions that give rise to a high density of delocalized electrons (13).

5.3 Electrochemical properties

The employment of DNA functionalised with SWCNT structures is favourable for electrochemical applications due to their high surface to volume ratios, fast heterogeneous charge transfer rates, and electrochemical stability.

The observable electrochemical properties are dependent on the ratio between the DNA and the SWCNTs. It was found that at 0.5 wt.% of DNA to SWCNT, the optimum current response is produced, where effective and efficient distribution of the DNA can be achieved on the SWCNT (13). In the work of Hu et al.(14), it was shown through the synthesis of DNA-SWCNTs, that the material has a wide potential window, well defined quasi-reversible voltammetry and quick electron transfer, for the tested electroactive species of Ferrocyanide ($Fe(CN)_6^{4-}/Fe(CN)_6^{3-}$) in their work, concluding that its use as an electrode for electrochemical analysis is appropriate.

5.4 DNA-Platinum-SWCNT material for electrochemical applications

The combination of platinum nanoparticles with carbon nanotubes (SWCNTs/MWCNTs) and DNA has previously been reported in the literature for electrochemical applications. This can range from the fabrication of a sensitivity-enhanced electrochemical DNA biosensor (15) to alternatively a method for non-covalent functionalization of DNA-wrapped single-walled carbon nanotubes (SWCNTs) using platinum-based DNA cross-linkers (16) to otherwise a more precise DNA-templated synthesis of Pt nanoparticles on SWCNTs (17). Modification of the CNTs with nitrogen can improve the catalytic activity and stability which has been reported to reduce the use of platinum (6). On the other hand, the employment of SWCNTs for supporting DNA-Pt adducts for fuel cell applications was explored by (17) where ssDNA was used for both dispersing the SWCNT bundles and also as a binding site for controlling the distribution of platinum along the individual nanotube surface.

Alternatively the combination of a range of metals including Pt, Au and Pd with DNA/SWCNT hybrids has been achieved by Su et al. (2013) (18) for the fabrication of a nanostructured sensor array. This used an ink jet printing process to pattern the metal ion (e.g. Au, Pt, and Pd) chelated DNA/SWCNTs onto pre-fabricated microelectrodes followed by electroless reduction to form metal nanoparticles (NPs). The DNA enables dispersion to be achieved and also acts a chelating agent (18).

5.5 Materials and methodology

5.5.1 Materials

The DNA-cisPt and cisPt material detailed and used in this work was synthesized and provided by Klaudia Englert (19), School of Chemistry, University of Birmingham. The functionalized SWCNT-DNA-cisPt material were fabricated and characterized by the author of this thesis in the methods detailed below. The material required and employed is outlined below.

Commercial purified SWCNTs were supplied by Nano-C (Batch (PT1112-88WP), Nano-C PT, 33 Southwest Park, Westwood, MA 02090) and were used as received, having been purified of the metal catalyst and residual amorphous carbon using an oxidative acid and/or sequences consisting of acid leaching and oxidation. All chemicals involved were of analytical grade and used without any purification. Sodium perchlorate (≥ 98 %), perchloric acid (70 %, 99.99 % trace metals), stock of salmon milt (sm)-DNA in a form of sodium salt, cisplatin (64.5 % min Pt content) were all purchased from Sigma Aldrich. Isopropanol (IPA, reagent grade > 99 %) was purchased from Fisher Scientific. All electrolytes were made up with de-ionised water (resistivity ≥ 18.2 MΩ.cm) (MilliQ, Millipore) and thoroughly degassed with dry nitrogen (oxygen-free, BOC Gases plc) prior to experimentation.

DNA-cisPt

DNA-cisPt adducts were synthesised in the same way described in chapter 4. In brief this involved dissolving salmon milt DNA (sm-DNA) in Milli-Q water (resistivity ≥ 18.2 MΩ.cm) followed by sonication to make a stock solution of the desired concentration. Then, cisPt in aqueous form, of a 1000 µM, was mixed with the sm-DNA and incubated at 37 °C overnight for 10 hours. Confirmation of the adduct formation was achieved using spectrophotometry using a Shimadzu UV-1800 spectrophotometer, Jasco J-810 spectropolarimeter and a Cary 5000 UV-Vis-NIR Spectrophotometer by Klaudia Englert, School of Chemistry, University of Birmingham (19).

5.5.2 Fabrication of SWCNT-DNA-cisPt material

The SWCNTs were prepared for the functionalisation reaction. Initially to disperse the SWCNTs prior to adsorption of the DNA-cisPt adducts, they were sonicated continuously for 90 minutes in a 50 % v/v IPA aqueous solution (DIW), to achieve full dispersion. A 1000 µM sample of CNTs was prepared and dispersed in a 50 % v/v IPA aqueous solution (DIW) via probe sonication using a 130 Watt ultrasonic processor, VCX 130 (Sonics). A Titanium alloy (Ti-6Al-4V) probe tip was used to break up the SWCNTs. The nanotubes were sonicated for 90 minutes until adequate dispersion was achieved (see figure 2) which is equivalent to an energy input of 702 KJ.

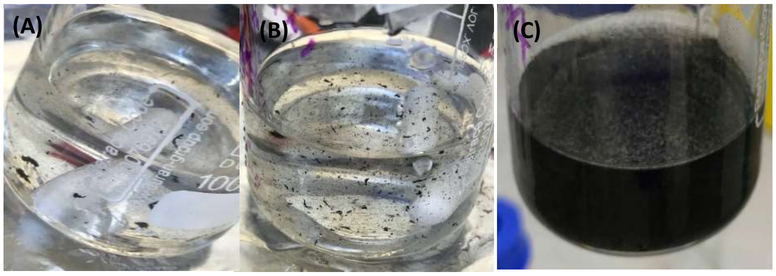

Figure 2*- The observable changes in the dispersion of the SWCNT's with time of probe sonication (A-C).*

To prepare the functionalised SWCNTs, a desired volume of the dispersed aqueous solution of the SWCNTs is sonicated with the prepared DNA-cisPt, DNA or cisPt aqueous solutions in an ice water bath at around 9 -10 °C, of the desired mass loadings and ratios. The temperature was monitored using a standard laboratory thermometer and was kept constant with ice.

5.5.3 Mass Loadings

Mass loadings of cisPt

Using the expression below, we can calculate the platinum mass loading in the samples based on the aliquot volume and the concentration of the prepared samples.

$$C = \frac{n}{V}\ Eq.(1)$$

$$\therefore n = C \times V = (1000 \times 10^{-6})\ molL^{-1} \times (25 \times 10^{-6})\ L = 2.5 \times 10^{-8}\ mol$$

Given the molecular weight of cisPt we can calculate the platinum loading as shown:

$$Mass = n \times M_r\ Eq.(2)$$

$$= 2.5 \times 10^{-8}\ mol \times 300.01\ gmol^{-1} = 7.5\ \mu g$$

Thus for the SWCNT-cisPt material, the mass loading of cisPt in a 25 µL aliquot would be equivalent to 50 % v/v i.e. 12.5 µL is cisPt, which is equivalent to a mass loading of 3.75 µg.

Mass loading of SWCNT

For the prepared 1000 µM sample in 50 mL, we have 60 µg of SWCNT in this volume. Hence in an aliquot of 25 µL this equates to 0.3 µg. Hence taking into account the volume percent, we can estimate the mass loadings of the CNTs, as summarised in Table 1.

***Table 1-** cisPt and SWCNTs mass loadings in an aliquot of 25 µL of prepared material based on volume ratios.*

Material (Volume ratio)	Calculated mass loading of cisPt in 25 µL/ µg	Calculated mass loading of SWCNT in 25 µL / µg
SWCNT	-	0.3
cisPt	7.5	-
4:1 SWCNT-DNA -cisPt	0.750	0.24
2:1 SWCNT-DNA-cisPt	1.25	0.2
0.5 : 1 SWCNT-DNA-cisPt	2.50	0.05
1:1 SWCNT-DNA -cisPt	2.5	0.1
SWCNT-DNA + cisPt	2.50	0.1
1 to 1 DNA-cisPt	3.75	-
SWCNT-cisPt	3.75	0.15

5.5.4 Experimental work

The fabricated material was then experimentally tested and characterized by the author of this thesis in the experimental methods described below.

5.5.4.1 Electrochemical Testing

Electrochemical experiments were conducted in a 3 electrode cell, using a glassy carbon electrode (GC) (d = 3mm, BASi) as the working, a saturated calomel (SCE, BASi) reference and a bright platinum mesh counter electrode. The cell was controlled by an Autolab 128N potentiostat running Nova 2.1 software (Metrohm-Autolab BV, Netherlands). All potentials are reported against a SCE, and all supporting electrolytes were 0.1 M to ensure full support was provided. The GC electrodes were polished on micro-cloth pads of a decreasing size alumina slurries (1.0, 0.3, 0.05 µm, Buehler IL), followed by rinsing with ultrapure water and drying under a gentle flow of nitrogen. Once dry, the electrodes were modified by drop casting an aliquot of the prepared SWCNT-DNA-cisplatin (cisPt) sample (25 µL) and drying under a lamp.

Characterization of the material

The surface morphology of the material was imaged using Scanning Transmission Electron Microscopy (STEM) operated in both dark-field and bright-field imaging using a JEOL2100F instrument. The STEM was operated in Z-contrast mode using a high angle annular dark field (HAADF) detector. The sample was prepared by drop casting 3 µL of the prepared material onto a 300 mesh Cu TEM grid, which was dried under a lamp. STEM-EDX imaging was employed to assess the purity of the carbon nanotubes from metals prior to functionalization. XPS was used to assess the elemental composition and surface chemical properties of the SWCNTs and the DNA-cisplatin adducts.

5.5.4.2 STEM imaging

The implementation of STEM-HAADF imaging for SWCNT based material characterisation and specifically carbon nanotubes decorated with platinum has previously been reported in the literature (20) , (21). This method is useful given that the distinguishment between platinum nanoparticles and carbon nanotubes can easily be made, since STEM imaging is dependent on atomic number (Z). As the platinum and carbon have different atomic numbers i.e. for carbon Z=6 and for platinum Z= 8, a difference in the contrast upon imaging can be seen.

The heavier Pt atoms in the electrocatalyst material appear as bright spots in dark field imaging, see figure 13(e), while in the bright field mode, they appear as black spots. The high Z-Pt atoms on the lower Cu holey carbon TEM grids are detectable at a high contrast. The Pt is densely dispersed on the tubes, mainly nanoclusters of cisPt, of a size around 2 nm, as illustrated in figures 13 (f) and (i). This is discussed in greater detail throughout this work and findings presented in this chapter.

5.6 Results and Discussion

5.6.1 XPS: Elemental Composition

The elemental composition was explored through XPS testing and was further supported with STEM - EDX mapping. Key and reassuring findings include the absence of any metallic impurities on the surface of the SWCNT and that the chemical composition is predominantly carbon. A detailed XPS characterization of the unmodified DNA-cisPt adducts has been explored in the previous chapter of this thesis, see chapter 4. The key information provided from these findings and of relevance to the experimental work in this chapter are provided in the Table 2.

Table 2- *Elemental composition of the synthesized DNA-cisPt (1000 µM) material and comparison of the binding energies compared to that reported in the literature by Millard* (22).

Name of element	**Binding energy (eV)**			**Atomic composition (%)**	
	1 to 0 DNA-cisPt	**1 to 0.82 DNA-cisPt*** (22)	**1 to 1 DNA-cisPt**	**1 to 1 DNA-cisPt**	**1 to 0 DNA-cisPt**
O 1s	532.58	531.7	533.1	27.6	26.2
C 1s	286.08	-	285.1	12.5	38.2
N 1 s	399.08	399.8	400.1	2.74	6.8
Na 1s	1071.08	-	1071.1	1.93	3.6
P 2p	133.08	133.08	134.1	5.04	4.6
Si 2p	100.8	100.8	99.1	45.1	5.0
Ca 2p		-	347.1	2.03	
Pt 4f		72.8	73.1	1.56	
Cl 2p		199.9	199.1	3.21	

*The value of 0.82 corresponds to 41 % Guanine-Cytosine (G-C) planes in the DNA, this is complete saturation of the N_7 (Guanine) sites. This is equivalent to the G-C content of the salmon milt DNA used in this work i.e. 41.2 % supplied by Sigma Aldrich.

Those results are a confirmation of the successful synthesis of the DNA-cisPt adducts under the incubation conditions employed, as previously detailed in chapter 4.

Surface chemical properties of SWCNT via XPS characterization

The SWCNT samples were prepared and sent to Harwell XPS facilities, (UK) for XPS characterisation of both the unmodified form i.e. solid SWCNT and the dispersed SWCNT form dispersed in 50 % v/v IPA aqueous solution. All the sample preparation was achieved by experienced users at the Harwell XPS team, which involved the drying of the SWCNT in solution onto the sample holder. This was found to contain sodium and other impurities including copper, which is the metal that the sample holder is made from. It was found that the dispersed SWCNTs in 50 % v/v IPA aqueous solution was more likely to contain contaminants compared with the solid SWCNT sample. The XPS results are displayed:

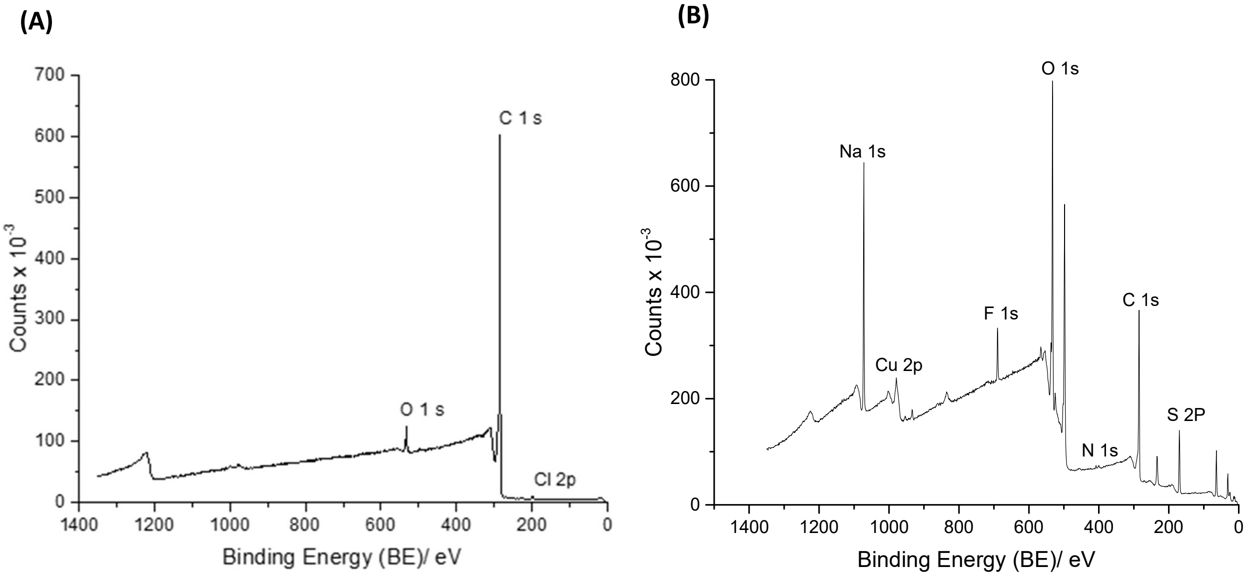

Figure 3- *XPS Elemental spectrum of 1000 µM SWCNT (A) in as purchased solid form and (B) dispersed in 50 % v/v IPA aqueous solution.*

Table 2- *Elemental Composition of 1000 µM SWNT in a 50 % v/v IPA aqueous solution and in solid form.*

Element	**Percentage composition (%)**	
	Aqueous form	**Solid form**
O 1s	31.75	3.02
C 1S	43.42	96.57
Cl 2p	0	0.41
Cu 2p	0.16	
Na 1s	12.37	
S 2p	8.46	
F 1s	3.40	

The two key findings from the XPS results include that there are no metallic impurities as initially suspected, such as iron (Fe) which is a commonly employed catalyst during the fabrication process of the SWCNTs. Secondly, that dispersion of the SWCNT in a IPA aqueous solution makes the SWCNT more prone to contamination with salt impurities such as sodium, sulphur and fluorine. Elemental mapping of the SWCNT was assessed via STEM-EDX. The usefulness of STEM in Energy Dispersive X-ray mode (EDX) in elemental mapping is detailed in appendix 3. A region of the prepared TEM grid with SWCNTs drop cast onto the surface undergoes STEM-EDX mapping (figure 4(A)) to produce the spectrum in figure 4(B). It is evident that the suspected impurity of iron (Fe) can be ruled out, as shown by the absence of peak in the proposed regions (circled in figure 4(B)), thus further consolidating the findings of the XPS results. This enables the utilization of the SWCNT for the functionalization reaction with the DNA-cisPt material for the Hydrogen Evolution Reaction (HER) without the need for further purification treatments or concern that the observed electrocatalysis is due to metallic impurities residing on the surface of the SWCNT.

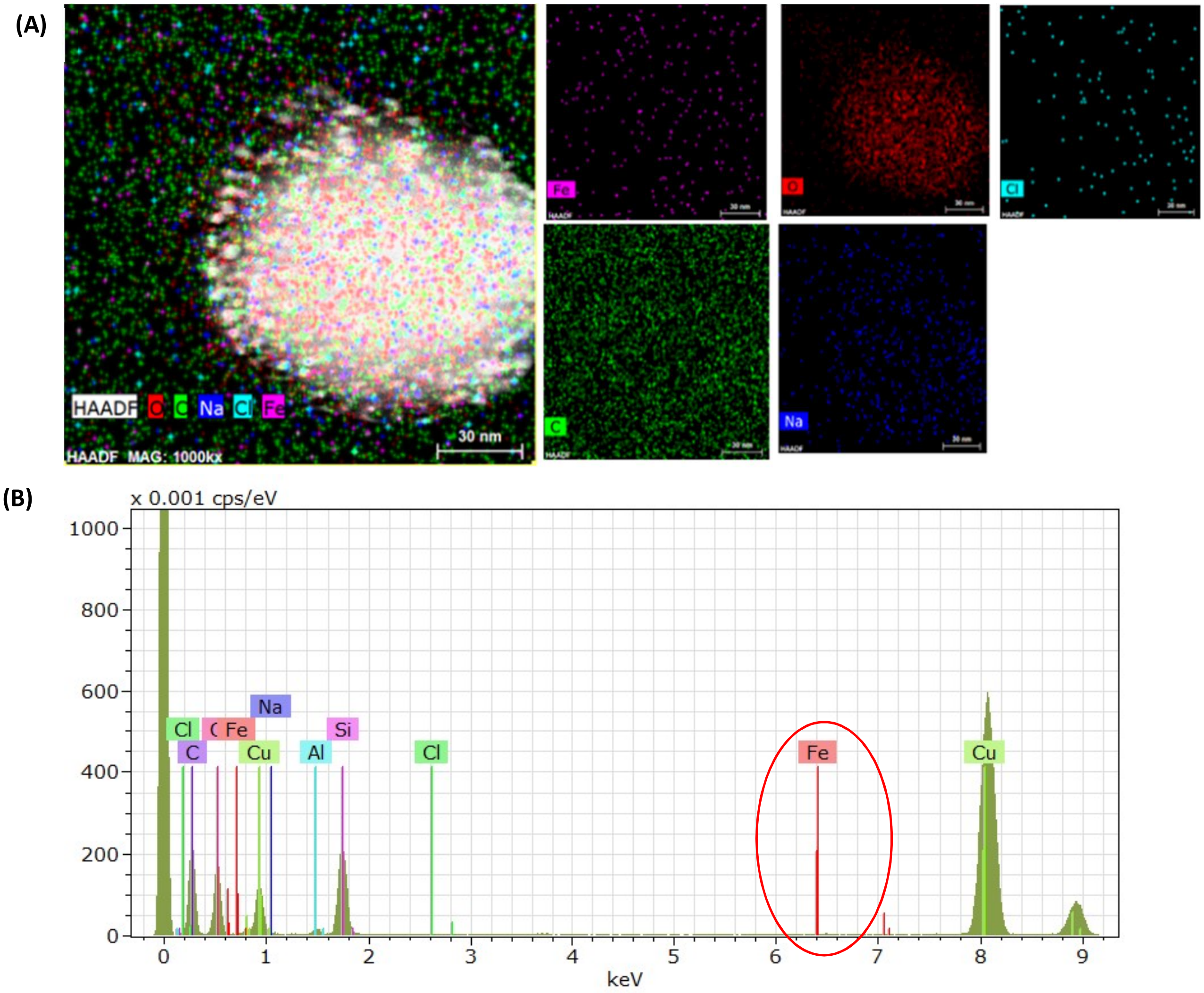

Figure 4- *STEM EDX mapping of 1000 µm SWCNT on a 300 Cu mesh holey carbon TEM (A) Distribution of proposed elements/impurities shown (B) EDX Spectrum, where the red lines mark where the Fe peaks should appear indicating the absence of the metal impurity.*

5.6.2 Optimization of the Process Parameters

In order to achieve the best electrocatalyst material for the HER and to optimise the electrocatalytic performance of the functionalised CNTs material with the DNA and cisPt for the HER, several process parameters need to be defined. This includes the sonication time period for the functionalisation reaction between the DNA-cisPt and SWCNT and also the volume ratios of the loadings of the SWCNT to DNA-cisPt used. In order to measure the influence of each of these parameters on the electrocatalytic performance of the material, the resulting changes in the voltammetry response for the HER in 1 mM $HClO_4$ and 0.1 M $NaClO_4$ is assessed at 50 mVs^{-1} and it is taken as the basis of the measurement. In addition, STEM characterisation is undertaken to assess the resulting changes to the surface morphology.

5.6.2.1 Sonication time

Different sonication times were explored for the synthesis of the SWCNT functionalised material with DNA-cisPt. An optimum reaction time was sought, and was explored as a function of the distribution of the cisPt clusters across the nanotube network. This was investigated for the 2:1 SWCNT-DNA-cisPt material. The resulting effect on the surface morphology of the material is displayed in the figure:

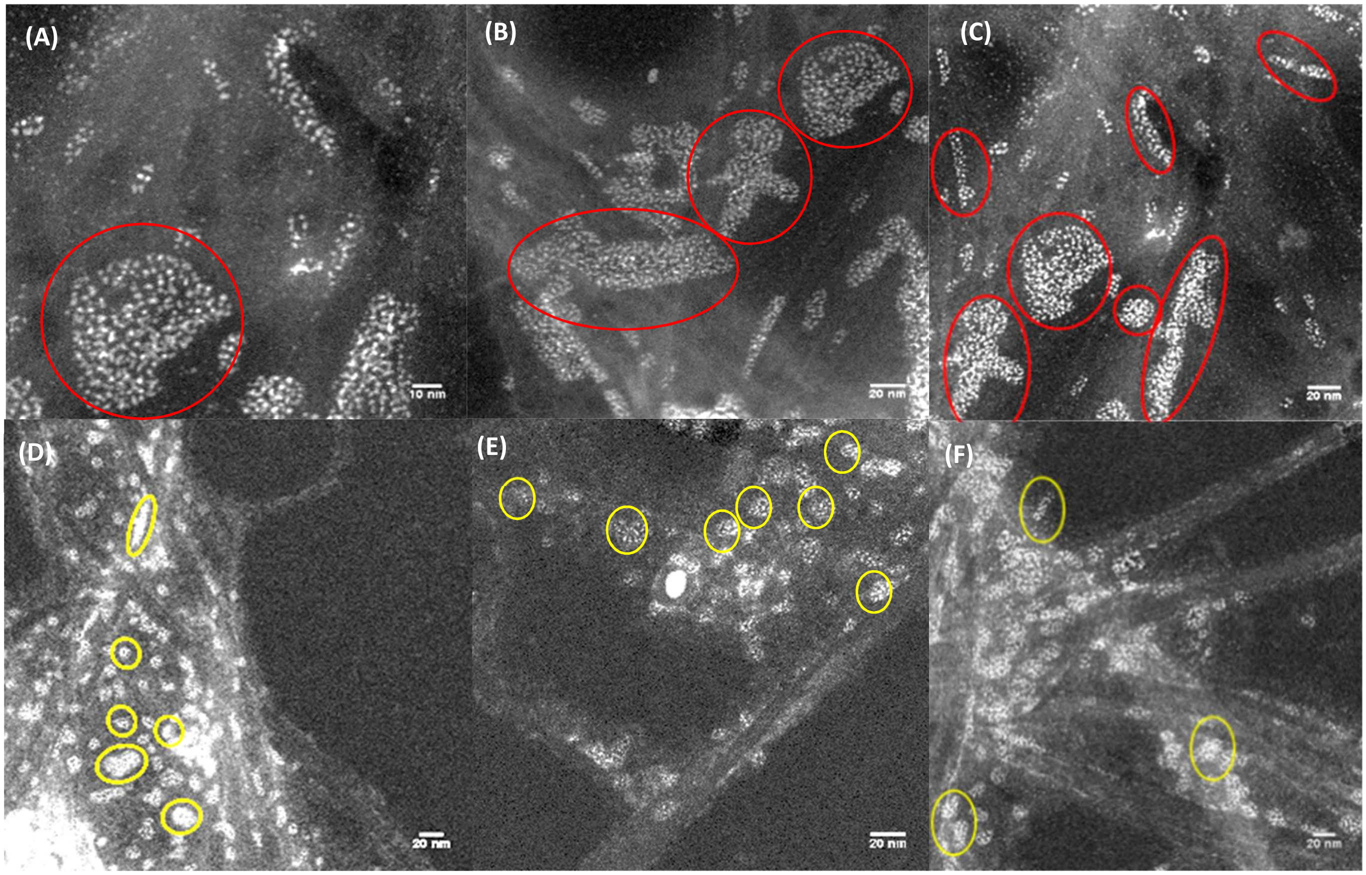

Figure 5- *2 to 1 SWCNT-DNA-cisPt preparation at different sonication times (A-C) 15 minutes (cisPt nanoclusters highlighted in red) (A) x 1000 k (B) x 600 k (C) x 600 k (D-F) 90 minutes (cisPt nanoclusters highlighted in yellow) (D) x 400 k (E) x 600 k (F) x 400 k.*

The diameter of the highlighted nanocluster groups of cisPt was measured from the STEM images, using Image J, see appendix 2. The average cluster size for the material prepared at 15 minutes was measured from figures 5(A-C) and was found to be around 50.1 ± 24.2 nm based on 11 measurements, see appendix 2. The large standard deviation error could be explained by the duration of 15 minutes being insufficient for achieving sufficient and uniform distribution of the nanoclusters across the entire surface of the material i.e. no resulting change in the dispersion of material from that at time equal to 0 minutes in some regions. However, after 90 minutes of sonication, a much smaller cisPt nanocluster size is measured, see (figures 5 (D-F)) and is found to be much smaller than at 15 minutes i.e. 12.3 ± 2.37 nm based on 44 measurements ,see appendix 2 , Tables A2.1- A2.2 for the raw data.

This means that as the sonication time is increased, there is improved distribution of the cisPt material, creating structures with an irregular non-uniform array of the metal centres. However, eventually there will be an optimum reaction time in which the material produced will no longer result in significant changes to the distribution of the cisPt. This is discussed further in the coming sections of this chapter.

5.6.2.1.1 Electrochemical performance for HER

To explore whether the resulting changes in the cisPt nanocluster size found from the STEM characterisation affects the electrochemical behaviour of the material for the HER, the 2 to 1 SWCNT-DNA-cisPt material was prepared at different sonication times of 15, 30, 45 and 90 minutes before casting onto GC stubs in the aforementioned ways (see chapter 4).The prepared working electrode was immersed into a 1 mM $HClO_4$, 0.1 M $NaClO_4$ electrolyte solution and cycled at 50 mVs^{-1}. The resulting change to the voltammetry as a function of sonication time is displayed in figure 6.

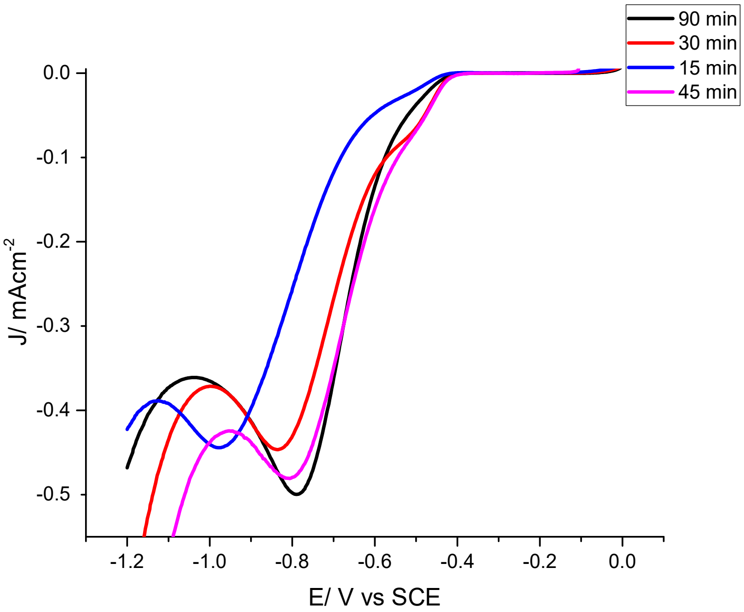

Figure 6- *The change in electrocatalytic performance with sonication time for electrocatalysis of HER (1 mM $HClO_4$ and 0.1 M $NaClO_4$) at 50 mV s^{-1} for the 2 to 1 SWCNT-DNA-cisPt/ GC surface.*

To compare between the resulting performances, the half-wave potential ($E_{1/2}$) can be defined for each material from figure 6. Table 4, summarizes these findings, and it is found that beyond 45 minutes of sonication, the resulting changes to the $E_{1/2}$ become insignificant.

Table 4- *Variation of half wave potential ($E_{1/2}$) with reaction sonication time.*

Time/ min	Half Wave Potential $E_{1/2}$ / V vs SCE
15	0.78 ± 0.015
30	0.68 ± 0.010
45	0.65 ± 0.012
90	0.66 ± 0.013

Figure 5 displayed an overview of the distribution of the cisPt onto the surface of the SWCNTs. The influence of sonication time on the size of cisPt molecule at a higher magnification, down to the atomic scale is explored below, see figure 7, and the average diameter was found using tools in Image J.

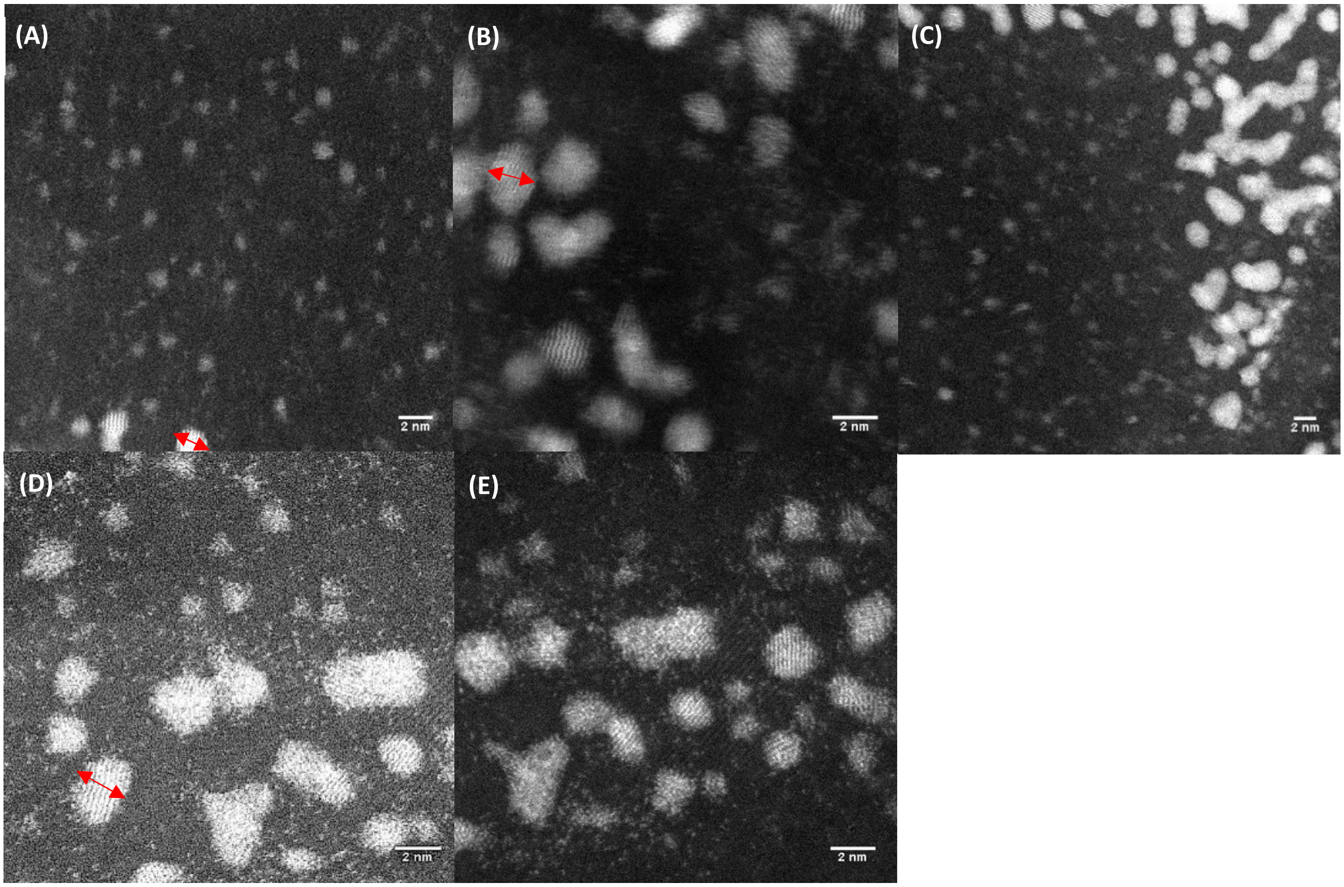

Figure 7- *2 to 1 SWCNT-DNA-cisPt preparation at different sonication times (A,B) 15 minutes (A)(x 1000 k) (B) (x 3000 k) (C) 30 minutes ,(x 1000 k) (D) 45 minutes,(x 8000 k) (E) 90 minutes, (x 8000 k).*

The resulting changes to the average diameter of the cisPt nanocluster (measured as indicated with arrows in figure 7), was found to be a function of sonication time i.e. energy input, with more evident changes from 15 to 30 minutes than 45 to 90 minutes. Specifically for the experimental conditions in this work, the power input of the sonication probe was 130 W, thus for the sonication times tested (15 to 90 minutes) the energy supplied ranged from 117 KJ at 15 minutes to 702 KJ at 90 minutes of sonication.

More specifically, the average nanocluster size changed in a similar manner to the measured half wave potential ($E_{1/2}$), as displayed in figure 8. It is clear from figure 8, that both the $E_{1/2}$ and the average size of the cisPt nanocluster i.e. platinum active centres correlate with one another. The size, shape and face of Pt nanoparticles are three key factors which determine the catalytic performance for the HER. It has been reported that the morphology of the nanoparticles can expose different crystal planes, leading to different atomic arrangements on the catalyst surface, of distinct electronic and geometric structures (23). In this work, we will focus on the size of the platinum nanoclusters and how this reflects in terms of the electrochemical performance. Platinum is an ideal catalyst for the HER in acidic environments and particularly those made up of edges or vertices i.e. nanoparticle or extended surface with a dispersion equivalent to that of a 2 nm diameter particle (24). A similar observation has previously been reported by (25),(26) , where it was shown in the work of Tan et al. (through their derived theoretical simulation model) that a nanoparticle size of 2.2 nm produced the maximum exchange current density output for the HER (26).

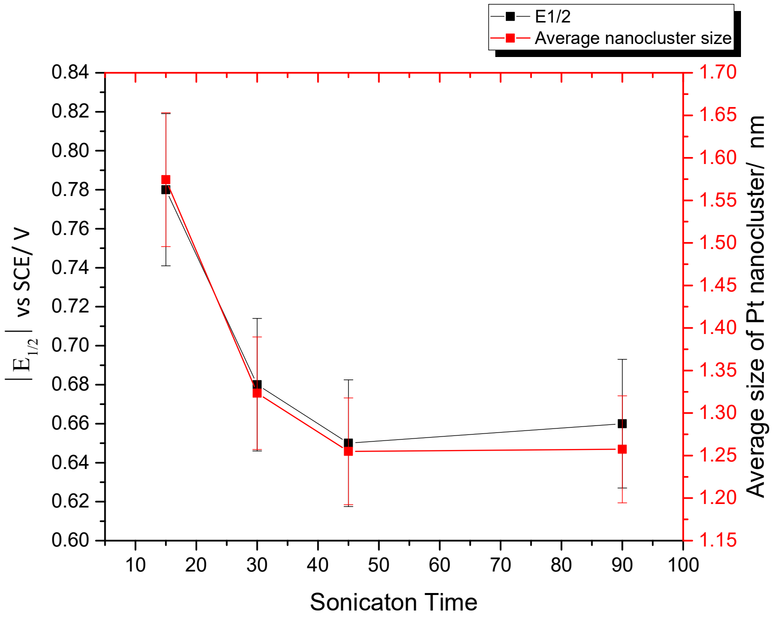

Figure 8- *The changes in the average platinum nanocluster size with sonication time and absolute half wave potential ($E_{1/2}$).*

However in terms of the ratio of edge to faces it was reported that in the 1-3 nm range a drop in catalytic performance for the HER is observed (23). The specific mass activity of the Pt nanoparticle decreases with the size in this range (23) and beyond 3 nm we start to observe a decay in the activity (25).

From figure 8, it becomes apparent that the particle size is affecting the half wave potential ($E_{1/2}$) of the HER. This is important given that the $E_{1/2}$ provides a first approximation to the formal cell potential (E_f^o), which can be used to calculate the Gibbs free energy of the reaction (see equation 30, chapter 2). For example, when $E_{1/2} > 0$, the Gibbs free energy is < 0, thus we have a spontaneous reaction. Therefore, from figure 8, we can propose that as the absolute cathodic (negatively charged) $E_{1/2}$ decreases, the Gibbs free energy becomes more favourable such that the reaction spontaneity increases.

Alternatively, previous observations made in the literature for the ORR (a more thoroughly studied PEMFC reaction) noted that as the experimental $E_{1/2}$ increased, the calculated d-band centre of the Pd metal changed in a 'volcano' type manner (27). This suggests that $E_{1/2}$ is a function of the d-band centre i.e. surface reactivity, and is reflective of the adsorption energies of the electroactive species and the departing reactants.

The d-band has also been reported to influence the activation energy and bond breaking in the HER, where the position of the d-band changes from the point of proton absorption to bond breaking to product generation. A d-band centre close to the Fermi level is reflective of strong adsorption whilst the opposite holds for weak adsorption. This justifies why platinum sits on the apex of the volcano plot, (see chapter 2, figure 7) since the intermediate M-H bond strength implies optimised adsorption and desorption for the HER, hence high catalytic efficiency (23).

On the other hand, what can be proposed from the experimental results (figure 8) is that changing nanoparticle size can shift the band structure consequently changing the Fermi level. This can also explain the shifts we observe in the half wave potential and is in line with observations made before in the literature for the d-band structure of the platinum metal and the ORR (28),(29). However, although the results suggest there is a link between electronic and electrocatalytic properties, the limitations are that the relation between d-band centre and electrocatalytic activity is more complicated and a direct correlation cannot simply be deduced (23).

In terms of the $E_{1/2}$ and the average size of the cisPt nanocluster in this work, it is evident that beyond 45 minutes less significant changes take place, see figure 8. After 15 minutes of sonication an average nanocluster size of 1.57 ± 0.64 nm was found. This was reduced at 30 minutes to 1.32 ± 0.52 nm, and at 45 minutes to 1.26 ± 0.57 nm. However at 90 minutes of sonication, the changes became less significant from those at 45 minutes i.e. a cisPt diameter size of 1.26 ± 0.37 nm was measured. For each of these sonication times an average size was calculated based on 86 measurements for 15 minutes, 96 for 30 minutes, 30 for 45 minutes and 161 measurements for 90 minutes, see appendix 2, Tables A2.3 –A2.6 for the raw data.

It is important not to conduct the functionalisation reaction beyond this reaction time i.e. 45 minutes, otherwise we risk re-aggregation of nanoclusters following break up by sonication. This could result from nucleation of smaller nanoclusters with increased exposure time to the surface of the SWCNT under favourable reaction conditions, since it has been reported that CNTs particularly those with defects on the CNTs act as nucleation sites for the growth of Pt nanoparticles (21).

In conclusion, we find that the optimum sonication reaction time of 45 minutes is sufficient for achieving improved distribution of the Pt active sites which consequently results in improved electrochemical performance for HER i.e. a smaller cathodic $E_{1/2}$ vs SCE.

5.6.2.2 Ratio of the SWCNT to DNA-cisPt

The influence of the ratio of SWCNT to DNA-cisPt was explored under the same reaction conditions mentioned at the optimum sonication reaction time found of 45 minutes. The distribution of the cisPt i.e. platinum nanoclusters was explored as a function of SWCNT loading. This entailed preparing the material for functionalisation at three different volume ratios including 0.5 to 1, 1 to 1 and 2 to 1 SWCNT: DNA-cisPt at the optimum reaction time found of 45 minutes. The surface morphology of the prepared material was then assessed using STEM imaging using the same methods described above. Figure 9 displays the STEM imaging results.

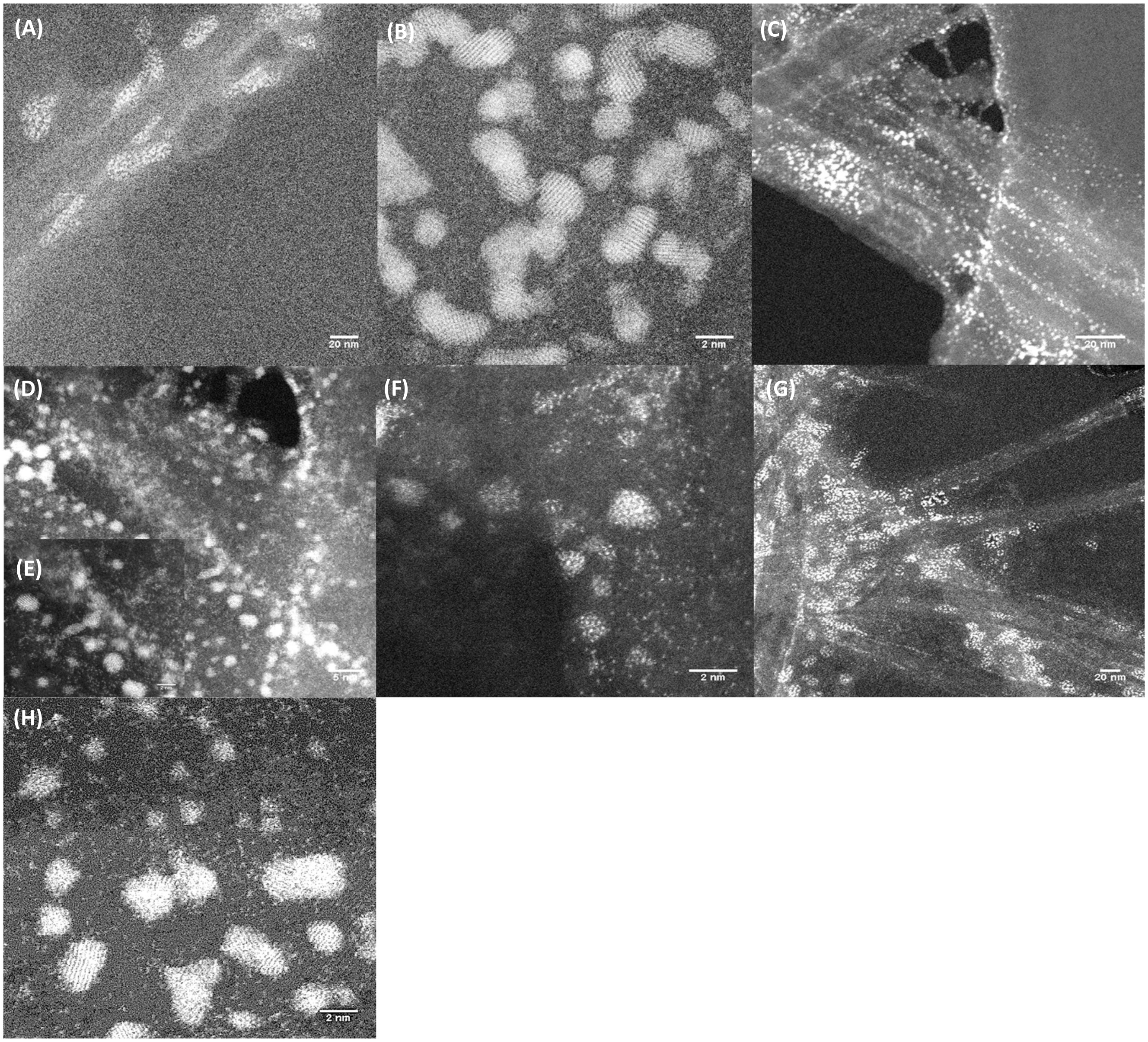

***Figure 9-** STEM imaging characterization of the different ratios of SWCNT: DNA-cisPt explored (A,B) 0.5 to 1 (A) x 600 k (B) x 8 million (C-F) 1 to 1 (C) x 1000 K (D) x 3 million (E)x 8 million (F) x 10 million (G-H) 2 to 1 (G) x 400 k (H) x 8 million.*

Similarly, by measuring the cisPt nanocluster size of the images in figure 9 using the tools in image J, we find that increasing the ratio of the SWCNTs to that of the DNA-cisPt reduces the clustering of the material, see Table 5. This is the hypothesis we would propose i.e. that at higher volume ratios of SWCNT, a larger surface area would be available to support the DNA-cisPt material, enabling improved distributions. All the measurements made are provided in appendix 2, Tables A2.7 –A2.9.

***Table 5**- The variation of the platinum nanocluster size with the ratio of SWCNT to DNA-cisPt.*

Ratio of SWCNT: DNA-cisPt	Average Particle size/ nm	Number of measurements the average is calculated from
0.5: 1	1.51 ± 0.67	11
1 :1	1.57 ± 0.55	51
2 : 1	1.26 ± 0.57	30

On the other hand, it could be argued that the resulting changes in the distribution of the DNA-cisPt on the SWCNT catalyst support are not influenced greatly by the volume ratio of SWCNT employed since the aggregation of the DNA-cisPt is primarily based on the initial incubation reaction conditions employed and the random and uncontrolled covalent interactions that take place. This can be highlighted as a limitation of the experimental findings made above.

5.6.2.2.1 Electrochemical performance for HER

To investigate the resulting effect of the volume ratio of the SWCNT to the DNA-cisPt employed on the electrochemical behaviour, the material synthesis via a functionalization reaction for the different volume ratios of 0.5:1, 1:1, 2:1 and 4:1 SWCNT-DNA-cisPt were prepared via sonication at 45 minutes. The prepared material was then tested electrochemically for the HER in the same ways mentioned before. The voltammetry response for the HER (1 mM $HClO_4$, 0.1 M $NaClO_4$) at 50 mV s^{-1} is displayed in figure 10.

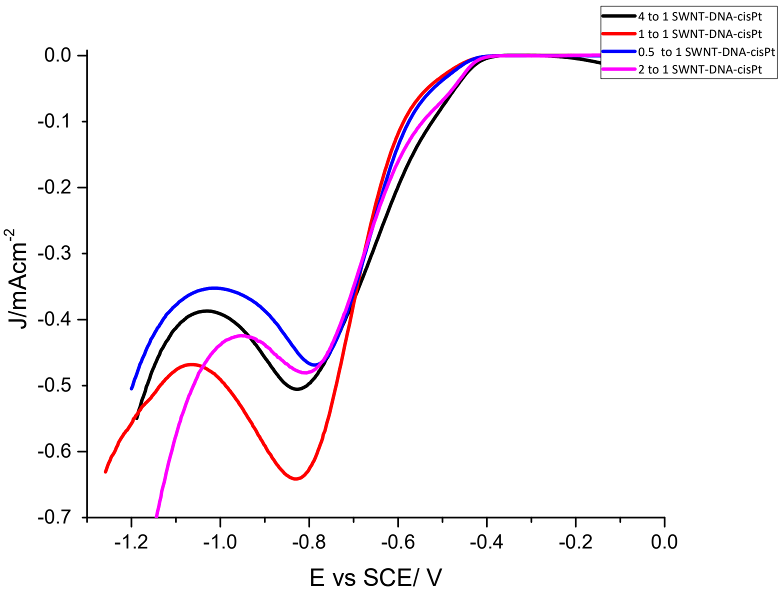

***Figure 10**- Voltammetry response of SWCNT-DNA-cisplatin at different ratios of SWCNTs in 1 mM $HClO_4$ and 0.1 M $NaClO_4$ at 50 m Vs^{-1} (1st cycle) prepared at 45 minutes of sonication time. The current density (J) is based on the geometric surface area of the working electrode.*

From an electrochemical stand point, it is evident that as we increase the ratio of SWCNT to DNA-cisPt the electrocatalytic response for the HER is improved. This is explained by there being an improved distribution of the platinum atoms hence the exposure and availability of more catalyst active centres for the H^+ electroactive species. This is in line with previous observations made in chapter 4 where literature reportings suggest that an average of 5 platinum atoms are required for the reduction of protons to molecular hydrogen in acidic environments (30).

The response in figure 10 can be translated in terms of electrochemical parameters i.e. half wave potential ($E_{1/2}$) vs SCE and peak current value (I_p) which better reflect the influence of the volume ratio of the SWCNT to DNA-cisPt on the electrochemical behaviour. This is presented in Table 6, where we find that the changes in the half wave potential are not significantly affected with the ratio of the SWCNT to DNA-cisPt employed. On the other hand, the 1 to 1 SWCNT: DNA-cisPt ratio displayed a much higher current output compared to the other ratios employed. Likewise, the size of the measured cisPt nanoclusters was also higher at this ratio compared to the others. This enables the suggestion of their being a link between the optimum platinum nanocluster size and electrocatalytic activity to be made which is reflected by the measured current density output, resulting from the changes we see with the employed volume ratio of the SWCNT to DNA-cisPt.

Table 6- *Changes in half wave potential ($E_{1/2}$) and Peak Current (I_p) with SWCNT loading.*

Ratio of SWCNT:DNA-cisPt	**Half-wave potential, $E_{1/2}$ / V vs SCE ± 0.01 V**	**Peak Current I_p/µA ± 1 µA**
0.5:1	-0.65	-33.0
1:1	-0.68	-45.3
2:1	-0.65	-33.9
4:1	-0.63	-35.7

The resulting changes in electrochemical behaviour is therefore not conclusive to the following statements: i.e. that the greater the surface area provided by the increased volume ratio of the catalyst support (SWCNT), the higher the distribution of the cisPt that can be attained (i.e. smaller nanocluster size) measured and consequently the higher the electrochemical activity (i.e. higher current density output) and the smaller the half wave potential. The relative loading of the metal to the catalyst support can therefore also affect the electrochemical performance and this has previously been reported in the literature where the metal loading was found to change not only the particle size and dispersion of the catalyst but simultaneously the selectivity and activity of the catalyst too (31).

5.6.3 Electrochemical performance for HER: SWCNT functionalisation with virgin DNA vs. bulk cisPt

The functionalisation of SWCNT with virgin sm-DNA and bulk cisPt was explored as a control measure for the DNA-cisPt adducts previously employed, at the optimum sonication reaction time of 45 minutes. The material was characterised through STEM imaging and electrochemical testing using the same methods and conditions outlined before. The resulting electrochemical behaviour is displayed in figure 11.

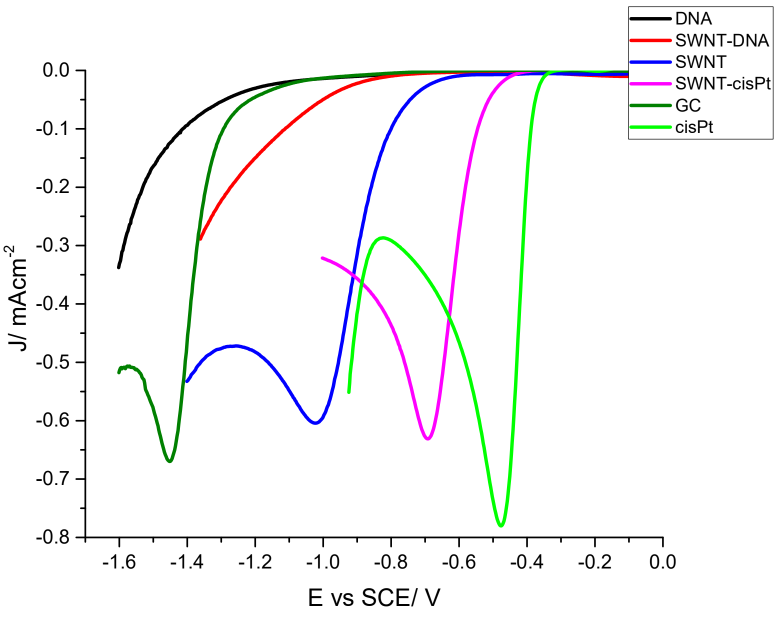

Figure 11- *Voltammetry response for the HER for SWCNT functionalised with virgin sm-DNA and bulk cisPt cast on GC (d=3 mm) at 50 mV s^{-1} (1 mM $HClO_4$, 0.1 M $NaClO_4$, pH 3).*

The electrochemical performance of the non-conductive DNA for the HER (1 mM $HClO_4$, 0.1 M $NaClO_4$, pH 3) can be improved by functionalisation with SWCNT as shown in figure 11. Although, the absence of peak current remains following functionalisation of the DNA with SWCNT, the onset potential of the SWCNT-DNA exceeds that of both the DNA and bare GC response. There is no observable peak at the SWCNT-DNA as it was previously reported that the maximum current response is obtained when a 0.5 wt.% of DNA to CNT is employed (32) , since at this weight percent (wt.%) the best dispersion of CNT can be established (32).

However, as we would expect, SWCNT-DNA does not outperform the electrocatalytic response of the SWCNT-cisPt. It was reported by (12) that the modification of carbon nanotubes with platinum nanoparticles provides 5d platinum electrons to valence band structure of the nanotubes. Which resulted from a higher density of electron states at the Fermi surface (12). In their work, it was also shown that as the loading of the platinum to the SWCNT increased, the number of *sp*^{3} and *sp*^{2} bonds in the carbon nanotubes did not change greatly (12), thus explaining why bulk cisPt outperforms SWCNT-cisPt, see figure 11.

In the following section, we move towards exploring how the functionalization of the SWCNT with DNA followed by cisPt compares to the direct functionalisation of the DNA-cisPt adducts with the nanotubes. This will entail electrochemical testing of the material for the HER and also the STEM imaging characterization to explore whether the cisPt distribution is affected.

5.6.4 Electrochemical response of the SWCNT-DNA + cisPt compared with SWCNT- DNA-cisPt

The incubation process involves the activation of the DNA molecules with Pt (II) complexes in the methods described before (see materials and experiments section). However in the presence of SWCNTs, if the SWCNTs have undergone oxidization with nitric acid, the platinum ions exhibit a higher cation adsorption capacity to the CNTs than on the DNA, resulting in complexation (33). In this work, the SWCNTs used have undergone a purification treatment using an oxidative acid thus have involved acid leaching and oxidation, therefore an improved Pt adsorption capacity is highly likely .

The fabrication of the SWCNT-DNA followed by functionalisation with cisPt enables the DNA to act as a non-covalent SWCNT dispersant (in aqueous solution) and to provide a binding site for Pt nanoparticles. The advantage of this approach is that the functionalization of the cisPt occurs through its covalent attachment to the encapsulating oligonucleotide and not through non-covalent interactions to the surface of the SWCNT. In this manner, the Pt binding is substantially stronger than simple physisorption, whilst simultaneously the SWCNT surface remains largely unperturbed hence preserving the inherent and desirable properties of the underlying nanotube.

It was reported by (34) that the DNA also serves as a capping molecule for Pt growth, which yields high uniformity of the resulting Pt nanoparticles. The fabricated material (prepared by sonication reaction at 45 minutes under the same conditions mentioned above) were electrochemically tested for the HER. The resulting voltammetry response are shown in figure 12.

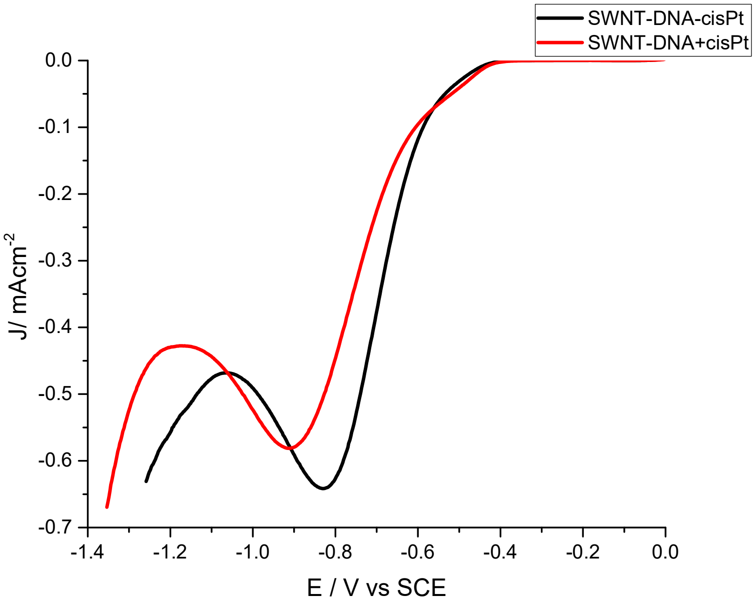

***Figure 12** - Cyclic voltammetry (1 mM $HClO_4$, 0.1 M $NaClO_4$) at 50 mVs^{-1} SWCNT-DNA functionalized with cisPt compared with SWCNT functionalized with DNA-cisPt adducts.*

***Table 7**- Changes in half wave potential ($E_{1/2}$) and Peak Current (I_p) with order of cisPt functionalization with SWCNTs.*

Material	**Half-wave potential, $E_{1/2}$ / V vs SCE ± 0.01 V**	**Peak current density, J_p /mAcm^{-2} ± 0.01**
SWCNT-DNA-cisPt	-0.68	-0.64
SWCNT-DNA +cisPt	-0.73	-0.58

The order of the functionalisation of the cisPt with the SWCNT gives rise to a small difference in the response of the voltammogram for the HER. It can be noted that the functionalisation of the SWCNTs with the DNA-cisPt adducts produced a higher electrochemical current density output of -0.64 mA cm^{-2} compared with -0.58 mA cm^{-2} for the functionalisation of SWCNT-DNA with cisPt. The half wave potential is also shifted and a more favourable response i.e. towards that of Pt ultra-microelectrode (UME) behaviour is seen with the SWCNT-DNA-cisPt material.

5.6.5 Evident changes to the surface morphology of the fabricated material

The resulting changes to the surface morphology of the SWCNT material after undergoing functionalisation with virgin DNA, bulk cisPt and DNA-cisPt adducts is investigated using STEM imaging. There is no controlled distribution of any of these materials along the tubes, however it is evident that the nanoclusters are smaller using the SWCNT as a catalyst support, compared to those observed in DNA-cisPt, see figure 13(H) compared to figure 13(J).

Figure 13(B) shows the appearance of bright spots which could be attributed to the presence of impurities along the bare SWCNTs. This is most likely to be salt deposits as revealed by the XPS atomic compositions previously.

On the other hand, comparing the morphology of the SWCNT-cisPt to the SWCNT-DNA-cisPt (figures 13 (F) and (I)), it seems that there is less clustering without the DNA and improved distribution of the platinum. This is explained by the nature of the globular compactness that the extended DNA chain arranges into upon interaction with the cisPt (35). The STEM images obtained correspond well with the literature reports made for cisPt on SWCNTs, whereby the recorded size of platinum nanoparticles was made to be between 1-2 nm on tube bundles for the work involving the functionalisation of single-walled carbon nanotubes as drug-delivery devices in the literature (36).

The materials demonstrated stability upon exposures to the electron beam of a 200 keV energetic energy with no observable shift in the Pt atoms or sintering suggesting that the Pt is well immobilised onto the SWCNT. The material presented here is a means for decreasing the Pt loading by increasing the available surface active sites. This was similar to findings reported in the work of (8).

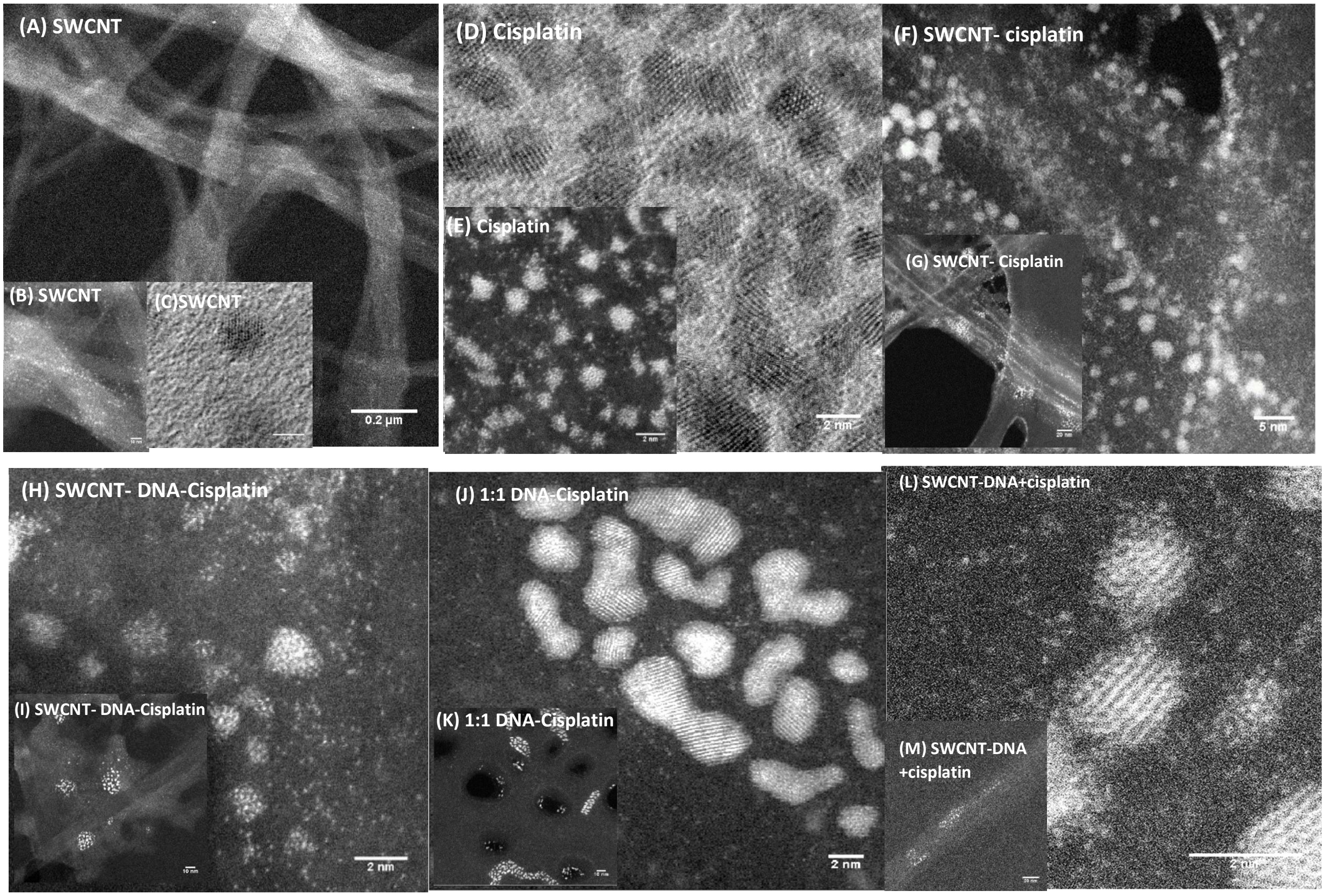

Figure 13- *STEM images of the functionalized SWCNT material (A-C) SWCNT, (x 100 k, x 1 million, x 8 million) (D, E) Cisplatin, (x 8 million) (F, G) SWCNT-cisPt , (x 3 million, x 1000 k) (H, I) SWCNT-DNA-cisPt , (x 10 million, x 800 k) (J, K) DNA-cisPt (x 8 million, x 800 k) (L, M) SWCNT-DNA + cisPt , (x 20 million, x 800 K).*

5.6.6 Half wave potential and how it compares to bulk Pt

The half wave potential attained at each of the catalytic material fabricated in this work, see table 1, can be expressed in terms of the calculated cisPt mass loading. This variation will reflect whether with increased cisPt loadings we can shift the performance of the material towards that of a bulk Pt ultra-micro electrode (UME).

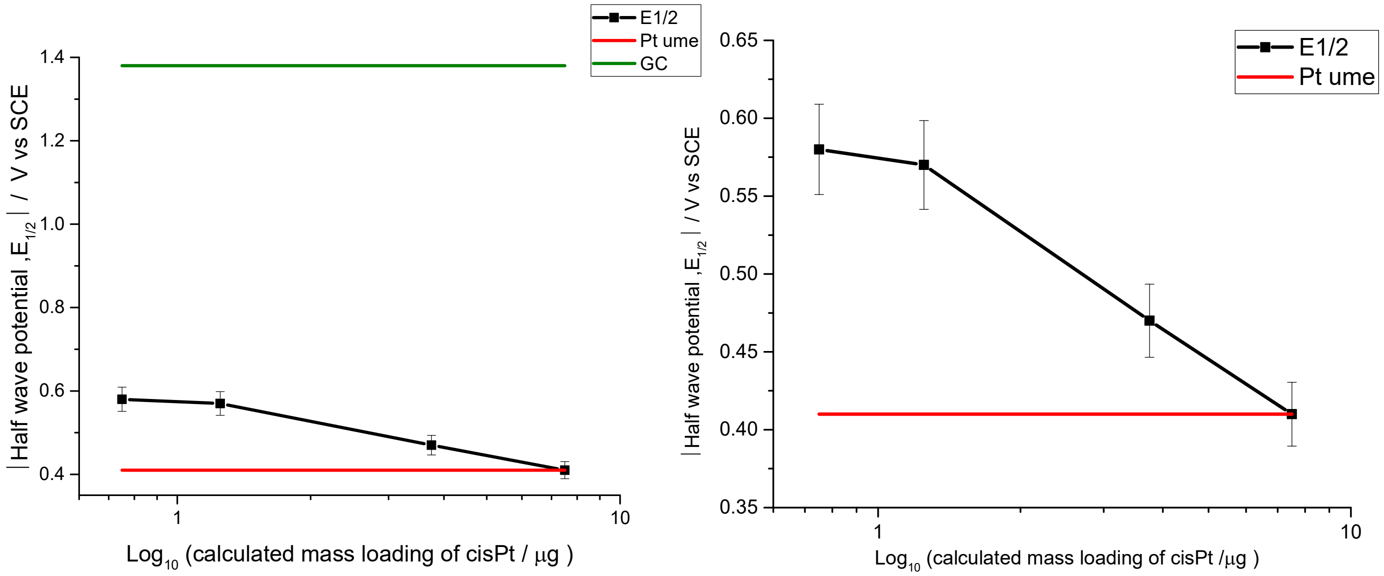

***Figure 14** - The variation of half wave potential with cisPt loading compared to Pt UME half wave potential.*

It is evident from figure 14 that the half wave potential tends towards that of a Pt UME as we increase the cisPt content in the materials explored (see Table 1). At the maximum concentration of platinum employed i.e.1000 µM of bulk cisPt (equivalent to a mass loading of 7.5 µg), the half wave potential meets the Pt UME bulk line as shown in figure 14. The $E_{1/2}$ is a first approximation of the formal potential of the electrode, thus at higher metal loadings, we expect to move away from the GC bulk line (the working surface in which the fabricated material is casted on), towards that of platinum.

5.6.7 Electrochemical parameters as a measure of catalytic performance

The HER is an archetypal simple electrocatalytic reaction to assess the electrochemical behaviour of the different fabricated materials in an acidic environment of pH 3. The potential (E) is the principal characteristic of electrocatalysis, however the rate of the reaction does not increase in the same way at for example potential E_1 compared to E_2. Hence for comparison purposes, an onset potential (σ) output is set as rational measure of performance of the electrocatalysis, defined at 0.1 mA cm^{-2}. In addition, the peak current density (J_p) can be reflective of the maximum catalytic activity. The current densities measured and reported in this work are based on the geometric surface area of the working electrode. The third electrochemical parameter will be the peak potential (E_p), reflective of how much voltage input is required to achieve the electrochemical reactions being tested. Table 8 displays the results.

***Table 8**- Comparison between the peak potential (E_p), current density (J_P) and onset potential ($\sigma_{0.1mAcm^{-2}}$) attained at the modified GC electrode surface with the different SWCNT/DNA/cisPt based material for the HER (1 mM $HClO_4$, 0.1 M $NaClO_4$) at 50 mV s^{-1}.*

Fabricated Material /GC modified Electrode Surface	Peak Potential (E_p) / V vs SCE ± 0.01 V	Current density* (J_p) /mA cm^{-2} ± 0.01	Onset Potential (σ) / V vs SCE @ 0.1 mA cm^{-2} ± 0.01 V
Bare GC	-1.45	-0.67	-1.29
DNA	-	-	-1.42
SWCNT-DNA	-	-	-1.11
SWCNT	-1.01	-0.60	-0.81
SWCNT-DNA + cisPt	-0.91	-0.58	-0.61
0.5 to 1 SWCNT-DNA-cisPt	-0.84	-0.53	-0.63
1 to 1 SWCNT-DNA-cisPt	-0.83	-0.64	-0.59
4 to 1 SWCNT-DNA-cisPt	-0.82	-0.5	-0.52
1 to 1 DNA-cisPt	-0.80	-0.53	-0.61
2 to 1 SWCNT-DNA-cisPt	-0.79	-0.50	-0.57
SWCNT-cisPt	-0.69	-0.63	-0.55
cisPt	-0.47	-0.78	-0.39

*Current density based on a geometric surface area of the working electrode

It is evident from Table 8 that as the volume ratio of the cisPt in the material is increased, (see Table 1) the electrochemical parameters shift towards a more favourable response i.e. like that of bulk cisPt. The functionalization of DNA with SWCNT shifts the onset potential ($\sigma_{0.1mAcm^{-2}}$) more favourably than the response attained for the virgin DNA. However, for the SWCNT, the reverse holds, and the changes in the response become unfavourable prior to the nanotubes functionalization with DNA. This is attributed to the non-conductive nature of the DNA material which has been reported by (13) to inhibit redox processes when immobilised onto the working surface. On the other hand, the SWCNT modified GC surface, has a higher conductivity thus redox processes can occur, and it can be proposed that the sp^3 and sp^2 bonds in the CNTs are contributing favourably to the SWCNT-DNA /GC working surface as reflected by the lower onset potential (-1.11 V vs SCE) compared to that measured at the virgin DNA/GC surface. The properties of the CNTs themselves i.e. their electrical and structural properties can enhance the kinetics of the charge transfer reactions taking place (13) .

Alternatively, as we have already mentioned, the functionalization of the SWCNT with cisPt improves the electrochemical response for the HER significantly compared to the untreated SWCNT, shifting the behaviour more closely towards that of bulk cisPt. The 1:1 volume ratio of the SWCNT-DNA-cisPt provides the highest current density output compared to the other volume ratios of the SWCNT-DNA-cisPt explored, although in terms of the electrical potential (both the peak potential and onset potential), this volume ratio does not provide the best performance. This means the SWCNTs functionalized with the DNA-cisPt adducts fall intermediate between the electrochemical behaviour observed for the unmodified SWCNT and that of the SWCNT-cisPt, as we would expect. However, clear conclusive remarks are limited given the range of electrochemical parameters used. For simplicity, a single measure of electrocatalytic performance should be made to investigate the effect of the different ratios of the SWCNT-DNA-cisPt on the reaction kinetics such as the measure of the kinetic rate constant (k) as part of future work recommendations.

One-dimensional diffusion profile in drop cast material

Scan rate studies were conducted to explore whether the electrochemical reactions on the DNA-cisPt-SWCNT /glassy carbon modified electrode were controlled by a diffusive process or an adsorptive process for the different material synthesised. The construction of the logarithmic plot of scan rate (ν) vs. current (I) can be used as a tool to evaluate whether we have a diffusive controlled response or an adsorptive response from the magnitude of the gradient. This is explored for the range of SWCNT/DNA-cisPt material employed in this study. If the slope is near the theoretical value for a diffusion controlled process i.e. 0.5 then it implies that the diffusion of the protons to the surface of the electrodes from the bulk solution is occurring (37). On the other hand, a slope with a magnitude ≥ 1 implies that the voltammetry response is dependent on an adsorbed reactant layer.

As an example, figure 15 illustrates the experimental data points attained for the SWCNT-DNA-cisPt/GC modified surface and how the magnitude of the slope was found for all the materials employed. This analysis was applied to the other volumes investigated, and the logarithmic plot of scan rate (υ) vs. peak current (I_p) was constructed to find that the gradient varied from 0.40 to 0.52 (within experimental error), thus indicating that we have a purely diffusional (semi-infinite) electrode response, in line with the observations previously made in chapter 4. The same plots were produced for the remaining materials fabricated in this work and are provided in appendix 2, figures A2.1-A2.7.

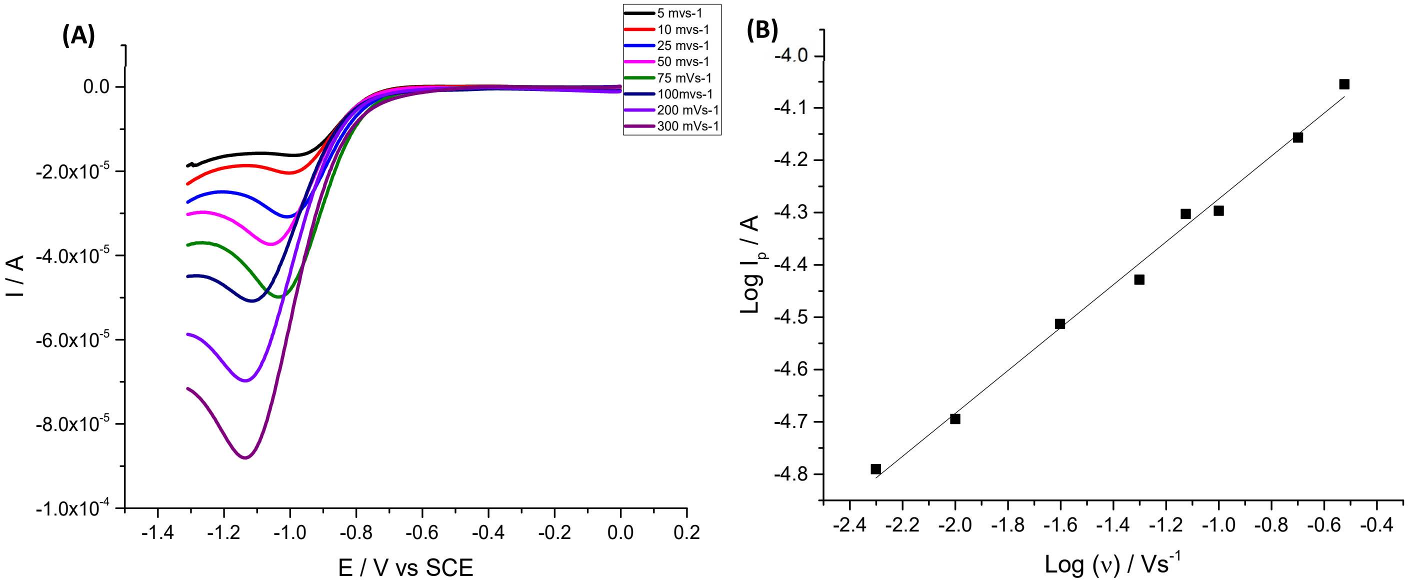

Figure 15*- (A) Scan rate study for the HER at SWCNT-DNA-cisPt/GC modified working surface in 1 mM $HClO_4$ and 0.1 M $NaClO_4$ (B) Resulting plot of log scan rate vs log peak current (y=0.409x – 3.864).*

5.6.8 Mechanism of the hydrogen evolution reaction (HER)

Tafel Plots at 50 mV s^{-1}

To further compare the electrocatalytic behaviour at the different SWCNT/DNA-cisPt materials explored in this work, Tafel plots were constructed to reveal the reaction mechanism of the HER at each working surface based on the theoretical information provided in the literature (38) , (39) and (40) and as has already been detailed in chapters 2 and 4 of this thesis. From the Tafel plots, the magnitude of the Tafel slope can be found and expressed as a function of cisPt loading as shown in figure 16. Table 9 presents the corresponding Tafel slope for each material tested.

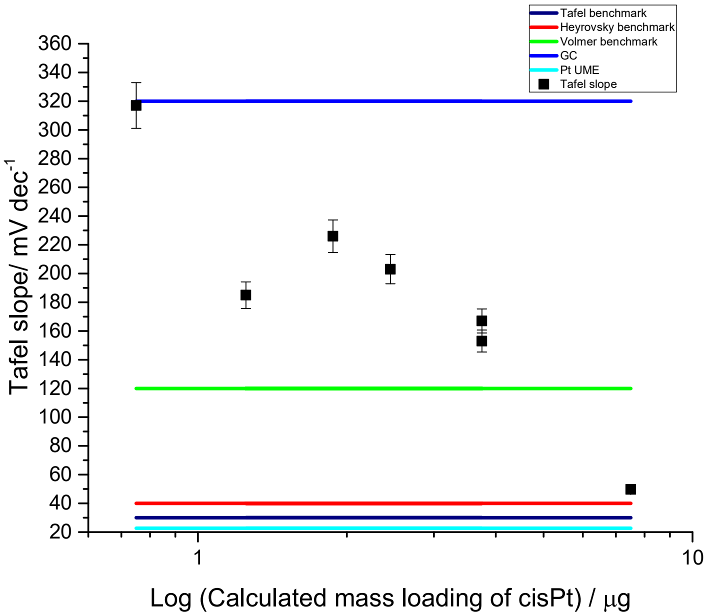

Figure 16*- The variation in the Tafel slope as a function of the calculated cisPt loading in the material compared with t the well reported slopes of the theoretical mechanisms proposed in the literature* (8) *,* (38) *,* (39) *and* (40)*.*

Table 9: *Tafel slopes and alpha values at the different SWCNT/DNA-cisPt synthesized material for the HER.*

Electrocatalyst Material	Tafel slope / mV dec^{-1}	Alpha
Pt UME mass transport corrected	22.7	-
cisPt	49.7	0.52
2 to 1 SWCNT to DNA-cisPt	185	0.14
0.5 to 1 SWCNT-DNA-cisPt	203	0.13
GC	180	0.14
SWCNT-DNA	348	0.07
SWCNT-DNA-cisPt	226	0.11
DNA	407	0.06
SWCNT	222	0.12
1 to 1 DNA-cisPt	153	0.17
4 to 1 SWCNT –DNA-cisPt	317	0.08
SWCNT-cisPt	167	0.15

It is evident from figure 16 and Table 9 that as the cisPt loading is increased in the SWCNT/DNA-cisPt material, the Tafel slope is reduced as we move away from the GC bulk line such as at the surface of virgin DNA (407 mV per decade) towards that of bulk cisPt (49.7 mV per decade). This change is thus reflective of the change in the mechanism of HER i.e. from the Volmer limit (SWCNT, SWCNT-DNA, DNA and DNA-cisPt/GC modified electrode) to the Heyrovsky reaction (at the cisPt/GC modified electrode). The rate limiting step for proton reduction therefore changes from being Eq. (7) to Eq. (8) outlined in chapter 4, which corresponds with the observations previously noted for the behaviour of the sm-DNA-cisPt material in chapter 4.

5.6.8.1 The Transfer coefficient, α

The transfer coefficient can be a means of gaining an insight into the influence of the applied voltage on the kinetics of the reaction. This is better understood using a more generic form of the correlation given by equation (3), which show that the rate constant (k) is directly proportional to alpha(α).

$$k = Aexp\left[\frac{-\alpha FE}{RT}\right] \quad Eq.(3)$$

Thus from Eq. (3) we are able to explore the effect of the applied potential on the kinetics from the transfer coefficient (α). The change in alpha is calculated directly using the magnitude of the Tafel slopes found, see appendix 3. This can then be presented as a function of cisPt loading as displayed in figure 17. Table 9 presents the transfer coefficient value specifically for each of the materials explored.

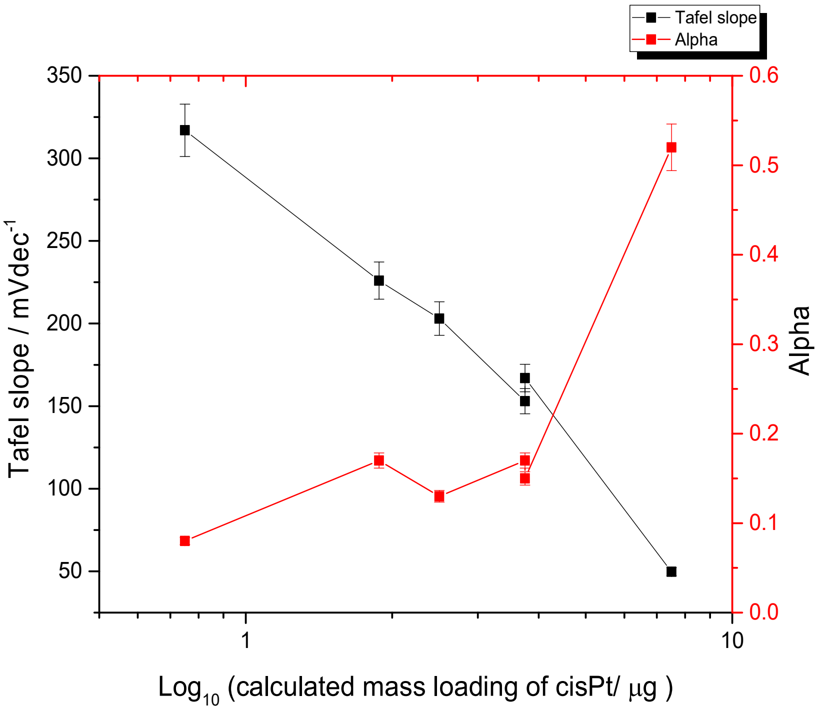

Figure 17-*The variation in Tafel slope and α as a function of cisPt loading.*

The evident trend is that with increased loadings of cisPt, the Tafel slope decreases whilst the value of the transfer coefficient increases. It can be proposed therefore that the transfer coefficient, which is reflective of the transition state, is more reactant like i.e. closer to zero at lower cisPt loadings. Therefore changing the applied potential will not result in significant changes to the rate constant.

This is in agreement with the experimental findings in this work, where for both the DNA and SWCNT-DNA, no electrochemical peak signals were observed within the electrochemical potential window. However, as the platinum metal loading is increased we move towards a transition state that is more product like, such as with the response of the bulk cisPt/GC working surface, as we approach a transfer coefficient value of 0.5. The applied potential will significantly increase the rate constant i.e. kinetics of the reaction, driving the electrochemical response through an electrochemical peak signal (see figure 11).

5.7 Conclusions and future work

In this work, the optimum sonication time for the functionalisation reaction of the SWCNT with the DNA/DNA-cisPt and cisPt material was found to be 45 minutes. This was justified by the experimental findings which showed that beyond this reaction time no significant changes were observed in the platinum nanocluster size, hence 45 minutes was sufficient for achieving optimum dispersion of the platinum onto the surface of the SWCNT. The resulting changes in the platinum nanocluster size were less statistically significant with the volume ratio of the SWCNT to the DNA-cisPt employed compared to the reaction time and no conclusive remarks could confidently be made to recommend an optimum volume ratio.

To conclude, it is clear from the data that the functionalisation of the SWCNTs with cisPt gives rise to exceptional improvements in the electrocatalytic performance towards the HER (pH 3). In addition the SWCNT functionalization with the DNA shifts the behaviour more favourably than the response of virgin DNA alone. However, less significant changes were noted in the voltammetry for the HER, upon the functionalization of the SWCNT with DNA-cisPt compared with the response of the DNA-cisPt adducts alone. However, the SWCNT-DNA-cisPt still outperforms the response of the unmodified SWCNTs. The electrochemical response of the SWCNT functionalized with the DNA-cisPt adducts fell intermediary between the electrochemical behaviour observed for the unmodified SWCNT and that of the SWCNT-cisPt for the HER (pH 3).

Insights into the mechanism of the reaction, as revealed by the Tafel slopes show that the Volmer-Heyrovsky mechanism dominates the kinetics of the HER over the surface of the fabricated structures and that the cisPt loading correlates strongly with the calculated transfer coefficient (α) and the Tafel slope.

Suggestions for future work could involve processing of the SWCNT-DNA-cisPt material to improve the conductivity of the DNA following functionalization. It can be proposed that this will significantly improve the electrochemical response for the HER (pH 3), whilst simultaneously enabling reduced cisPt loadings to be employed. Alternatively, future work could employ much lower ratio loadings of the DNA-cisPt adducts in the fabrication process compared to those used in this work. This will can improve the platinum metal utilization and consequently reduce the costs of material production.

References

1. Iijima S. Helical microtubules of graphitic carbon. Nature. 1991;354(November):56–8.
2. Al Sheheri SZ, Al-Amshany ZM, Al Sulami QA, Tashkandi NY, Hussein MA, El-Shishtawy RM. The preparation of carbon nanofillers and their role on the performance of variable polymer nanocomposites. Des Monomers Polym. 2019;22(1):8–53.
3. Atif R, Inam F. Reasons and remedies for the agglomeration of multilayered graphene and carbon nanotubes in polymers. Beilstein J Nanotechnol. 2016;7(1):1174–96.
4. Ribeiro B, Botelho EC, Costa ML, Bandeira CF. Carbon nanotube buckypaper reinforced polymer composites: A review. Polimeros. 2017;27(3):247–55.
5. Wee JH, Lee KY, Kim SH. Fabrication methods for low-Pt-loading electrocatalysts in proton exchange membrane fuel cell systems. J Power Sources. 2007;165(2):667–77.
6. Luo C, Xie H, Wang Q, Luo G, Liu C. A Review of the Application and Performance of Carbon Nanotubes in Fuel Cells. J Nanomater. 2017;2015.
7. Chen WX, Lee JY, Liu Z. Microwave-assisted synthesis of carbon supported Pt nanoparticles for fuel cell applications. Chem Commun. 2002;8(21):2588–9.
8. Tavakkoli M, Holmberg N, Kronberg R, Jiang H, Sainio J, Kauppinen EI, et al. Electrochemical Activation of Single-Walled Carbon Nanotubes with Pseudo-Atomic-Scale Platinum for the Hydrogen Evolution Reaction. ACS Catal. 2017;7(5):3121–30.
9. Sharma A, Andreas R, Nehra SP. Synthesis of SWNT/Pt nanocomposites for their effective role in hydrogen storage applications. 2018;30148:30148.
10. Cozzarini L, Bertolini G, Šuran-Brunelli ST, Radivo A, Bracamonte MV, Tavagnacco C, et al. Metal decorated carbon nanotubes for electrocatalytic water splitting. Int J Hydrogen Energy. 2017;42(30):18763–73.
11. Bittencourt C, Hecq M, Felten A, Pireaux JJ, Ghijsen J, Felicissimo MP, et al. Platinum-carbon nanotube interaction. Chem Phys Lett. 2008;462(4–6):260–4.
12. Dobrzańska-Danikiewicz A, Łukowiec D, Kubacki J. Investigations of electron properties of carbon nanotubes decorated with platinum nanoparticles with their varying fraction. J Nanomater. 2016;2016.
13. Paul A, Bhattacharya B. DNA functionalized carbon nanotubes for nonbiological applications. Mater Manuf Process. 2010;25(9):891–908.
14. Hu C, Zhang Y, Bao G, Zhang Y, Liu M, Wang ZL. DNA functionalized single-walled carbon nanotubes for electrochemical detection. J Phys Chem B. 2005;109(43):20072–6.
15. Zhu N, Chang Z, He P, Fang Y. Electrochemical DNA biosensors based on platinum nanoparticles combined carbon nanotubes. Anal Chim Acta. 2005;545(1):21–6.
16. Ostojic GN, Ireland JR, Hersam MC. Noncovalent Functionalization of DNA-Wrapped Single-Walled Carbon Nanotubes with Platinum-Based DNA Cross-Linkers. 2008;(37):9784–9.
17. Dong L. DNA-templated synthesis of Pt nanoparticles on single-walled carbon nanotubes. Nanotechnology. 2009;20(46).
18. Su HC, Zhang M, Bosze W, Lim JH, Myung N V. Metal nanoparticles and DNA co-functionalized single-walled carbon nanotube gas sensors. Nanotechnology. 2013;24(50).

19. Englert K. DNA Origami Catalysts. [PhD thesis]. Birmingham (UK): University of Birmingham; 2019.

20. Thoi VS, Usiskin RE, Haile SM. Platinum-decorated carbon nanotubes for hydrogen oxidation and proton reduction in solid acid electrochemical cells. Chem Sci. 2015;6(2):1570–7.

21. Gurylev V, Chin T-K, Tsai H-Y. Carbon Nanotubes Decorated with Platinum Nanoparticles for Field-Emission Application. ACS Omega. 2019;4(13):15428–34.

22. Millard, M.M, Macquet , J.P and Theophanides, T. X-Ray Photoelectron Spectroscopy of DNA-Pt Complexes. Evidence Of 06 (Gua) - N~(Gua) chelation with DNA. 1975;2:166–70

23. Zhu J, Hu L, Zhao P, Lee LYS, Wong KY. Recent Advances in Electrocatalytic Hydrogen Evolution Using Nanoparticles. Chem Rev. 2020;120(2):851–918.

24. Zalitis CM, Kucernak AR, Sharman J, Wright E. Design principles for platinum nanoparticles catalysing electrochemical hydrogen evolution and oxidation reactions: edges are much more active than facets. J Mater Chem A. 2017;5(110):23328–38.

25. Wei GF, Liu ZP. Restructuring and hydrogen evolution on Pt nanoparticle. Chem Sci. 2015;6(2):1485–90.

26. Tan TL, Wang LL, Zhang J, Johnson DD, Bai K. Platinum nanoparticle during electrochemical hydrogen evolution: Adsorbate distribution, active reaction species, and size effect. ACS Catal. 2015;5(4):2376–83.

27. Shao MH, Huang T, Liu P, Zhang J, Sasaki K, Vukmirovic MB, et al. Palladium monolayer and palladium alloy electrocatalysts for oxygen reduction. Langmuir. 2006;22(25):10409–15.

28. Toyoda E, Jinnouchi R, Hatanaka T, Morimoto Y, Mitsuhara K, Visikovskiy A, et al. The d-band structure of Pt nanoclusters correlated with the catalytic activity for an oxygen reduction reaction. J Phys Chem C. 2011;115(43):21236–40.

29. Han BC, Miranda CR, Ceder G. Effect of particle size and surface structure on adsorption of O and OH on platinum nanoparticles: A first-principles study. Phys Rev B - Condens Matter Mater Phys. 2008;77(7):1–9.

30. Dick JE, Bard AJ. Recognizing Single Collisions of PtCl62- at Femtomolar Concentrations on Ultramicroelectrodes by Nucleating Electrocatalytic Clusters. J Am Chem Soc. 2015;137(43):13752–5.

31. Akbarzadeh O, Mohd Zabidi NA, Abdul Wahab Y, Hamizi NA, Chowdhury ZZ, Merican Aljunid Merican Z, et al. Effects of cobalt loading, particle size, and calcination condition on Co/CNT catalyst performance in Fischer-Tropsch reactions. Symmetry (Basel). 2019;11(1):1–18.

32. Mirzapoor A, Ranjbar B. Biophysical and electrochemical properties of Self-assembled noncovalent SWNT/DNA hybrid and electroactive nanostructure. Phys E Low-Dimensional Syst Nanostructures. 2017;93(June):208–15.

33. Wang X, Liu F, Andavan GTS, Jing X, Singh K, Yazdanpanah VR, et al. Carbon nanotube-DNA nanoarchitectures and electronic functionality. Small. 2006;2(11):1356–65.

34. Ostojic GN, Ireland JR, Hersam MC. Noncovalent functionalization of DNA-wrapped single-walled carbon nanotubes with platinum-based DNA cross-linkers. Langmuir. 2008;24(17):9784–9.

35. Sirajuddin M, Ali S, Badshah A. Drug-DNA interactions and their study by UV-Visible, fluorescence spectroscopies and cyclic voltametry. J Photochem Photobiol B Biol.

2013;124:1–19.

36. Bhirde A, Gutkind JS, Diego S, Leapman RD, Rusling JF. NIH Public Access. 2009;(October).

37. Gowda JI, Nandibewoor ST. Electrochemical behaviour of paclitaxel and its determination at glassy carbon electrode. Asian J Pharm Sci. 2014;9(1):42–9.

38. Shinagawa T, Garcia-esparza AT, Takanabe K. Insight on Tafel slopes from a microkinetic analysis of aqueous electrocatalysis for energy conversion. Nat Publ Gr. 2015;(May):1–21.

39. Tavares M., Machado SA., Mazo L. Study of hydrogen evolution reaction in acid medium on Pt microelectrodes. Electrochim Acta. 2001;46(28):4359–69.

40. Marković NM, Grgur BN, Ross PN. Temperature-dependent hydrogen electrochemistry on platinum low-index single-crystal surfaces in acid solutions. J Phys Chem B. 1997;101(27):5405–13.

Chapter 6-

Graphitization of the DNA-Cisplatin via Electron Beam Irradiation for the Electrocatalysis of the Hydrogen Evolution Reaction (HER)

Chapter 6: Graphitization of the DNA-Cisplatin via electron beam irradiation for the electrocatalysis of the Hydrogen Evolution Reaction (HER)

6.1 Introduction

In order to achieve improved conductive and electronic properties of the DNA material as a catalyst support, the non-conductive nature of the DNA molecule needs to be changed such that both improved electrochemical activity and durability is achieved. In this work, the following methods have been explored as a means of achieving this including:

- Functionalization of single walled carbon nanotubes (SWCNT's) with DNA-cisplatin (chapter 5).
- Graphitization of the DNA through the evacuation of the hydrogen and oxygen atoms upon high dose exposure to an electron beam i.e. graphitization (chapter 6).
- Carbonisation via a low temperature pseudo pyrolysis process at lower temperatures (255 °C) than the conventional temperatures used (chapter 7).

The previous chapter discussed the experimental results of the functionalization of the single walled carbon nanotubes (SWCNT's) with DNA-cisplatin. This chapter will focus on the conversion of the DNA scaffold into a graphitic material via electron beam (e-beam) irradiation. The processed material is consequently characterized and tested for the hydrogen evolution reaction (HER) (pH 3) using similar ways to the previous work presented. Figure 1 provides an overview of the steps involved in the e-beam treatment process.

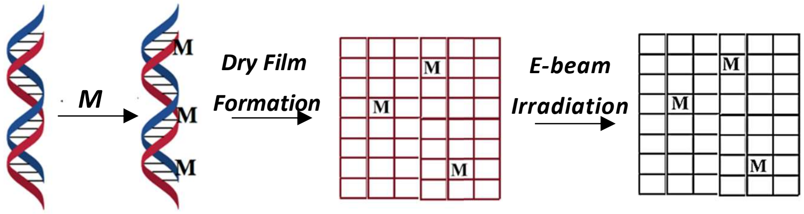

***Figure 1**- Schematic representation of the fabrication process of the catalytic material used in this study. In this work, M = Pt and the process of electron beam (e-beam) irradiation.*

The employment of DNA for nanostructure fabrication is a great means of achieving programmable and self-assembled material instead of the conventional top down nanofabrication methods employed. However, the issue with DNA in electrocatalytic applications arises from its resistive nature leading to poor electronic transfer across the polypeptide based material (as discussed in chapter 4 and 5) compared to the conductive properties of the commonly employed materials for fuel cell technology applications.

In addition, in terms of fuel cell applications under acidic conditions, the DNA material will most likely degrade following its prolonged exposures to the acid. This means the electrocatalytic response will eventually diminish consequently leading to poor durability of the assembled material. As a result, the work in this chapter will focus on the graphitization of the DNA scaffold in order to carbonize the amorphous hydrocarbon atoms in the DNA polymer consequently improving both the material electronic conductivity and durability.

The advantage of the synthesis of a graphitic-based electrocatalyst material evolves from their high stability and controllability compared to a metal based material. This makes their use more appropriate in fuel cells, energy storage and conversion devices and for the electrolysis of water (1).

It has been previously emphasized that both a nitrogen and phosphorous doped graphene (N-P-graphene) provides a higher electrocatalytic performance than either a nitrogen doped or phosphorous doped graphene alone (N-graphene) or (P-graphene) respectively (1). This is discussed in more detail in the next chapter of this thesis i.e. chapter 7. The advantage therefore in the employment of DNA as the source of amorphous carbon is associated with the surface chemical moieties it contains including nitrogen, oxygen and phosphorous which contribute favourably to the catalytic performance of the material. This is important in terms of supporting the fabrication of a metal free electrocatalyst and ensuring that the electrochemical performance competes with that of a commercial Pt/C catalyst. Research work focusing on the effects of dopants on graphene material for catalysing fundamental electrochemical reactions occurring in the electrolysis process of water i.e. Hydrogen Evolution Reaction (HER) (2) and the Oxygen Reduction Reaction (ORR) have already been explored in the literature (3).

6.2 Electron Beam Lithography (EBL)

Lithography is a process of producing patterns on a substrate using different techniques for example electron beam lithography uses an electron beam whilst photolithography uses light to imprint patterns onto the surface of the substrate, see figure 2. The relevance of these methods to the aims of this project evolve from being able to achieve graphitisation through electron beam lithography (EBL) as an alternative to the commonly employed heat treatments (4). Instead, the reported methods utilize a direct electron beam writing technique, which is favoured over conventional EBL, as a processing technique with fewer stages. Using electrons for direct writing has been reported to provide high resolution and three-dimensional flexibility (5). This method has been used by several authors (5),(6) for developing graphene structures with metals deposited on the surface. In addition, it has been used for the treatment of non-metal based atoms such as carbon films as demonstrated in the work of (6) and (7). Alternatively, Aikawa et al. (7) demonstrated that it was possible to obtain catalytic graphitization by using a focused electron beam via a transmission electron microscope to graphitize an amorphous carbon film in the presence of sputtered nickel particles (7). This portrays the feasibility of using e-beam irradiation to achieve graphitic nanostructures from an amorphous carbon source.

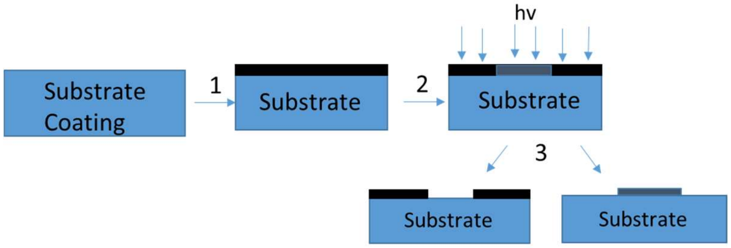

Figure 2*- Overview of Electron Beam Lithography 1: Coating of the substrate (normally Si wafer), 2: Exposure at a selected acceleration voltage, 3: Development -Positive tone (left) - Negative tone (right).*

6.3 DNA nanolithography

The shared characteristics between methods of lithography and DNA nanolithography for fabrication of nanomaterials lies in the ability to precisely assemble matter down to the atomic level. The unique programmability and folding properties of DNA enable its use as a scaffold for the construction of structures of a variety of shapes and sizes, see chapter 2. It can replace the conventional methods of lithography techniques such as electron beam lithography (EBL) since the DNA origami technique can be a means of achieving complex architectures at lower costs, higher throughput and higher resolutions (8). The DNA molecule can be used in both top-down and bottom-up approaches for nanofabrication. For example in top down techniques, the DNA structure is used as an etch mask for

transferring the desired structure/patterns onto an underlying substrate like silicon oxide and graphene (9), (10) and (11).
Alternatively, since DNA acts as a building block for the formation of self-assembled nanostructures, Zhan et al. successfully fabricated 3D gold plasmonic nanostructures by coating the gold nanoparticles with DNA strands, such that DNA origami scaffolds placed the individual gold nanoparticles precisely into defined patterns within close proximity such that the gold nanoparticles behaved as nano-lenses (12).

Similarly, Gallego et al. demonstrated that two-dimensional DNA origami templates can be used to transfer DNA with defined patterns (DNA ink) onto the gold surfaces (13). However, the limitation of DNA nanolithography is an issue of scalability, which can be overcome through its combination with other lithography methods such as electron beam lithography as reported in the literature (8),(14).

However, the chemical and mechanical properties of the DNA must be changed to provide more desirable attributes for its use including stability and preservation of the nanostructure shape (8). This was explored by Jin et al. who achieved complex nano-patterning on a graphene substrate by using metallized DNA nanostructures as a lithographic mask. In their work, the DNA was incubated with glutaraldehyde to enable seeding of silver particles followed by coating with gold. The metallisation of the DNA template establishes a lithographic gold mask on the graphene which maintains the original template structure. Through the metallisation of the DNA, enhanced chemical stability was observed whereby the DNA template can undergo further etching steps and can function as a positive relief mask (15).

Finally, other methods have demonstrated how the chemical stability of the DNA nanostructures can be achieved via a carbonisation process in a low pressure H_2 atmosphere at 800 - 1000 °C (16). This is highly desirable given that carbon based materials have higher stability under extreme environments i.e. both high temperatures and pH conditions compared to DNA (16). Similar methods are reviewed and addressed in chapter 7.

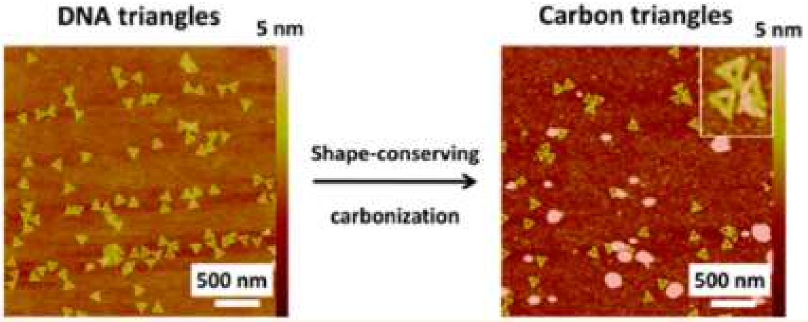

Figure 3– *AFM topographic images of shape-conserved carbon triangles (right) from DNA triangles (left) taken from Zhou et al.* (16) *produced under a high H_2 atmosphere at high temperatures (800 -1000 °C).*

In the following section, the graphitization process specifically through electron beam irradiation is reviewed and the way in which the DNA nanostructure material responds upon its interaction with the electron beam is considered. Herein, e-beam irradiation is explored as a processing technique for improving the properties of the DNA material as an electrocatalyst for the HER.

6.4 Literature review

6.4.1 Electron beam irradiation of amorphous carbon and carbon nanostructures

The successful nano-graphitization of amorphous carbon films has previously been achieved via electron beam irradiation by (17) & (18) which report the success of producing graphitic based structures from the low electron beam dose exposures of amorphous carbon. This is achieved following the interaction of the amorphous carbon with the beam from which a graphitic based inter-columnar network is produced. However, it was reported that the irradiation effects of the electron beam vary depending on the nature of the carbon material and structure used (19).

The chemical changes that the thin carbon film material undergoes following electron beam irradiation is explained by (20) as the resulting change of the carbon film from an sp^3 to an sp^2 carbon hybridization. The transitions made because of this graphitisation process are revealed by a range of characterisation techniques employed in their work including X-ray photoelectron spectroscopy (XPS) (20). Alternatively, more specific to the application interests of this project, the electron beam irradiation of carbon nanostructures for PEMFC technology are reported by (21) and is discussed further below.

6.4.2 Platinum Group Material (PGM): Fullerene based ligands and platinum e-beam lithography

An attempt to reduce the loadings of platinum group materials (PGM) in PEMFC electrocatalyst has been previously reported by (21). This is different to the approach used in this work, since the material used entails a platinum material bound to a fullerene molecule (21), see figure 4. Two kinds of ligands were used, both involved a fullerene molecule linked to a pyrrolidine and a platinum metal centre with a co-ordinating bipyridine ligand as displayed in figure 4. The assembled structures underwent treatment with an electron beam inside a scanning transmission microscope (SEM), resulting in the change to the compound with the C_{60} decomposing and the formation of glassy carbon impregnated with single platinum and also ruthenium atoms (21).

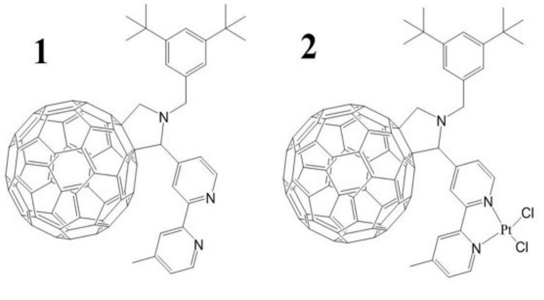

Figure 4- *4-methyl,4'-(2-(N(3,5-di-tert-butylphenlymethyl))fulleropyrrolidineo)-bipyridine, 2 - 4-methyl,4'-(2-(N- (3,5-di-tert-butylphenylmethyl)) fulleropyrrolidineo)-bipyridine platinum chloride copied from Courtney* (21).

These findings reflect the success of using e-beam treatment to achieve chemical conversion of the amorphous carbon based material in both the presence and absence of platinum metal. In the next section, we move towards reviewing literature reportings made on how the DNA material responds to e-beam irradiation.

6.4.3 Electron beam exposure of DNA complex films as a resist material

The exposure of DNA to an electron beam was previously studied by Jones et al. (22) & (23), focusing on the electron beam treatment of DNA-hexadecyltrimethylammonium chloride (DNA-CTMA) thin film complexes. In their initial study (22) they showed that upon exposure the e-beam can lead to either the combination or the dissociation of the DNA-CTMA complex. This entails the breaking of the double stranded (ds)-DNA into a single stranded (ss)-DNA or smaller segments, breaking off the alkyl chains on the DNA, and the breaking of the ionic bond between the DNA and surfactant or alternatively the electrons can directly charge the DNA: CTMA molecule. This led to changes in the hydrophobic character of the material (22).

The initial study shows the feasibility of using electron beam energies for achieving nanoscale patterning of an inorganic complex through using DNA and CTMA (hexadecyltrimethylammonium chloride) complexes. The CTMA is cationic which resembles similar properties to the cisplatin (cisPt) complex that will be employed in this work. Upon interaction with the CTMA metal complex, the DNA molecule becomes insoluble in water however has a high solubility in organic solvents (22). Their findings imply that different types of resists can be obtained depending on the development solutions employed (see figure 2). In their work they achieved electron beam patterning of the DNA: CTMA thin films using a direct write electron beam lithography system. Prior to this, they had soft baked the thin films of the DNA:CTMA at 100 °C for 60 seconds (22).

In their follow up work, they show that the DNA has dual mode resist characteristics which was evident from the changes in the solubility of the exposed DNA with beam dosage via spectrophotometric methods like UV absorption and circular dichroism (23). However, several issues can occur during the e-beam writing of the DNA-CTMA complex including: breaking of the bond between the DNA and CTMA due to the high energy of electrons which can disassociate the complex , denaturing of the DNA i.e. breaking of the double helix structure due to the high energy of electrons and lastly , charging of the DNA-complex which can change its hydrophobic nature and consequently change its solubility properties (22).

These points could be proposed as potential issues upon electron beam irradiation of the DNA-cisPt material. However, the unique ability of DNA films to act as both a positive and negative resist supports its application for the fabrication of DNA-based devices (23).

Herein, we report the processing of DNA-cisPt electrocatalytic material with electron beam irradiation and observe the resulting effects through comparing and contrasting the electrochemical response for the HER in acidic media before and following treatment. Through the implementation of e-beam irradiation it is hoped that the DNA-cisPt thin films become more suited for PEMFC applications, since we expect to see improved electrical and conductive properties of the DNA scaffold.

6.5 Materials and Experiments

6.5.1 Material Synthesis

Deoxyribonucleic Acid (DNA), sodium salt from salmon testes, cisplatin (99.99 % purity (based on trace metal analysis)) were purchased from Sigma Aldrich. DNA-cisPt adducts were synthesized by dissolving the salmon milt DNA (sm-DNA) in Milli-Q water (resistivity ≥ 18.2 MΩ.cm) and sonicating to prepare a stock solution. Cisplatin in aqueous form was mixed with the sm-DNA and incubated at 37 °C overnight for 10 hours. Confirmation of the adduct formation was achieved using spectrophotometric techniques using Shimadzu UV-1800 spectrophotometer, Jasco J-810 spectropolarimeter and Cary 5000 UV-Vis-NIR Spectrophotometer by Klaudia Englert, School of Chemistry ,University of Birmingham (24).

The ultimate goal of this project is to synthesise a pre-cursor catalyst material with optimum electrocatalytic activity at the lowest platinum (i.e. cisplatin) loading possible. The range of loadings prepared and tested in this work are displayed in Table 1.

***Table 1**- Ratio and concentrations of the DNA-cisPt samples synthesized and characterized.*

Ratio of DNA to cisPt	***Concentration of cisPt /µM***	***Concentration of sm-DNA /mM***
1:0	0	1
1:10^{-4}	0.1	1
1: 10^{-3}	1	1
1: 10^{-2}	10	1
1: 0.1	100	1
1:1	1000	1
cisPt	1000	0

[3]

6.5.2 Electrochemical Testing Experimental Method

6.5.2.1 Film formation on a glassy carbon (GC) macroelectrode

A glassy carbon (GC) macroelectrode was polished on microcloth pads with decreasing size alumina slurries (1.0, 0.3, 0.05 µm, Buehler Inc., IL, USA), followed by rinsing with de-ionised water (DIW) and drying under a gentle flow of nitrogen. Once dry, the electrodes were modified by drop casting an aliquot of the prepared DNA-cisPt sample (42 µL onto a 5 mm GC electrode) and drying under a lamp.

6.5.2.2 Electrochemical testing

The samples prepared (see Table 1) were electrochemically tested using a 3 electrode cell, involving a glassy carbon electrode (GC, 5 mm, BASi) as the working, a saturated calomel (SCE, BASi) reference and a bright platinum mesh counter electrode. The cell was controlled by an Autolab 128N potentiostat running Nova 2.1 software (Metrohm-Autolab BV, Netherlands). All potentials are reported against a SCE. All chemicals involved were used in their analytical grade and used without any purification. Perchloric acid (70 %, 99.99 % trace metals) (1 mM, pH 3) and sodium perchlorate (≥ 98 %) as the supporting electrolyte (0.1 M) supplied by Sigma Aldrich. All electrolytes were made up with deionised water (resistivity ≥ 18.2 MΩ.cm) (MilliQ, Millipore) and thoroughly degassed with dry nitrogen (oxygen-free, BOC Gases plc) prior to experimentation.

6.5.2.3 Electron Microscopy

The surface morphology of the material was attained using High Angle Annular Dark Field Scanning Transmission Electron Microscopy (HAADF-STEM) operated in both dark field and bright field imaging using a JEOL2100F instrument. The samples were prepared for imaging by casting 3 µL of the sample onto a 300 Cu mesh holey carbon TEM grid and drying under a lamp. The STEM was operated in Z-contrast mode using a HAADF detector at 200 kV acceleration voltage.

6.5.2.4 Surface chemical properties

XPS characterization was conducted at Harwell XPS, (UK) facilities to obtain the binding energies (BE) and survey spectra of the samples synthesized, using α-Kl as the X-ray source (characteristic energy of 1486.68 eV). The BE is reflective of the oxidation states of the elements in the DNA-cisPt adducts including Pt, Cl, C, P, N and O. The surface chemical properties of the 1:10^{-3} DNA-cisPt loading and the 1000 µM DNA following e-beam irradiation of the material were explored to assess the elemental

---

[3] All material synthesis was by Klaudia Englert, School of Chemistry, and University of Birmingham.

composition and investigate the graphitic content of the processed material i.e. sp^2 and sp^3 carbon content.

6.5.3 Flood Electron Beam irradiation

An aliquot of the desired DNA: cisPt sample was drop cast onto a GC electrode stub and dried under a lamp. The prepared electrode was loaded into the chamber of the converted scanning transmission microscope (SEM) tool operated under vacuum conditions, (see schematic diagram, figure 7 in chapter 3). The material was exposed to an electron beam at an acceleration voltage of 5 keV for a duration of 24 minutes i.e. the optimum reaction time found (discussed in detail in the results and discussion section). The SEM like tool was set such that the electron beam elevation consisted of the following coordinates (60, 25,102) for a (x, y, z) system. At these points, the e-beam is ideally centred, to achieve uniform distribution. A tungsten filament (Agar scientific, UK) consisting of 0.5 mm diameter Wehnelt aperture is used to generate the electron beam in the gun.

6.6 Results and Discussion

6.6.1 Optimum reaction time of electron beam irradiation

The initial step in the process of the e-beam treatment of the DNA-cisPt material was finding out the optimum time for the exposure of the material with the electron beam at an electron energy of 5 keV. As a starting point, an intermediate loading of the platinum metal i.e. $1:10^{-3}$ DNA-cisPt was selected to explore the effects of the irradiation duration (time) on the electrochemical response of the material for the HER (1 mM $HClO_4$, 0.1 M $NaClO_4$) at 50 mV s^{-1}, as illustrated by figure 5.

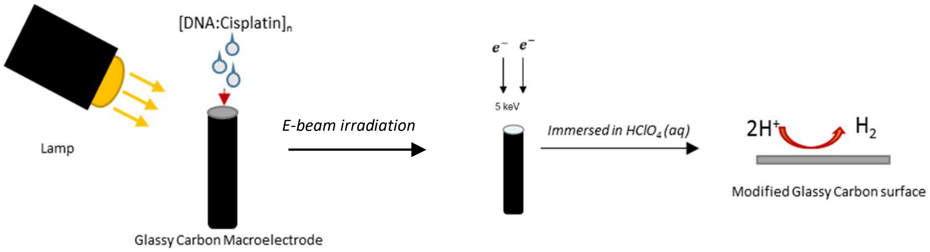

Figure 5- *Overview of the experimental methods involved in the preparation and electrochemical testing of the electron beam irradiated DNA-cisPt material.*

The voltammetry response for the HER (pH 3) is shown in figure 6(A) and the resulting changes in the peak potential (E_p) and the peak current density (J_P) as a function of the duration of the e-beam irradiation is displayed in figures 6(B) &(C).

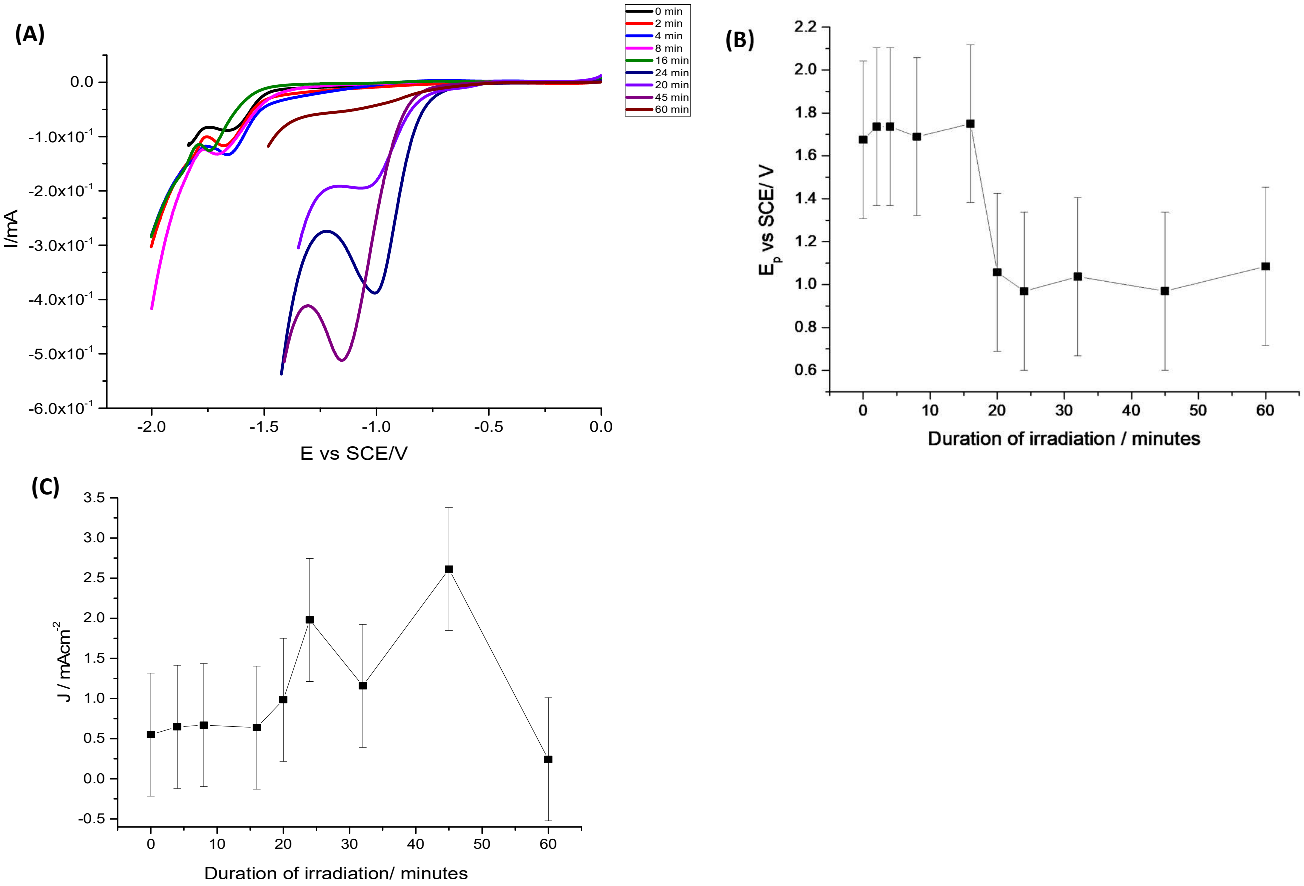

Figure 6- *(A) Voltammetry response for HER (1 mM $HClO_4$, 0.1 M $NaClO_4$, 50 mV s^{-1}), 42 µL of 1 to 10^{-3} DNA-cisPt drop-cast on a 5 mm GC at different exposure times of a 5 keV electron beam (B) Variation of peak potential (E_p) with duration of e-beam irradiation (C) Variation of peak current density (J_p) with duration of e-beam irradiation. Error bars are based on a standard deviation error.*

It is evident that the shifts in the peak potential (E_P) become less significant beyond 24 minutes of exposure. However in terms of the electrocatalytic activity i.e. peak current density (J_P) , two optimum peaks are observed, one at 24 minutes and a second at 45 minutes corresponding to a J_p of 2 and 2.5 mAcm^{-2} respectively. The measured E_P at 32 minutes of exposure does not correlate with the trend of the other data points, so is a likely outlier and will be omitted from the analysis after this point.

The electrochemical testing was repeated and the response with the number of cycle was compared and contrasted for the different exposure times employed. The optimum performance defined in terms of the electrochemical peak potential and the peak current density was found to display similar findings to those shown in figure 6 i.e. interchangeable between 24 minutes displaying optimum behaviour and 45 minutes, see appendix 3, figure A3.1 for the experimental data.

The influence of e-beam irradiation on the different loadings of DNA-cisPt employed in this work (see Table 1) is explored in a similar method outlined above with the 1:10^{-3} DNA-cisPt sample. This will enable us to explore whether the cisPt loading i.e. platinum metal content influences the graphitization process as a function of the duration time of electron beam exposure. For simplicity, the electrocatalytic performance will be defined by the measured peak potential (E_p) value. The results are shown in figure 7.

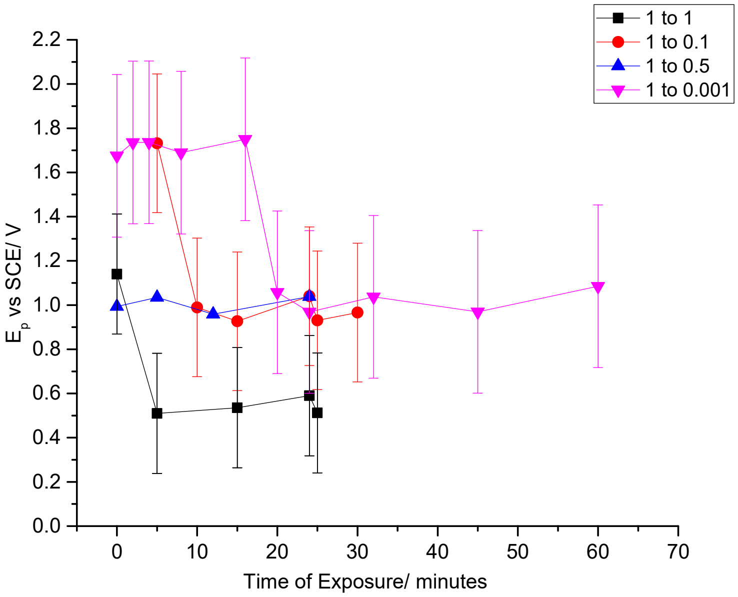

Figure 7- *Variation of the peak potential (E_p) measured for the HER (1 mM $HClO_4$, 0.1 M $NaClO_4$) at 50 mV s^{-1}. 42 µL of the desired DNA-cisPt sample drop-cast onto a 5 mm GC and tested at different exposure times of a 5 keV electron beam. Error bars are based on a standard deviation error. 1 to 1 implies a ratio of 1 to 1 DNA-cisPt in the legend.*

Figure 7 shows that with increased platinum metal content in the material, a lower e-beam exposure time is required to achieve an improved response for the electrocatalysis of the HER. This observation is based on the more rapid establishment of a steady state i.e. quicker rate of levelling off of the E_p , for example after 5 minutes at the 1:1 DNA-cisPt loading compared to after 24 minutes for the 1:10^{-3} DNA-cisPt loading. It can be proposed that at higher metal loadings an increased catalytic contribution to the graphitisation process is provided by the metal. This is supported by previous observations made in the literature where in the presence of metal atoms, specifically nickel, a favourable catalytic contribution to the carbonisation process of the amorphous carbon under an electron beam was observed (7).

To further study, compare and contrast the influence of e-beam irradiation for the range of DNA-cisPt ratios employed in this work, the electrochemical response for the HER (pH 3) was tested in the same methods described above. Figure 8 displays the voltammetry response for the HER for each electron beam treated material.

The presence of DNA results in improved electrochemical behaviour upon e-beam irradiation of the material compared to in its absence. This is down to their being a preference for a high carbon content for achieving more effective graphitization results. These observations are explained below where we see less of a significant effect of the e-beam irradiation on the bulk cisPt, figure (8A), compared to the improvements attained in electrocatalysis of the HER presented in figures 8(B-G).

At a 1:1 DNA-cisPt loading, following e-beam irradiation, the voltammetry is shifted towards the response of that of bulk cisPt in terms of the peak potential (E_p) i.e. 0.45 V vs SCE. It could be proposed that this occurs since at this loading we have much higher Pt loadings that can then form large nanoclusters to display bulk metal behaviour. Literature findings support this observation, since it was noted that electron beam irradiation of metal nanoparticles can result in dissipation of the metal nanoparticles, leading to structural changes, or alternatively at low electron beam intensities, diffusion is improved leading to coalescence of the metal nanoparticles (25). This is similar to the observations made by (26), whereby following e-beam irradiation, the platinum metal nanoparticles

in the exposed area had migrated and consequently came into contact with one another, resulting in agglomerated nanostructures (26).
Furthermore, in the work of (27) involving focused-electron-beam-induced deposition (FEBID) of platinum metal onto the surface of carbon nanotubes (CNTs), they reported that upon gradual removal of amorphous carbon they observed increased platinum nanocluster growth resulting in coalescence. The dissociation of the amorphous carbon is the first step in the electron irradiation process, which is followed by the second phase that entails the graphitization process. This involves increased electron-carbon interactions enabling thin graphitic layers to form at the surface (27).

Thus we can expect that in the absence of amorphous carbon, i.e. bulk cisPt, or higher metal loadings to amorphous carbon i.e. 1:1 DNA-cisPt, the electron beam irradiation process will result in increased coalescence of the platinum nanoclusters, with possible decomposition of the organoplatinum molecule. On the other hand, as the ratio of the DNA compared to the platinum nanoclusters is increased, we will reduce this clustering, since there will be more carbon decomposition taking place followed by graphitisation as opposed to a bulk cisPt material where the e-beam is more likely to directly interact with the platinum metal leading to its agglomeration.

From Table 2, it becomes clear that following e-beam irradiation, the onset potential (σ) of the 1 to 1 DNA-cisPt is also shifted towards that of bulk cisPt. However, in the absence of cisPt, i.e. virgin DNA, the voltammetry response is not significantly improved to result in the observance of an electrochemical peak with a measurable peak current density output and a sigmoidal response still holds, see figure 8(C). This therefore further supports the proposals made for the experimental findings in figure 7 i.e. that the presence of the platinum metal even at the lowest loading ratio ($1:10^{-4}$) is contributing favourably to the graphitization process.

On the other hand, at the lower loadings employed, a peak potential (E_p) of around -1 V vs SCE is measured given that at these low metal loadings, only small nanoclusters can be formed, since the low metal loading limits the extent of coalescence. This hypothesis can be investigated through STEM imaging characterisation to assess the changes on the catalyst surface. It is evident that following e-beam irradiation, increased aggregation of the platinum nanoclusters is observed compared to the untreated counterpart. This is discussed and analysed in more detail in ‘surface morphology following e-beam irradiation’ section of this chapter.

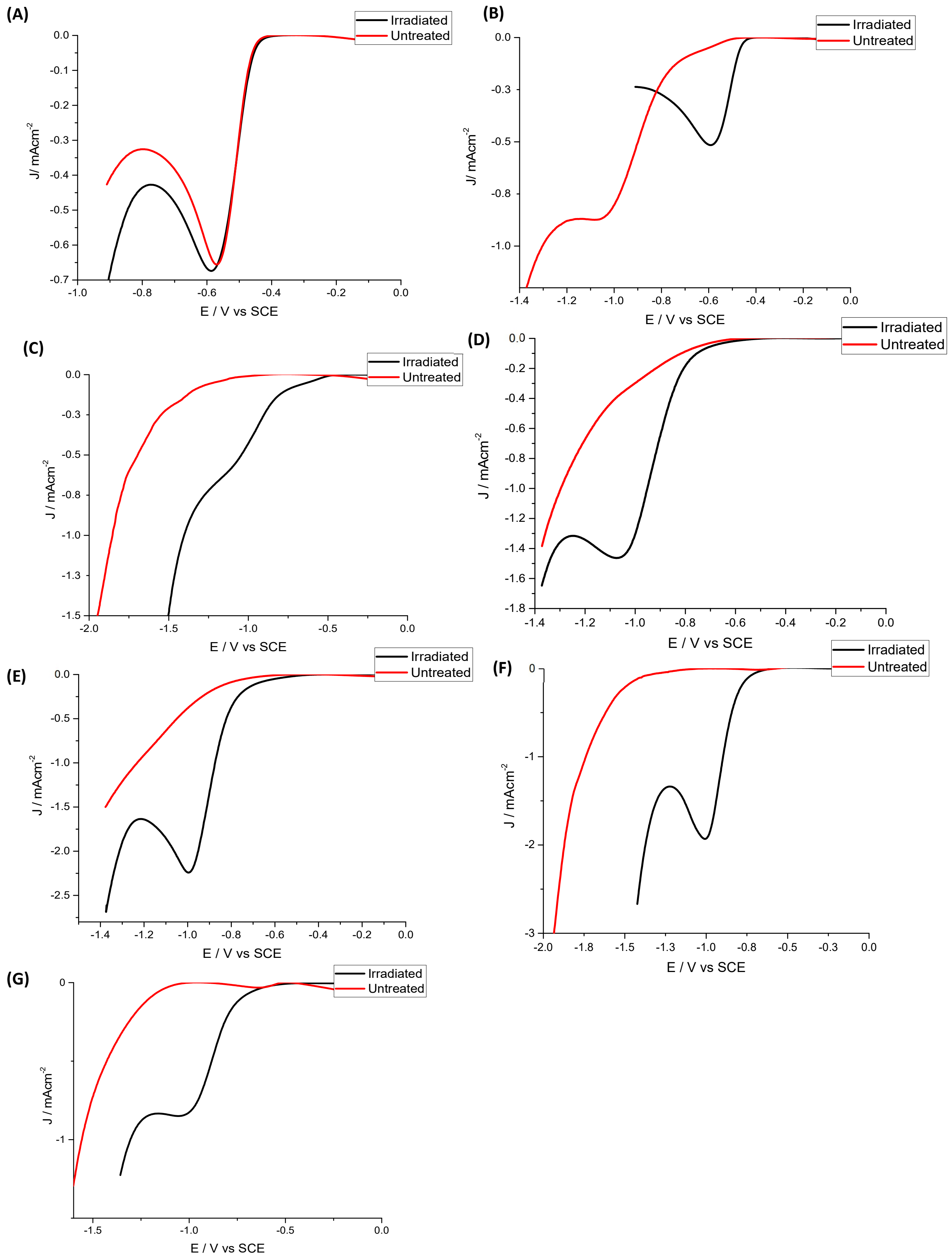

Figure 8- *Voltammetry response (1st cycle) for the HER pH 3 (1 mM $HClO_4$, 0.1 M $NaClO_4$ 50 mV s^{-1}) before and after e-beam irradiation of the material (5 Kev, 24 minutes) (A) 1000 µM bulk cisPt (B) 1 to 1 DNA- cisPt (C) 1000 µM virgin DNA (D) 1 to 10^{-1} DNA- cisPt (E) 1 to 10^{-2} DNA- cisPt (F) 1 to 10^{-3} DNA- cisPt (G) 1 to 10^{-4} DNA- cisPt.*

Table 2*- Comparison between the peak potential (E_p), peak current density (J_p) and the onset potential (σ) attained at the modified GC electrode surfaces with DNA-cisplatin material before and after electron beam irradiation at 5 keV, 24 minutes.*

Ratio of DNA to cisPt modified on GC	Peak Potential (E_p) / V vs SCE ± 0.01 V	Peak Current density* (J_p) /mA cm^{-2} ± 0.01	Onset Potential (σ) / V vs SCE @ 0.1 mA cm^{-2} before e-beam irradiation	Onset Potential (σ) / V vs SCE @ 0.1 mA cm^{-2} following e-beam irradiation (Graphitisation)
Bare GC	-1.45	-0.67	-1.29	-
1 to 1	-0.59	-0.51	-0.70	-0.48
1 to 10^{-1}	-1.07	-1.46	-0.82	-0.75
1 to 10^{-2}	-1.00	-2.24	-0.82	-0.68
1 to 10^{-3}	-1.00	-1.94	-1.39	-0.73
1 to 10^{-4}	-1.02	-0.83	-1.34	-0.73
0 to 1	-0.59	-0.67	-0.47	-0.47
1 to 0	-1.16	-0.58	-1.34	-0.77

From Table 2 it is clear that the onset potential (σ), defined at a current density output of 0.1 mA cm^{-2}, is significantly reduced following e-beam irradiation for all loadings tested, with the exception of bulk cisPt which is unchanged from -0.47 V vs SCE.

For the low metal loadings of the DNA-cisPt material, the optimum performance is attained at the 1 to 10^{-2} DNA-cisPt loading, whereby the lowest onset potential ($\sigma_{0.1\ \mathrm{mAcm}^{-2}}$) is measured (-0.68 V vs SCE) and the highest peak current density output of -2.24 mA cm^{-2} is produced.

However in general, the electrochemical activity i.e. the peak current density output (J_P) is found to be much higher for the lower platinum loadings of the e-beam treated material than the higher metal containing adducts i.e. 1 to 1 DNA-cisPt and bulk cisPt. This could be resulting from both the increased surface area and availability of the platinum active sites since the material has an increased inter-particle distance with reduced cisPt loadings.

This proposal is in line with the literature findings where for example for the ORR (a more thoroughly studied electrochemical fuel cell reaction) it was noted that that for the carbon-supported Pt nanoparticles, full catalytic activity was achieved when the inter-particle distance was higher than 20 nm (28). As the loading is reduced the inter-particle distance is increased between the platinum nanoclusters and single localised platinum atoms are more likely to be observed with the preferred edge to face ratio for the HER (see discussion in chapter 5). On the other hand, increasing the metal loading can result in a reduced diffusion flux of the reactants to the internal parts of the catalytic surface (29). This experimental observation is also noted for the material synthesised via the pseudo pyrolysis of the DNA-cisPt, presented in the next chapter (chapter 7) of this thesis.

On the other hand, insignificant changes are measured in terms of the peak potential (E_P vs SCE) between the low loadings of the DNA-cisPt (i.e. material loadings ≤ 1:1 DNA-cisPt), where the E_p ranged from -1.00 to -1.07 ± 0.01 V vs SCE. However, for all of the DNA-cisPt containing material, the e-beam irradiation improves the electrochemical response of the HER.

Alternatively, the improved electrocatalysis of the e-beam irradiated material may be resulting from the introduction of surface defects which can contribute favourably to the catalysis such oxygen vacancies. For example, similar to the concept of e-beam irradiation, literature reportings on microwave irradiation of lithium-manganese rich oxides (LMR-NMC) material has been shown to result in the formation of more oxygen vacancies (defects) resulting in a reduced particle size of the metal (Mn), an enhanced electronic conductivity and improved charge transfer at the electrode or particle surface (30). This is because the oxygen vacancy can improve the physicochemical properties of the material (31) and act as active sites thus improving the electrocatalysis. To explore whether surface defects are responsible for the improved electrochemical response of the electrocatalysis material, XPS characterisation and Raman spectroscopy can be conducted to check the extent of defects and specifically for the O 1s spectra as part of future work recommendations.

6.6.2 Technical challenges and issues

There are limitations associated with the experimental data attained, resulting from technical issues with the e-beam tool. Specifically, this was concerned with the lack of monitoring and control over the electron beam current being produced during the exposures. This means a different current dose could have been delivered during the irradiation of the material as there was no means of measuring or controlling this parameter. This was because of the nature of the tool, which was an old converted SEM instrument, so a connecting port for an ammeter was not available, making the current readings impossible. An assumption is therefore proposed to suggest that insignificant variation in the current dosage occurs, to enable comparison to be made between the experimental data collected in this work.

6.6.3 Mechanism of the hydrogen evolution reaction (HER)

6.6.3.1 Tafel Plots at 50 mV s^{-1}

To further compare how the electrocatalytic behaviour is changed following electron beam irradiation of the material, we assess the mechanism of the reaction by considering the resulting changes to the magnitude of the Tafel slope. Initially, Tafel plots were constructed to reveal the reaction mechanism of the HER at each working electrode surface based on the theoretical information provided in the literature (32),(33) and (34), and as already discussed in detail in chapters 2 and 3. See appendix 4, figure A4.2 for the constructed Tafel plots.

From the Tafel plots, the magnitude of the Tafel slope can be found and expressed as a function of cisPt loading in the material as shown in figure 9. This is then compared to the widely accepted and reported theoretical limits implying that the rate determining steps for the Volmer, Heyrovsky and Tafel reactions correspond to a Tafel slope of 120, 40 and 30 mV dec^{-1} respectively. Table 3 presents the corresponding Tafel slope for each material tested.

Table 3*- The changes in the Tafel slope found before and after e-beam irradiation with different DNA-cisplatin loadings.*

Ratio of DNA-cisPt /GC modified surface	***Tafel slope of untreated material / mVdec^{-1}***	***Tafel slope of e-beam irradiated material / mVdec^{-1}***
Bare GC	180	-
DNA (1 mM)	425	331.1
1:10^{-4}	395	107.9
1:10^{-3}	381	114
1:10^{-2}	331	137.3
1:10^{-1}	327	133.7
1:1	68.6	50.4
cisPt (1 mM)	48.1	-
Pt UME	27.3	-

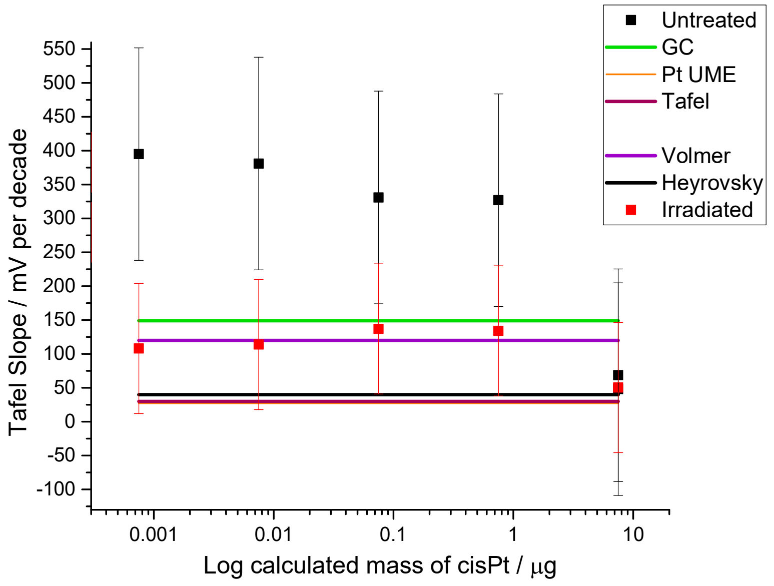

***Figure 9**- The variation in the Tafel slope as a function of the calculated cisPt loading in the material before and after e-beam irradiation (5 keV, 24 minutes) and how it compares against the well reported slopes of the theoretical mechanisms proposed in the literature.*

The most obvious correlation which has also been noted previously in chapter 4, is that with increased platinum metal loadings, there is a reduction in the magnitude of the Tafel slope as we move to the maximum platinum loading in the bulk cisPt. This reflects the change in the mechanism of the apparent rate limiting step for proton reduction i.e. from a Volmer (Eq.1) to a Heyrovsky (Eq.2) mechanism. The more interesting result is the significant reduction in the Tafel slope for the e-beam treated DNA-cisPt material for all loadings of the metal. The results in figure 9 further support the experimental observations previously made to suggest that the electrochemical response of the HER is improved following e-beam treatment, since this is also reflected in the change of mechanism of the HER. This entails the transition from a Volmer reaction to a Volmer-Heyrovsky step, thus moving towards the electrochemical proton (H^+) reduction step.

6.6.4 Surface Morphology following e-beam irradiation

The changes to the platinum and DNA following e-beam irradiation of the material is best characterized using HAADF-STEM imaging. The material was prepared for electron microscopy imaging using the same method described above (see materials and experiments section). Following the preparation of the TEM grid, the drop cast material on the grid surface was loaded into the flood gun tool (onto the converted SEM tool sample holder) to undergo e-beam irradiation at a beam energy of 5 keV for a duration of 24 minutes.

The surface morphology and STEM imaging characterization of the untreated bulk cisPt (1 mM) has been discussed more thoroughly in chapter 4. In this chapter, the focus will be on the STEM imaging characterization of the material following e-beam irradiation and the resulting changes to its surface morphology.

6.6.5 STEM imaging of DNA

The imaging of unprocessed natural DNA material using electron microscopy has long been faced with challenges since this high angle scattering process, i.e. scanning/transmission electron microscopy, is highly dependent on the atomic number (Z) of the element projected under the electron beam by the relationship of $Z^{1.5}$. Therefore, heavier nuclei can be definitively discriminated from light nuclei through this dependence. However the four different types of nucleotide bases of the DNA differ by only a few atoms and all of the differing atoms are light elements thus making the material indistinguishable via electron microscopy imaging (35). Various methods have been employed to improve the contrast of the DNA material under an electron beam in the literature, from negative staining of the DNA (36) to chemical modification of the single stranded DNA with clusters of heavy atoms as shown in figure 10 (35).

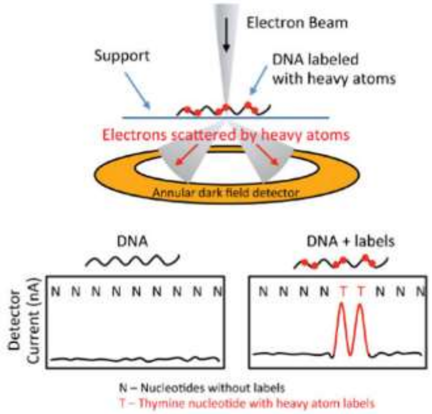

***Figure 10**- Heavy atom labels detected within DNA (A) How the placement of heavy nuclei on DNA can improve the scattering of the projected electron beam (B) Unlabelled DNA bases scatter fewer electrons than the heavy atom labelled bases distinguished by detector current . Reproduced from Bell et al.* (35).

Specifically, in the work of Bell et al.(35), the DNA bases Thymine/Uridine were modified with a single mercury atom, thus enabling improved STEM contrast to be established than in the unmodified DNA, which enabled successful STEM imaging of the DNA to be achieved.

In this work, the projection of the flood electron beam of 5 keV for a duration of 24 minutes can result in various changes to the material, however studying the resulting mechanism of change closely is beyond the scope and research interests of this research work.

Nevertheless, it can be proposed that the e-beam irradiation can result in the cross linking of the DNA chains, in line with the observations reported by Jones et al. (22) , where it was found that it led to the combination (or the dissociation) of the DNA-CTMA complex. This therefore gives rise to a higher Z number, consequently enabling successful STEM imaging of the DNA material, see figures 11 (C) and (E-H), which was not possible before, as shown in the STEM imaging characterisation results in chapter 4.

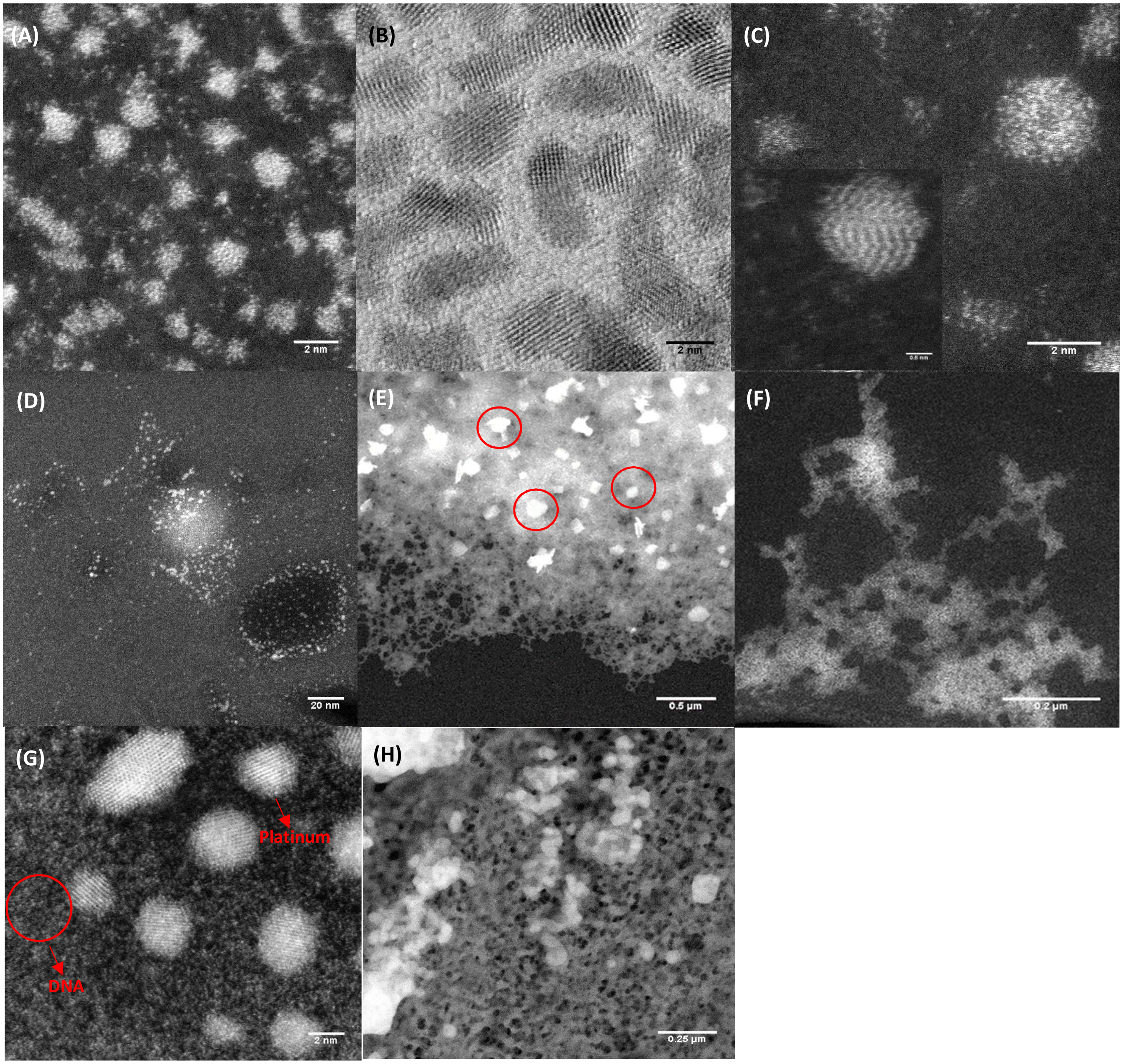

Figure 11- *HAADF STEM imaging of (A,B) 1 mM bulk cisPt (untreated) (C) 1 mM virgin DNA (D-G) 1 to 1 DNA-cisPt (H) 1 to 0.1 DNA-cisPt. Named material in figures 11 (C) & (E-H) have undergone e-beam irradiation at 5 keV , 24 minutes cast on a 3 mm holey carbon TEM grid. Figure 11(D) is untreated 1 to 1 DNA-cisPt material.*

However, it can be observed from the surface morphology of the DNA presented in figure 11(C) compared with that shown in figures 11(D-G) that the presence of the platinum metal atoms along the nucleotide bases of the DNA is improving the contrast of the e-beam processed DNA polymer under the electron microscope. It could be proposed that the platinum metal is contributing to the electron scattering in similar ways to those suggested in figure 10 and reported in the literature (35). This could explain the observance of a higher resolution of the film deposits in the presence of platinum metal i.e. figure 11(F) compared to in its absence (figure 11(C)). Equally, the observations made before to suggest that the platinum metal catalysed the graphitization process of the DNA via the e-beam irradiation could be supported by this drastic difference in the morphology of the material in figure 11(F) compared to 11(C). This hypothesis is supported by the findings reported in the literature by Sokolov et al. (37), whereby it was possible for graphitization of the DNA templates to be achieved, resulting in the formation of nano-graphitic ribbons, although their work used a Chemical Vapour Deposition (CVD) process.

However, there are limitations in drawing up any conclusive remarks and the nanoclusters shown in figure 11(C) cannot be confidently attributed to the DNA matter. This is because it can be suggested that what is being observed could be a mixture of matter from the buffer solution employed in the synthesis of the DNA-cisPt (including salts such as sodium, phosphor and chloride), detailed in the material synthesis procedure by (24). To further explore this, elemental mapping of the surface could be implemented in future work via STEM-EDX to match the surface morphology directly with chemical composition (as achieved in the work of chapter 7 of this thesis). However, this does not invalidate the observations and findings made for this work.

6.6.6 Changes to the surface morphology of the platinum metal following e-beam irradiation

It can be inferred from figures 11(D & E) that for the 1:1 DNA-cisPt loading, the e-beam irradiation results in aggregation of the Pt nanoclusters (circled in red) compared to the more distributed arrangement of the platinum nanoclusters before e-beam treatment (figure 11(D)). This supports the proposals and discussions made before which explained the resulting changes in the electrochemical response attained following e-beam treatment, where the response shifts towards that of bulk cisPt following e-beam irradiation of 1:1 DNA-cisPt.

In addition, by comparing figures 11(E) and 11(H) it becomes evident that the higher platinum content in the material (1:1 DNA-cisPt) gives rise to platinum metal of an increased nanocluster size (larger bright spots highlighted in figure 11(E) as opposed to the absence of these nanoclusters on the surface of a material containing a lower platinum metal content i.e. 1:0.1 DNA-cisPt, see figure 11(H).

This is further explained from the changes to the surface morphology seen in figure 12, where it can be noted from figures 12(A-C) that as the cisPt loading is reduced i.e. platinum metal loading, the distribution of the platinum is improved with less aggregation being observed on the DNA scaffold. This could be explained by there being an increased likelihood of the clustering of the platinum metal with loading since the inter-particle distance is reduced on the DNA scaffold. This is in-line with the observations previously made in chapter 4.

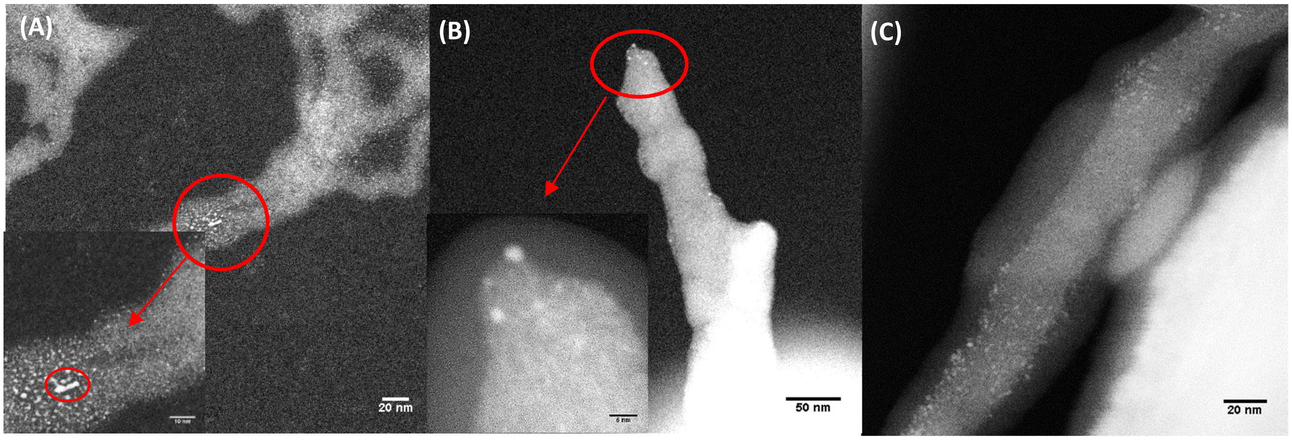

***Figure 12** – HAADF STEM imaging of e-beam irradiated material (5 keV, 24 minutes) (A) 1 to 1 DNA-cisPt (B) 1 to 0.1 DNA-cisPt (C) 1 to 10^{-3} DNA-cisPt.*

In order to gain an insight into the chemical changes resulting from the electron beam irradiation of the DNA-cisPt material, XPS testing is carried out for the 1:10^{-3} DNA-cisPt and 1 mM virgin DNA films to explore whether the presence of platinum metal has an effect on the chemical composition of the material. The XPS characterization of the untreated DNA-cisPt material has been discussed in chapter 4, where the samples in aqueous form were tested and analysed. However, in this work, the sample preparation differs and entails drop casting 42 µL of the material onto a polished GC stub (5 mm) and consequently drying under a lamp. For the electron beam exposure of the material, the prepared sample of the dry film on the GC substrate is consequently loaded into the chamber of the electron flood gun tool and a 5 keV electron beam was projected onto the sample for a duration of 4 and 24 minutes, resulting in the preparation of four samples.

The samples were consequently sent to Harwell XPS facilities (UK) where the XPS testing took place, with the aim of discovering whether or not following e-beam irradiation, the DNA was converted to chemically acquire graphitic like characteristics. In addition, the influence of the duration of the e-beam irradiation on the graphitic content was also tested for. The results (provided by the Harwell XPS) are displayed below.

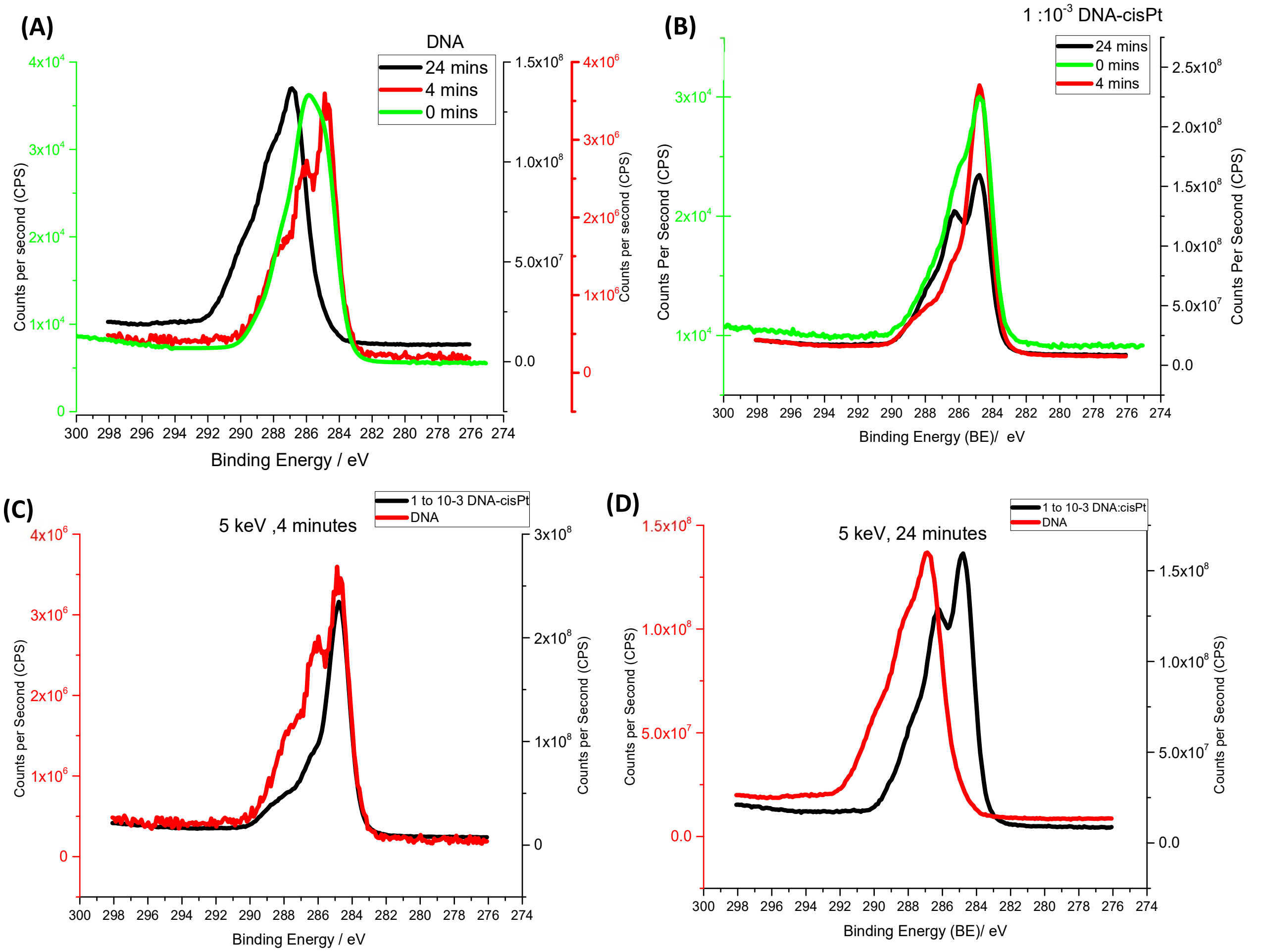

***Figure 13**- High-resolution XPS spectra of the C 1s regions for electron beam irradiated films (5 keV) of: (A) DNA (B) 1 to 10^{-3} DNA: cisPt for a duration of 4 and 24 minutes. (C,D) How the duration of the e-beam irradiation affects the spectra for the C 1s in the presence and absence of platinum metal.*

It has been reported that the material can be described as being graphitic if it consists of regions of sp^2 and sp^3 character (37). Sokolov et al. (37) states that that the area under the curve of the peak at 284.5 eV can be assigned to the sp^2 contribution /ratio in the material, while the area under the peak centred between 285.0 and 285.5 eV is assigned to the sp^3 character.

From figure 13(B), the XPS results show the appearance of two peaks for the 1 to 10^{-3} DNA-cisPt after 24 minutes of e-beam irradiation at 287 eV and 284.5 eV, compared to the single peak observed at 286 eV prior to e-beam treatment of the material. This implies that in the presence of platinum metal, the material acquires some sp^2 character following e-beam treatment. Surprisingly, after 4 minutes of irradiation, a single shift of a higher count per second (CPS) at around 284.5 eV is observed suggesting the presence of a higher ratio of sp^2 character compared to after 24 minutes of e-beam exposures. This is further supported by the measured graphitic content values of the material i.e. 1.15 % at 4 minutes compared with 0.96 % at 24 minutes (see Table 4).

The e-beam treatment of the DNA material after 4 minutes results in the occurrence of two peaks at 287 eV and 284.5 eV (see figure 13 (A)) compared to the untreated DNA film where a broad C 1s signal is observed around 286 eV. The results presented for 24 minutes deviate from the correlations made of a peak signal at a higher eV (288 eV). It has been reported by (37) that a peak between 287.6–

288.1 eV in DNA material can be assigned to oxidized carbon atoms (C–O or C=O). However, charging issues were faced during the XPS testing thus the results for the 24 minutes cannot be used with confidence to make conclusive remarks during the analysis.

Table 4- *XPS Characterization of the material following e-beam irradiation (5 keV) and percentage composition (%) of the graphitic carbon content.*

Sample	Duration time of e-beam irradiation / minutes	Measured percentage composition of the graphitic content / %
1 to 10^{-3} DNA-cisPt	4	1.15
	24	0.96
DNA (1 mM)	4	1.64
	24	0.34

The results in Table 4, imply that a very low content of graphitic carbon is detected in both materials tested. However, from figures 13 (C &D) for the XPS of the C 1*s* spectra, the presence of the peak at 284.5 eV (sp^2 character) is more noticeable for the 1 to 10^{-3} DNA-cisPt than in the absence of the platinum. This is supported by the findings reported in the literature (37), where they reported that a significant amount of sp^2 carbon is formed only for metalized DNA.

However, given the charging issues faced during the XPS testing, the results presented cannot solely be used to conclude with confidence that the e-beam irradiation of the DNA material is resulting in its graphitisation. Future work would be required, involving repeated testing of the material via XPS and investigating how the sampling methods can be modified to achieve improved and stronger signals.

6.7 Conclusions

In this chapter, we demonstrated the feasibility of electron beam (e-beam) irradiation of the DNA-cisPt/ DNA films as a processing technique to improve the catalytic properties of the nanomaterial, making its use more suited for electrochemical applications. This was evident from the significant improvements noted in the electrochemical performance of the material for the electrocatalysis of the HER (pH 3) following its exposure to an e-beam as opposed to the untreated material. This proves the hypothesis made to suggest that the conductive properties of the DNA can be improved through this processing method to overcome the highly resistive nature of the polynucleotide.

Furthermore, the e-beam irradiation of the material via a flood source enables successful STEM imaging of natural unmodified DNA. This is not commonly reported in the literature as a DNA sample preparation method for electron microscopy imaging. It is noted from the STEM imaging characterization that the presence of the platinum metal (even at the lowest loadings employed in this study i.e. 1:10^{-4} DNA-cisPt (equivalent to 0.75 ng) contributes favourably towards both the electrocatalysis of the HER following e-beam irradiation of the material and the resolution of the STEM imaging, when compared to the material absent of metal i.e. virgin DNA.

In addition, in terms of the influence of the platinum metal loading in the e-beam treated DNA-cisPt material on the electrocatalytic performance , the experimental findings have shown that interestingly, much higher catalytic activities can be measured at lower platinum loadings (minimum of 0.75 ng) compared to much higher loadings i.e. bulk cisPt (7.5 µg). This was reflected in the measured peak current density values (J_p, mA cm^{-2}), which were calculated using the geometric surface area of the working electrode. This finding was justified by comparison to reporting's made in the literature, which noted improvements in the diffusion profile of the catalyst film when the inter-particle distance reached a certain point. As the metal loading increased in the DNA-cisPt film, there was increased clustering of the platinum metal, which was shown through evident changes in the surface morphology of the material (appearance and abundance of larger bright spots) and also in the electrochemical response, whereby the peak potential (E_p) shifted towards that of a bulk platinum metal response i.e. bulk cisPt.

Suggestions for future work include focusing on detailed characterization of the chemical properties of the resulting material following e-beam irradiation of the DNA in the presence and absence of platinum metal. Although an attempt has been made to use XPS testing to explore the resulting changes to the material following the e-beam irradiation process, charging issues faced during the testing prevent conclusive remarks from being drawn with confidence on whether the graphitization of the DNA material was successful through e-beam irradiation. Thus, these tests need to be improved by exploring how the XPS sampling methods employed can be modified to achieve improved signals in future work. In addition, comparisons between the performances of the e-beam treated DNA-cisPt material at all the platinum loadings tested should be made with a commercial Pt/C catalyst for the HER, under the same experimental conditions to see if the DNA-cisPt material is competitive with this well-known rivalry catalyst.

References

1. Kumatani A, Miura C, Kuramochi H, Ohto T, Wakisaka M, Nagata Y, et al. Chemical Dopants on Edge of Holey Graphene Accelerate Electrochemical Hydrogen Evolution Reaction. Adv Sci. 2019;6(10).
2. Kumatani A, Miura C, Kuramochi H, Ohto T, Wakisaka M, Nagata Y, et al. Chemical Dopants on Edge of Holey Graphene Accelerate Electrochemical Hydrogen Evolution Reaction. Adv Sci. 2019;6(10).
3. Behan JA, Mates-Torres E, Stamatin SN, Domínguez C, Iannaci A, Fleischer K, et al. Untangling Cooperative Effects of Pyridinic and Graphitic Nitrogen Sites at Metal-Free N-Doped Carbon Electrocatalysts for the Oxygen Reduction Reaction. Small. 2019;1902081:1–10.
4. Pierson HO. Handbook of Carbon, Graphite, Diamond and Fullerenes - Properties, Processing and Applications. William Andrew Publishing/Noyes;
5. Höflich K, Jurczyk J, Zhang Y, Puydinger dos Santos M V., Götz M, Guerra-Nuñez C, et al. Direct Electron Beam Writing of Silver-Based Nanostructures. ACS Appl Mater Interfaces. 2017;9(28):24071–7.
6. Tsuchiya T, Jomori T, Ura Y, Sugano K, Tabata O. Fabrication of free-standing fullerene nanowire using direct electron beam writing and sacrificial dry etching. Proc IEEE Int Conf Micro Electro Mech Syst. 2008;689–92.
7. Aikawa S, Kizu T, Nishikawa E. Catalytic graphitization of an amorphous carbon film under focused electron beam irradiation due to the presence of sputtered nickel metal particles. Carbon N Y. 2010;48(10):2997–9.
8. Du K, Park M, Ding J, Hu H, Zhang Z. Sub-10 nm patterning with DNA nanostructures: A short perspective. Nanotechnology. 2017;28(44).
9. Diagne CT, Brun C, Gasparutto D, Baillin X, Tiron R. DNA Origami Mask for Sub-Ten-Nanometer Lithography. ACS Nano. 2016;10(7):6458–63.
10. Zhou F, Michael B, Surwade SP, Ricardo KB, Zhao S, Liu H. Mechanistic study of the nanoscale negative-tone pattern transfer from DNA nanostructures to SiO2. Chem Mater. 2015;27(5):1692–7.
11. Kang SH, Hwang WS, Lin Z, Kwon SH, Hong SW. A robust highly aligned DNA nanowire array-enabled lithography for graphene nanoribbon transistors. Nano Lett. 2015;15(12):7913–20.
12. Heck C, Prinz J, Dathe A, Merk V, Stranik O, Fritzsche W, et al. Gold Nanolenses Self-Assembled by DNA Origami. ACS Photonics. 2017;4(5):1123–30.
13. Gállego I, Manning B, Prades JD, Mir M, Samitier J, Eritja R. DNA-Origami-Aided Lithography for Sub-10 Nanometer Pattern Printing. Proceedings. 2017;1(4):325.
14. Szymonik M, Davies AG, Walti C. DNA self-assembly-driven positioning of molecular components on nanopatterned surfaces. Nanotechnology. 2016;27(39):1–7.
15. Jin Z, Sun W, Ke Y, Shih CJ, Paulus GLC, Hua Wang Q, et al. Metallized DNA nanolithography for encoding and transferring spatial information for graphene patterning. Nat Commun. 2013;4:1663–9.
16. Zhou F, Sun W, Ricardo KB, Wang D, Shen J, Yin P, et al. Programmably Shaped Carbon Nanostructure from Shape-Conserving Carbonization of DNA. ACS Nano. 2016;10(3):3069–77.
17. Iwamura E, Aizawa T. Nano-graphitization in amorphous carbon films via electron beam

irradiation and the iron implantation. Mater Res Soc Symp Proc. 2007;960(January):105–11.

18. Iwamura E. Evolution of graphitic structures in amorphous carbon thin films.Internal report: Presto, Japan Science and Technology Agency and University of Tokoyo. n/a.

19. Banhart F. Irradiation effects in carbon nanostructures Florian. Rep Prog Phys. 1999;62:1181–221.

20. Pacala O, Ciuca I, Logofatu C, Polosan S. Low energy electron irradiation of carbon thin films. Mater Res Express. 2018;5(5).

21. Courtney JM. Alternative chemical methods for the catalytic processes within hydrogen fuelled proton exchange membrane fuel cells by. 2016;(June).

22. Jones RA, Li WX, Spaeth H, Steckl AJ. Direct write electron beam patterning of DNA complex thin films. J Vac Sci Technol. 2008;26(6):2567–71.

23. Li W, Jones R, Spaeth H, Steckl AJ. Dose effects in electron beam irradiation of DNA-complex thin films Dose effects in electron beam irradiation of DNA-complex thin films. 2010;(August):1–4.

24. Englert K. DNA Origami Catalysts. [PhD thesis]. Birmingham (UK): University of Birmingham; 2019.

25. Tanaka M, Takeguchi M, Furuya K. Behavior of metal nanoparticles in the electron beam. Micron. 2002;33(5):441–6.

26. Xu B, Tanaka SI. Formation and bonding of platinum nanoparticles controlled by high energy beam irradiation. Scr Mater. 2001;44(8–9):2051–4.

27. Ke X, Bittencourt C, Bals S, Van Tendeloo G. Low-dose patterning of platinum nanoclusters on carbon nanotubes by focused-electron-beaminduced deposition as studied by TEM. Beilstein J Nanotechnol. 2013;4(1):77–86.

28. Vidal-Iglesias FJ, Montiel V, Solla-Gullón J. Influence of the metal loading on the electrocatalytic activity of carbon-supported (100) Pt nanoparticles. J Solid State Electrochem. 2016;20(4):1107–18.

29. Chumillas S, Busó-Rogero C, Solla-Gullón J, Vidal-Iglesias FJ, Herrero E, Feliu JM. Size and diffusion effects on the oxidation of formic acid and ethanol on platinum nanoparticles. Electrochem commun. 2011;13(11):1194–7.

30. Nkosi F, Palaniyandy N, Raju K, Ozoemena KI. Influence of Microwave Irradiation and Combustion Fuels on the Rate Capability and Cycle Performance of Li1.2Mn0.52Ni0.13Co0.13Al0.02O2 Layered Material. Electroanalysis. 2020;32(12):3159–69.

31. Kabongo G, G N, K O, S D. Microwave Irradiation Induces Oxygen Vacancy in Metal Oxides based Materials and Devices: A Review. J Nanosci Curr Res. 2018;3(2).

32. Shinagawa T, Garcia-esparza AT, Takanabe K. Insight on Tafel slopes from a microkinetic analysis of aqueous electrocatalysis for energy conversion. Nat Publ Gr. 2015;(May):1–21.

33. Tavares M., Machado SA., Mazo L. Study of hydrogen evolution reaction in acid medium on Pt microelectrodes. Electrochim Acta. 2001;46(28):4359–69.

34. Marković NM, Grgur BN, Ross PN. Temperature-dependent hydrogen electrochemistry on platinum low-index single-crystal surfaces in acid solutions. J Phys Chem B. 1997;101(27):5405–13.

35. Bell DC, Thomas WK, Murtagh KM, Dionne CA, Graham AC, Anderson JE, et al. DNA base identification by electron microscopy. Microsc Microanal. 2012;18(5):1049–53.

36. Mallik L, Dhakal S, Nichols J, Mahoney J, Dosey AM, Jiang S, et al. Electron Microscopic Visualization of Protein Assemblies on Flattened DNA Origami. ACS Nano. 2015;9(7):7133–41.

37. Sokolov AN, Yap FL, Liu N, Kim K, Ci L, Johnson OB, et al. Direct growth of aligned graphitic nanoribbons from a DNA template by chemical vapour deposition. Nat Commun. 2013;4(May):1–8.

Chapter 7- Carbonisation of the DNA-Cisplatin via a pseudo pyrolysis process for the electrocatalysis of the Hydrogen Evolution Reaction (HER)

Chapter 7: Carbonisation of the DNA-Cisplatin via a pseudo pyrolysis process for the electrocatalysis of the Hydrogen Evolution Reaction (HER)

7.1 Introduction

The electrochemical response of the DNA-cisPt material for the range of platinum loadings employed was hindered by the highly electrical resistive nature of the DNA, reducing the attainable electrocatalytic performance of the material (1). As previously discussed in chapters 4-6, in order to achieve improved conductive and electronic properties of the DNA for its appropriate use as an electrocatalyst support, the non-conductive nature of the DNA molecule needs to be overcome such that both improved electrochemical activity and durability can be measured.

To do so, the work presented up till this point in the thesis has focused on functionalization of the single walled carbon nanotubes (SWCNTs) with DNA-cisplatin (chapter 5) and the graphitization of the DNA through the evacuation of the hydrogen and oxygen atoms upon high dose exposure to an electron beam (i.e. graphitization) (chapter 6). This chapter will focus on achieving the carbonisation of the DNA scaffold via a heat treatment process i.e. pseudo pyrolysis reaction at lower temperature conditions than the conventional i.e. 255 °C. The fabricated material is consequently characterized and tested for the Hydrogen Evolution Reaction (HER) under acidic conditions (pH 3). Figure 1 provides an overview of the material fabrication and steps towards its processing via pseudo pyrolysis.

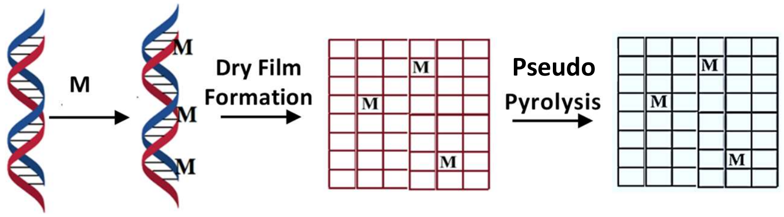

Figure 1*- Schematic representation of the fabrication process of the DNA based catalytic material used in this study. In this work, M = Pt and the process of carbonisation via pseudo pyrolysis.*

This processing method will introduce favourable characteristics to the DNA/DNA-cisPt electrocatalyst material, including improved conductivity of the DNA scaffold as reflected by the improved electrochemical response for the HER (detailed further in the chapter). In addition, the process of carbonisation will result in the formation of a material with attributes such as a large surface area, rich electronic state, thermal and chemical stability and good mechanical properties. These are favourable characteristics that are commonly associated with a graphitic based catalyst support (2), as previously discussed and detailed in chapter 6.

In this chapter, the successful process treatment of DNA via a pseudo pyrolysis reaction is presented and characterization of the resulting carbonised DNA-cisPt material is achieved using similar methods to those employed and discussed in the previous chapters of this thesis for the range of platinum loadings in this work (see Table 1). In addition, an outline of how the optimum reaction conditions (255 °C, 30 minutes) for the pseudo pyrolysis process were found is made and justified within the interest and scope of this study. Finally, the characterisation results of the processed DNA/DNA-cisPt is discussed to investigate the resulting effects of pseudo pyrolysis on the properties of the material (including the chemical and physical changes) and how this effects its use for its intended application i.e. fuel cell technology.

7.2 Literature review

7.2.1 DNA-cisPt electrocatalyst material for HER

Research focusing on supporting the development of renewable energy and fuel cell technology has received great interest, particularly the Polymer Electrolyte Membrane Fuel Cell (PEMFC) and it begins with researchers focusing on improving the electrocatalyst material for one of its fundamental reactions like the hydrogen evolution reaction (HER). This has been reviewed and discussed more thoroughly in chapters 2 & 4. Generally, it is found that much of the research efforts have focused on the development of inexpensive catalyst materials that could replace platinum, the conventional and ideal electrocatalyst for the two fundamental reactions of PEMFCs i.e. the HER and Oxygen Reduction Reaction (ORR) in acidic conditions (3).

A variety of research strategies have been adopted, ranging from lowered platinum loadings (4), (5) (6) &(7), to metal-free electrocatalysts (i.e. doped carbons) (8), (9), (10) &(11) or modified catalyst supports for example nitrogen-doped carbon material as catalyst support for platinum nanoparticles (12), (13) & (14). Hence the synthesis of a platinum-free electrocatalyst or a material of ultra-low platinum metal loadings is of great interest in supporting the commercialisation of fuel cells.

In this work, DNA (made of the four nucleotide bases adenine, guanine, cytosine and thymine) is employed as a catalyst support for the platinum metal i.e. a naturally containing source of both nitrogen and phosphorous rich carbon support. The use of DNA as a scaffold for metal complexes is known (15) &(16) and has previously been employed for directly attaching or growing platinum nanoclusters for the catalysis of HER/ORR in the literature (17),(18) and (19).

Therefore, the use of DNA as a template for the catalyst material and a source of a nitrogen-phosphorous-doped carbon (NP-doped carbon), which will consequently be carbonised, is promising since literature work has shown that NP-doped carbons and graphene based material exhibit high electrocatalytic activities and durability for the ORR (2), which is a popular and commonly studied reaction. This reporting is promising for the HER explored in this study, since it has long been acknowledged that the value of the exchange current density in H_2/O_2 fuel cells for the reduction of oxygen on the surface of platinum is around 5-6 times lower than the value measured for the hydrogen oxidation reaction (20).

7.2.2 Improving the electrical conductivity of DNA

The process of graphitisation can greatly reduce the electrical resistance of the DNA (21), despite the highly resistive nature of the DNA polymer (22), as detailed in chapter 4. Commonly employed methods for the graphitisation of the DNA have involved high temperature treatments of the material (800 - 1000 °C) under a H_2 atmosphere (23). However, the main issue with the conventional graphitization methods is associated with the thermal decomposition of bulk DNA upon its exposure to temperatures exceeding 250 °C (24). The use of soft materials including the use of DNA for nanofabrication has been reviewed by (24). Normally the drying process of DNA containing solutions can collapse or rupture the DNA structure and methods to improve its mechanical strength have been reported (25).The carbonisation of DNA based structures via thermal and non-thermal treatments have been reported by several authors (1),(26), (27), (28), & (29). For example, the growth of graphitic nanoribbons using copper (Cu^{2+}) DNA templates has been successfully reported by (30) via a Chemical Vapour Decomposition (CVD) process. The metallic Cu atoms have the catalytic role in the process of the graphitic synthesis. However conservation of the DNA template structure is not reported in their work. On the other hand, (31) report shape conservation between the initial DNA nanostructure and the final resulting carbonised DNA nanostructure by coating the DNA nanostructures with a thin film of Al_2O_3 via an atomic layer deposition (ALD) process prior to carbonisation of the DNA (at 800−1000 °C) under a low pressure H_2 atmosphere.

Normally the best candidates for carbonisation includes materials with aromatic rings in their structures (31). DNA is a polynucleotide polymer, made of a phosphate backbone, a sugar moiety and the four nucleotide bases (A, G, C and T). Upon thermal treatment, the sugar is converted into amorphous carbon and the nucleotide bases have structural resemblance to a large number of compounds such as polyimide that normally successfully undergo carbonisation (25). In this chapter, carbonisation of the DNA based electrocatalyst material is achieved through a pseudo pyrolysis process.

7.2.3 Pyrolysis

By definition, pyrolysis refers to the thermal decomposition of molecules under an inert atmosphere (32). Specifically in biotechnology, the exposure of the polymeric network or macromolecules to thermal energy results in the thermal degradation of the sample into volatile products (32). In addition, it has been reported by (32) that final pyrolysis temperatures usually occurs between 400 and 900 °C, while thermal degradation resulting from temperatures below 300 °C is usually called thermal decomposition. The volatile products that evolve during the pyrolysis of the complex materials (through the removal of hydrogen/oxide groups) can be monitored via gas chromatography (Py-GC) or mass spectrometry (Py-MS). Since the 1970s and 80s, it has been reported that for DNA material, temperatures of between 200 and 300 °C were sufficient for achieving fractionation (32). Similarly, (33) reported that pyrolysis of calf thymus DNA was achievable at a temperature range of 220 -250 °C. It was reported that up to 30 % by weight of the DNA material is collected as a sublimate and that the major volatile products from the pyrolysis of nucleic acids are based on a range of furanyl compounds (33).

Temperature is a key process parameter in the pyrolysis process since different heating levels lead to different chemical compositions and consequently different properties of the final products. For example, this can range from reduced oxygen content to increased electrochemical capacitance (34). However, through the implementation of this heat treatment process, we are able to form a carbonised DNA material of increased stability, making its use more suited for nano-electronic based applications (35). To summarise, the above suggests that we can successfully achieve the pyrolysis of DNA in the temperature range of 220 to 250 °C with preservation of its moieties.

7.3 Materials and experiments

7.3.1 Material synthesis

Deoxyribonucleic Acid (DNA), sodium salt from salmon testes, cisplatin (99.99 % purity (based on trace metal analysis)) were purchased from Sigma Aldrich. DNA-cisPt adducts were synthesized by dissolving the salmon milt DNA (sm-DNA) in Milli-Q water (resistivity ≥ 18.2 MΩ.cm) and sonicating to prepare a stock solution. Cisplatin in aqueous form was mixed with the sm-DNA and incubated at 37 °C overnight for 10 hours. Confirmation of the adduct formation was achieved using spectrophotometric techniques using Shimadzu UV-1800 spectrophotometer, Jasco J-810 spectropolarimeter and Cary 5000 UV-Vis-NIR Spectrophotometer, by Klaudia Englert, School of Chemistry ,University of Birmingham (36).

The ultimate goal of this project is to synthesise a pre-cursor catalyst material with optimum electrocatalytic activity at the lowest platinum (i.e. cisplatin) loading possible (37). The range of loadings prepared and tested in this work are displayed in Table 1.

***Table 1**- Ratio and concentrations of the DNA-cisPt samples synthesized and characterized.*

Ratio of DNA to cisPt	***Concentration of cisPt /μM***	***Concentration of sm-DNA /mM***
1:0	0	1
$1:10^{-4}$	0.1	1
$1: 10^{-3}$	1	1
$1: 10^{-2}$	10	1
1: 0.1	100	1
1:1	1000	1
cisPt	1000	0

7.3.2 Electrochemical Testing Experimental Method

7.3.2.1 Film formation on a glassy carbon (GC) macroelectrode

A glassy carbon (GC) macroelectrode was polished on microcloth pads with decreasing size alumina slurries (1.0, 0.3, 0.05 μm, Buehler Inc., IL, USA), followed by rinsing with de-ionised water (DIW) and drying under a gentle flow of nitrogen. Once dry, the electrodes were modified by drop casting an aliquot of the prepared DNA-cisPt sample (42 μL onto a 5 mm GC electrode) and drying under a lamp.

7.3.2.2 Electrochemical testing

The samples prepared (see Table 1) were electrochemically tested using a 3 electrode cell, involving a glassy carbon electrode (GC, 5 mm, BASi) as the working, a saturated calomel (SCE, BASi) reference and a bright platinum mesh counter electrode. The cell was controlled by an Autolab 128N potentiostat running Nova 2.1 software (Metrohm-Autolab BV, Netherlands). All potentials are reported against a SCE. All chemicals involved were used in their analytical grade and used without any purification. Perchloric acid (70 %, 99.99 % trace metals) (1 mM, pH 3) and sodium perchlorate (≥ 98 %) as the supporting electrolyte (0.1 M) supplied by Sigma Aldrich. All electrolytes were made up with Milli-Q water (resistivity ≥ 18.2 MΩ.cm) (MilliQ, Millipore) and thoroughly degassed with dry nitrogen (oxygen-free, BOC Gases plc) prior to experimentation.

7.3.2.3 Electron Microscopy

The surface morphology of the material was attained using High Angle Annular Dark Field Scanning Transmission Electron Microscopy (HAADF-STEM) operated in both dark field and bright field imaging using a JEOL2100F instrument. The samples were prepared for imaging by casting 3 μL of the sample onto a 300 Cu mesh holey carbon TEM grid and drying under a lamp. Once the TEM grids were prepared, they were loaded into the furnace to achieve carbonisation of the material prior to their STEM imaging characterisation. The STEM was operated in Z-contrast mode using a HAADF detector at 200 kV acceleration voltage. STEM-EDX imaging was employed to observe the distribution of the platinum atoms in the DNA-cisPt nanomaterial.

7.3.2.4 Low temperature pseudo pyrolysis process

The low temperature pseudo pyrolysis of DNA was achieved in quartz tube within a tubular Carbolite MTF 12/38/400. The DNA-cisPt films prepared on the GC stub were loaded into a corundum boat which was then placed into the tubular furnace operating under an inert nitrogen atmosphere, which was purged at a rate of 50 mL min^{-1}. The optimum reaction temperature was investigated for in the temperature range of 160 - 350 °C for 30 minutes (1), which is equivalent to a heat flow rate range of 91.5 - 158.7 kJs^{-1} (see appendix 4, section titled '*heat flow rate and heating rate calculations*' for detailed derivations of the calculations). Under these reaction conditions, the heating rate changes from 4.5 to 10.8 °C min^{-1} as the temperature is increased, detailed in appendix 4.

All the samples were carbonised at the optimised reaction conditions found of 255 °C for 30 minutes. This is equivalent to a heat flow rate of 129.8 kJs^{-1} and a heating rate of 7.7 °C min^{-1}.

7.3.3 Surface chemical properties

7.3.3.1 XPS

XPS characterization was conducted at Harwell XPS, UK facilities to obtain the binding energies (BE) and survey spectra of the samples synthesized using α-Kl as the X-ray source (characteristic energy of 1486.68 eV). The BE is reflective of the oxidation states of the elements in the DNA-cisPt adducts including Pt, Cl, C, P, N and O. The surface chemical properties of the 1 to 10^{-4} DNA-cisPt loading and the 1 mM virgin DNA films following pseudo pyrolysis of the material were explored to assess for any resulting changes in the elemental composition following treatment and most importantly to investigate and test for any graphitic content in the material.

7.3.3.2 Raman characterization

Raman was carried out with Renishaw system (RL633) with a 532 nm source and a laser power of 1 mW. The integration time for each scan was set at 10 seconds and the instrumentation was controlled using a WIRE software. The sample was prepared by drop casting an aliquot (42 µL) of the 1 to 10^{-4} DNA-cisPt and the 1 mM virgin DNA onto a 5 mm GC stub and drying under a lamp.

7.4 Results and Discussion

7.4.1 Optimum reaction conditions for the pseudo pyrolysis process

In order to achieve the successful carbonisation of the DNA based material, the optimum temperature and the time duration for the pseudo pyrolysis process first had to be found. We previously identified that pyrolysis of DNA in the temperature range of 220 -250 °C (33) was feasible. A more recent finding by Nakoa et al. (1) suggested that a temperature of 250 °C for a duration of 30 minutes was sufficient for achieving the pyrolysis of DNA (1). At these process conditions, they were able to make fluorescent carbon nanowires (CNW) by aligning DNA nanofibers on a surface (1).

To investigate and find the ideal temperature for the pseudo pyrolysis of the sm-DNA material, firstly, differential scanning calorimetry (DSC)[4] testing was performed. Through this testing, the exothermic peak and consequently combustion temperature of sm-DNA in both solid and aqueous form could be found.

7.4.2 Differential Scanning Calorimetry (DSC)

Initially, the sample was prepared for testing by pipetting 1 µL of the aqueous 1mM DNA solution into an aluminium pan and leaving it overnight to evaporate. On the other hand, the solid unmodified form of the sm-DNA sample (used as provided by the supplier i.e. Sigma Aldrich) was placed into an aluminium pan and loaded directly into the sample holder of the DSC instrumentation. This was purged with nitrogen gas at an interchangeable rate between 40 and 60 mL min^{-1}. The exothermic peak(s) for the material can simply be found from the resulting DSC curves that are produced. Figure 2 displays the results.

---

[4] The DSC testing was carried out with the assistance of Greg O'Callaghan (School of Chemistry, University of Birmingham)

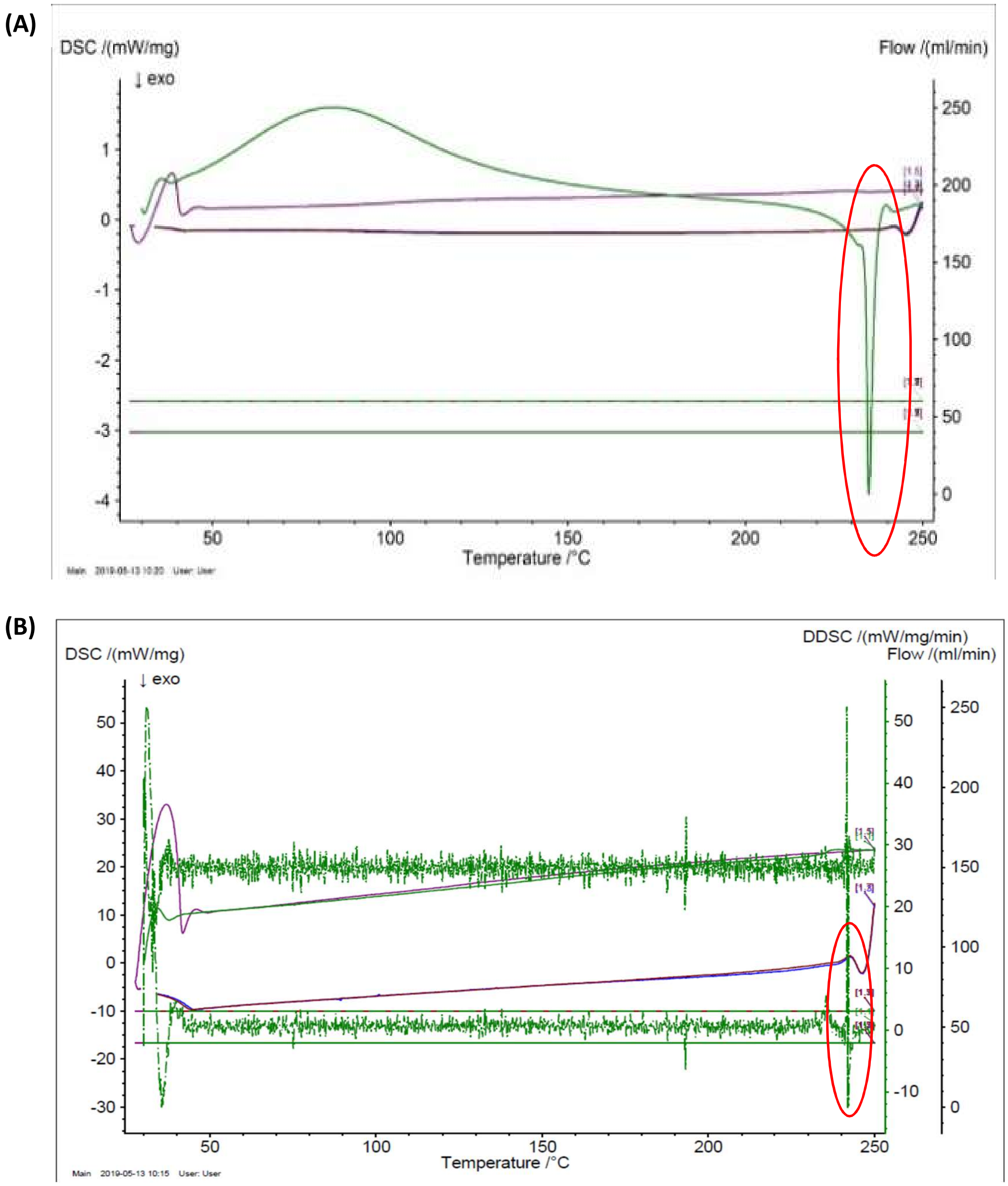

***Figure 2**- Direct Scanning Calorimetry results displaying the **(A)** Exothermic peak for the solid DNA sample **(B)** Exothermic peak for the evaporated aqueous DNA sample.*

The DSC testing shows that for the solid sm-DNA sample, an exothermic peak around 235 °C is measured, while for the aqueous DNA solution a weak signal at around 242 °C can be observed as highlighted in figures 2(A) and (B). These exothermic temperatures along with the findings reported in the literature (1) provide us with guidance on the ideal temperature range that should be used to investigate for the optimum temperature conditions for the pseudo pyrolysis process of DNA. As a start, a temperature range between 160 - 350 °C and a process duration of 30 minutes is selected, and is supported by the literature reportings by (1).

7.4.3 Changes in the electrochemical response for the HER with pseudo pyrolysis process temperature

The choice of the DNA-cisplatin loading

To begin with, an investigation to seek an optimum reaction temperature and time for the pseudo pyrolysis process is conducted. This was achieved using an intermediate platinum loading in the DNA-cisPt material as a representative of all loadings employed in this study (see Table 1), to conduct the experimental testing with i.e. $1{:}10^{-3}$ DNA-cisPt. A volume of 42 µL was drop cast onto a 5 mm GC stub surface and dried under a lamp. The furnace was prepared for the reaction by purging with nitrogen and setting to the desired temperature via a temperature controller. The prepared sample was placed into a corundum boat and loaded into the furnace. The pseudo pyrolysis process was conducted under an inert N_2 atmosphere for a duration of 30 minutes at the desired temperature (i.e. in the range of 160 to 350 °C).

As discussed throughout this thesis, the HER (pH 3) is an archetypal simple electrocatalytic reaction and is therefore used as a means of monitoring the resulting changes to the electrocatalyst material following pseudo pyrolysis and specifically the influence of the process temperature and time. Specifically, the resulting changes to the peak potential (E_P / V vs SCE) and current density (J /mA cm^{-2}) will be measured to reflect the electrocatalytic performance of the resulting material under each of these conditions. The current density value produced is based on the geometric surface area of the working electrode.

The electrochemical testing is conducted using cyclic voltammetry at a scan rate of 50 mV s^{-1} in an electrolyte solution of 1 mM $HClO_4$, 0.1 M $NaClO_4$. Figure 3(A) displays the electrochemical response (forward scan) of the prepared 1 to 10^{-3} DNA-cisPt for the range of pyrolysis temperatures investigated.

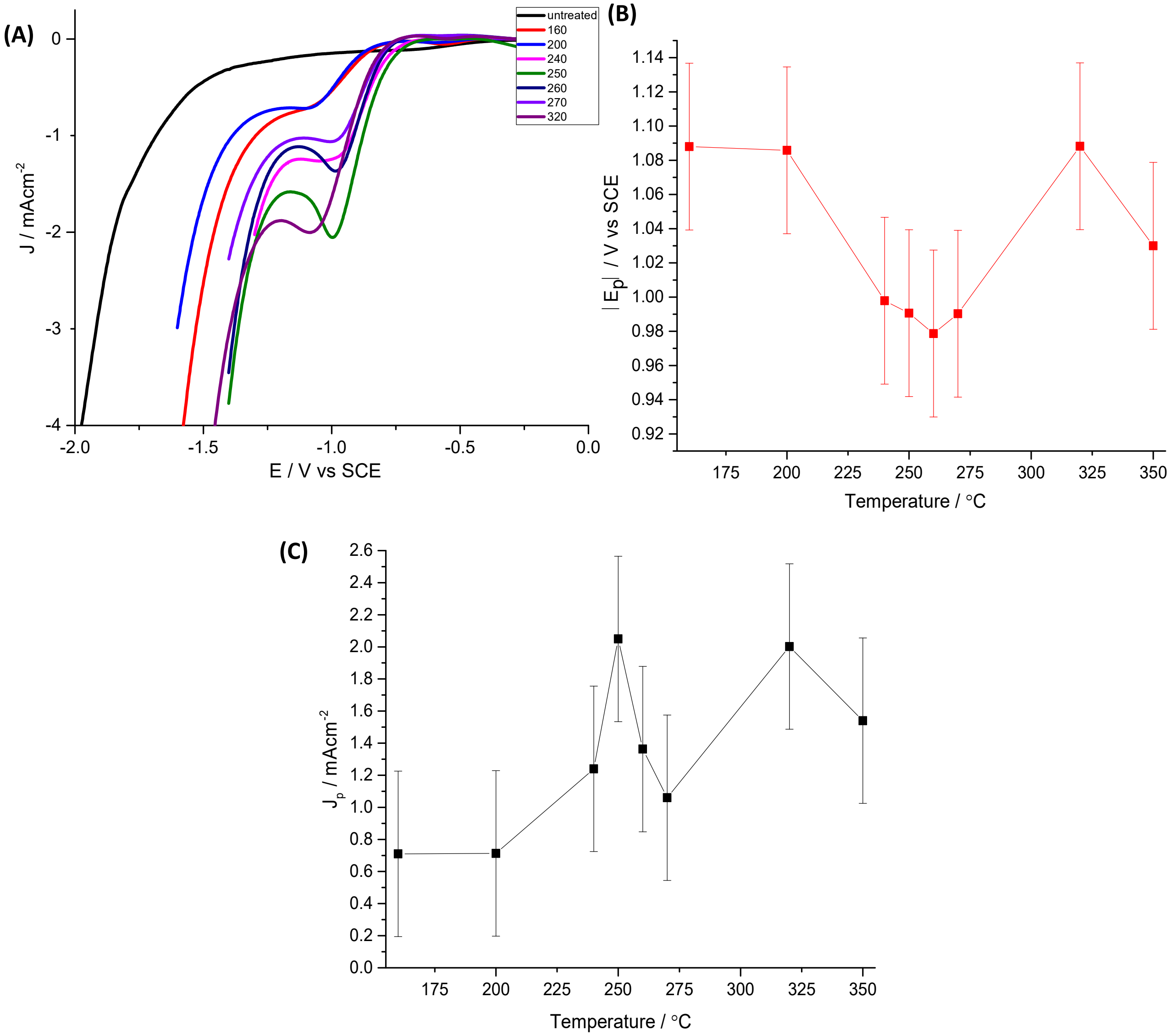

***Figure 3** - (A) The electrochemical response for the HER (1 mM $HClO_4$, 0.1 M $NaClO_4$) 50 mV s^{-1} following pseudo pyrolysis in the temperature range of 160-350 °C, 30 minutes. The corresponding variation of (B) Peak Potential (E_P) (C) Peak current density (J_p) with temperature, * error bars based on a standard deviation error.*

It is evident from figure 3(A) that the electrochemical response of the 1 to 10^{-3} DNA-cisPt is significantly improved following pseudo pyrolysis, which suggests that carbonisation has been achieved. The enhanced electrocatalytic activity is reflected by the appearance of a peak with a current density output of around 2 mA cm^{-2} compared with the sigmoidal response of the untreated material. The absence of the electrochemical peak in the untreated 1 to 10^{-3} DNA-cisPt reflects the materials highly resistive nature, which is overcome via pseudo pyrolysis as shown across all temperatures investigated. In addition, it is also indicative of the lack of electrical contact across some regions of the catalyst films, which has previously been explained in our previous work (37) and chapter 4 of this thesis.

The absolute value of the peak potential (E_p) and peak current density (J_P) are noted and plotted as a function of temperature, see figure 3 (B & C) respectively. Both of these electrochemical parameters provide favourable catalytic behaviours i.e. whereby as the reaction temperature is increased, the E_p

is reduced and the catalytic activity i.e. J_p, is increased reaching an optimum temperature at 250 °C. However at 320 °C, although the peak current density output (J_p) is similar to that achieved at 250 °C, the E_p is unfavourably higher (1.08 V vs SCE) compared to 0.98 V vs SCE at 250 °C.

From these findings, (see figure 3(B & C)), we deduce that temperatures beyond 200 °C give rise to significant changes in electrochemical response i.e. J_p and E_p. On the other hand, beyond a temperature of 300 °C, in terms of E_p, the electrochemical response shifts unfavourably towards the response of the carbonised material prepared at the lower end of the temperature range studied (i.e. < 200 °C). Furthermore, to define an optimum temperature, ideally a compromise between both electrochemical parameters i.e. E_p and J_P should be made. A single parameter which allows us to do so would be the kinetic rate constant value (k^0) of the reaction, however modelling the data to attain this measurement is beyond the scope of this study.

The findings from the results in figure 3 suggest that we can narrow the temperature range initially proposed (i.e. 160-350 °C) to seek the optimum temperature for the pseudo pyrolysis process in a much more definitive range of 250-260 °C. Additionally, the trends in the electrochemical response observed in figure 3 can be described and correlated with the surface morphology of the material via STEM imaging characterisation. This enables a fair selection of the optimum temperature conditions for the pseudo pyrolysis to be made, with considerations to the resulting effects of temperature on the platinum nanoparticles (in the carbonised DNA-cisPt material), as detailed in the following section.

7.4.4 How the surface morphology changes with the temperature of the pseudo pyrolysis process

The effects of reaction temperature on the surface morphology of the platinum nanoparticles in the carbonised DNA-cisPt material can be revealed by studying the material properties via STEM imaging characterisation. An aliquot of 3 µL of the 1 to 10^{-3} DNA-cisPt sample is drop cast onto a 3 mm holey carbon TEM grid and prepared for carbonisation by insertion into the furnace at the desired temperature conditions chosen (250, 260 and 350 °C). The STEM imaging of the prepared TEM grids is achieved to test the hypothesis proposed i.e. that as the pseudo pyrolysis temperature increases, larger platinum nanoclusters will be measured. Figure 4 displays the results in both dark field (DF) and bright field (BF) mode. The size of the nanocluster is measured using the analytical tools in Image J software, see appendix 4 for detailed method.

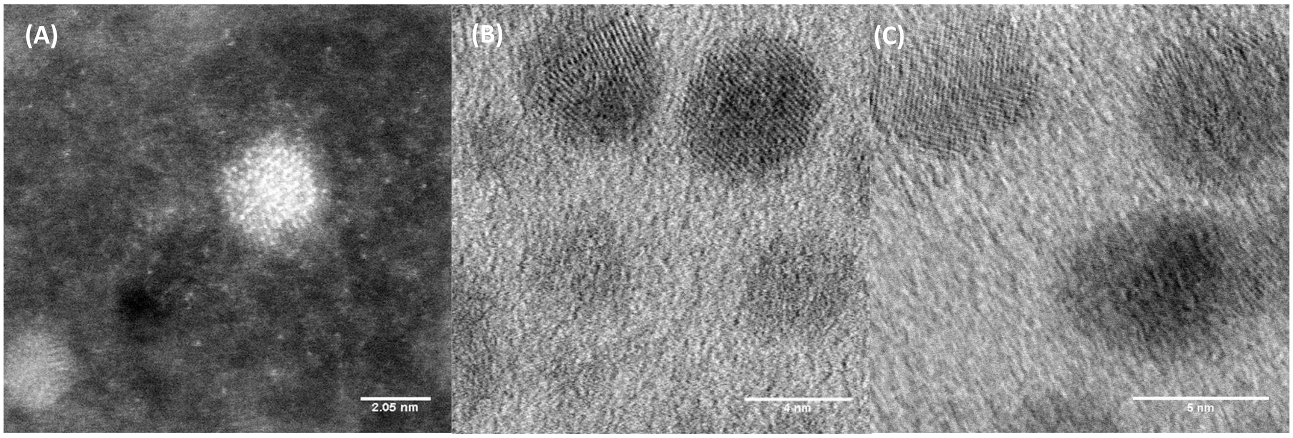

Figure 4*- HAADF STEM imaging of 1 to 10^{-3} DNA-cisPt carbonised via a pseudo pyrolysis process for a 30 minute duration at (A) 250 ° C (DF) (B) 260 ° C (BF) (C) 350 °C (BF) on a 300 mesh holey carbon TEM grid.*

It is evident by comparing figures 4(A) to 4(B &C) that much larger platinum nanoclusters are produced as the temperature is increased which is reflected in the quantitative measurements (Table 2). The carbonised material at 250 °C produces platinum nanoparticles of an average size of 2.53 ± 0.25 nm, as opposed to the near two fold increase in size, from just a 10 °C increase in temperature (i.e. 4.00 ± 0.77 nm at 350 °C).

Table 2- *The changes in the size of the platinum nanoclusters with temperature for carbonisation of 1 to 10^{-3} DNA-cisPt for the pseudo pyrolysis process of a 30 minute duration.*

Temperature condition of the pseudo pyrolysis process / °C	Platinum Nanocluster size* / nm
250	2.53 ± 0.25
260	4.00 ± 0.77
350	4.69 ± 1.51

*error bars are based on a standard deviation error.

It has been reported that the agglomeration of metallic nanoparticles depends on the temperature of the system, film thickness and process duration (38). Taking into consideration these factors, we can develop an understanding of the effect of temperature change on the platinum nanoparticles, such as how it leads to the activation and diffusion of the metal particles on the DNA surface.

During the diffusion of the platinum, inter-collision between the atoms takes place, resulting in the nucleation of the tiny nanoclusters (38). Therefore the agglomeration continues and increases at higher thermal energy inputs, which explains why the platinum nanocluster size measured (4.69 ± 1.51 nm) at 350 °C is higher than the other temperatures tested. The increase in the standard deviation error with temperature is reflective of the increased non-uniformity in the size of the catalyst material across the DNA surface, as we expose it to a higher thermal energy level.

This therefore explains the trends that we see in figure 3 i.e. reduced electrochemical performance for the HER with increased temperatures, since the platinum nanocluster size increases with heat input, resulting in deviations from the ideal catalyst size of 2.2 nm reported in the literature (39) for the HER in an acidic environment. Furthermore, these observations consolidate with the previous suggestions made to state that the optimum reaction temperature lies somewhere between the 250-260 °C range given that it is between these two temperatures that the nanocluster size is drastically changed.

7.4.5 Optimum reaction temperature in the range of 250 - 260 °C

The pseudo pyrolysis process is tested at three temperatures (250, 255 and 260 °C), following the same methods outlined above. In addition to the 1 to 10^{-3} DNA-cisPt loading, the changes in the electrochemical response of the 1 to 10^{-4} DNA-cisPt loading is also tested at these temperatures. Measuring the electrochemical response under the same reaction conditions as those applied above i.e. the HER (pH 3), the resulting changes to the average peak potential (E_p) and peak current density (J_P) can be found as a function of temperature, see figure 5. The current density is measured based on the geometric surface area of the working electrode.

The average values were found from repeated measurements of the carbonised material in this temperature range, see appendix 4, figure A4.1 for the resulting electrochemical response. The variation in the results obtained is accounted for by taking an average value of the E_p and J_p and observing the correlation between these parameters and pyrolysis temperature.

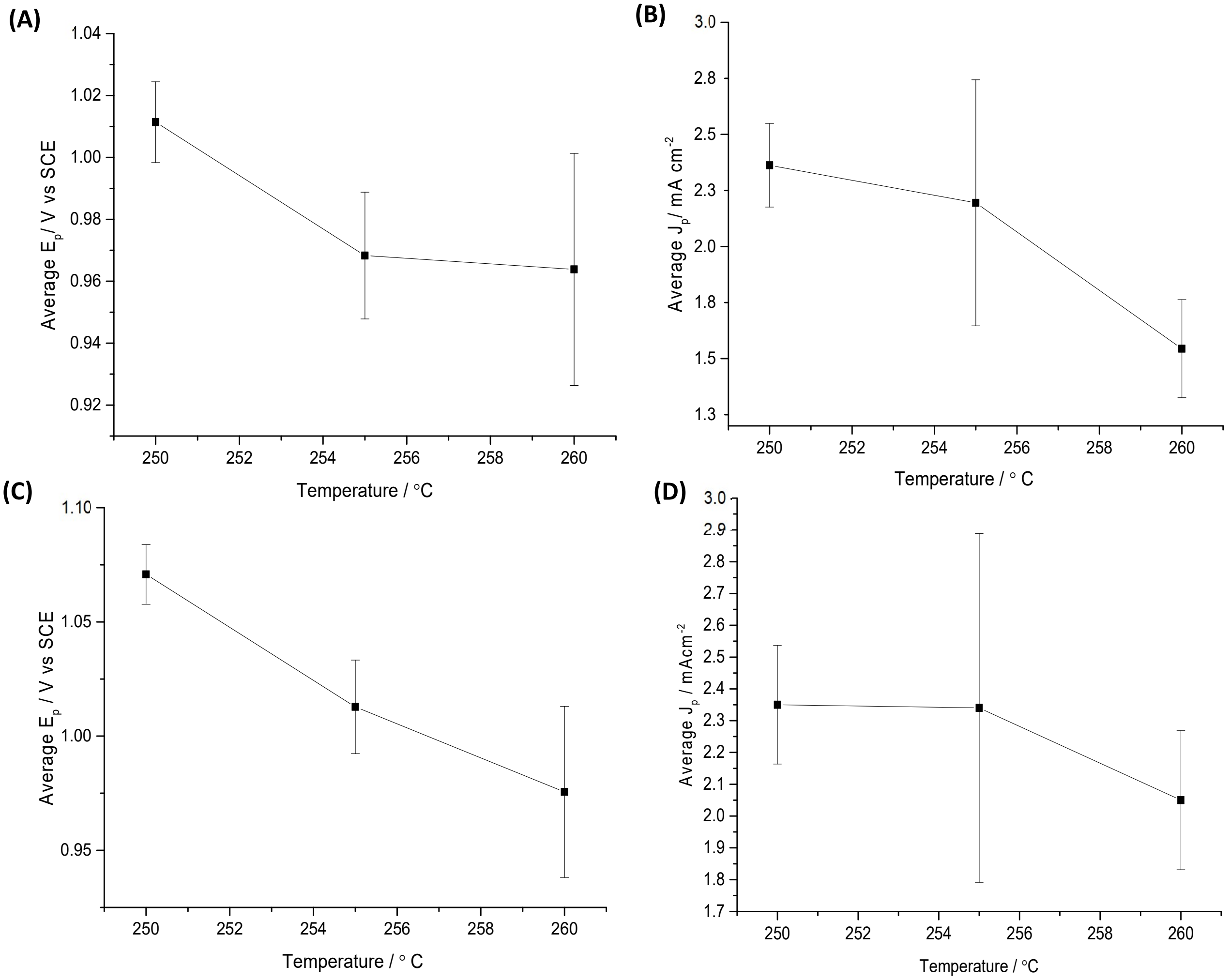

Figure 5- *The effect of changing the pyrolysis process temperature (250 - 260 °C) on the average Peak Potential (E_p) and Peak current density (J_p) for (A, B) 1 to 10^{-3} DNA-cisPt/GC (C, D) 1 to 10^{-4} DNA-cisPt/GC response for the HER (1 mM $HClO_4$ and 0.1 M $NaClO_4$) at 50 mV s^{-1} *Error bars displayed are based on a standard deviation error.*

From figure 5, it is evident that across this smaller temperature range, the changes in the magnitude of these electrochemical parameters i.e. E_p and J_p is also smaller, with overlapping error bars. Thus drawing conclusive remarks with statistical confidence is challenging.

However for both loadings of cisPt, an optimum J_p is measured around 2.3 and 2.35 mAcm^{-2} at 1 to 10^{-3} and 1 to 10^{-4} DNA-cisPt/GC surfaces respectively when the pseudo pyrolysis is conducted at 255 °C. Although the measured E_p at 260 °C is lower than at 255 °C (for both DNA-cisPt loadings), the difference in the value is insignificant (< 5 mV).

Thus from these findings we can conclude that a temperature of 255 °C provides a compromise between J_p and E_P and is sufficient for achieving the best electrochemical performance for the electrocatalysis of the HER by the DNA-cisPt material. The next part of this study will focus on investigating whether the duration time of the pseudo pyrolysis process at 255 °C can be changed to improve the electrochemical performance further.

7.4.5 Influence of duration time of the pseudo pyrolysis process

The material was prepared using the same methods described above and an optimum time for the pseudo pyrolysis reaction at 255 °C is explored using the 1 to 10^{-4} DNA-cisPt material. The electrochemical testing involved the use of a new saturated calomel reference electrode (SCE) thus we account for possible deviations in the measurements of the peak potential (E_P) presented here, compared to the previous measurements using a different SCE reference. To do so, a study of the stability of the saturated calomel reference electrode is made and detailed in appendix 6. The findings of this study reveal that insignificant deviations across the different SCEs tested is seen, suggesting that the potential measurements made against the two SCE references in this work can be compared without concern. The resulting changes to the E_p and J_P with the duration time of the pseudo pyrolysis process is displayed in the figure below.

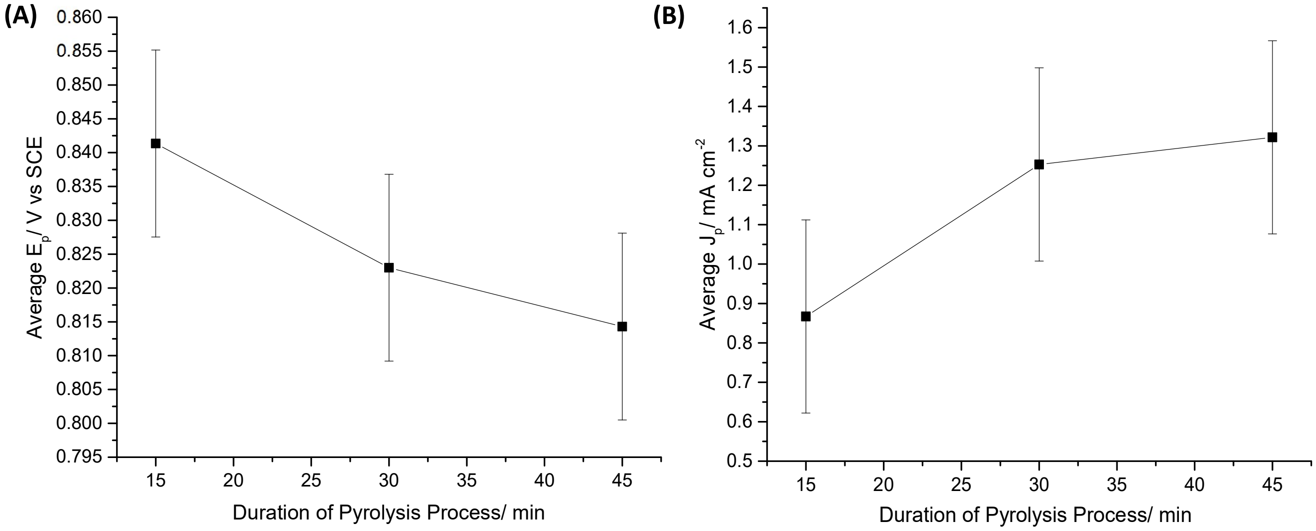

Figure 6- *The effect of changing the duration time of the pseudo pyrolysis process at 255 °C on the average (A) Peak Potential (Ep) and (B) Peak current density (J_p) for the 1 to 10^{-4} DNA-cisPt/GC response for the HER (1 mM $HClO_4$ and 0.1 M $NaClO_4$) at 50 mV s^{-1} *Error bars displayed are based on a standard deviation error.*

From figure 6, it is evident that, like the other process parameter explored before in this work i.e. temperature, the selected reaction time for the pseudo pyrolysis process needs to compromise between the E_p and J_p. We find that for each of these electrochemical parameters, the shift is more favourable with duration time of the reaction i.e. a higher J_p and lower E_p. However, since the changes between 30 and 45 minutes are smaller than that observed between 15 and 30 minutes, it is sensible to decide on 30 minutes as being the optimum reaction time for the pseudo pyrolysis given that the energy costs associated with running the process for longer times are not justified with the outcome of the catalytic response at a lower energy level i.e. a small difference in the E_p and J_P result at 45 minutes compared with 30 minutes for the 1 to 10^{-4} DNA-cisPt loading. Similar observations are made for the electrochemical response of the 1 to 10^{-3} DNA-cisPt material, to conclude that 30 minutes offers the best compromise between the E_p and J_P. The experimental results are provided in appendix 4, figures A4.2 to A4.4.

This therefore brings us onto making the following proposal of whether changing the pseudo pyrolysis temperature and process duration are interrelated factors, which we can combine to reduce the overall energy costs associated with the process. For example, whether we can achieve the carbonisation of the material at a higher temperature but lower reaction time. This is investigated and discussed below.

7.4.6 How temperature and time are interrelated parameters for the pseudo pyrolysis reaction

Up till this point, the resulting changes in the electrochemical response has been explored as a function of either the process temperature or reaction time individually. The experimental findings have shown that conducting the pseudo pyrolysis reaction at 255 °C for a duration of 30 minutes was sufficient for achieving the carbonisation of DNA. Herein, we investigate the hypothesis proposed to explore whether time and temperature are interrelated factors, with a combined effect, such that the same improved electrocatalytic behaviour can be attained at a higher temperature and lower reaction time and vice versa. This would be favourable in terms of reducing the energy production costs for future considerations. In this work, three pyrolysis reaction conditions are selected including: (1) 280 °C, 10 minutes (2) 255 °C, 30 minutes and (3) 200 °C, 60 minutes for the carbonisation of 1 to 10^{-4} DNA-cisPt material. Figure 7 displays the electrochemical response for the HER (pH 3) under the conditions specified.

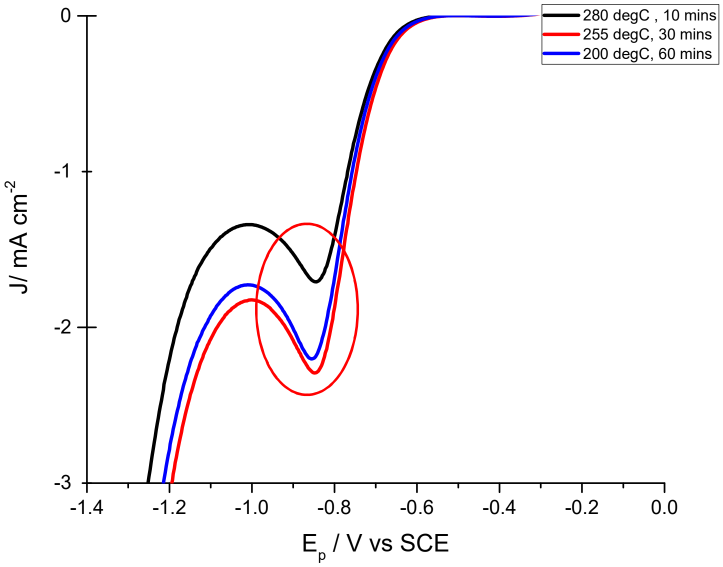

Figure 7- *The electrochemical response for the HER (1 mM $HClO_4$, 0.1 M $NaClO_4$) at 50 mVs^{-1} at different temperature conditions and times for the pseudo pyrolysis process of 1 to 10^{-4} DNA-cisPt casted on 5 mm GC.*

Based on the results in figure 7, it is clear that as we increase the pseudo pyrolysis reaction time, higher current density outputs can be measured. Meanwhile, conducting the pseudo pyrolysis process at a higher temperature results in a small shift in the E_p towards that of a bulk platinum response i.e. in the direction to the right of the voltammogram.

Table 3- *How temperature and time are interrelated parameters for the pseudo pyrolysis process.*

Pseudo pyrolysis temperature (° C) , Duration time (min)	E_p / V vs SCE	J_p / mAcm^{-2}
200 , 60	-0.848	-2.20
255 , 30	-0.841	-2.28
280 , 10	-0.840	-1.71

From Table 3 it can be seen that at condition (2) i.e. 255 °C, 30 minutes, optimum reaction conditions are provided for the pseudo pyrolysis while at a higher temperature but shorter exposure time, a significant reduction in the current density output is measured i.e. -1.71 mA cm^{-2} compared with -2.2 vs. -2.28 mA cm^{-2} measured at conditions (1) and (2) respectively. Thus what we can conclude from these findings is that the temperature effect is greater than time as a process parameter for the pseudo pyrolysis reaction.

This consolidates with our previous findings to suggest that 255 °C and 30 minutes are the optimum conditions for the pseudo pyrolysis process. The carbonisation of the DNA-cisPt material employed in this study can therefore be achieved and consequently, characterisation of the resulting material can be made using both electrochemical methods and STEM imaging characterisation under these conditions.

7.4.7 Pseudo pyrolysis at the optimum reaction conditions for a range of DNA-cisPt loadings

7.4.7.1 Electrochemical response

Preliminary experiments involving the preparation of the samples using the same ways described above, were performed on both carbonised and untreated DNA-modified GC and cisPt modified GC, as the working electrode to determine how the absence and presence of platinum metal affects the electrochemical response for the HER at pH 3. All current densities (J_p) measured were based on a geometric surface area of the working electrode and the onset potential was defined at a current density output of 0.1 mA cm^{-2} ($\sigma_{0.1\ mAcm^{-2}}$).

The results displayed in figure 8(A) demonstrate the significant improvements that can be attained in the electrochemical response for the HER (pH 3) over the surface of DNA/GC modified electrode following carbonisation of the material. This is reflected in the increased current density output (J_P) and smaller onset potential ($\sigma_{0.1\ mAcm^{-2}}$) which shifts from -1.12 V to -0.69 V vs SCE.

However, in the absence of DNA, the thermal treatment of bulk cisPt results in unfavourable changes to the electrochemical response of the electrocatalyst material compared with the untreated counterpart. It can be proposed that this due to the resulting changes in the size of platinum nanoclusters following exposure of the material to heat. This is explored further in the latter section of this chapter using STEM imaging characterization.

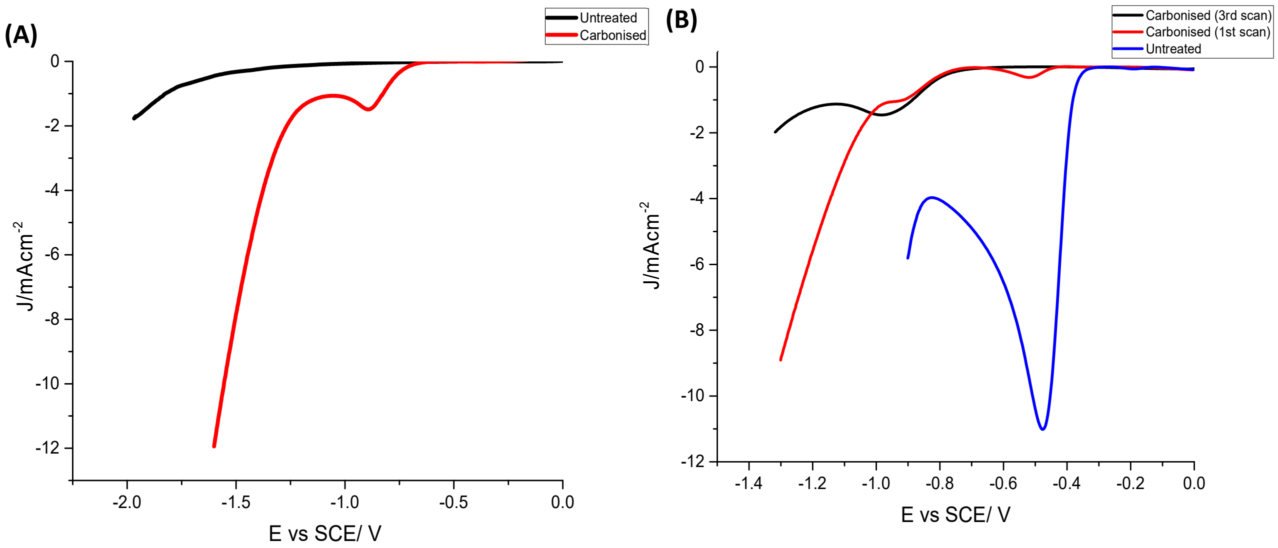

Figure 8*- The influence of the pseudo pyrolysis temperature employed on the electrochemical response of 42 µL of (A) 1 mM DNA (B) 1 mM cisPt cast on GC (d = 5 mm) for the HER (1 mM $HClO_4$, 0.1 M $NaClO_4$) at 50 mVs^{-1} (Carbonization at 255 °C, 30 minutes).*

The electrochemical response of the heat treated cisPt changes with the cycle number of the voltammogram over the surface of the working electrode. This is evident from the disappearance of the first peak in the 3rd cycle, which was observed in the first scan at around -0.51 V vs SCE, and the higher current density output (J_p) at the second peak at -0.89 V vs SCE in the third scan compared to the smaller J_p at this potential in the 1st scan. Furthermore, the unfavourable changes resulting in the heat treated cisPt material are reflected by comparing the values of the onset potential ($\sigma_{0.1\ mAcm^{-2}}$) with those of the untreated cisPt, which is found to be much lower than the heat treated cisPt, see Table 4. However, the combination of DNA with cisPt at a range of low loadings of the platinum metal results in more favourable results in the electrochemical response for the HER (pH 3) following carbonisation of the material via pseudo pyrolysis compared to its absence, as shown in figure 9.

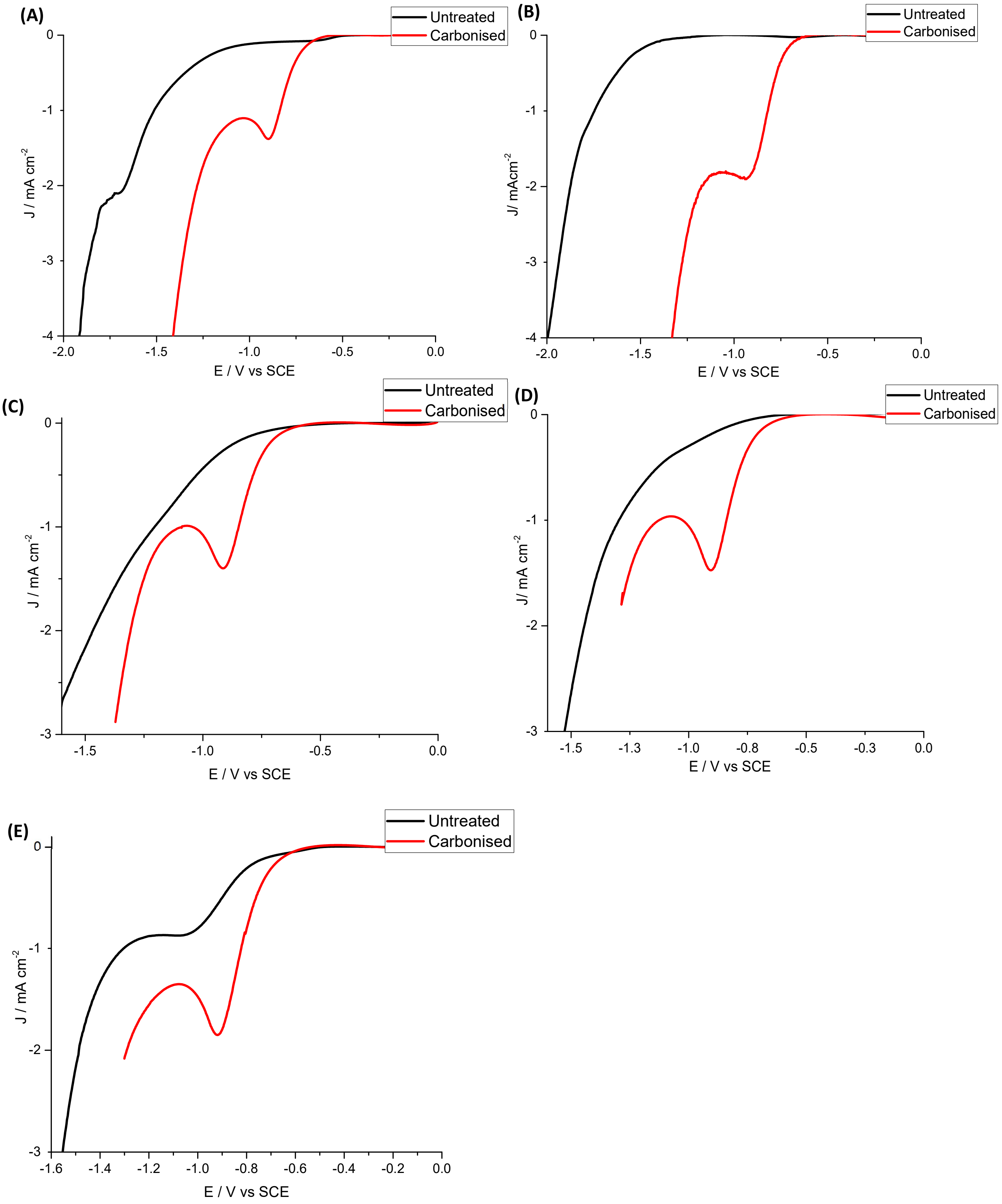

Figure 9- *The resulting change in the voltammetry response for the electrocatalysis of the HER (1 mM $HClO_4$, 0.1 M $NaClO_4$) at 50 mVs^{-1} after undergoing pyrolysis at 255 °C for 30 minutes (A) 1 to 10^{-4} DNA-cisPt (B) 1 to 10^{-3} DNA-cisPt (C) 1 to 10^{-2} DNA-cisPt (D) 1 to 10^{-1} DNA-cisPt (E) 1 to 1 DNA-cisPt.*

From figure 9, the electrochemical parameters, shown in Table 4, can be deduced to compare and contrast between the performances of the synthesized material for the range of platinum loadings employed.

Table 4- *Comparison between the peak potential, current density and onset potential (σ) attained at the modified GC electrode surfaces of the different ratios of the DNA-cisPt material before and after carbonisation via pseudo pyrolysis at 255 °C, 30 minutes.*

Ratio of DNA:cisPt/GC modified Electrode Surface	Peak potential (E_p) / V vs SCE ± 0.01	Peak current density* (J_p) /mA cm^{-2} ± 0.01	Onset potential (σ) / V vs SCE @ 0.1 mA cm^{-2} Untreated	Onset potential (σ) / V vs SCE @ 0.1 mA cm^{-2} Heat treated via pseudo pyrolysis
Bare GC	-0.88	-3.99	-0.61	-
1:1	-0.92	-1.84	-0.71	-0.65
1:10^{-1}	-0.91	-1.47	-0.81	-0.67
1:10^{-2}	-0.91	-1.40	-0.77	-0.67
1:10^{-3}	-0.92	-1.87	-1.43	-0.69
1 :10^{-4}	-0.90	-1.38	-0.93	-0.67
0:1 untreated	-0.47	-11.0	-0.35	-
0:1 (1st scan)	-0.51, -0.90	-0.315, -1.07	-0.35	-0.47
0:1 (3rd scan)	-0.98	-1.46	-0.35	-0.73
1:0	-0.89	-1.49	-1.12	-0.69

*Current density measurements are based on a geometric surface area of the working electrode

From Table 4, it becomes clear that similar to the observations made for the DNA/GC working electrode, following carbonisation, the onset potential for the HER (pH 3) is significantly reduced for all the cisPt loadings employed in the DNA-cisPt films. Furthermore, the electrocatalytic activity i.e. J_p is much higher over the surface of the carbonised films compared to before its treatment, due to the highly resistive nature of the material prior to the pseudo pyrolysis process. To explore whether the mass loading of the platinum metal (i.e. cisPt loading) in the material is influencing the catalysis significantly, the electrochemical parameters defined in Table 4 are graphically constructed as a function of cisPt loading as shown in figure 10.

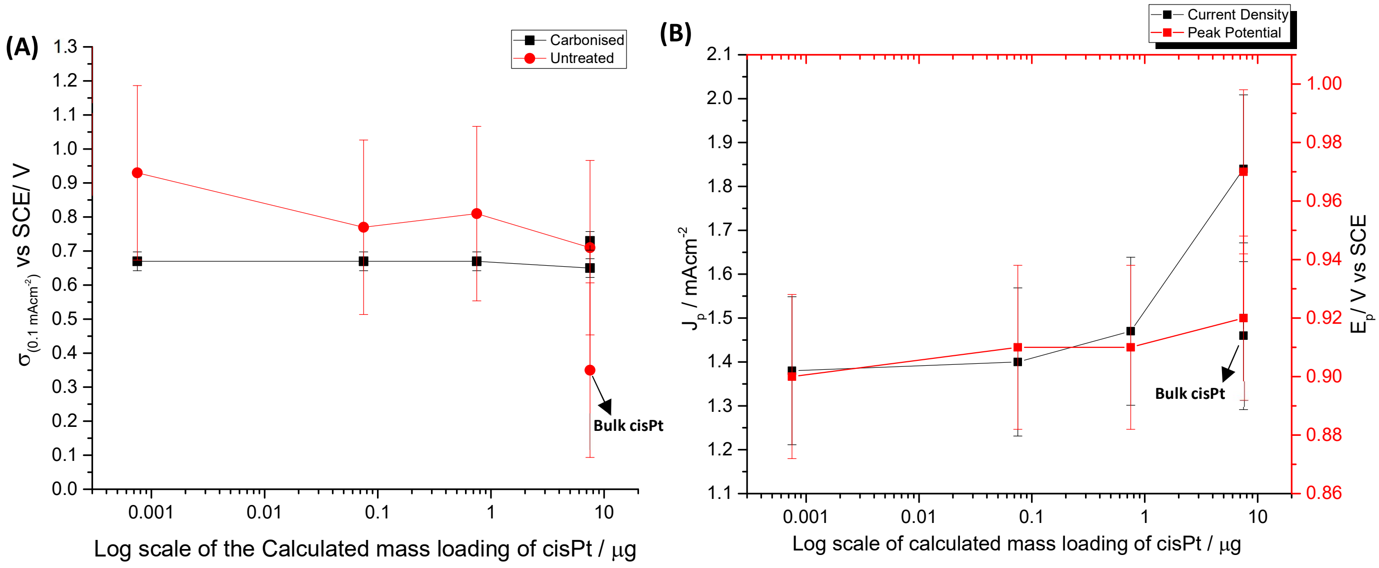

Figure 10- *The variation in (A) onset potential ($\sigma_{0.1\ mAcm^{-2}}$) (B) peak current density (J_p) and peak potential (E_p) as a function of cisPt loading in the DNA–cisPt material following carbonisation (255 ° C, 30 minutes) compared to the untreated DNA-cisPt based material.*

From figure 10 (A) it is evident that for the range of cisPt loadings studied i.e. platinum metal loading ranging from 0.75 ng to 7.5 µg , the onset potential does not drastically change with metal content following carbonisation of the DNA-cisPt material (from -0.67 V to -0.65 V vs SCE), see Table 4. Similarly, we find that changes in the peak potential are statistically insignificant with cisPt loading, ranging from -0.9 to -0.92 ± 0.01 V vs SCE, as illustrated in figure 10(B). Alternatively, the electrocatalytic activity i.e. peak current density (J_p) increases with the cisPt loading (excluding the bulk cisPt response) from -1.38 to -1.84 mA cm^{-2} following carbonisation of the material as shown in figure 10(B).

It can be proposed that this results because of the dependence of the catalysis of an electrochemical process on the inter-particle distance between the catalyst sites. For example, it has been reported by Chumillas et al. that for the catalysis of the oxidation reactions of formic acid and ethanol, full catalytic activity was observed when the inter-particle distance of the Pt nanoparticles on the carbon support was higher than 20 nm (40). Thus a similar idea is proposed here for the HER i.e. that as the loading of the cisPt is reduced, the inter-particle distance is increased between the platinum nanoclusters i.e. towards the ideal inter-particle spacing resulting in higher current density (J_P) outputs.

However, the heat treatment of the material in the absence of DNA i.e. bulk cisPt, produces a much lower current density output (J_P). It can be proposed that this reduced electrocatalytic activity (compared to the catalytic response before the pseudo pyrolysis) can arise from the increased clustering of the platinum which reduces the diffusion flux of the reactants (H^+) to the internal parts of the catalyst surface (41) resulting in a reduced access to the active sites of the platinum. The continued diffusion and consequently increased agglomeration of the platinum metal result in further deviations from both the preferred geometry and ideal particle size for the catalysis of the HER. A more detailed discussion on this, specific to the HER in acidic conditions has already been made in chapters 4 and 5.

To carry out a further in depth analysis and understanding of the changes in the electrochemical performance with cisPt loadings, correlations could be made with the resulting changes to the surface morphology of the material i.e. the size of the platinum nanoclusters following carbonisation via pseudo pyrolysis. This is detailed in the following section.

7.4.7.2 How the changes in the surface morphology of carbonised DNA-cisPt changes with cisPt loading

Initially, STEM imaging of a heat treated blank holey carbon TEM grid was made (blank experiment) to rule out any characteristics in the surface morphology of this substrate from being associated with the morphology we observe when testing the DNA-cisPt material that is casted on it, see figure 11 (F). Appendix 4, figure A4.5 illustrates the range of the surface characteristics resulting to the TEM grid as a result of its heat treatment. This enables us to effectively distinguish between the resulting changes to the carbon in the TEM grid substrate from the carbon in the drop cast films of our DNA-cisPt based material following heat treatment, see figures 11 (A-E).

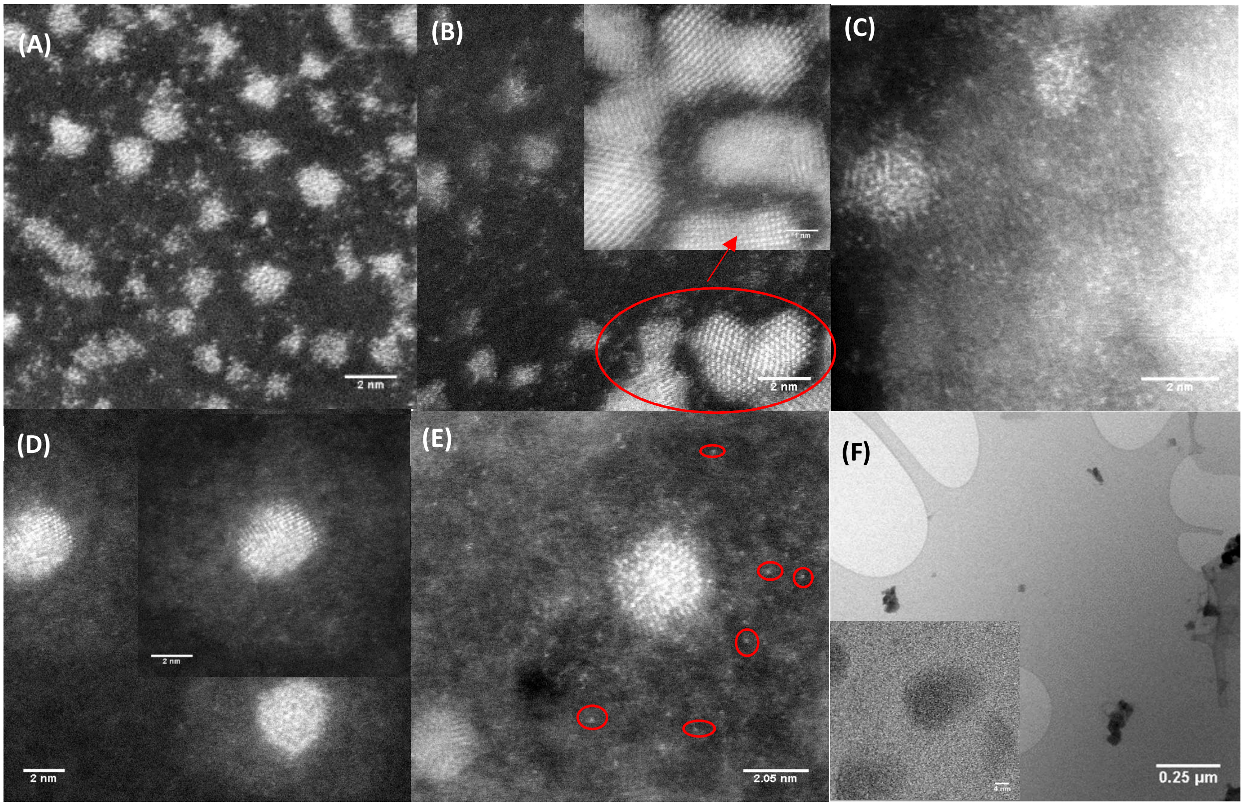

Figure 11- *(A, B) untreated bulk cisPt solution (1 mM) (C) 1 mM cisPt carbonised at 255 °C, 30 minutes (D) 1 to 1 DNA-cisPt carbonised at 255 °C, 30 minutes (E) 1 to 10^{-3} DNA-cisPt carbonised at 255 °C, 30 minutes drop cast on 300-Mesh Cu Holey Carbon TEM grid (F) blank 300-Mesh Cu Carbon TEM grid carbonised at 255 °C, 30 minutes.*

The influence of the temperature conditions on the surface morphology of platinum has previously been studied by Guo et al. (42), for a wide temperature range (200 – 800 °C) (42). From their experimental work, they found that for ultra-thin layers of platinum films casted on a TiO_2-terminated $SrTiO_3$ (001) substrate, the morphology was changed from that of thin continuous films to much larger nanoclusters as the temperature was increased. This is similar to the findings we made previously in this chapter, and specifically the observations noted for the 1 to 10^{-3} DNA-cisPt material. However, focusing on the resulting changes to the platinum nanoparticle size following heat treatment in the absence of DNA, we find that despite the significant change in the voltammetry (unfavourable), surprisingly, the size of the observed platinum nanoclusters is not changed significantly following its heat treatment, (comparing the morphology of the material in figures 11(A &B) to that in figure 11(C)). By measuring the size of the platinum nanoclusters in figures 11(A) & (C) using the tools in Image J, we find that an average size of 1.76 ± 0.27 nm is found for the platinum nanoclusters following heat treatment of the material (255 °C, 30 minutes) which is comparable to the average diameter of the untreated cisPt (1.81 ± 0.26 nm) of the same concentration found (see chapter 4), based on 27 measurements and a standard deviation error. These values are within the range of the measurements reported in the literature for platinum nanoclusters in the cisPt molecule i.e. 1.84 nm (43).

7.4.7.3 Changes in the platinum nanocluster size in the carbonised DNA-cisPt material

In the presence of DNA, the carbonized material has platinum nanoclusters of a much larger size i.e. an average nanocluster diameter of 3.51 ± 0.04 nm (figure 11 (D)) compared to in its absence i.e. carbonised cisPt (figure 11(C)). Thus it becomes clear from these observations that the heat treatment results in changes to the surface morphology of the material and that the increased size of the platinum nanoclusters following heat treatment is much more significant in the presence of DNA (figure 11(C) vs. (D)).

Furthermore, the morphology of the material is also influenced by the metal loading, whereby an average diameter of 2.46 ± 0.25 nm was measured for the platinum nanoclusters in the 1 to 10^{-3} DNA-cisPt carbonised material as opposed to 3.51 ± 0.04 nm in the carbonised 1 to 1 DNA-cisPt material. In addition, at a lower platinum metal loading, we are more likely to observe localised individual platinum atoms (highlighted in figure 11(E)) compared to a higher platinum loading (figure 11(D)). These findings support the trends in figure 10, whereby despite the 1 to 1 DNA-cisPt having a much higher cisPt loading, the nanocluster size of the platinum catalyst at a lower metal ratio i.e. < 1:1 DNA-cisPt, is closer to the ideal platinum catalyst size of 2.2 nm for the HER under acidic conditions (38) . From an electrochemical standpoint it has been estimated that a minimum of 5 atoms of Pt are required to electrolyse acidic solutions (44) which suggests that at lower platinum loadings, the DNA-cisPt films may reduce to form large enough clusters sufficient for the HER. This phenomena has previously been explained in chapter 4.

7.4.7.4 Surface morphology of carbonised DNA

The more interesting result is in the small variation in the onset potential of carbonised DNA compared with the metal containing carbonised DNA-cisPt material. Specifically, the higher current density output measured at the surface of the carbonised DNA compared to $\leq 1:10^{-1}$ DNA-cisPt loadings is particularly interesting and requires further investigation. Additionally, a lower peak potential (E_p) is measured for the carbonised DNA compared to $\leq$ 1:1 carbonised DNA-cisPt films, suggesting great potential in the use of carbonised DNA as a metal free electrocatalyst.

These findings can be further understood by investigating the resulting changes to the surface morphology of the DNA following its carbonisation. The lattice structures and rings observed in the surface morphology of the carbonised DNA (figures 11 (B) &(C)) compared with the amorphous carbon in the virgin untreated DNA film imply the development of a new material following this heat treatment process. A range of different surface morphologies are observed across the TEM grid surface via STEM imaging characterisation as shown in figures 12(B) &(C). See appendix 4 for the range of surface morphologies observed via STEM imaging of the carbonised DNA films.

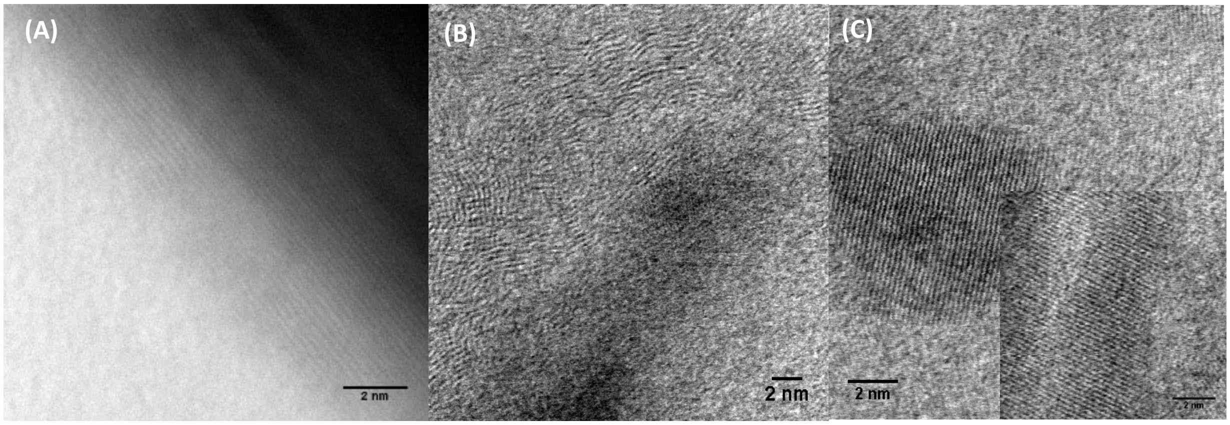

Figure 12- *STEM imaging in Bright Field (BF) mode of 3 µL films of (A) 1 mM virgin untreated DNA solution (B,C) carbonised 1 mM virgin untreated DNA solution (255 °C, 30 minutes) drop cast on 300-Mesh Cu holey carbon TEM grid.*

7.4.8 Measurement of lattice spacing: FFT and D-spacing functions

To characterize this material accurately, the lattice spacing's measurements can be attributed to a spacing that it corresponds to in the literature. For the range of morphologies observed, a built in tool based on the Fast Fourier Transform (FFT) function in image J enables lattice spacing measurements to be made. By moving the cursor to the point on the plane that represents a lattice, the spacing can be found and is displayed in the status bar as illustrated in figure 13 (A) & (B).

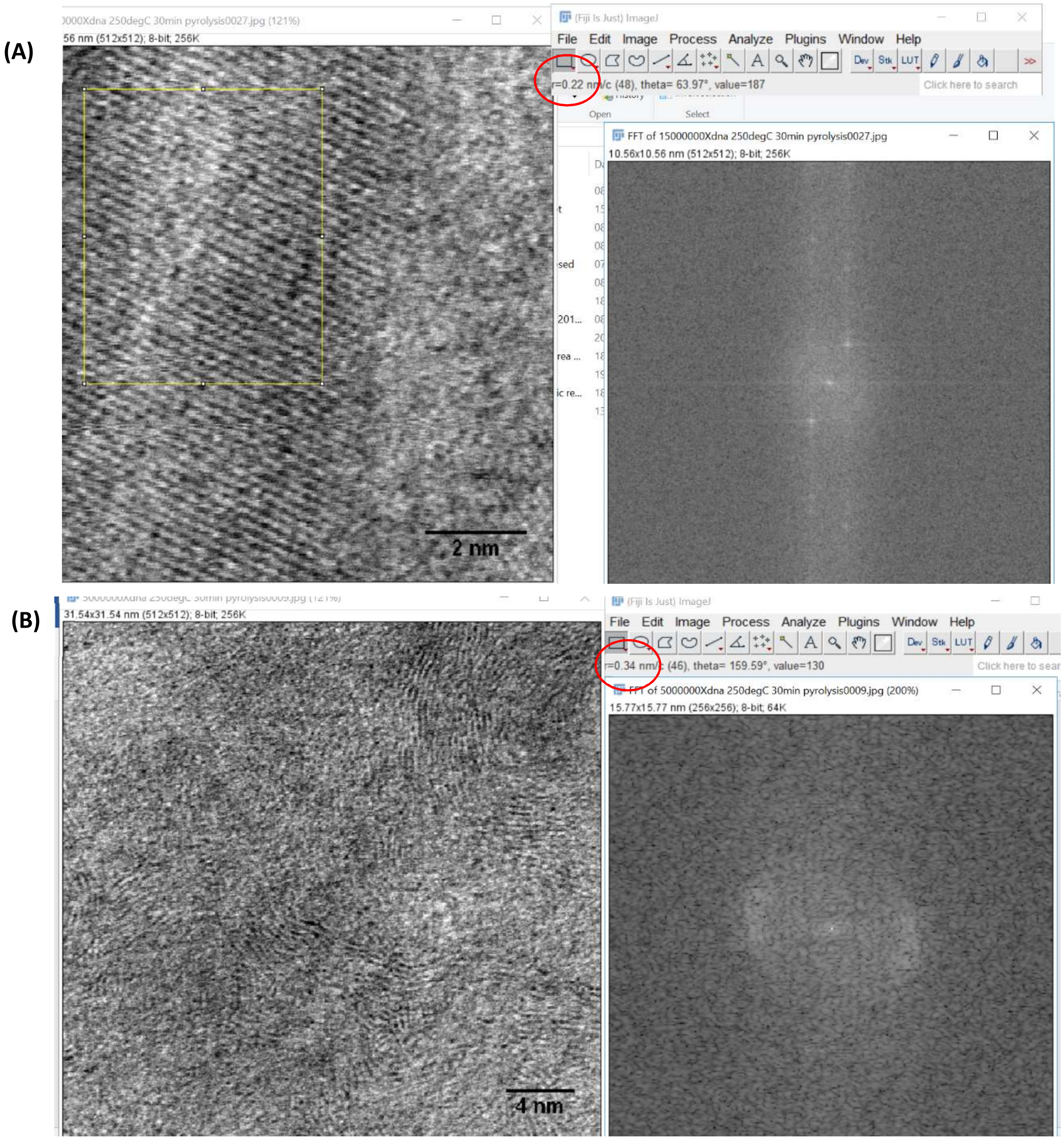

```
r=0.22 nm/c (48), theta= 63.97°, value=187
```

```
r=0.34 nm/c (46), theta= 159.59°, value=130
```

Figure 13- *STEM Imaging characterization of the lattice spacing of carbonised DNA (255 °C, 30 minutes) using Fast Fourier Transform in image J (A) Onion-carbon regions (B) Graphitic like region.*

These measurements were further consolidated using another measuring tool in Image J known as the d-spacing tool, to support the measurement findings using the FFT function. An example of the produced d-plot from the line drawn across the area of interest on the STEM image is shown:

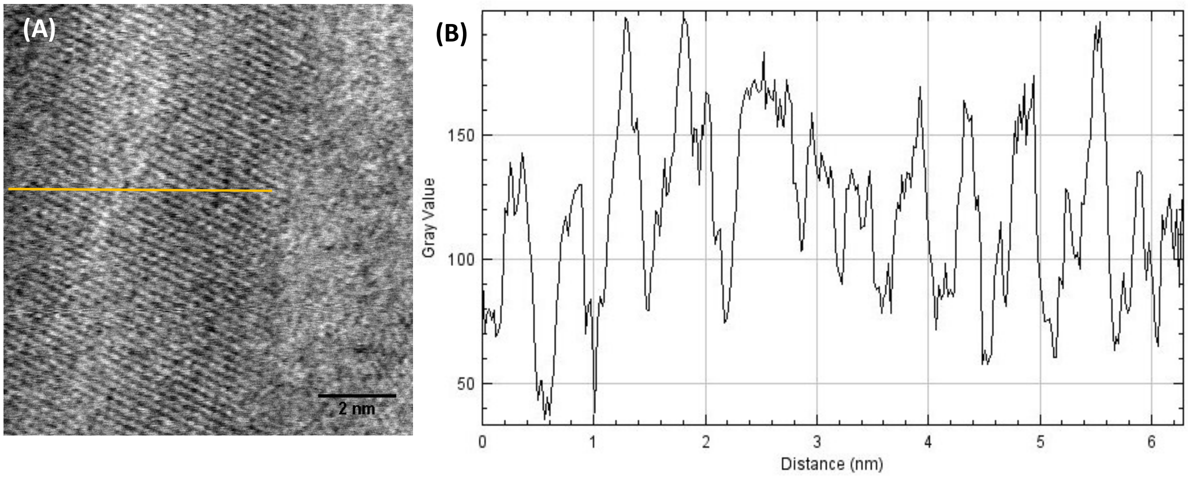

Figure 14- *STEM HAADF imaging in bright field (BF) mode of 3 µL of (A) 1 mM virgin untreated DNA solution carbonised (255 °C, 30 minutes) (B) Corresponding d-plot for lattice spacing using the d-spacing tool in Image J.*

The d-spacing i.e. distance per number of points is found from the graph displayed in figure 14 (B) and corresponds to a lattice spacing of 0.206 nm. This is in line with the measurements found using the FFT function (figure 13). These measurements are also made for the 1 to 10^{-3} DNA-cisPt, the 1 to 1 DNA-cisPt and the 1000 µM cisPt, all carbonised at the optimum reaction conditions (255 °C, 30 minutes). In addition, the lattice spacing of the untreated cisPt (1000 µM) using the FFT function and the d-plots was also found, and are presented in Table A4.1 in appendix 4.

7.4.8 Literature reportings on lattice spacing

The pseudo pyrolysis process of a complex polymer like DNA will inevitably lead to challenges being faced when trying to ascertain the resulting material being made purely from the morphology that the material develops following its heat treatment i.e. pseudo pyrolysis process. It has been reported in the literature (45) that heat treatment of carbonaceous materials such as aromatics, phenolic and polymeric hydrocarbons commonly results in the formation of carbon black. A more complex morphology is normally observed in polygonised carbon black prepared by pseudo pyrolysis. This is reported by (45) to be a complex three dimensional interweaving net of graphite-like layers. Therefore on some regions we may find that regions of carbon black found in the amorphous carbon film may contain poorly crystallized regions of the graphite-like structure (45) as shown below:

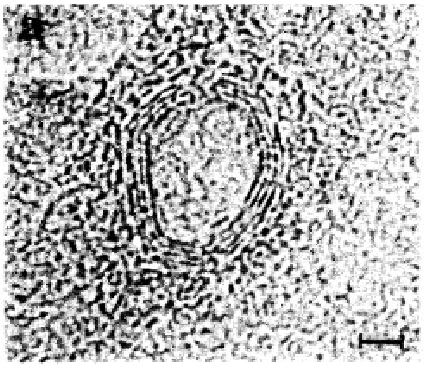

Figure 15- *HR-TEM image of a hollow shell made up four layers of graphite, which are surrounded by a layer of amorphous carbon. Markers indicate a scale of 20 Angstroms, copied from Iijima* (45).

The structure of the starting material influences how graphitic the final product made is. For example, thermal decomposition of aromatic rings are more likely to result in the growth of regions of a graphitic-like structure via a graphitization process since the hexagonal ring is preserved considerably during the decomposition process. Commonly, a lattice spacing of 0.34 nm is normally reported for graphite (45). These literature reportings suggest that the region on the TEM grid containing the carbonised DNA in figure 13 (B) has a lattice spacing of graphitized carbon.

On the other hand, a lattice fringement spacing of an average of 0.21 nm corresponds to the lattice spacing commonly reported for nano-diamond (ND) particles (46). The arrangement of crystalline carbon with a lattice spacing of 0.21 nm in ND as reported in the literature (46) is shown in figure 16(A &B). This can be correlated well with the surface morphology of the virgin sm-DNA films (see figure 16 (C)) that are casted and subsequently heat treated (255 °C, 30 minutes) on the TEM grids, where a lattice spacing equivalent to 0.21 nm can also be measured using the FFT function as shown in figures 16 (D &E).These lattice spacing measurements are consolidated with further measurements made using the d-plot function to equate to a 0.213 nm spacing, see figure A4.19, appendix 4.

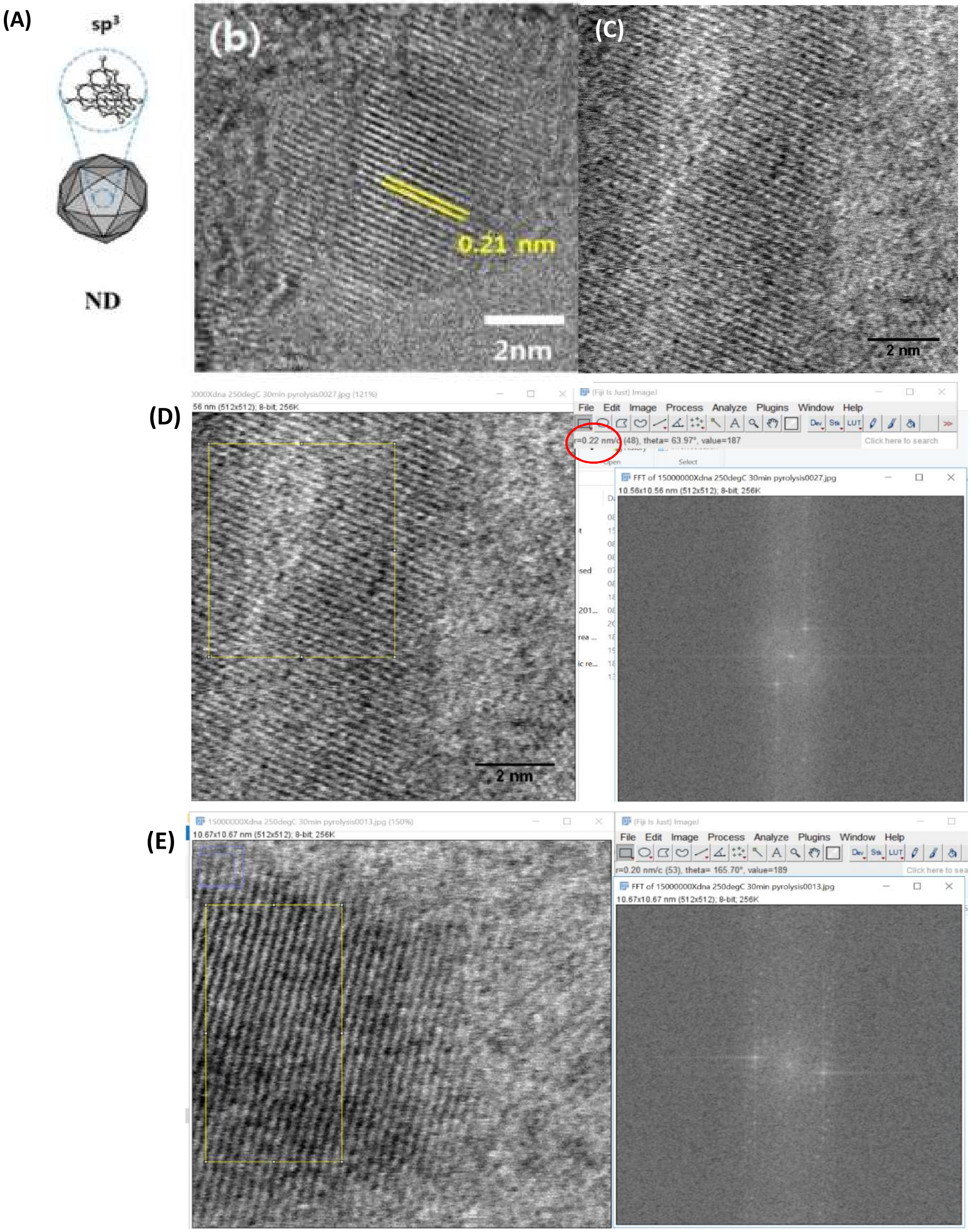

```
r=0.22 nm/c (48), theta= 63.97°, value=187
```

```
r=0.20 nm/c (53), theta= 165.70°, value=189
```

Figure 16 – *(A) Literature reportings of a schematic diagram of Nano Diamond (ND) and (B) HR-TEM photomicrographs of the lattice spacing of the Nano Diamond (ND) copied from Choi & Kim* (46). *STEM imaging of 1000 μM virgin DNA solution used in this work cast on holey carbon TEM grid and subsequently heat treated at 255 °C, 30 minutes at a magnification of (C) 15 million (D) 20 million (E) 15 million and their corresponding FFT measurements.*

Therefore, we can conclude that the carbonisation of the DNA polymer results in the fabrication of a carbon based material with a complex surface morphology consisting of regions of graphitic character. It can be proposed that based on the findings from the lattice space measurements, (figures 13(A) and 14), we may have also fabricated regions of nano-diamond structures via this pseudo pyrolysis process. However, there is a need for further testing of the material, such as its chemical composition via X-ray Diffraction (XRD) and or X-ray Photoelectron Spectroscopy (XPS) to validate these observations being made.

It can be proposed that depending on which component/region of the DNA is being exposed during the STEM imaging process, i.e. the phosphate backbone or the nucleotide bases, non-uniformity in the morphology is likely giving rise to the different lattice spacing measurements we obtain. In addition, the nature of the drop-casting techniques could result in a non-uniform film thickness across the carbon TEM grid which can affect the morphology observed. To discover the chemical nature of the material that is developed following carbonisation via a heat treatment process, Raman spectroscopy and X-ray Photoelectron Spectroscopy (XPS) analysis are employed to investigate the chemical composition of the material and consequently validate the findings of the lattice space measurements from the STEM imaging characterisation.

7.4.9 Raman spectroscopy

A volume of 42 µL of 1 mM virgin DNA solution was drop cast onto GC stubs of 5 mm diameter to prepare the sample for carbonisation. The material was consequently carbonised via a pseudo pyrolysis process at 255 °C for a duration of 30 minutes and consequently loaded into the chamber of the Raman spectroscopy instrumentation operating at the conditions specified above, see materials and experiments section. The following Raman spectrum was produced and is presented in figure 17(B) below.

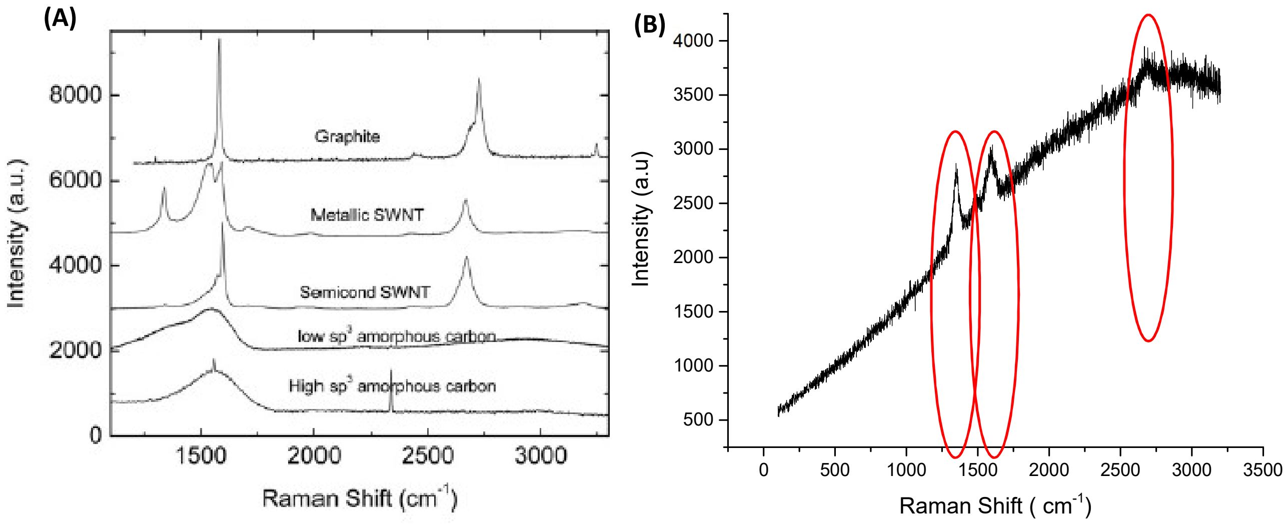

Figure 17- *Raman spectra of graphite, metallic and semi-conducting carbon nanotubes, low and high sp^3 amorphous carbon, copied from Ferrari* (47) *(B) Raman Spectra of carbonised 1mM DNA drop cast on GC (d=5 mm) (255 °C, 30 minutes).*

It was reported by (47) that for graphene and graphite based materials, the appearance of the peaks on the spectra commonly occur at the regions shown in figure 17 (A). Comparing and contrasting between the appearance of the peaks and regions that they occur at, we find that there is close resemblance to the spectra of the carbonised DNA with the spectra reported for graphite in the literature, as opposed to the other materials shown. The small peak around 2725 cm^{-1} and the two peaks around the 1500 cm^{-1} could be associated with a material of a graphitic character. However, although the results are promising conclusive remarks from these results cannot be made confidently, thus repeated testing is required to attain an improved signal with reduced noise in the spectra shown in figure 17(B). In addition, specific testing for surface defects is suggested as future work recommendations via Raman spectroscopy and XPS. This will detect whether the presence of defects such as oxygen vacancies or nitrogen are responsible for the improved electrocatalysis observed following heat treatment.

7.4.10 XPS characterization

In order to gain an insight into the chemical changes resulting from the carbonisation of the DNA-cisPt material via pseudo pyrolysis, XPS testing is carried out for the 1:10^{-4} DNA-cisPt and 1 mM virgin DNA films to explore whether the presence of platinum metal has an effect on the chemical composition resulting from heat treatment of the material. The XPS characterization of the untreated material has been discussed previously in chapter 3. The samples were prepared for XPS characterisation by drop casting 42 µL of the material onto a polished GC stub and consequently drying under a lamp. The prepared films were then carbonised by placing into a furnace operating under an inert nitrogen atmosphere set at 255 °C for a duration of 30 minutes. The samples were sent for characterisation by Harwell XPS facilities (UK), where the sample preparation and testing took place. The aim of XPS characterization is to discover whether following pseudo pyrolysis, the DNA is affected and changed to acquire more graphite-like characteristics. The results in figure 18 display the XPS results for the C 1s spectra.

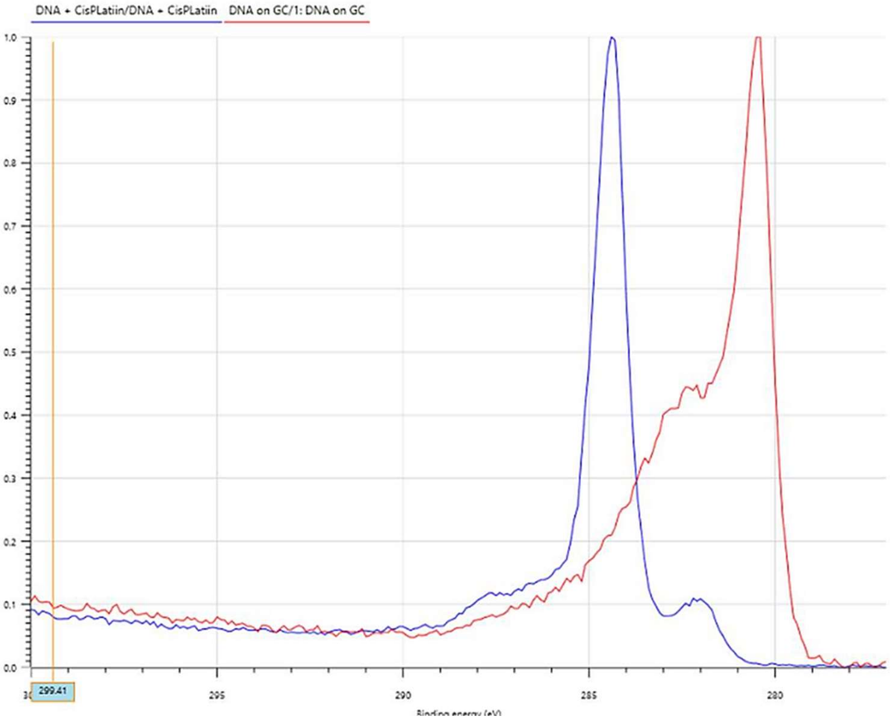

Figure 18- *XPS C 1s spectra for carbonised material via heat treatment on drop cast films on GC (Blue) 1 to 10^{-4} DNA-cisPt and (Red) 1000 µM sm-DNA (255 °C, 30 minutes).*

From figure 18, it is evident that there is a large difference in the carbon spectra of the DNA compared with that of the DNA in the presence of platinum. A material can be described as being graphitic if it consists of regions of sp^2 and sp^3 character (27). It has been reported by Sokolov et al. (27) that the area under the curve of the peak at 284.5 eV can assigned to the sp^2 contribution /ratio in the material, while the area under the peak centred between 285.0 and 285.5 eV is assigned to the sp^3 character. This has also been detailed before in chapter 6. The 1 to 10^{-4} DNA-cisPt reports a much higher sp^3 carbon content and around 14 % sp^2 carbon, while the DNA material appears to be predominantly graphitic. Future work, focusing on repeating the XPS tests for the range of platinum loadings used in this study is recommended.

7.4.11 Electrochemistry of the carbonised DNA compared with a nitrogen, phosphorus doped carbon

The use of DNA has previously been reported as a precursor material for the synthesis of nitrogen doped carbons (48). Previous findings made on the pyrolysis of DNA have shown that as the pyrolysis temperature increased, the nitrogen content in the material increased and high amounts of pyridinic-N and graphitic-N could be produced particularly at high temperatures (800 °C) (48).

Pyridinic-N and graphitic-N are two types of nitrogen species that can be identified at the atomic level. Pyridinic-N refers to N bonded to two C nearest neighbours, while graphitic-N refers to N bonded to three C nearest neighbours (49). It has therefore been claimed that following carbonisation, different amounts of N-bonding configurations are formed leading to higher contents of pyridinic-N and graphitic-N and consequently improving the electrocatalytic performance for the oxygen reduction reaction (ORR) (48), which is a more commonly studied electrochemical reaction.

Similarly for the HER, it has been reported that an improved performance of the phosphorous nitrogen doped graphene (PNG) can be attributed to the higher crystallinity and better distribution of a large number of catalytic active sites i.e. pyridinic-N on the material (50).

It can therefore be proposed that DNA in this study acts as a precursor material for a nitrogen and phosphorous doped carbon, which following carbonisation is converted to acquire characteristics of a graphitic carbon. Following heat treatment, the resulting changes to the nitrogen configuration in the DNA gives rise to an improved electrochemical performance, which is equivalent to the performance attainable by a platinum metal containing DNA-cisPt material.

In addition, Hung et al. (51) showed that a phosphorous-nitrogen doped graphene had a higher performance than individually doped nitrogen or phosphorous graphene due to the combination of higher crystallinity, the P-C bonds being in proximity to graphitic-N, and a higher fraction of pyridinic-N which could create a synergistic effect (51). Therefore, we can suggest that in a DNA-cisPt material, the interactions of Pt with the nitrogen in the DNA suppress electronic contributions from being made by the nitrogen atoms such that the catalyst support becomes equivalent to a phosphorous doped graphene as opposed to a NP-doped carbon in the absence of cisPt. This is supported with the literature reportings (52) for the ORR where for the graphitized nitrogen-carbon nano-onion rings, the enhancement in the activity of the material is assigned to the improved electron transport and abundance of exposed catalytic sites, resulting from the mesoporosity and doping of the heteroatom.

7.4.12 Mechanism of the Hydrogen Evolution Reaction (HER)

7.4.12.1 Tafel Plots at 50 mV s^{-1}

To further compare how the electrocatalytic behaviour changes following carbonisation of the material, we assess the mechanism of the reaction by considering the changes in the magnitudes of the Tafel slopes. Tafel plots were constructed to reveal the reaction mechanism of the HER at each working surface based on the theoretical information provided in the literature (53),(54) and (55) and has already been discussed in detail in chapters 2-6. From the Tafel plots, the magnitude of the Tafel slope can be found and expressed as a function of cisPt loading as shown in figure 19, which compares the magnitude of the slope to the widely accepted and reported theoretical limits. The rate determining reactions for the Volmer, Heyrovsky and Tafel steps correspond to a Tafel slope of 120, 40 and 30 mV dec^{-1} respectively. Table 6 presents the corresponding Tafel slope for each material tested.

Table 6*-The changes in the Tafel slope found before and after heat treatment (255 ° C, 30 minutes) and before and after e-beam irradiation (5 keV, 24 minutes) at the different DNA-cisPt loadings.*

DNA-cisPt ratio/GC modified surface	***Tafel slope of Untreated material / mVdec^{-1}***	***Tafel slope of heat treated material / mVdec^{-1}***	***Tafel slope of e-beam irradiated material / mVdec^{-1}***
Bare GC	149	-	-
DNA (1 mM)	425	138	331.1
$1:10^{-4}$	395	152	107.9
$1:10^{-3}$	381	-	114
$1:10^{-2}$	381	179	137.3
$1:10^{-1}$	331	170	133.7
1:1	327	157	50.4
cisPt (1 mM)	68.6	142	-
Pt UME	27.3	-	-

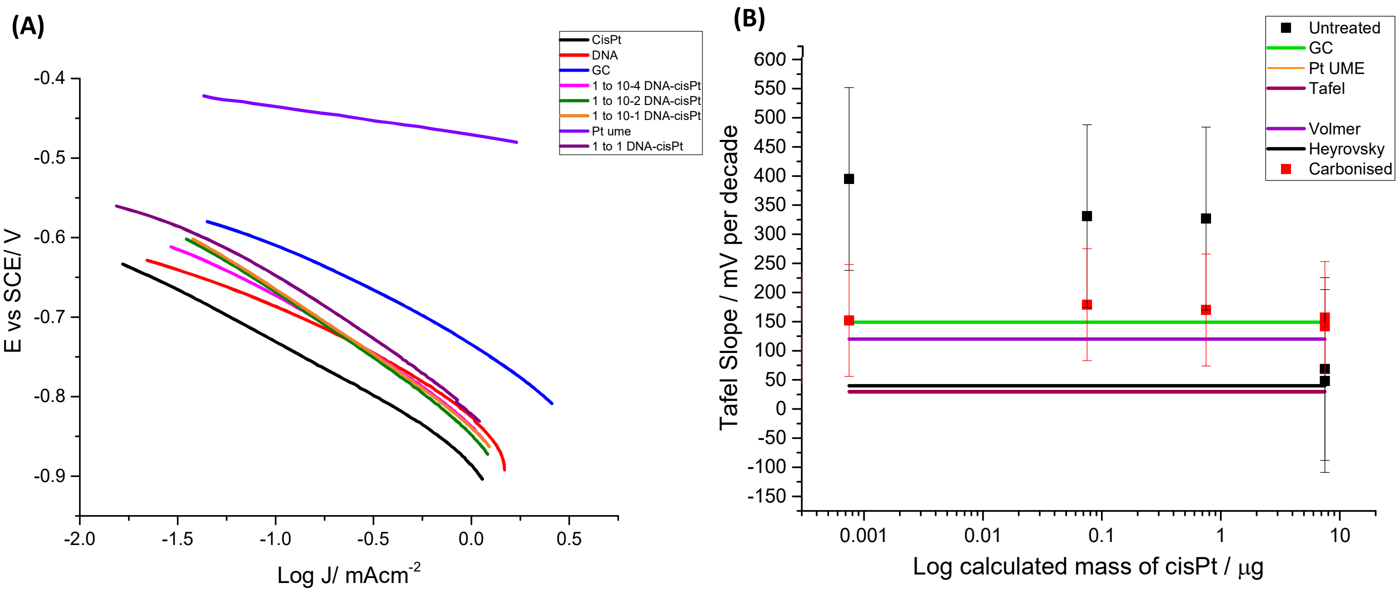

Figure 19*- (A) Tafel plots for HER (1 mM $HClO_4$, 0.1 M $NaClO_4$) 50 mVs^{-1} carbonised via a pseudo pyrolysis process at 255 °C, 30 minutes (B) The variation in the Tafel slope as a function of the calculated cisPt loading in the material before and after carbonisation (255 ° C, 30 minutes) and how it compares against the well reported slopes of the theoretical mechanisms proposed in the literature.*

The most obvious correlation that has also been noted in chapter 4, is that with increased platinum metal loadings, there is a reduction in the magnitude of the Tafel slope as we move to the maximum platinum loading i.e. bulk cisPt. This reflects the change in the mechanism of the apparent rate limiting step for proton reduction i.e. from a Volmer to a Heyrovsky mechanism, see Eq. (7) & (8) respectively in chapter 4. The more interesting result is the significant reduction in the Tafel slope for a given cisPt loading following carbonisation of the material via pseudo pyrolysis.

This is also reflected in the change of reaction mechanism of the HER in figure 19(B). This entails the transition from a Volmer reaction to a Volmer-Heyrovsky reaction. This corresponds with the experimental observations made previously to suggest that the electrochemical response for the HER is improved following e-beam treatment of the DNA-cisPt material in a similar way to chapter 6 and as shown in the data presented in Table 6.

It is evident that for both the heat treated and e-beam irradiated DNA-cisplatin material, a high Tafel slope is measured (> 120 $mVdec^{-1}$) despite the improved electrocatalytic performance. From literature reportings, high Tafel slopes are commonly attributed to a (highly) porous electrode material such as carbonised porous conducting polymers , where a Tafel slope in the range of 150 - 205 mV dec^{-1} was measured for the HER (56). Similarly, for a 3D porous carbon material a Tafel slope of 154 $mVdec^{-1}$ is reported for HER (in a 0.1 M potassium hydroxide supporting electrolyte (KOH)) (56).

Despite these high Tafel slopes, high electrocatalytic activities can still be attained and have been explained as resulting from the high surface area from the porous and homogeneous morphology of the material for catalysing the HER (57). This is pivotal towards the development of more suited electrocatalyst materials for HER, whereby the porous structure at the nanoscale will provide a large and electrochemically accessible surface area to enable fast charge transfer reactions to take place (58).

7.5 Conclusions

In this work, we have shown that carbonisation of the DNA/GC and DNA-cisPt /GC modified electrode can significantly improve the electrochemical behaviour towards the catalysis of the HER in pH 3, compared to the untreated counterpart. The temperature conditions employed for the carbonisation process of the DNA-cisPt material has a positive correlation with the measured nanocluster size of the platinum metal and this is also reflected in the electrochemical response for the HER. The best electrocatalytic performance is measured at the optimum pseudo pyrolysis conditions of 255 °C for a duration of 30 minutes.

In addition, we find that at reduced loadings of platinum in the presence of carbonised DNA, a smaller platinum nanocluster size is measured for example in the 1 to 10^{-3} DNA-cisPt material compared to the 1 to 1 DNA-cisPt loading.

The carbonised DNA is compared with an N, P-doped graphene, which explains the improved electrocatalytic performance equivalent to that attained in the presence of the platinum metal in the DNA-cisPt films for the HER. The STEM imaging characterization of the resulting carbonised DNA material demonstrates the formation of graphitic features and nano-diamond structures, based on the measurements of lattice spacing's. The XPS characterization reveals that in the absence of cisPt, a predominantly graphitic based material is formed following carbonisation compared to the higher sp^3 content reported in the DNA-cisPt material. From the Raman spectroscopy characterization, we can attribute our experimental findings to those reported in the literature with a Nitrogen Phosphorus doped graphene material.

To conclude, the work presented in this chapter suggests that DNA is a feasible precursor material as a nitrogen/phosphorous doped carbon catalyst support, which can be converted to attain graphitic character following carbonisation. This can enable metal free electrocatalyst to be used for the HER, as we have shown in this work through the attainable electrochemical performance, which is equivalent to that of a platinum metal containing material.

References

1. Nakao H, Tokonami S, Yamamoto Y, Shiigi H, Takeda Y. Fluorescent carbon nanowires made by pyrolysis of DNA nanofibers and plasmon-assisted emission enhancement of their fluorescence. Chem Commun. 2014;50(80):11887–90.

2. Choi J a-Y, Lee Un D, Chen Z. Nitrogen-doped Activated Graphene Supported Platinum Electrocatalyst for Oxygen Reduction Reaction in PEM Fuel Cells. J Chem Inf Model. 2012;2(50):1815–22.

3. Dubouis N, Grimaud AJL. The Hydrogen Evolution Reaction: From Material to Interfacial Descriptors. Chem Sci. 2019;

4. Ozdemir OK. Effect of Sputtering Power on the Electrochemical Properties of Low Loaded Pt Catalysts for PEM Fuel cell. Electrochem Soc Japan. 2015;83(2):76–9.

5. Fofana D, Natarajan SK, Hamelin J, Benard P. Low platinum, high limiting current density of the PEMFC (proton exchange membrane fuel cell) based on multilayer cathode catalyst approach. Energy. 2014;64:398–403.

6. Billy E, Maillard F, Morin A, Guetaz L, Emieux F, Thurier C, et al. Impact of ultra-low Pt loadings on the performance of anode/cathode in a proton-exchange membrane fuel cell. J Power Sources. 2010;195(9):2737–46.

7. Mukerjee S, Srinivasan S, Appleby AJ. Effect of sputtered film of platinum on low platinum loading electrodes on electrode kinetics of oxygen reduction in proton exchange membrane fuel cells. Electrochim Acta. 1993;38(12):1661–9.

8. Yadav R, Subhash A, Chemmenchery N, Kandasubramanian B. Graphene and Graphene Oxide for Fuel Cell Technology. Ind Eng Chem Res. 2018;57(29):9333–50.

9. Qu L, Liu Y, Baek J-B, Dai L. Nitrogen-doped reduced-graphene oxide as an efficient metal-free electrocatalyst for oxygen reduction in fuel cells. asc nano. 2010;4(3):1321–6.

10. Behan JA, Mates-Torres E, Stamatin SN, Domínguez C, Iannaci A, Fleischer K, et al. Untangling Cooperative Effects of Pyridinic and Graphitic Nitrogen Sites at Metal-Free N-Doped Carbon Electrocatalysts for the Oxygen Reduction Reaction. Small. 2019;1902081:1–10.

11. Zheng W, Zhang Y, Niu K, Liu T, Bustillo K, Ercius P, et al. Selective nitrogen doping of graphene oxide by laser irradiation for enhanced hydrogen evolution activity. Chem Commun. 2018;54(97):13726–9.

12. Perini L, Durante C, Favaro M, Perazzolo V, Agnoli S, Schneider O, et al. Metal-support interaction in platinum and palladium nanoparticles loaded on nitrogen-doped mesoporous carbon for oxygen reduction reaction. ACS Appl Mater Interfaces. 2015;7(2):1170–9.

13. Jukk K, Kongi N, Rauwel P, Matisen L, Tammeveski K. Platinum Nanoparticles Supported on Nitrogen-Doped Graphene Nanosheets as Electrocatalysts for Oxygen Reduction Reaction. Electrocatalysis. 2016;7(5):428–40.

14. Kondo T, Suzuki T, Nakamura J. Nitrogen doping of graphite for enhancement of durability of supported platinum clusters. J Phys Chem Lett. 2011;2(6):577–80.

15. Duchemin N, Heath-Apostolopoulos I, Smietana M, Arseniyadis S. A decade of DNA-hybrid catalysis: From innovation to comprehension. Org Biomol Chem. 2017;15(34):7072–87.

16. Mohamed HDA, Watson SMD, Horrocks BR, Houlton A. Chemical and electrochemical routes to DNA-templated rhodium nanowires. J Mater Chem C. 2015;3(2):438–46.

17. Anantharaj S, Karthik PE, Subramanian B, Kundu S. Pt Nanoparticle Anchored Molecular Self-Assemblies of DNA: An Extremely Stable and Efficient HER Electrocatalyst with Ultralow Pt Content. ACS Catal. 2016;6(7):4660–72.

18. Tiwari JN, Nath K, Kumar S, Tiwari RN, Kemp KC, Le NH, et al. Stable platinum nanoclusters on genomic DNA-graphene oxide with a high oxygen reduction reaction activity. Nat Commun. 2013;4:1–7.

19. Ma J, Wang J, Zhang G, Fan X, Zhang G, Zhang F, et al. Deoxyribonucleic acid-directed growth of well dispersed nickel-palladium-platinum nanoclusters on graphene as an efficient catalyst for ethanol electrooxidation. J Power Sources. 2015;278:43–9.

20. Yuan XZ, Song C, Wang H, Zhang J. Electrochemical Impedance Spectroscopy in PEM Fuel Cells: Fundamentals and Applications. Springer London; 2009.

21. Wang B, Wolfe DE, Terrones M, Haque MA, Ganguly S, Roy AK. Electro-graphitization and exfoliation of graphene on carbon nanofibers. Carbon N Y. 2017;117:201–7.

22. Guo X, Gorodetsky AA, Hone J, K. BJ, Nuckolls, Colin. Conductivity of a single DNA duplex bridging a carbon nanotube gap. nat nanotechnol. 2008;3(3):163–7.

23. Zhou F, Sun W, Ricardo KB, Wang D, Shen J, Yin P, et al. Programmably Shaped Carbon Nanostructure from Shape-Conserving Carbonization of DNA. ACS Nano. 2016;10(3):3069–77.

24. Ariga K, Jia X, Shrestha LK. Soft material nanoarchitectonics at interfaces: Molecular assembly, nanomaterial synthesis, and life control. Mol Syst Des Eng. 2019;4(1):49–64.

25. Zhou F. DNA NANOSTRUCTURE BASED NANOFABRICATION. Pittsburgh; 2015.

26. Aoi K, Takasu A, Okada M. DNA-based polymer hybrids. Part 1. Compatibility and physical properties of poly(vinyl alcohol)/DNA sodium salt blend. Polymer (Guildf). 2000;41(8):2847–53.

27. Sokolov AN, Yap FL, Liu N, Kim K, Ci L, Johnson OB, et al. Direct growth of aligned graphitic nanoribbons from a DNA template by chemical vapour deposition. Nat Commun. 2013;4(May):1–8.

28. Zhou F, Sun W, Ricardo KB, Wang D, Shen J, Yin P, et al. Programmably Shaped Carbon Nanostructure from Shape-Conserving Carbonization of DNA. ACS Nano. 2016;10(3):3069–77.

29. Kim H, Surwade SP, Powell A, O'Donnell C, Liu H. Stability of DNA origami nanostructure under diverse chemical environments. Chem Mater. 2014;26(18):5265–73.

30. Sokolov AN, Yap FL, Liu N, Kim K, Ci L, Johnson OB, et al. Direct growth of aligned graphitic nanoribbons from a DNA template by chemical vapour deposition. Nat Commun. 2013;4(May):1–8.

31. Zhou F, Sun W, Ricardo KB, Wang D, Shen J, Yin P, et al. Programmably Shaped Carbon Nanostructure from Shape-Conserving Carbonization of DNA. ACS Nano. 2016;10(3):3069–77.

32. Drevin I, Johansson BL, Son EL. Pyrolysis in biotechnology. Biotechnol Genet Eng Rev. 2001;18(1):3–28.

33. Jarman M. Pyrolysis of Deoxyribonucleic Acid: Isolation and mass spectrometry of individual pyrolysis products. J Anal Appl Pyrolysis. 1980;2:217–23.

34. Al-Muhtaseb SA, Ritter JA. Preparation and properties of resorcinol-formaldehyde organic and carbon gels. Adv Mater. 2003;15(2):101–14.

35. Deng Z, Mao C. Molecular lithography with DNA nanostructures. Angew Chemie - Int Ed. 2004;43(31):4068–70.

36. Englert K. DNA Origami Catalysts. [PhD thesis]. Birmingham (UK): University of Birmingham; 2019.

37. Englert K, Hendi R, Robbs PH, Rees N V., Robinson APG, Tucker JHR. Cisplatin adducts of DNA as precursors for nanostructured catalyst materials. Nanoscale Adv. 2020;

38. Sui M, Li M, Kunwar S, Pandey P, Zhang Q, Lee J. Effects of annealing temperature and duration on the morphological and optical evolution of self-assembled Pt nanostructures on c-plane sapphire. 2017;1–18.

39. Tan TL, Wang LL, Zhang J, Johnson DD, Bai K. Platinum nanoparticle during electrochemical hydrogen evolution: Adsorbate distribution, active reaction species, and size effect. ACS Catal. 2015;5(4):2376–83.

40. Vidal-Iglesias FJ, Montiel V, Solla-Gullón J. Influence of the metal loading on the electrocatalytic activity of carbon-supported (100) Pt nanoparticles. J Solid State Electrochem. 2016;20(4):1107–18.

41. Chumillas S, Busó-Rogero C, Solla-Gullón J, Vidal-Iglesias FJ, Herrero E, Feliu JM. Size and diffusion effects on the oxidation of formic acid and ethanol on platinum nanoparticles. Electrochem commun. 2011;13(11):1194–7.

42. Guo W, Posadas A, Demkov A. Temperature dependence of the morphology and electronic structure of ultrathin platinum on TiO 2 -teminated SrTiO 3 (001) Temperature dependence of the morphology and electronic structure of ultrathin platinum on TiO2-teminated SrTiO3 (001) View onlin. 2017;3(November).

43. Sheader AA, Varambhia AM, Fleck RA, Flatters SJL, Nellist P. Observation of metal nanoparticles at atomic resolution in Pt-based cancer chemotherapeutics. 1865;1–16.

44. Dick JE, Bard AJ. Recognizing Single Collisions of PtCl62- at Femtomolar Concentrations on Ultramicroelectrodes by Nucleating Electrocatalytic Clusters. J Am Chem Soc. 2015;137(43):13752–5.

45. Iijima S. Direct Observation of the Tetrahedral Bonding in Graphitized Carbon Black By. J Cryst Growth. 1980;50:675–83.

46. Choi EY, Kim CK. Fabrication of nitrogen-doped nano-onions and their electrocatalytic activity toward the oxygen reduction reaction. Sci Rep. 2017;7(1):1–9.

47. Ferrari AC. Raman spectroscopy of graphene and graphite: Disorder, electron-phonon coupling, doping and nonadiabatic effects. Solid State Commun. 2007;143(1–2):47–57.

48. Wang H, Bo X, Luhana C, Guo L. Nitrogen doped large mesoporous carbon for oxygen reduction electrocatalyst using DNA as carbon and nitrogen precursor. Electrochem commun. 2012;21(1):5–8.

49. Kondo T, Casolo S, Suzuki T, Shikano T, Sakurai M, Harada Y, et al. Atomic-scale characterization of nitrogen-doped graphite: Effects of dopant nitrogen on the local electronic structure of the surrounding carbon atoms. Phys Rev B - Condens Matter Mater Phys. 2012;86(3):1–37.

50. Gurylev V, Chin T-K, Tsai H-Y. Carbon Nanotubes Decorated with Platinum Nanoparticles for Field-Emission Application. ACS Omega. 2019;4(13):15428–34.

51. Hung Y-H, Dutta D, Tseng C-J, Chang J-K, Bhattacharyya AJ, Su C-Y. Manipulation of Heteroatom Substitution on Nitrogen and Phosphorus Co-Doped Graphene as a High Active Catalyst for Hydrogen Evolution Reaction. J Phys Chem C. 2019;123(36):22202–11.

52. Shaikh A, Singh BK, Mohapatra D, Parida S. Nitrogen-Doped Carbon Nano-Onions as a Metal-Free Electrocatalyst. 2019;222–31.

53. Shinagawa T, Garcia-esparza AT, Takanabe K. Insight on Tafel slopes from a microkinetic analysis of aqueous electrocatalysis for energy conversion. Nat Publ Gr. 2015;(May):1–21.

54. Tavares M., Machado SA., Mazo L. Study of hydrogen evolution reaction in acid medium on Pt microelectrodes. Electrochim Acta. 2001;46(28):4359–69.

55. Marković NM, Grgur BN, Ross PN. Temperature-dependent hydrogen electrochemistry on platinum low-index single-crystal surfaces in acid solutions. J Phys Chem B. 1997;101(27):5405–13.

56. Lahiri A, Li G, Endres F. Highly efficient electrocatalytic hydrogen evolution reaction on carbonized porous conducting polymers. J Solid State Electrochem. 2020;24(11–12):2763–71.

57. Nivetha R, Gothandapani K, Raghavan V, Jacob G, Sellappan R, Bhardwaj P, et al. Highly Porous MIL-100(Fe) for the Hydrogen Evolution Reaction (HER) in Acidic and Basic Media. ACS Omega. 2020;5(30):18941–9.

58. Zeng M, Li Y. Recent advances in heterogeneous electrocatalysts for the hydrogen evolution reaction. J Mater Chem A. 2015;3(29):14942–62.

Chapter 8- Cisplatin DNA Nanostructures for the Electrocatalysis of the Hydrogen Evolution Reaction (HER)

Chapter 8: Cisplatin DNA nanostructures for the electrocatalysis of the Hydrogen Evolution Reaction (HER)

8.1 Introduction

Many research objectives have focused on ways in which the platinum metal can be used to enable improved utilisation of this precious metal and consequently reduce the operating costs of the fuel cell it is used in. The development of the Polymer Electrolyte Membrane Fuel Cell (PEMFC) has been explored by focusing on improving the utilisation of the available platinum catalyst material. This includes increasing the utilisation of the 'true' catalyst surface area on the electrode by: (1) increasing the catalyst layer (CL) thickness for a given Pt catalyst loading or (2) increasing the amount of Pt catalyst in the CL. Through this, increased performance of the electrodes can be established (1). However, they have limitations, for example increasing the CL thickness reduces the attainable rate of diffusion of the electroactive species to the platinum active sites. While increased loadings of the Pt metal in the CL results in an increased particle size of the catalyst hence reducing the attainable fuel cell efficiency (1).

Alternatively, to improve Pt utilisation, other methods have focused on improving the distribution of the catalyst using a metal organic framework (MOF). MOFs are favourable for catalytic applications as they enable high surface areas and distributions of the active metal atoms to be achieved consequently improving the attainable current density (2). In particular, the usefulness of DNA templates and DNA nanofabrication has been emphasised throughout the thesis, and particularly in chapters 2 and 6. This mainly evolves from the ability to assemble complex frameworks via self-assembly using DNA and achieve precise control of the structures down to atomic level. In particular, nanofabrication using DNA has enabled researchers to construct assemblies suited for a use as nanomaterials for redox reactions and for magnetic and catalytic applications (3).

The properties of DNA including its small size and robust structure enable its successful use in nanotechnology. Its application becomes more interesting when fabrication of nanostructures in multiple dimensions is required, for example branched DNA. It has been reported that DNA nanostructures demonstrate great potential as molecular masks for the preparation of nanoscale patterns (4). The use of DNA for fabricating patterns of precise structures is highly desirable for applications such as nano-circuits, nano-sensors and nano-fluidics (4).

In the previous work presented in chapter 4 of this thesis, DNA-cisPt adducts were successfully fabricated using random uncontrolled interactions of the cisPt with the salmon milt (sm)-DNA. Therefore precise placement and control of the metal atoms along the DNA could not be achieved. Alternatively, the work described in this chapter involves a bottom-up synthesis approach to fabricate cisPt DNA nanostructures with a more precise and controlled means of the platinum metal placement. This is achieved by using the well-established and reported chemistry studies on the interactions of the cisPt to the purine bases on the DNA (5,6). Therefore, in-house designed DNA strands of a specific base sequence can be synthesised for the controlled reaction of it with cisPt, to ensure the metal complex binds specifically at the desired site along the DNA, using common methods reported in the literature (7). In this work, this is achieved using two forms of DNA nanostructures, including DNA origami and DNA Holliday Junction (HJ) arrays.

However, a limitation of MOFs is in their highly resistive nature and consequently limited charge transport properties (2). In this thesis, pseudo pyrolysis (i.e. heat treatment) of the DNA at the optimum reaction conditions (255 °C, 30 minutes) was shown to significantly improve the electrocatalytic performance for the hydrogen evolution reaction (HER), see chapter 6. Thus the same processing procedure will be employed for the fabricated DNA nanostructures presented in this chapter. The distribution of platinum in the fabricated DNA nanostructures i.e. DNA origami triangles and DNA HJ arrays is compared and contrasted with the distribution attained on the sm-DNA scaffold using Scanning Transmission Electron Microscopy (STEM) imaging with Energy Dispersive X-ray Spectroscopy (EDX) mapping.

8.1.1 Holliday Junction arrays (HJ arrays)

Holliday junctions are important structural intermediates in recombination, viral integration, and DNA repair (8).The Holliday junction is made up of four DNA strands, bound together to form four double-helical arms (9). These structures were originally proposed by Holliday and have been fabricated and used in the literature (8), (10), (11), (12) and (13). In addition, DNA structures can be used to precisely arrange metal atoms as demonstrated with gold (14). The ultimate goal of this work is to synthesise a precursor catalyst material with optimum electrocatalytic activity at the lowest platinum loading possible.

The Holliday junction contains four DNA strands (where each member of a pair of aligned homologous chromosomes is composed of two DNA strands) bound together to form four double-helical arms flanking at a branch point. The idea is simple and involves using synthetic branched DNA molecules with programmed sticky ends which then self-assemble into the desired structure. This can be a closed object or a crystalline array (9). This has been explained in greater detail in appendix 5.

8.1.2 DNA Origami

The first report of the assembly of DNA into programmable nanostructures and in particular the DNA origami triangle was made by Rothemund (2006) (15). These DNA origami structures were explored further by (16), leading to the DNA origami being reported as a good template for bottom up fabrication at high resolution levels. These literature reports initiated our design idea for a platinum decorated DNA origami triangle material for use as an electrocatalyst for the HER, as shown in this work.

8.2 Materials and experiments

8.2.1 Material Synthesis

All the material processed and characterised in this work was synthesised and provided by Klaudia Englert, School of Chemistry, University of Birmingham (17) . An overview of the experimental methods used by Englert (17) to achieve the material is provided in appendix 6.

Experimental work

The material received was experimentally tested and characterized by the author of this thesis in the experimental methods described below.

8.2.2 Electrochemical testing

The prepared samples were electrochemically tested using a 3 electrode cell, involving a glassy carbon electrode (GC, 5 mm, BASi) as the working, a saturated calomel (SCE, BASi) reference and a bright platinum mesh counter electrode. The cell was controlled by an Autolab 128N potentiostat running Nova 2.1 software (Metrohm-Autolab BV, Netherlands). All potentials are reported against a SCE. All chemicals involved were used in their analytical grade and used without any purification. Perchloric acid (70 %, 99.99 % trace metals) (1 mM, pH 3) and sodium perchlorate (≥ 98 %) as the supporting electrolyte (0.1 M) supplied by Sigma Aldrich. All electrolytes were made up with deionised water (DIW) (resistivity ≥ 18.2 MΩ.cm) (MilliQ, Millipore) and thoroughly degassed with dry nitrogen (oxygen-free, BOC Gases plc) prior to experimentation.

8.2.3 Dry film preparation on Glassy Carbon (GC)

A series of glassy carbon (GC) stubs (d=5 mm) were polished on microcloth pads in order of decreasing size of alumina slurry (1.0, 0.3, 0.05 µm, Buehler Inc., IL, USA), followed by rinsing with ultrapure water and drying under a gentle flow of nitrogen. Once dry, the electrodes were modified by drop casting an aliquot of 20 µL of the prepared DNA-cisPt nanostructured material onto the 5 mm GC stub and drying under a lamp. Once the stubs were prepared, they were loaded into the furnace to achieve carbonisation of the material.

8.2.4 Low temperature pseudo pyrolysis process

The low temperature pseudo pyrolysis of DNA was achieved in quartz tube within a tubular Carbolite MTF 12/38/400. The DNA-cisPt nanostructure films prepared by casting the solutions onto the GC stubs, as detailed above and subsequently loaded into a corundum boat which was then placed in a tubular furnace, operating under an inert nitrogen atmosphere purged at 50 mL min^{-1}. All the samples were carbonised at the optimised reaction conditions found of 255 °C for 30 minutes, see chapter 7.

8.2.5 Electron Microscopy

To study the morphology of the material and explore how the distribution of the platinum changes between the different DNA scaffold structures employed, Scanning Transmission Electron Microscopy (STEM) imaging was used to achieve resolution at an atomic scale. A JEOL2100F instrument was used, using both dark field (DF) and bright field (BF) mode operated in Z-contrast mode using a high angle annular dark field (HAADF) detector at a 200 keV acceleration voltage. All stage alignment was achieved using gold nanoparticles on a copper holey carbon TEM grid, as detailed before in chapter 4. Dry films of HJ, HJ-cisPt, DNA-cisPt origami and 1 to 10^{-3} sm-DNA-cisPt adducts were prepared individually by drop casting 3 µL of the solution onto a holey carbon 300 mesh copper TEM grid and drying under a lamp. To improve the contrast of the DNA in the imaging, the prepared TEM grids of the HJ, HJ-Pt and 1 to 10^{-3} sm-DNA-cisPt were further processed via a pseudo pyrolysis reaction (heat treatment at 255 °C for 30 minutes) in a furnace operating under an inert nitrogen atmosphere (50 mL min^{-1}). The DNA origami prepared TEM grid was left untreated. The ultimate goal is to produce a material that consists of localised and anchored single platinum atoms allowing for both increased utilisation efficiency and catalytic activity of the platinum. STEM Energy Dispersive X-ray Spectroscopy (STEM-EDX) imaging was employed to map the distribution of the platinum metal atoms on the DNA scaffold, for the range of DNA nanostructures used and presented in this work.

8.2.6 Atomic Force Microscopy (AFM)

AFM imaging was used to observe the topography of the fabricated DNA origami triangles and observe the platinum metal atoms on the nanostructure. This validates the success of the material fabrication under the reaction conditions employed. The surface topography was assessed via AFM imaging using a Dimension 3100 Atomic Force Microscope (AFM) (Veeco Digital Instruments, Bruker), equipped with a NanoScope IIIa controller. 5 µL of the DNA origami sample was drop cast onto a cleaved mica surface (cleaved with cellotape) and was left to dry in air for 10 minutes before carrying away the remaining solution using a stream of nitrogen gas. The microscope was operated in tapping mode. Cantilevers provided by Apex Probes Ltd (Bracknell, UK) of a length of 225 µm, frequency of 75 kHz and a force constant of 2.8 N m^{-1} (FM-10) were employed in air mode imaging.

8.3 Results and Discussion

8.3.1 AFM imaging of DNA origami nanostructures with platinum metal atoms

The DNA origami nanostructure was prepared for AFM imaging (in air) using the methods described above (see materials and experiments section). Tapping mode was applied between the material on the mica surface and cantilever tip. Figure 1 shows the resulting surface topography of the material.

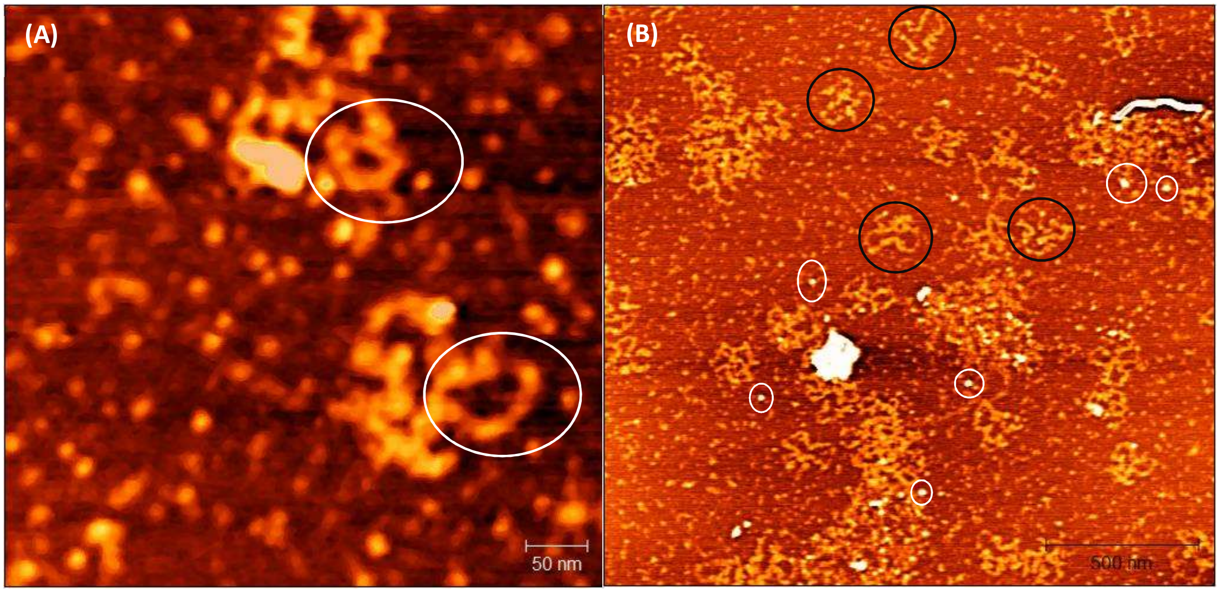

***Figure 1- (A)** AFM imaging of DNA origami triangles with cisPt **(B)** DNA origami cisPt nanomaterial evident with bright spots attributed to cisPt (highlighted in white) and DNA origami triangles (highlighted in black) on a mica surface imaged in air.*

Figure 1(A) shows distorted triangular based DNA origami nanostructures (circled) on the mica surface. The bright white spots are attributed to the platinum atoms in cisPt molecule, as highlighted in figure 1(B). The results from the AFM imaging correspond with the expected size of the DNA origami structures of being approximately 200 nm as reported in the literature (16) for the Alexa 647 origami. However, the limitations of the AFM images obtained arises from the preparation techniques and imaging conditions employed, since it is evident that the DNA origami triangles undergo major distortion under the current imaging conditions used.

It can be suggested that future work should focus on exploring the different ways of preparing the DNA origami sample for effective AFM imaging, such as using the reported and proven methods mentioned in the literature. For example, Zhou et al. reported successful AFM imaging of deposited DNA triangle origami nanostructure (which were also prepared from synthetic and M13mp18 DNA), by AFM imaging of the material on a silicon wafer. They prepared the DNA material for imaging by deposition using a hot Piranha solution ((7:3 (v/v) of concentrated H_2SO_4: 35 % H_2O_2)). Subsequently, the incubation of the DNA origami onto the substrate could occur prior to AFM imaging as detailed in their work (18). This preparation method could be tested for the AFM imaging of the cisPt DNA origami triangles in future work.

8.3.2 STEM imaging characterization

To observe the surface morphology of the fabricated DNA nanostructures i.e. cisPt DNA origami, HJ arrays and HJ-cisPt arrays and particularly that of the platinum metal at an atomic level, STEM imaging characterisation was used. The samples were prepared for the imaging in the ways described above (see materials and experiments section). For the HJ array and HJ-cisPt array nanomaterial, the prepared TEM grids were processed via a pseudo pyrolysis reaction, using the methods described in the materials and experiments section. This enables carbonisation of the DNA scaffold and simultaneously improves the contrast of DNA due to its improved interactions with the electron beam. A detailed discussion for each of the DNA nanostructures characterised is made based on the findings of figure 2. All quantitative measurements of the nanoclusters were achieved using the tools provided in Image J (see chapter 2).

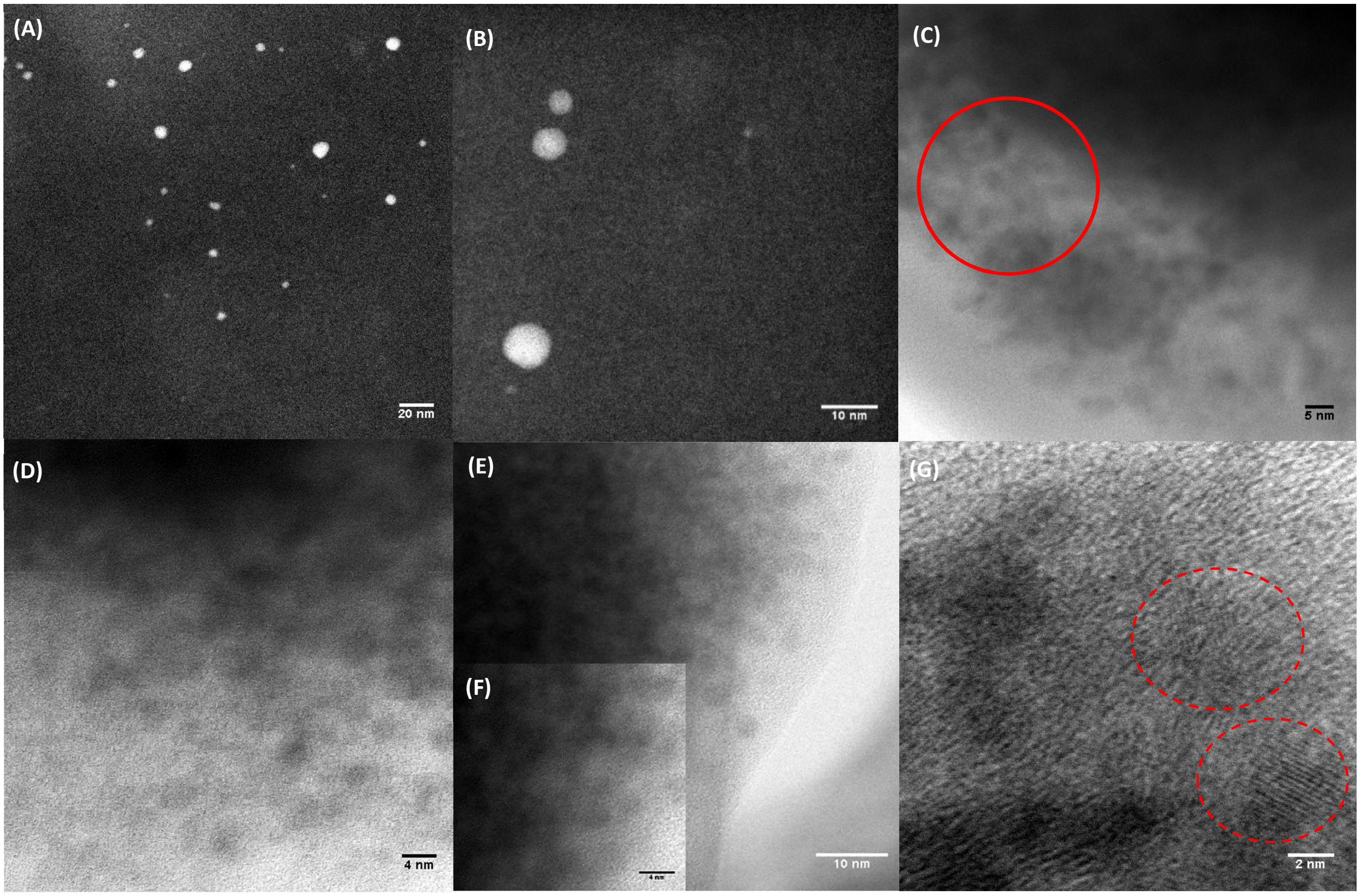

Figure 2- *HAADF STEM imaging of 3 µL of (A) x600 k (B) x2000 k* ***cisPt DNA origami,*** *Bright Field (BF) STEM imaging of (C) x2000 k (D) x3000 k carbonised* ***HJ arrays*** *(255 °C, 30 minutes) (E) 2500 k (F) 6000 k (G)x 8000 k carbonised* ***HJ-cisPt*** *arrays (255 °C, 30 minutes) , drop cast on holey carbon 300 mesh Cu TEM grid.*

cisPt DNA Origami

The average particle size of the structures displayed in figure 2(B) is found to be 6.25 ± 2.5 nm. This is therefore much smaller than the expected size of the DNA origami structure (i.e.200 nm) and much larger than what we found for the size of platinum nanoclusters in bulk cisPt (i.e.1.8 nm) (19), see chapter 4. Therefore we can propose that the resulting structures are potentially agglomerated salt crystals from the buffer solution. In addition, from figures 2 (A, B) it is evident that STEM imaging of the unprocessed cisPt DNA origami nanostructure is more challenging, and obtaining images of a high resolution is difficult, thus a processing step such as electron beam irradiation (see chapter 6) would be recommended for future work to improve the contrast of the DNA under the electron beam. Alternatively, to improve the imaging resolution, carbonisation of the DNA origami material via a pseudo pyrolysis process can be achieved, (as presented and shown to be successful in chapter 7 of this thesis). In this work, the latter method is employed as a processing step prior to the STEM imaging of the HJ and HJ-cisPt arrays.

HJ arrays

The 3LL structure of the fabricated DNA HJ arrays is apparent from the STEM imaging characterization conducted, both in the absence and presence of the platinum metal atoms on the scaffold, see figures 2(C-G). Moreover, we can compare and contrast the fabricated DNA nanostructures in this work to the observations made in the literature. For example, from figure 3 the resemblance in the surface morphology of the HJ-array with that reported by Malo et al.(20) is more apparent, both showing a 3LL sample of a honeycomb appearance.

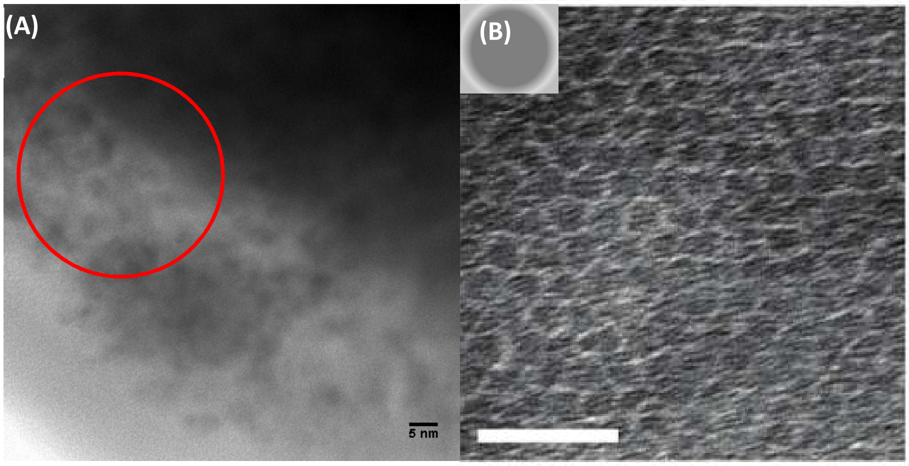

Figure 3*- (A) BF STEM image of carbonised HJ array (255 °C, 30 minutes) on holey carbon 300 mesh Cu TEM grids (B) TEM image of the 3LL lattice reported in the literature copied from Malo et al.* (21)*. DNA is negatively stained so it appears light against a dark background. Scale bar: 50 nm.*

The image in our work is at a scale bar of 5 nm compared to 50 nm in the work of Malo et.al (21). However, both illustrate that the HJ arrays form extensive sheets of the order of micrometres squared (μm^2) in size. In the work of (20), further TEM characterisation using reciprocal space imaging of the 3LL was made to show that the structures have an approximately hexagonal lattice (20). Given the close resemblance in the surface morphology of the HJ arrays in our work with theirs, we can expect our material to also have a similar lattice structure.

HJ-cisPt arrays

The honeycomb structure can also be observed in the surface morphology of the platinated HJ arrays, as shown in figures 2(E) & (F). In addition to this, spaced nanoclusters of around 2 nm in size can be seen in the material, as highlighted in figure 2(G), which resemble the morphology of the platinum metal nanocluster previously observed in the STEM imaging characterization of bulk cisPt films prepared in the same way for STEM imaging (19), see chapter 4. The average diameter of the platinum metal nanocluster was measured to be around 1.8 nm which correlated well with the literature reports, as discussed in chapter 4.

However, to closely follow the platinum metal distribution on the different DNA scaffolds employed, STEM Energy dispersive X-ray (EDX) imaging was employed to achieve elemental mapping of the platinum metal and observe how its distribution changed on the different DNA scaffolds employed. This is detailed below.

8.3.2.1 STEM EDX imaging characterization

STEM Energy dispersive X-ray (EDX) analysis of the material was employed to gain an insight into the distribution of the platinum on the different types of DNA scaffolds employed i.e. DNA origami triangles, 3-layer log-pile (3LL) HJ arrays and the bulky salmon milt (sm)-DNA, as shown in figure 4. To confirm that the EDX mapping is valid, the appearance of the platinum peak on the EDX spectrum in the regions we expect is confirmed. The EDX spectrum is provided in appendix 6.

The phosphorous is taken as the representative element of the DNA phosphate backbone, thus can be means of mapping the distribution of DNA in the nanomaterial. While the platinum metal represents the cisPt molecule and is of most interest in this study, since this forms the active site in the fabricated electrocatalyst nanomaterial.

The effectiveness of using structured DNA templates is revealed by comparing and contrasting the platinum metal distribution shown in figure 4. For example, in comparison to the STEM-EDX analysis of the 1 to 10^{-3} sm-DNA-cisPt, the distribution of platinum is much more highly spaced in the fabricated DNA origami triangle nanostructures, as shown in figure 4(C) compared to figure 4(F).

Firstly, this is attributed to the much lower platinum metal loading used in the synthesis of the DNA origami compared with the loadings employed in the fabrication of the sm-DNA-cisPt adducts. Secondly, the platinum interactions with the DNA base is controlled via a specific base pairings using the in-house designed base sequence, in both the HJ and DNA origami scaffolds, as opposed to the random interactions of the cisPt with the bulky sm-DNA bases in the 1 to 10^{-3} DNA-cisPt material. This is reflected by the close match between the mapped locations of the Pt metal and phosphorous (P) on both the HJ array and DNA origami scaffolds, as illustrated in figures 4(F-G) and figures 4(I- J). In contrast, a more apparent mismatch between Pt and P can be seen in figures 4(C- D) when sm-DNA is used as the scaffold. This portrays the effectiveness of using controlled assembly to an atomic level precision, whereby highly spaced distributions of platinum atoms can be achieved on the DNA, as evident from the comparison of figures 4(C) with figures 4(F) & (I). This is really important since it can greatly enhance the electrochemical performance of the material, improve the use of the 'true' available surface area and consequently increase the platinum metal utilization, reducing the overall costs. This is demonstrated for the electrocatalysis of the HER in acidic conditions, as presented in the following section.

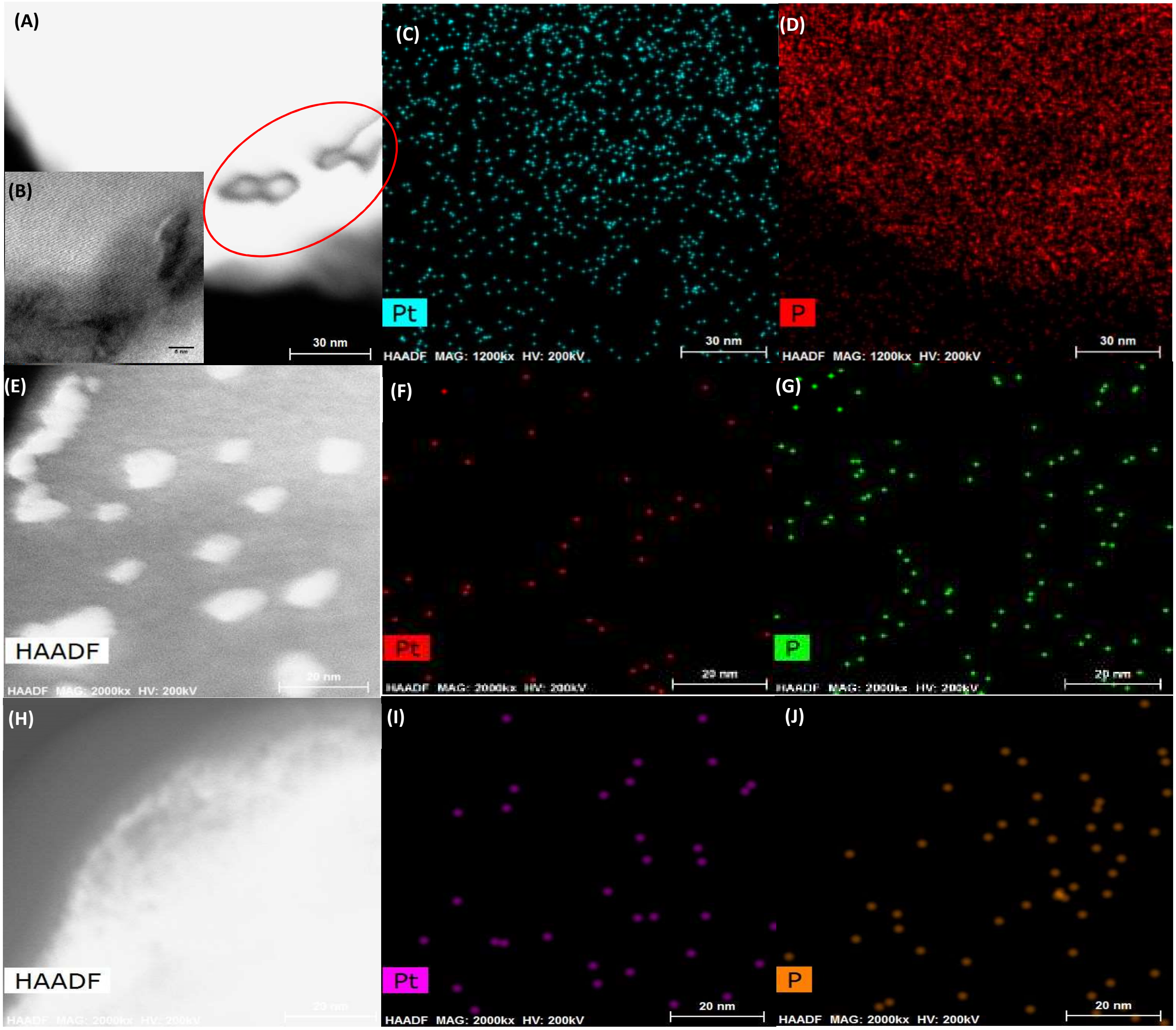

Figure 4- *(A,B) STEM image and (C,D) corresponding EDX-elemental mapping of carbonised* ***1 to 10^{-3} sm-DNA-cisPt****, *showing Pt (blue) ,P (red) (x 2000 k) (E) STEM image and (F,G) corresponding EDX-elemental mapping of* ***cisPt- DNA origami****, showing Pt (red) ,P (green), x 2000 k. (H) STEM image and (I,J) corresponding EDX-elemental mapping of carbonised* ***HJ-cisPt arrays****, showing Pt (Pink) P (orange) (x 2000 k) drop cast on a 3 mm holey carbon 300 mesh copper TEM grid.* ******* *carbonised via a pseudo pyrolysis process (255 ° C, 30 minutes).*

8.3.3 Electrochemical parameters as a measure of catalytic performance

The HER is an archetypal simple electrocatalytic reaction to assess the electrochemical behaviour of the different fabricated samples in an acidic environment of pH 3. The potential (E) is the principal characteristic of electrocatalysis, however the rate of the reaction does not increase in the same way at for example potential E_1 compared to E_2. Hence for comparison purposes, a current density output is set as rational measure of performance of the electrocatalysis, measured at the peak potential. The onset potential (σ) is reported for a defined current density output of 0.1 mA cm-2 to enable comparison between the electrocatalytic responses of the materials.

In addition, the current density can be reflective of the catalytic activity. The current densities measured and reported in this work are based on the geometric surface area of the working electrode. The third electrochemical parameter will be the peak potential (E_p) which is reflective of how much voltage input is required to achieve the electrochemical reactions of the electroactive species i.e. proton reduction in this study.

8.3.3.1 Electrochemical behaviour of the HER

To assess the electrochemical performance of the fabricated DNA based nanostructures with and without cisPt for the HER in acidic conditions (pH 3), an aliquot of the material was drop cast onto the surface of the GC to prepare the working electrode. For example, 5 µL of the cisPt DNA origami sample was drop cast onto a 3 mm GC macro-electrode, while 20 µL of the 1 to 10^{-3} DNA-cisPt, HJ and HJ-cisPt material was drop cast onto a 5 mm GC stub. The prepared working electrode surface was consequently immersed into the electrolyte solution (1 mM $HClO_4$, 0.1 M $NaClO_4$) to test the HER at 50 mVs^{-1} using cyclic voltammetry. The resulting electrochemical response is shown:

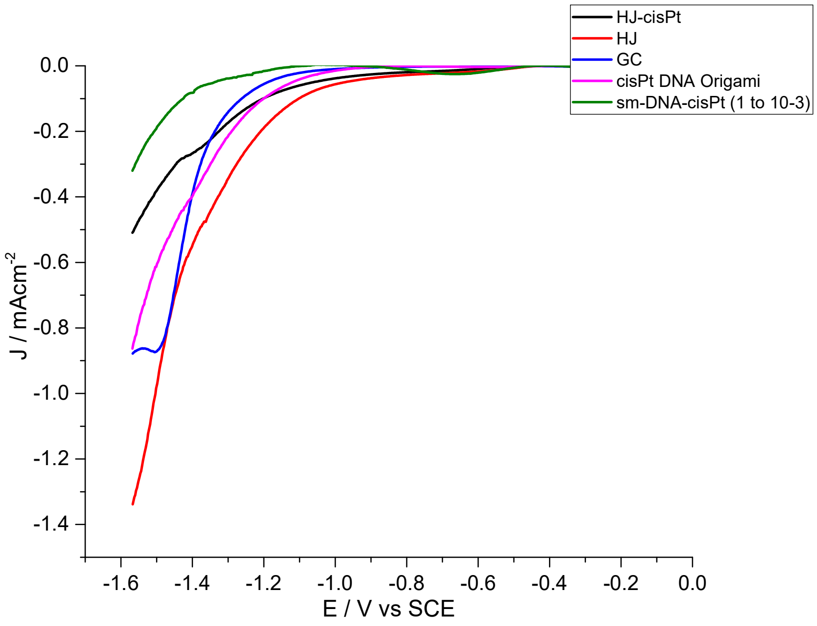

Figure 5- *The electrochemical response for the HER (1 mM $HClO_4$, 0.1 M $NaClO_4$) 50 mV s^{-1} for the named DNA nanostructure drop-cast on a GC working electrode. Current density (J) is measured based on the geometric surface area of the working electrode surface.*

Table 1- *Onset Potential (σ) defined at 0.1 mA cm^{-2} for the untreated material drop cast on GC.*

Material drop cast on GC	**$\sigma_{0.1\ mAcm^{-2}}$ / V vs SCE ± 0.01 V**
Bare GC	-1.26
HJ	-1.10
HJ-cisPt	-1.20
cisPt DNA origami	-1.20
sm-DNA-cisPt (1 to 10^{-3})	-1.43

It can be seen from figure 5 and consequently the defined onset potential from the presented electrochemical response, that the probable onset potential ($\sigma_{0.1\ mAcm^{-2}}$) for all of the DNA nanostructures fabricated i.e. cisPt DNA origami, HJ arrays and HJ-cisPt, is lower than that observed for the 1 to 10^{-3} sm-DNA-cisPt material, despite it having a higher platinum metal loading. It can be proposed that this arises because of the improved utilization of the 'true' available catalyst surface area, which is in agreement with the suggestions made in the literature where an improved electrocatalytic performance can be attained (1). Furthermore, in line with the observations made in the previous work (19) and that in chapter 6, there is an optimum platinum inter-particle distance that enables high electrocatalytic performance to be attained.

The assembly of the DNA scaffold into a defined structure provides increased surface areas, as shown in this work for the platinum metal DNA organic framework. The performance in terms of $\sigma_{0.1\ mAcm^{-2}}$ for the drop cast films of the DNA nanostructure assemblies is even lower than that of the bare GC substrate (-1.1 V vs SCE compared to -1.26 V vs SCE) ± 0.01 V, with the exception of the sm-DNA-cisPt , see Table 1.

However, the highly resistive nature of the DNA impedes the electrical conductivity of the material, which justifies the reasoning behind the absence of the electrochemical peak signal in figure 6 i.e. sigmoidal response. This has thoroughly been discussed throughout the thesis and particularly in chapters 7 and 6. To overcome this issue, carbonisation of the DNA via a low temperature pseudo pyrolysis process was shown to result in a significant improvement in the electrocatalytic performance, where higher catalytic activities could be measured following this process treatment (as detailed in chapter 7). In the following section, carbonisation of the HJ, HJ-cisPt arrays and the sm-DNA-cisPt is achieved to compare and contrast the electrochemical response of the material for the HER (pH 3) at different DNA nanostructures as a catalyst support.

8.3.3.2 Carbonisation of the DNA nanostructures via a pseudo pyrolysis process

To achieve the pseudo pyrolysis of both the platinated and non-platinated Holliday Junction arrays (HJ-Pt) and (HJ) respectively, the working electrode (WE) was prepared by casting a volume of 20 µL onto a 5 mm GC stub and drying under a lamp. The prepared WE was then loaded into in the furnace tube, operating under an inert nitrogen atmosphere (purged at 50 mL min^{-1}) to achieve the carbonisation of the DNA at 255 °C for a duration of 30 minutes. The prepared electrode was then immersed into an electrolyte solution (1 mM $HClO_4$, 0.1 M $NaClO_4$) to test for the HER at 50 mVs^{-1} using cyclic voltammetry. The resulting electrochemical response is compared to that of the untreated material, as shown in the figure below.

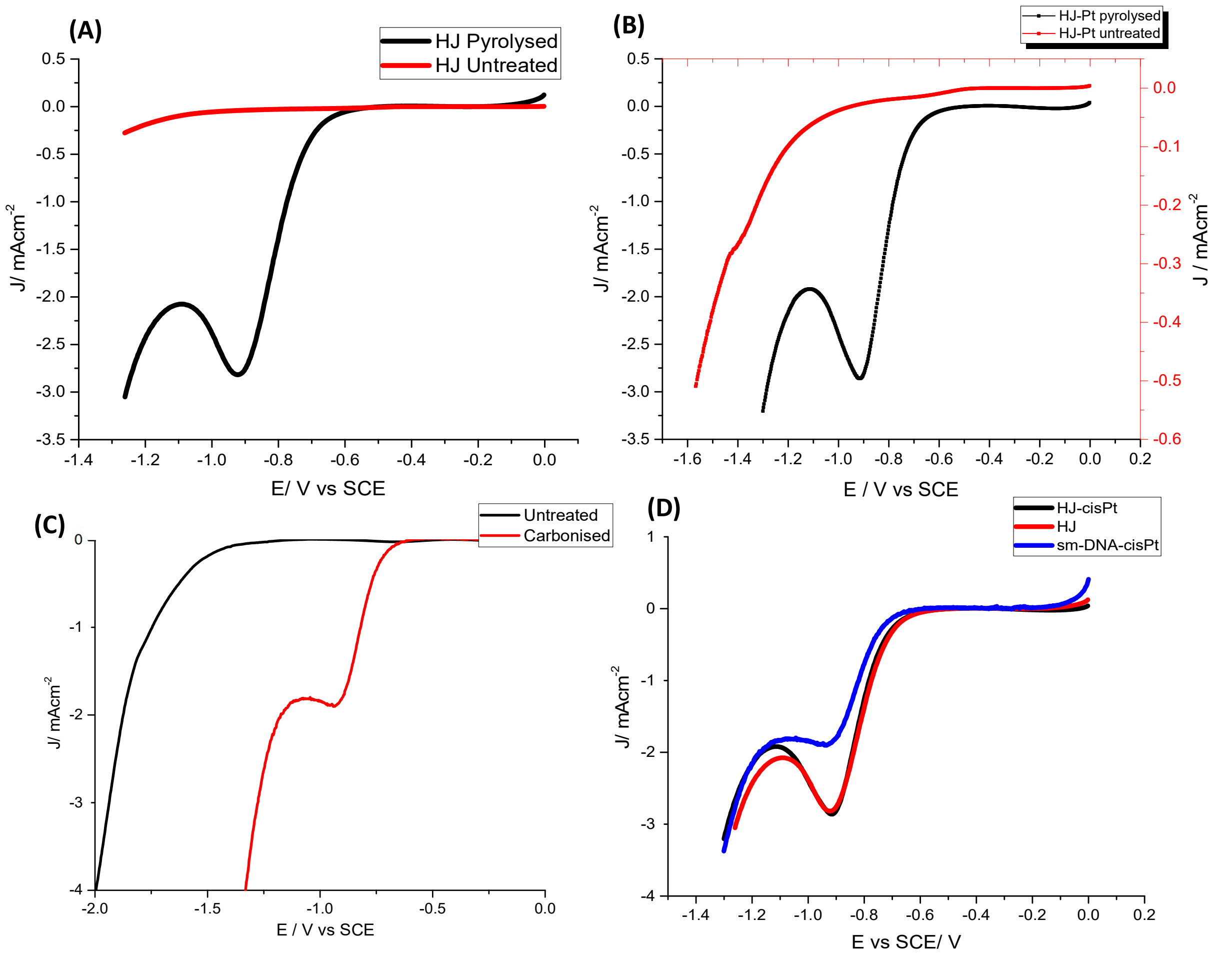

***Figure 6-** The influence of carbonisation via pseudo pyrolysis (255 °C, 30 minutes) on the electrochemical response of **(A)** the HJ array **(B)** HJ-Pt array **(C)** 1 to 10^{-3} sm-DNA-cisPt **(D)** Comparing different DNA nanostructure supports for HER , (1 mM HClO$_4$, 0.1 M NaClO$_4$) at 50 mV s^{-1}.*

***Table 2**- Comparison between the peak potential, current density and onset potential attained at the modified GC electrode surfaces of the different scaffold structures of the DNA-cisPt/ DNA based material before and after carbonisation via pseudo pyrolysis at 255 °C, 30 minutes for HER (1 mM $HClO_4$, 0.1 M $NaClO_4$) at 50 mVs^{-1}.*

DNA nanostructure modified GC Electrode Surface	**Peak Potential (E_p) vs SCE/ V ± 0.01 V**	**Peak Current density* (J_p) /$mAcm^{-2}$ ± 0.0045**	**Onset Potential (σ) / V vs SCE @ 0.1 $mAcm^{-2}$ Untreated**	**Onset Potential (σ) / V vs SCE @ 0.1 $mAcm^{-2}$ Heat treated via pseudo pyrolysis**
Bare GC	-1.45	-0.67	-1.29	-
HJ	-0.92	-2.82	-1.10	-0.634
HJ-cisPt	-0.92	-2.86	-1.20	-0.636
sm-DNA-cisPt (1 to 10^{-3})	-0.92	-1.87	-1.43	-0.69

*Current density measurements are based on a geometric surface area of the working electrode

From figure 6, it becomes clear that following carbonisation, the electrochemical performance for the HER (at pH 3) is significantly improved for all of the different DNA scaffold templates employed i.e. HJ arrays and bulky sm-DNA for the platinum metal catalyst. This improvement is evident both in the presence and absence of the platinum, as we see with the HJ arrays (figure 6(A)). The experimental results demonstrate that this heat treatment provides a means of overcoming the highly resistive nature of the DNA, consequently improving its electrical conductivity and enabling the proton (H^+) reduction to occur in the acidic environment. This is reflected in the voltammetry, shifting the response from a sigmoidal to that of a transient response with the appearance of an electrochemical peak (E_P).

The E_p is not changed with the different scaffolds employed, which implies that the geometry of the DNA scaffold does not influence the thermodynamics and kinetics of the reaction process greatly, or in other words, cannot be driven beyond this electrical voltage i.e. thermodynamic limit. The onset potential ($\sigma_{0.1\ mAcm^{-2}}$) is lower on the HJ array compared with that of a bulky sm-DNA, although the change is not that significant. However, a much higher electrocatalytic activity can be measured on the HJ arrays as opposed to the bulky sm-DNA, where a current density (J_P) of -2.81 mA cm^{-2} and -2.86 mA cm^{-2} in the absence and presence of platinum metal respectively is measured, see Table 2. It could be suggested that this occurs because more efficient use of the 'real' surface area and catalyst active sites is made when the nanomaterial is assembled into a defined geometry as opposed to the random interactions on the bulky sm-DNA material. Therefore, with an improved distribution and availability of the platinum active sites for the electroactive species i.e. H^+, the catalyst efficiency is greatly improved (1).

This is in agreement with the observations made for the resulting surface morphology of the material, whereby more highly distributed platinum (and phosphorous) can be observed on the DNA HJ arrays than on the sm-DNA support, see figure 2. Ideally, platinum made up of edges or vertices i.e. nanoparticles or extended surfaces with a dispersion equivalent to that of a 2 nm diameter particle serve as the best HER catalysts, for acidic environments (22).

The insignificant change between the electrocatalytic response of the HJ arrays in the presence and absence of platinum metal can potentially arise from the carbonised DNA being compared with a nitrogen-phosphorous doped carbon material. This hypothesis is the same as that made in chapter 7, whereby previous literature reports on the pyrolysis of DNA have shown that with increased process temperatures, the nitrogen content in the material is increased, and high amounts of pyridinic-N and graphitic-N could be produced, particularly at higher temperatures (800 °C) (23). It has therefore been claimed that following carbonisation different amounts of N-bonding configurations are formed leading to higher content of pyridinic-N and graphitic-N , consequently improving the electrocatalytic performance for the ORR (23) (a more thoroughly studied electrochemical reaction). Similarly for the HER, it has been reported that the improved performance of Phosphorous Nitrogen doped Graphene (PNG) was attributed to the higher crystallinity and good distribution of a large number of catalytic active sites i.e. pyridinic-N (24). It can therefore be proposed that DNA in this study is a precursor material for nitrogen and phosphorous (NP) doped carbon, which following carbonisation is converted to a graphitic like material. Following heat treatment, the resulting changes to the nitrogen configuration gives rise to improved electrochemical performances of DNA equivalent to the performance that was attainable by a platinum metal containing DNA-cisPt material. This has previously been discussed in chapter 7.

In addition, Hung et al. (25) showed that a phosphorous-nitrogen doped graphene had a higher performance than individually doped nitrogen or phosphorous graphene due to the combination of higher crystallinity, the P-C bonds being in proximity to graphitic-N, and a higher fraction of pyridinic-N which could create a synergistic effect (25). Therefore we can suggest that for the HJ-cisPt arrays, the interactions of Pt with the N in the DNA, reduces the available electron density on the N, and since electronic contributions are reduced, the catalyst support is described as being equivalent to a phosphorous doped graphene , whereas in the absence of cisPt, the DNA is equivalent to a NP-doped carbon. This is validated with the reporting's made in the literature (26) where for graphitized nitrogen-carbon nano-onion rings, the enhancement in the activity of the material is assigned to the enhanced electron transport and abundance of exposed catalytic sites resulting from the mesoporosity and doping of the heteroatom for their study on the ORR (26). These observations have been previously noted for the carbonised DNA material in chapter 6.

8.3.4 Mechanism of the hydrogen evolution reaction (HER)

8.3.4.1 Tafel Plots at 50 mV s^{-1}

To further compare how the electrocatalytic behaviour changes following carbonisation of the different DNA nanostructures, we assess the mechanism of the reaction by considering the changes in the magnitudes of the Tafel slopes. Tafel plots were constructed to reveal the reaction mechanism of the HER at each working surface based on the theoretical information provided in the literature (27) , (28) and (29) and as has already been discussed in detailed in chapter 2 and 3.

From the Tafel plots (figure 7), the magnitude of the Tafel slope can be found and expressed as a function of DNA nanostructure. This is then compared with the widely accepted and reported theoretical limits which reflect the rate determining reaction, such as the Volmer, Heyrovsky and Tafel steps depending on the corresponding Tafel slope of 120, 40 and 30 mV dec^{-1} respectively. Table 3 presents the corresponding Tafel slope for each material tested.

***Table 3**-The changes in the Tafel slope found before and after carbonisation via a pseudo pyrolysis process (255 ° C, 30 minutes) at different DNA nanostructures.*

DNA nanostructure /GC modified Electrode Surface	***Tafel slope of untreated material / mVdec^{-1}***	***Tafel slope of carbonised material / mVdec^{-1}***	***Mechanism of HER after carbonisation***
Bare GC	149	-	-
HJ	423	123	Volmer
HJ-cisPt	546	127	Volmer
sm-DNA-cisPt (1 to 10^{-3})	305	103	Volmer
Pt UME	27.3	-	Tafel

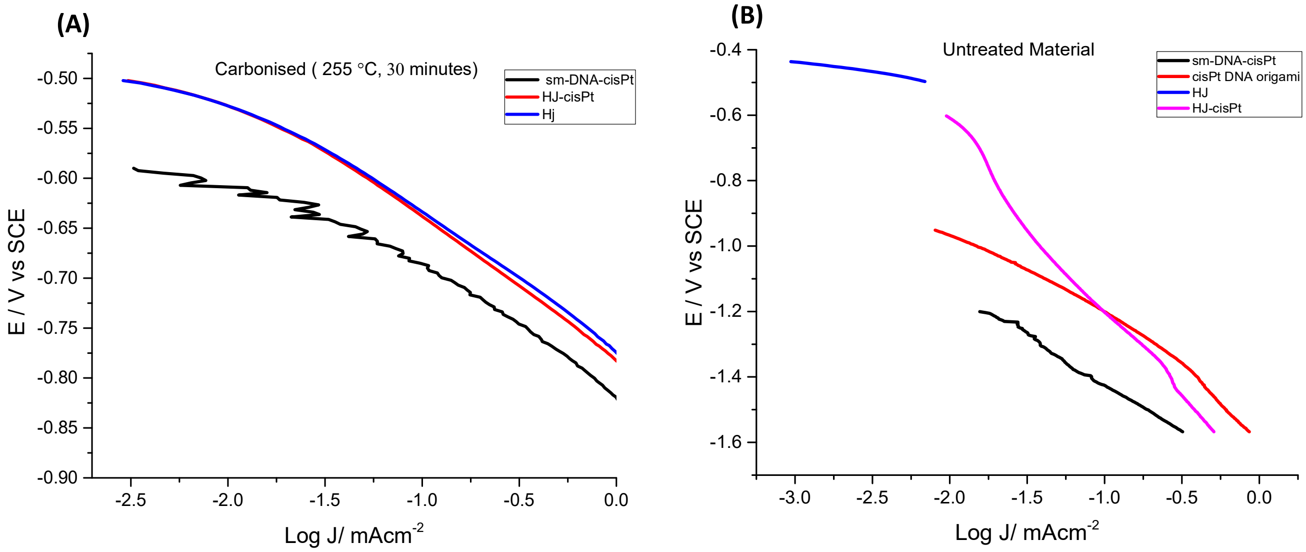

***Figure 7**- Tafel plots for HER 50 mVs^{-1} for different DNA material **(A)** carbonised via a pyrolysis process at 255 °C, 30 minutes **(B)** untreated material.*

Literature reportings have shown that for a nitrogen-doped ultra-thin carbon network, the N species in the nitrogen doped carbon nanosheets (NCNS) was pivotal for the catalysis of the HER. In particular, for the HER in an acidic environment, Tafel slopes of 31 mV dec^{-1}, 81 mV dec^{-1}, 101 mV dec^{-1}, 124 mV dec^{-1}, 127 mV dec^{-1} and 125 mV dec^{-1} were reported for the Pt/C, NCNS-(1000), NCNS-(1100), NCNS-(900), NCNS-(800) and CNS-(1000) respectively, where the number of times the material has been cycled is displayed in the bracket. Thus, a Tafel slope of 81 mV dec^{-1} indicates that the NCNS-(1000) follows the Volmer–Heyrovsky reaction mechanism (30). This portrays the similarity between the magnitudes of the Tafel slope reported in the literature for a nitrogen doped carbon catalyst with the experimental findings measured in this work for the carbonised HJ arrays. This further supports the hypothesis made to suggest that the DNA material acts as a precursor material, equivalent to a N-doped carbon catalyst support.

8.4 Conclusions

In this work, we have shown that the synthesis of DNA nanostructures with controlled placement of the platinum metal atoms on the scaffold, at an atomic precision level, can enable improved distributions of the platinum metal to be achieved. This is evident with the HJ-cisPt arrays and the cisPt DNA origami nanostructures, where a close match between the mapped locations of the Pt metal with P on these templates can be made through the STEM EDX characterisation, as opposed to the more apparent mismatch observed for bulky sm-DNA template. This illustrates the effectiveness of controlled assembly to atomic precision, whereby highly spaced distributions of platinum atoms can be established and enhanced electrochemical performances of the material can be achieved. This is reflected by the higher electrocatalytic activity measured (J_p, $mAcm^{-2}$) for the HER at the HJ arrays and HJ-cisPt as opposed to the 1 to 10^{-3} sm-DNA-cisPt material of a higher metal loading. This is attributed to the higher surface area resulting from the assembly of the DNA into a specific geometry instead of a bulky catalyst material and consequently increased availability and exposure of the catalyst active site. This is a stepping stone towards improving the use of the 'true' available surface area and consequently improving the platinum metal utilization, providing reduced costs of the electrocatalyst material.

In addition, carbonisation of the DNA via a pseudo pyrolysis process can significantly improve the electrochemical performance towards the catalysis of the HER (pH 3), compared to the untreated counterpart. The carbonised DNA scaffold is compared to a N-P-doped carbon, which explains the improved electrocatalytic performance, which is comparable with the performance attained in the presence of the platinum metal on the DNA (i.e. DNA-cisPt material) for the HER. The measured Tafel slopes for the HER, further consolidate this observation, given that similarities can be drawn with the literature reports for a nitrogen doped carbon catalyst (for the HER in acidic media). To conclude, the work presented in this chapter suggests that DNA is a feasible precursor material for the assembly of a metal organic framework to fabricate a highly efficient platinum electrocatalyst. In addition, the DNA not only serves as a building tool for these assemblies, it also acts a source of a nitrogen and or phosphorous doped carbon material, which can be converted to a graphitic character, following its carbonisation. This can enable a metal free electrocatalyst to be used for the HER as we have shown in this work, through the attainable electrochemical performance, which is found to be equivalent to that of a platinum metal containing material.

References

1. Pollet BG, Valzer EF, Curnick OJ. Platinum sonoelectrodeposition on glassy carbon and gas diffusion layer electrodes. Int J Hydrogen Energy. 2011;36(10):6248–58.
2. Roy S, Huang Z, Bhunia A, Castner A, Gupta AK, Zou X, et al. Electrocatalytic Hydrogen Evolution from a Cobaloxime-Based Metal-Organic Framework Thin Film. J Am Chem Soc. 2019;141(40):15942–50.
3. McLaughlin CK, Hamblin GD, Sleiman HF. Supramolecular DNA assembly. Chem Soc Rev. 2011;40(12):5647–56.
4. Deng Z, Mao C. Molecular lithography with DNA nanostructures. Angew Chemie - Int Ed. 2004;43(31):4068–70.
5. Poklar N, Pilch DS, Lippard SJ, Redding EA, Dunham SU, Breslauer KJ. Influence of cisplatin intrastrand crosslinking on the conformation, thermal stability, and energetics of a 20-mer DNA duplex. Proc Natl Acad Sci. 1996;93(15):7606–11.
6. Hasenknopf B, Lehn JM, Baum G, Fenske D. Self-assembly of a heteroduplex helicate from two different ligand strands and Cu(II) cations. Proc Natl Acad Sci U S A. 1996;93(4):1397–400.
7. Poklar N, Pilch DS, Lippard SJ, Redding EA, Dunham SU, Breslauer KJ. Influence of cisplatin intrastrand crosslinking on the conformation, thermal stability, and energetics of a 20-mer DNA duplex. Proc Natl Acad Sci U S A. 1996;93(15):7606–11.
8. Eichman BF, Vargason JM, Mooers BHM, Ho PS. The Holliday junction in an inverted repeat DNA sequence: Sequence effects on the structure of four-way junctions. Proc Natl Acad Sci U S A. 2000;97(8):3971–6.
9. Seeman NC. DNA in a material world. Nature. 2003;421(6921):427–31.
10. Wheatley EG, Pieniazek SN, Mukerji I, Beveridge DL. Molecular dynamics of a DNA Holliday junction: The inverted repeat sequence d(CCGGTACCGG) 4. Biophys J. 2012;102(3):552–60.
11. Simmons CR, Zhang F, Birktoft JJ, Qi X, Han D, Liu Y, et al. Construction and Structure Determination of a Three-Dimensional DNA Crystal. J Am Chem Soc. 2016;138(31):10047–54.
12. Hansen MN, Zhang AM, Rangnekar A, Bompiani KM, Carter JD, Gothelf K V., et al. Weave tile architecture construction strategy for DNA nanotechnology. J Am Chem Soc. 2010;132(41):14481–6.
13. Mao C, Sun W, Seeman NC. Designed two-dimensional DNA holliday junction arrays visualized by atomic force microscopy. J Am Chem Soc. 1999;121(23):5437–43.
14. Ap A, Kp J, Xg P, Te W, Cj L, Mp B, et al. Organization Of Nanocrystal Molecules Using DNA. Nature. 1996;382(6592):609–11.
15. Rothemund PWK. Folding DNA to create nanoscale shapes and patterns. Nature. 2006;440(7082):297–302.
16. Gopinath A, Rothemund PWK. Optimized assembly and covalent coupling of single-molecule DNA origami nanoarrays. ACS Nano. 2014;8(12):12030–40.
17. Englert K. DNA Origami Catalysts. [PhD thesis]. Birmingham (UK): University of Birmingham; 2019.

18. Zhou F, Sun W, Ricardo KB, Wang D, Shen J, Yin P, et al. Programmably Shaped Carbon Nanostructure from Shape-Conserving Carbonization of DNA. ACS Nano. 2016;10(3):3069–77.

19. Englert K, Hendi R, Robbs PH, Rees N V., Robinson APG, Tucker JHR. Cisplatin adducts of DNA as precursors for nanostructured catalyst materials. Nanoscale Adv. 2020;

20. Malo J, Mitchell JC, Turberfield AJ. A Two-Dimensional DNA Array : The Three-Layer Logpile. 2009;13574–5.

21. Malo J, Mitchell JC, Turberfield AJ. A two-dimensional DNA array: The three-layer logpile. J Am Chem Soc. 2009;131(38):13574–5.

22. Zalitis CM, Kucernak AR, Sharman J, Wright E. Design principles for platinum nanoparticles catalysing electrochemical hydrogen evolution and oxidation reactions: edges are much more active than facets. J Mater Chem A. 2017;5(110):23328–38.

23. Wang H, Bo X, Luhana C, Guo L. Nitrogen doped large mesoporous carbon for oxygen reduction electrocatalyst using DNA as carbon and nitrogen precursor. Electrochem commun. 2012;21(1):5–8.

24. Gurylev V, Chin T-K, Tsai H-Y. Carbon Nanotubes Decorated with Platinum Nanoparticles for Field-Emission Application. ACS Omega. 2019;4(13):15428–34.

25. Hung Y-H, Dutta D, Tseng C-J, Chang J-K, Bhattacharyya AJ, Su C-Y. Manipulation of Heteroatom Substitution on Nitrogen and Phosphorus Co-Doped Graphene as a High Active Catalyst for Hydrogen Evolution Reaction. J Phys Chem C. 2019;123(36):22202–11.

26. Shaikh A, Singh BK, Mohapatra D, Parida S. Nitrogen-Doped Carbon Nano-Onions as a Metal-Free Electrocatalyst. 2019;222–31.

27. Shinagawa T, Garcia-esparza AT, Takanabe K. Insight on Tafel slopes from a microkinetic analysis of aqueous electrocatalysis for energy conversion. Nat Publ Gr. 2015;(May):1–21.

28. Tavares M., Machado SA., Mazo L. Study of hydrogen evolution reaction in acid medium on Pt microelectrodes. Electrochim Acta. 2001;46(28):4359–69.

29. Marković NM, Grgur BN, Ross PN. Temperature-dependent hydrogen electrochemistry on platinum low-index single-crystal surfaces in acid solutions. J Phys Chem B. 1997;101(27):5405–13.

30. Wang H, Yi Q, Gao L, Gao Y, Liu T, Jiang YB, et al. Hierarchically interconnected nitrogen-doped carbon nanosheets for an efficient hydrogen evolution reaction. Nanoscale. 2017;9(42):16342–8.

Chapter 9- Conclusions and Future Work

Chapter 9: Conclusions and Future Work

In this study, a novel DNA-cisplatin (cisPt) based nano-material has been synthesised in-house and characterised to measure its electrochemical properties in order to assess the materials feasibility for its use as an electrocatalyst for fuel cell applications. The initial work, involving the complex formation between salmon milt DNA and cisPt focuses on investigating the ideal and optimum platinum metal loading on the DNA scaffold for the hydrogen evolution reaction (HER) in an acidic environment (pH 3). The studies reveal interesting trends in catalytic behaviour as a function of platinum loading for the HER and the influence of this on the resultant surface morphology of the material via STEM imaging characterisation. This includes increased electrocatalytic performances with increased metal loadings although simultaneously we observed increased clustering of the metal atoms and poorer distribution of it on the DNA support.
However, the highly resistive and non-conductive nature of the DNA material was greatly hindering the attainable electrocatalytic performance at all loadings of the platinum metal investigated. Thus, an integral study focusing on different processing treatments of the DNA is achieved to improve the conductive and electronic properties of the DNA material as an electrocatalyst support. This will improve both the electrochemical activity and durability of the nanomaterial. The resulting effect of three different methods have been detailed throughout the thesis including the method of: functionalization of single walled carbon nanotubes (SWCNT's) with the DNA-cisPt material, the graphitization of the DNA through the evacuation of the hydrogen and oxygen atoms upon high dose exposure to an electron beam and finally carbonisation of the DNA via a low temperature pseudo pyrolysis process (255 °C, 30 minutes).

It is clear from the experimental findings that the functionalisation of the SWCNTs with cisPt gives rise to exceptional improvements in the electrocatalytic performance towards the HER (pH 3) compared with the unmodified nanotubes. In addition, the SWCNT functionalization with the DNA shifts the behaviour more favourably than the response of the virgin DNA alone. However, less significant changes were noted upon the functionalization of the SWCNT with DNA-cisPt adducts compared to the response measured for the non-functionalised DNA-cisPt, although the SWCNT-DNA-cisPt outperforms the unmodified SWCNTs. The electrochemical response of the SWCNT functionalized with the DNA-cisPt adducts (SWCNT-DNA-cisPt) fell intermediary between the electrochemical behaviour observed for the unmodified SWCNT and that of the SWCNT-cisPt for the HER (pH 3), as we would expect.

Insights into the mechanism of the HER reaction, as revealed by the Tafel slopes show that the Volmer-Heyrovsky reaction mechanism dominates for the HER over the surface of the fabricated structures and that the cisPt loading on the SWCNTs correlates strongly with the calculated transfer coefficient (α) and the Tafel slope.

Suggestions for future work can be made which involve process treatment of the SWCNT-DNA-cisPt material to achieve the carbonisation of the DNA, which will consequently improve the conductivity of the DNA following its functionalization with cisPt. It can be proposed that this will significantly improve the electrochemical response of the HER (pH 3), whilst simultaneously enabling reduced cisPt loadings to be employed. In this fabrication process, much lower loading ratios of the DNA-cisPt adducts can be used i.e. < 1 to 1 DNA-cisPt to improve the platinum metal distribution and utilization and consequently reduce costs.

On the other hand, the process treatment of the DNA via its projection to a flood electron beam (e-beam) led to significant improvements in the electrochemical performance of the material for the electrocatalysis of the HER (pH 3) compared to the untreated counterpart. This proves the hypothesis made to suggest that the flood electron beam irradiation of the DNA can improve this polymers conductivity via this process treatment.

Furthermore, the e-beam irradiation of the material via a flood electron source enables successful STEM imaging of the unmodified DNA, which is not commonly reported in the literature. It is noted from the STEM imaging characterization that the presence of the platinum metal, even at the lowest loadings employed in this study i.e. 0.75 ng, contributes favourably towards both the electrocatalysis of the HER and improved STEM imaging of the material as opposed to the untreated virgin DNA.

In addition, in terms of the effect of changing the platinum metal loading in the e-beam treated DNA-cisPt material , the experimental findings have shown that much higher catalytic activities can be observed at the lower platinum metal loadings (minimum loading of 0.75 ng) compared with the bulk cisPt (7.5 µg). This was reflected by the higher current density output (J, mA cm^{-2}), calculated using the geometric surface area of the electrode. This finding was justified with similar reportings in the literature, whereby the diffusion profile in the catalyst film is improved when the inter-particle distance reaches a certain threshold. As the metal loading increased in the DNA-cisPt film, there was increased clustering of the platinum metal, which was evident from the resulting changes to the surface morphology of the material (i.e. appearance of larger bright spots) and also in the electrochemical response, whereby the peak potential (E_p) shifted towards that of a bulk platinum metal response i.e. bulk cisPt.

Suggestions for future work include focusing on a detailed characterization and chemical analysis of the resulting material following e-beam irradiation of the DNA in the presence and absence of platinum metal. Although an attempt has been made to use XPS testing to explore the resulting changes to the material following the e-beam irradiation process, charging issues faced during the testing process prevented conclusive remarks from being drawn, such as whether or not the graphitization of the DNA material was successful through e-beam irradiation. Thus, these tests need to be improved by exploring how the sampling methods employed can be modified to achieve improved signals.

Lastly, carbonisation of the DNA/glassy carbon (GC) and DNA-cisPt /GC modified electrode via a heat treatment process at the optimum experimental pseudo pyrolysis conditions found (255 °C for a duration of 30 minutes) was also proven to be successful in significantly improving the electrocatalytic performance of the material for the HER (pH 3) compared to the untreated counterpart.

Carbonization of the virgin DNA via a pseudo pyrolysis process can significantly improve the electrochemical performance for the catalysis of the HER (pH 3) and the performance attained is equivalent to the performance of a platinum metal containing catalyst i.e. carbonised DNA-cisPt. The carbonised DNA can thus be described as being equivalent to a nitrogen, phosphorus-doped (N, P-doped) carbon with graphitic like characteristics, which explains the improved electrocatalytic performance.

The STEM imaging characterization of the resulting carbonised DNA material have shown the formation of a combination of both graphitic and nano-diamond structures, based on the lattice spacing's measurements of the material. The XPS characterization reveals that in the absence of cisPt i.e. virgin carbonised DNA, a predominantly graphitic based material is formed following carbonisation compared to the higher *sp*^{3} content reported in the DNA-cisPt material (1:10^{-4} DNA-cisPt). From the Raman spectroscopy characterization, we can attribute our experimental findings to those reported in the literature with a nitrogen phosphorus doped graphite material. However, further repeated testing is required to improve the spectra response and reduce the noise associated with the signal.

To conclude, this work demonstrates that DNA is a feasible precursor material as a source of a nitrogen and phosphorous doped carbon catalyst support, which can be converted to attain graphitic character following its heat treatment via pseudo pyrolysis. This can enable metal free electrocatalysts to be used for the HER i.e. carbonised DNA, as we have shown in this work through the attainable electrochemical performance, which was found to be equivalent to that of a platinum metal containing material.

In addition, the measured Tafel slopes for the HER further consolidates this observation, given that similarities can be drawn in the magnitude of the Tafel slope for the carbonised DNA with literature reporting's for a nitrogen doped carbon catalyst material (for the HER in acidic media). To summarise, the work presented suggests that DNA is a feasible precursor material for the assembly of a metal organic framework to fabricate a highly efficient platinum electrocatalyst material; which not only serves as a building tool for these assemblies, but also acts a source of a nitrogen/phosphorous doped carbon which can be converted to attain graphitic like characteristics following carbonisation via pseudo pyrolysis. Future work should focus on studying thoroughly the chemical structure of the resulting carbonised material and investigating the properties of the nanomaterial more closely using XPS and Raman spectroscopy as a function of platinum metal loading on the DNA scaffold.

The experimental results have shown that cisPt is an effective source of platinum metal and its combination with DNA is ideal for establishing controlled placement of the platinum metal atoms on the scaffold, at an atomic precision level via covalent bonding. This enables improved distribution of the platinum metal on the DNA catalyst support, thus increasing the utilisation of the expensive metal and consequently reducing costs. To achieve this distribution, self-assembled nanostructures such as triangular DNA origami structures and Holliday Junction (HJ) arrays have been fabricated in the final part of this work. The experimental results have shown that electrocatalysts of reduced platinum metal loadings can be made without compromising the fuel cell performance, as demonstrated through the electrochemical studies for the HER (pH 3). Finally, carbonisation of the DNA in the HJ arrays is achieved as means of overcoming the highly resistive nature of the DNA, making the fabricated material more suited for the HER.

The atomic precision is demonstrated through STEM EDX characterisation, where for both the HJ-cisPt arrays and the cisPt DNA origami nanostructures, a close match between the mapped locations of the Pt metal with phosphorus (P) (which represents the DNA phosphate backbone) is made compared to the more apparent mismatch observed for the salmon milt DNA scaffold, where there is no controlled placement of the Pt. This illustrates the effectiveness of using a controlled assembly approach to establish highly spaced distributions of platinum atoms and thus enhanced electrochemical performances. This is reflected by the higher electrocatalytic activity measured for the HJ arrays and HJ-cisPt as opposed to the 1 to 10^{-3} salmon milt DNA-cisPt material, despite there being a much higher Pt metal loading on the salmon milt DNA. This is explained as resulting from the higher surface areas that can be attained by the assembly of the DNA into a specific nanostructure as opposed to the use of the bulky salmon milt DNA as a catalyst support. As a result of this, there is increased availability and access to the catalyst active sites. This is a stepping stone towards improving the utilisation of the 'true' available surface area, consequently leading to more effective and efficient use of the platinum metal and most importantly reducing costs.

In addition to the work presented in this thesis, preliminary studies have been made to test the electrochemical behaviour of the DNA-cisPt adducts and the functionalised DNA-cisPt SWCNTs for the oxygen reduction reaction (ORR). The experimental findings suggest promising performances of the DNA material for the ORR, however due to the capacity of the project, further experimental investigations could not be made. Therefore, as part of future work, it is recommended that we focus our attention to the use of the DNA-cisPt material for the ORR and explore whether carbonisation of the DNA can improve the electrochemical response attained, in similar ways to those observed for the HER. In addition, another important parameter is the durability of the material, thus future work should assess the stability of the DNA-cisPt catalyst after prolonged use and exposure to the acidic environment. In addition, further in-depth investigations should be made focusing on the surface chemical properties of the DNA material following both heat treatment and e-beam irradiation. Specifically, this means assessing the impact of the presence of surface defects on the electrocatalytic performance of the material and whether the surface defects are responsible for the improved electrochemical response of the electrocatalyst using common methods such as XPS characterisation and Raman spectroscopy. These studies can detect the presence of any functional groups present at the material surface, such as oxygen vacancies via the O 1s spectra. This can reveal the extent of defects and whether more oxygen vacancies (defects) have been formed following process treatment of the DNA.

Appendices

Appendix 1- Chapter 4: Electrochemical Testing and Characterization of salmon milt DNA-cisplatin adducts for the electrocatalysis of the Hydrogen Evolution Reaction (HER)

Synthesis of Salmon Milt DNA complexes: mass loadings and concentrations

Salmon milt (sm)-DNA from salmon testes was obtained as a dry form of sodium salt. The material is transferred into a sterile tube and dissolved in MilliQ water by stirring vigorously overnight. This was followed by sonication which was applied for 9 minutes in a 10 seconds on, 20 seconds off fashion. Dilution to a concentration of around 16,000 µM was carried out which served as a stock solution for preparation of 1000 µM samples. Cisplatin (cisPt) was obtained from Sigma Aldrich and dissolved in MilliQ water to a concentration of 8300 µM to serve as a stock solution. [5] The table below outlines the volume quantities of the DNA and cisPt employed in each of the different ratios of materials synthesised. The molecular weight of salmon DNA and cisPt is expressed as 1.3 x 106 Daltons and 300.01gmol-1 respectively. From a stock solution of 16,000 µM, to prepare a 1000 µL solution of a 1000µM DNA concentration:

$$C_1V_1 = C_2V_2$$

$$\therefore V_1 = \frac{(\,1000\,\mu M\ \times (1000\,\mu L)}{(16{,}000\,\mu M)} = 60.7\,\mu L$$

Table A1.1- *Volume loadings of prepared DNA-cisPt samples of 1000 µL.*

sm-DNA: cisPt loading	***Volume of cisPt / µL***	***Volume of DNA/ µL***	***Volume of Water/ µL***
1:0	0	60.7 from 16,000 µM	939.3
1:10^{-4} (0.1 µM)	1 µL from 100 µM	60.7 from 16,000 µM	938.3
1:10^{-3} (1 µM)	10 µL from 100 µM	60.7 from 16,000 µM	929.3
1:10^{-2} (10 µM)	100 µL from 100 µM	60.7 from 16,000 µM	839.3
1:10^{-1} (100 µM)	12 µL from 8300 µM	60.7 from 16,000 µM	327.3
1:1 (1000 µM)	120.5 µL from 8300 µM	60.7 from 16,000 µM	818.8
0:1 (1000 µM)	120.5 µL from 8300 µM	0	879.5

---

[5] Preparation of the material was conducted by Klaudia Englert, school of Chemistry, University of Birmingham.

Mass loadings

To determine the mass loading of the DNA and the cisPt in each solutions prepared, the following is employed as an example.

1 to 0 DNA-cisPt 1000 µL solution

Using the simple expression between moles (n), volume (V) and concentration (C):

$$n = C \times V = 60.7 \times 10^{-6}\, L \times 16{,}000\, MolL^{-1} = 9.71 \times 10^{-7}\, mol$$

$$Mass = n \times M_w = 9.71 \times 10^{-7}\, mol \times (1.3 \times 10^{6}) gmol^{-1}$$

$$= 1.2625\, g\ in\ a\ 1000\, \mu L\ solution$$

Thus in a 25 μL drop cast volume, it equates to 0.03156 g of DNA.

cisPt loadings: 1 to 1 DNA-cisPt

Using the simple expression between moles (n), volume (V) and concentration (C):

$$n = C \times V = 8300\, \mu M \times 120.5\, \mu L = 1.00015 \times 10^{-6}\, mol$$

$$Mass = n \times M_w = 1.00015 \times 10^{-6}\, mol \times 300.01\, gmol^{-1}$$

$$= 3.00 \times 10^{-4}\, g\ in\ a\ 1000\, \mu L\ solution$$

Thus in a 25 μL drop cast volume, it equates to 7.5 x 10^{-6} g of cisPt.

1 to 10^{-1} DNA-cisPt

Using the simple expression between moles (n), volume (V) and concentration (C):

$$n = C \times V = 8300\, \mu M \times 12\, \mu L = 9.96 \times 10^{-8}\, mol$$

$$Mass = n \times M_w = 9.96 \times 10^{-8}\, mol \times 300.01\, gmol^{-1}$$

$$= 2.98809 \times 10^{-5}\, g\ in\ a\ 1000\, \mu L\ solution$$

Thus in a 25 μL drop cast volume, it equates to 7.5 x 10^{-7} g of cisPt.

1 to 10^{-4} DNA-cisPt

Using the simple expression between moles (n), volume (V) and concentration (C):

$$n = C \times V = 100\, \mu M \times 1\, \mu L = 1 \times 10^{-10}\, mol$$

$$Mass = n \times M_w = 1 \times 10^{-10}\, mol \times 300.01\, gmol^{-1}$$

$$= 3.0001 \times 10^{-8}\, g\ in\ a\ 1000\, \mu L\ solution$$

Thus in a 25 μL drop cast volume, it equates to 7.5 x 10^{-10} g of cisPt.

Table A1.2*- Mass loadings of prepared DNA-cisPt samples of 1000 µL.*

sm-DNA: cisPt loading	***Mass of cisPt / g***	***Mass of DNA/ g***	***Mass of cisPt in 25 µL / g***	***Mass of DNA in 25 µL / g***
1:0	0	1.276	0	0.0319
1:10^{-4} (0.1 µM)	3.000×10^{-8}	1.276	7.50 x 10^{-10}	0.0319
1:10^{-3} (1 µM)	3.000×10^{-7}	1.276	7.50 x 10^{-9}	0.0319
1:10^{-2} (10 µM)	3.000×10^{-6}	1.276	7.50 x 10^{-8}	0.0319
1:10^{-1} (100 µM)	2.989×10^{-5}	1.276	7.50 x 10^{-7}	0.0319
1:1 (1000 µM)	3.00×10^{-4}	1.276	7.50 x 10^{-6}	0.0319
0:1 (1000 µM)	3.00×10^{-4}	1.276	7.50 x 10^{-6}	0.0319

An estimation of the total number of molecules i.e. atoms of cisPt and DNA can be achieved by using the correlations between the Avogadro's constant and number of moles.

Table A1.3*- Mass loadings of prepared DNA-cisPt samples of 1000 µL.*

Material	***Number of cisPt molecules /DNA in 1000 µL solution***	***Number of cisPt molecules /DNA in 25 µL solution***
Cisplatin (1000 µM) from 8300 µM stock	6.024 x 10^{17}	1.506 x 10^{16}
1 to 1 DNA-cisPt	6.024 x 10^{17}	1.506 x 10^{16}
1 to 10^{-4} DNA-cisPt	6.023 x 10^{13}	1.506 x 10^{12}
1:10^{-3} DNA- cisPt	6.023 x 10^{14}	1.506 x 10^{12}
1 to 10^{-2} DNA- cisPt	6.023 x 10^{15}	1.506 x 10^{14}
1 to 10^{-1} DNA-cisPt from 8300 µM stock	5.998 x 10^{15}	1.499 x 10^{15}
1 to 0 DNA-cisPt from 16 000 µM	5.850 x 10^{17}	1.462 x 10^{16}

Accessibility of all N7 atoms to a 2.2 Å radius sphere, which corresponds to the size of the cisplatin molecule (1).

Validating fully electroactive geometric area assumption

It was reported that the area occupied by one square planar cisPt molecule equates to 0.328 nm^2. Thus given the number of molecules in an aliquot of 25 µL, it equates to 4.92 x 10^{15} nm^2. Thus much larger than the geometric surface area of a 3 mm GC electrode (0.0707 cm^2).

How the thickness of the DNA-cisPt film changes with the volume of the material drop cast

Theory

The buoyant density of DNA is reported to be a function of the G-C content in the material. It was reported that the dehydrated density of E.coli DNA is 2 gcm^{-3}, whereas the buoyant density varied as a function of G-C content (2) and is around 1.72 gcm^{-3}

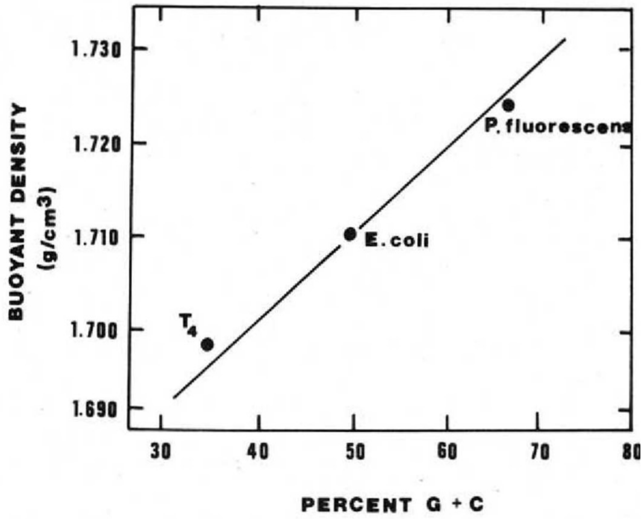

Figure A1.1- *Experimental curve showing the relationship between buoyant density in 7.7 M CsC of double-stranded DNA from various sources and base composition.* (2).

However a more profound method has been reported in the literature, exploring density measurements of Calf thymus DNA films to be 1.41 ± 0.03 gcm^{-3} (3). Other authors have reported a density measurement of salmon DNA of 1.14 gcm^{-3} for their work involving a wet-templating approach of silver (Ag) onto DNA, however have not made the association of this density with that of dry film (4). If we assume that the difference in the density of salmon DNA and calf thymus DNA is insignificant then we find that we can estimate the film thickness of the material drop-cast onto the working electrode surface, as outlined below.

$$Volume = Surface\ Area\ \times Thickness\ Eq.(1)$$

$$\rho_{DNA\ film} = \frac{Mass\ of\ DNA\ in\ the\ film}{Volume\ of\ DNA\ in\ the\ film}\ Eq.(2)$$

Hence using equations (1) and (2), we can model the thickness of the films with the volume of the material drop cast. The findings are shown in the figure, where the film thickness changes from 0.59 to 4.19 µm.

Ideally, if the total contents of the aliquot deposited is made up of the DNA, then for every 1 µL casted onto a 3 mm diameter electrode, the thickness goes up by:

$$0.001\ cm^3 = 0.0707\ cm^2\ \times Thickness$$

$$\therefore \text{ Thickness} = \ 0.014\ cm$$

Therefore, as an example, for 25 µL, we should get a film thickness of 0.35 cm.

However, the max solubility of the salmon milt DNA is reported to be 1 mg/mL by Sigma-Aldrich (supplier), therefore in a 1 Litre solution we have an equivalent mass of 1 g of DNA.

For the reported density of 1.14 gcm^{-3} for DNA, the volume of DNA in the film of a 1000 cm^{-3} solution is therefore:

$$V = \frac{mass}{\rho} = \frac{1}{1.14} = 0.877\ cm^3$$

So 999.123 cm^{-3} is water in the solution. In other words, for the 1 µL aliquot, that would mean 0.999 µL is water and 0.000877 µL is DNA.

To account for solubility, this means, the actual thickness of the DNA film, for example in the 25 µL aliquot is smaller by a factor of 877 than the originally proposed film thickness of 0.35 cm. such that the DNA film thickness is 3.99 µm. using the same approach the DNA film thickness is found with drop casting volume.

References

[1]. Melnikov S V., Söll D, Steitz TA, Polikanov YS. Insights into RNA binding by the anticancer drug cisplatin from the crystal structure of cisplatin-modified ribosome. Nucleic Acids Res. 2016;44(10):4978–87.

[2]. Panijpan B. The buoyant density of DNA and the G + C content. J Chem Educ. 1977;54(3):172–3.

[3]. Śmiałek MA, Jones NC, Hoffmann SV, Mason NJ. Measuring the density of DNA films using ultraviolet-visible interferometry. Phys Rev E - Stat Nonlinear, Soft Matter Phys. 2013;87(6):1–4.

[4]. Takeshima T, Sun L, Wang Y, Yamada Y, Nishi N, Yonezawa T, et al. Salmon milt DNA as a template for the mass production of Ag nanoparticles. Polym J. 2014;46(1):36–41.

How the voltammetry response changes with the drop-cast Volumes of 1 to 1 DNA-cisPt on Glassy Carbon (GC) for HER (1 mM $HClO_4$, 0.1 M $NaClO_4$) at different scan rates of: 10, 25 and 50 mV s^{-1}

50 mV s^{-1}

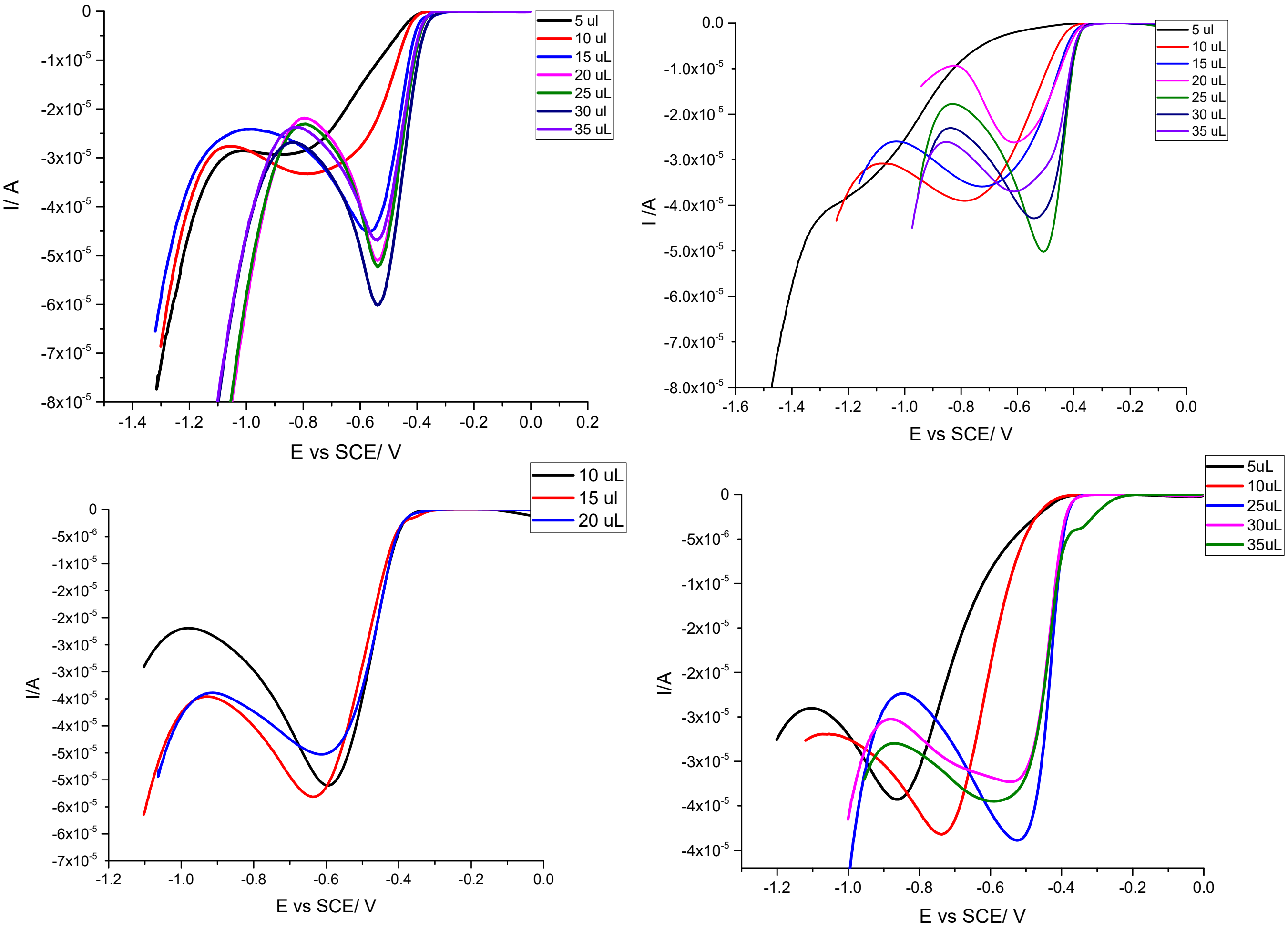

***Figure A1.2**- The voltammetry response for the HER (1mM $HClO_4$, 0.1M $NaClO_4$) 50 mVs^{-1} at different volumes of 1-1 DNA-cisPt cast on GC (d=3 mm).*

25 mV s^{-1}

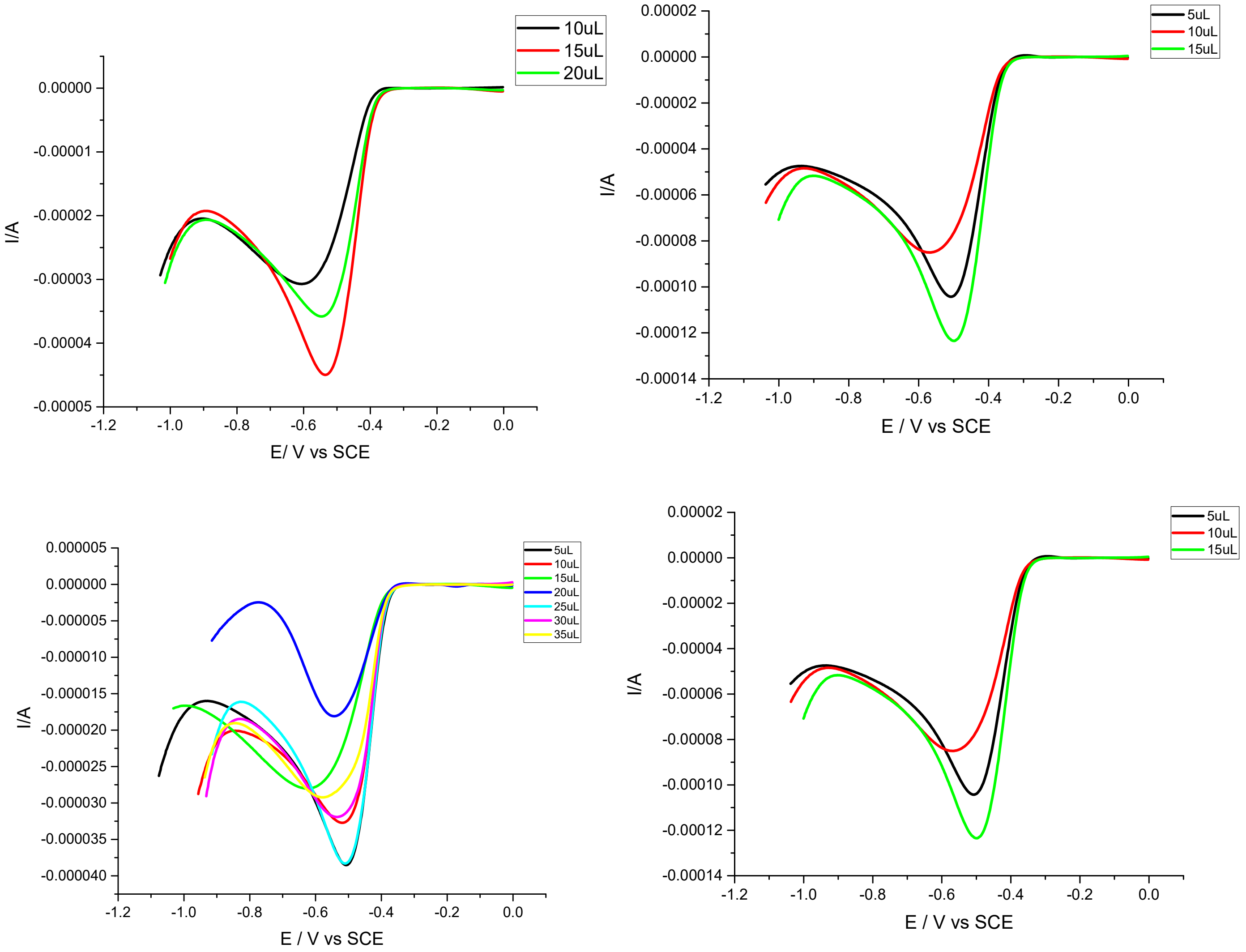

Figure A1.3*- The voltammetry response for the HER (1mM HClO$_4$, 0.1M NaClO$_4$) 25 mVs^{-1} at different volumes of 1-1 DNA-cisPt cast on GC (d=3 mm).*

10 mV s^{-1}

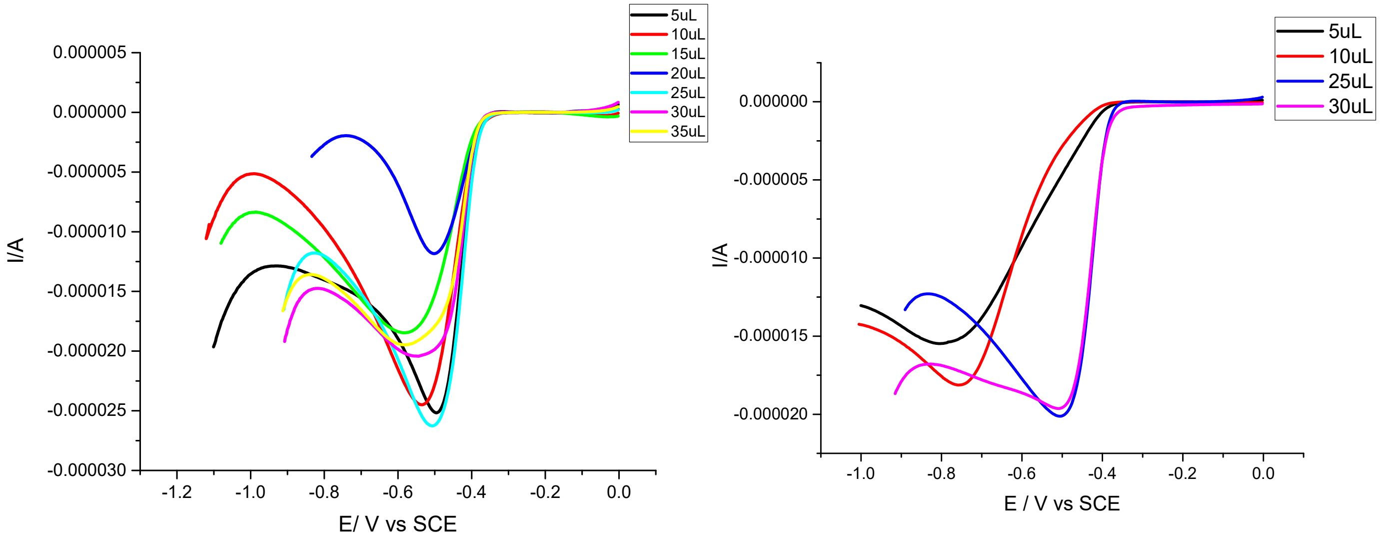

Figure A1.4- *The voltammetry response for the HER (1mM $HClO_4$, 0.1M $NaClO_4$) 10 mV s^{-1} at different volumes of 1-1 DNA-cisPt cast on GC (d=3 mm).*

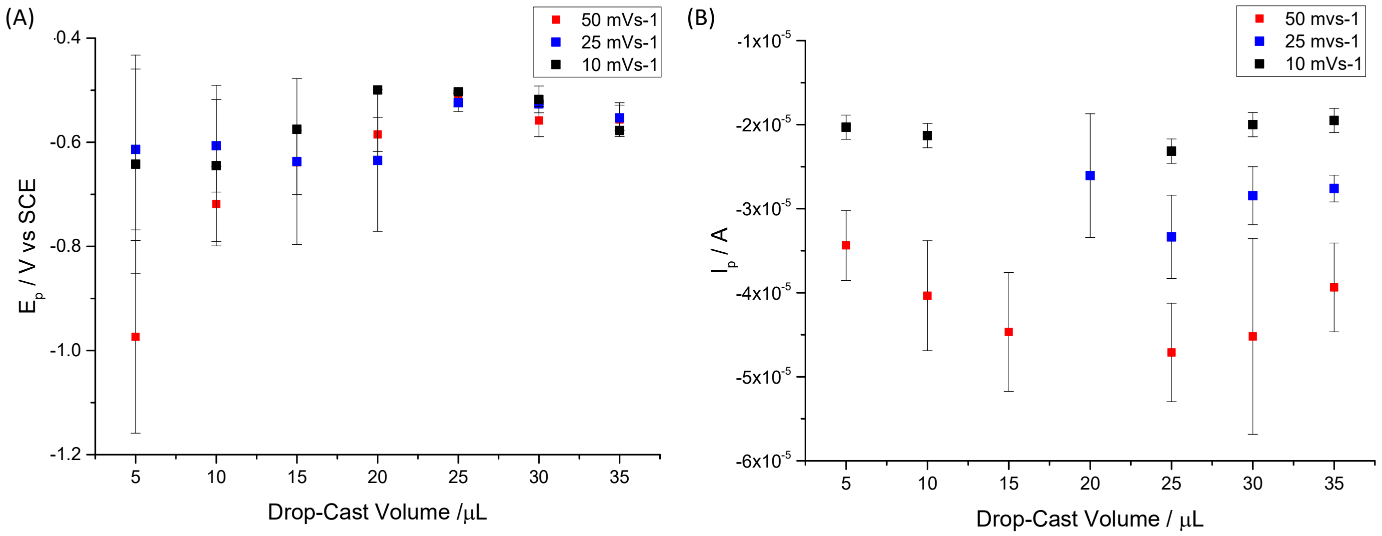

Figure A1.5 - *(A) The change in the peak potential with drop-cast volume (B) The change in peak current with drop-cast volume cast for the voltammetry response of the HER (1 mM $HClO_4$, 0.1 M $NaClO_4$) at the defined scan rate for the 1-1 DNA-cisPt on GC (d=3mm) material.*

The error bars are based on a standard deviation error.

XPS survey spectra results - Binding energies

Table A1.3 *-The variation of the binding energy with DNA-cisplatin loading.*

Name of element	**Binding energy (eV)**			
	1 to 10^{-4} DNA-cisplatin	*1 to 10^{-3} DNA-cisplatin*	*1 to 10^{-2} DNA-cisplatin*	*1 to 10^{-1} DNA-cisplatin*
O 1S	532.08	533.08	533.08	533.08
C 1S	286.08	285.08	286.08	285.08
N 1 S	399.08	399.08	399.08	399.08
Na 1S	1071.08	1071.08	1071.08	1071.08
P 2P	133.08	133.08	133.08	133.08
Si 2P	100.8	99.08	99.08	99.08
Ca 2p	347.08	347.08	-	347.08
Pt 4f	-	-	73.08	72.08

Table A1.4- *Survey spectra results for Nitrogen.*

Name of element	**Binding energy (eV)**					
	1 to 0 DNA-cisplatin	*1 to 10^{-4} DNA-cisplatin*	*1 to 10^{-3} DNA-cisplatin*	*1 to 10^{-2} DNA-cisplatin*	*1 to 10^{-1} DNA-cisplatin*	*1 to 1 DNA-cisplatin*
N 1 S	399.08	399.08	399.08	399.08	399.08	400.08

Table A1.5- *Survey spectra results for Oxygen.*

Name of element	**Binding energy (eV)**					
	1 to 0 DNA-cisplatin	*1 to 10^{-4} DNA-cisplatin*	*1 to 10^{-3} DNA-cisplatin*	*1 to 10^{-2} DNA-cisplatin*	*1 to 10^{-1} DNA-cisplatin*	*1 to 1 DNA-cisplatin*
O 1 S	532.58	532.08	533.08	533.08	533.08	533.08

Table A1.6- *Survey spectra results for Carbon.*

Name of element	Binding energy (eV)					
	1 to 0 DNA-cisplatin	*1 to 10^{-4} DNA-cisplatin*	*1 to 10^{-3} DNA – cisplatin*	*1 to 10^{-2} DNA-cisplatin*	*1 to 10^{-1} DNA-cisplatin*	*1 to 1 DNA-cisplatin*
C 1S	286.08	286.08	285.08	286.08	285.08	285.08

Diameter measurements of platinum nanoclusters using 'Image J' software tool

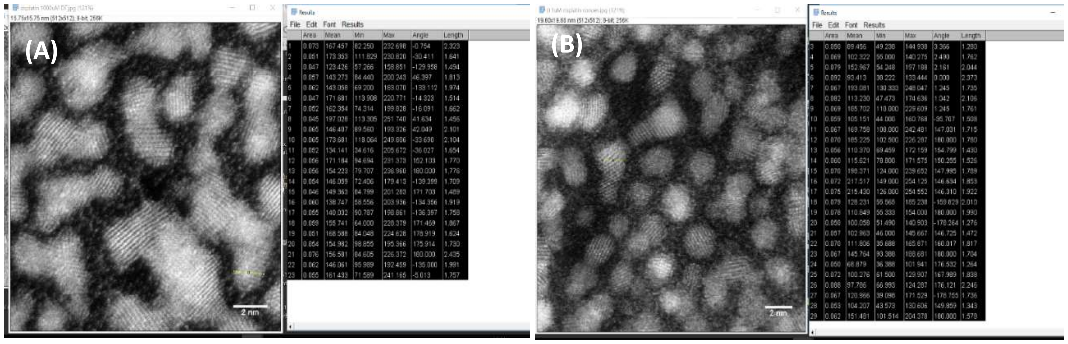

	Area	Mean	Min	Max	Angle	Length
1	0.073	167.457	82.250	232.698	-0.754	2.323
2	0.051	173.353	111.829	230.820	-30.411	1.641
3	0.047	123.426	57.266	158.851	-129.958	1.494
4	0.057	143.273	84.440	200.243	46.397	1.813
5	0.062	143.058	69.200	183.070	-133.112	1.974
6	0.047	171.681	113.908	220.771	-14.323	1.514
7	0.062	162.354	74.314	199.828	-16.091	1.662
8	0.045	197.028	113.305	251.740	41.634	1.456
9	0.065	146.407	89.560	193.326	42.049	2.101
10	0.065	173.681	118.064	249.806	-33.690	2.104
11	0.052	134.141	34.616	205.672	-36.027	1.654
12	0.056	171.184	94.694	231.373	162.133	1.770
13	0.056	154.223	79.707	238.960	180.000	1.776
14	0.054	146.059	72.406	179.413	-139.399	1.709
15	0.046	149.363	84.799	201.283	171.703	1.489
16	0.060	138.747	58.556	203.936	-134.356	1.919
17	0.055	140.032	90.787	198.861	-136.397	1.758
18	0.059	155.741	64.000	220.379	171.469	1.867
19	0.051	168.588	84.048	224.628	178.919	1.624
20	0.054	154.982	98.855	195.366	175.914	1.730
21	0.076	156.581	84.605	226.372	180.000	2.435
22	0.062	146.061	95.989	192.459	-135.000	1.991
23	0.055	161.433	71.589	241.165	-5.013	1.757

	Area	Mean	Min	Max	Angle	Length
3	0.050	89.456	49.238	144.938	3.366	1.280
4	0.069	102.322	55.000	140.275	2.490	1.762
5	0.079	152.967	54.248	197.188	2.161	2.044
6	0.092	93.413	38.222	133.444	0.000	2.373
7	0.067	193.081	130.333	248.047	1.245	1.735
8	0.082	113.230	47.473	174.636	1.042	2.106
9	0.069	165.702	110.000	229.609	1.245	1.761
10	0.059	105.151	44.000	160.768	-35.707	1.508
11	0.067	169.758	108.000	242.481	147.031	1.715
12	0.070	165.225	102.500	226.287	180.000	1.780
13	0.056	110.370	69.459	172.159	154.799	1.430
14	0.060	115.621	78.800	171.575	150.255	1.526
15	0.070	198.371	124.000	239.652	147.995	1.789
16	0.072	217.517	149.000	254.125	146.634	1.853
17	0.076	215.430	126.000	254.552	146.310	1.922
18	0.079	128.231	55.565	185.238	-159.829	2.010
19	0.078	110.849	55.333	154.000	180.000	1.990
20	0.050	100.058	51.490	140.903	-178.264	1.276
21	0.057	102.963	46.000	145.667	146.725	1.472
22	0.070	111.806	35.688	165.871	160.017	1.817
23	0.067	145.764	93.388	188.681	180.000	1.704
24	0.050	68.879	36.388	101.941	176.532	1.264
25	0.072	100.276	61.500	129.907	167.989	1.838
26	0.088	97.786	66.993	124.287	176.121	2.246
27	0.067	120.966	39.096	171.529	-178.755	1.736
28	0.053	104.207	43.573	130.606	149.859	1.343
29	0.062	151.481	101.514	204.378	180.000	1.579

Figure A1.5- *Diameter measurements made in Image J of platinum nanoclusters observed in STEM of drop cast films of (A) 1000 µM cisPt solution (B) 0.1 µM cisPt solution.*

Table A1.7- *Diameter Measurements of platinum nanoclusters in 0.1 µM Cisplatin in Image J processing program.*

0.1 µM Cisplatin			
Measurement number	***Diameter size/ nm***	***Measurement number***	***Diameter size/ nm***
1	2.093	16	1.853
2	1.863	17	1.922
4	1.762	18	2.01
5	2.044	19	1.99
6	2.373	20	1.276
7	1.735	21	1.472
8	2.106	22	1.817
9	1.761	23	1.704
10	1.508	24	1.264
11	1.715	25	1.838
12	1.78	26	2.246
14	1.526	27	1.736
15	1.789	29	1.578
Average (3 significant figures)	***1.80***		
STDEV ERROR (3 significant figures)	***0.27***		

Table A1.8- *Diameter Measurements of platinum nanoclusters in 1000 µM cisplatin in Image J processing program.*

1000 µM Cisplatin			
Measurement number	***Diameter size/ nm***	***Measurement number***	***Diameter size/ nm***
1	2.323	16	1.709
2	1.641	17	1.489
4	1.494	18	1.919
5	1.813	19	1.758
6	1.974	20	1.867
7	1.514	21	1.624
8	1.662	22	1.73
9	1.456	23	2.435
10	2.101	24	1.991
11	2.104	25	1.757
12	1.654		
14	1.77		
15	1.776		
Average (3 significant figures)	***1.81***		
STDEV ERROR (3 significant figures)	***0.26***		

Table A1.9- *Diameter Measurements of platinum nanoclusters in 1 to 1 DNA- cisPt solution in Image J processing program.*

1 to 1 DNA-cisPt solution			
Measurement number	***Diameter size/ nm***	***Measurement number***	***Diameter size/ nm***
1	3.79	11	7.98
2	2.67	12	5.84
4	4.92	14	3.62
5	6.39	15	4.11
6	6.65	16	2.01
7	1.59	17	1.86
8	1.89	18	3.00
9	2.26	19	2.47
10	2.83		
Average (3 significant figures)	3.83		
STDEV ERROR (3 significant figures)	1.85		

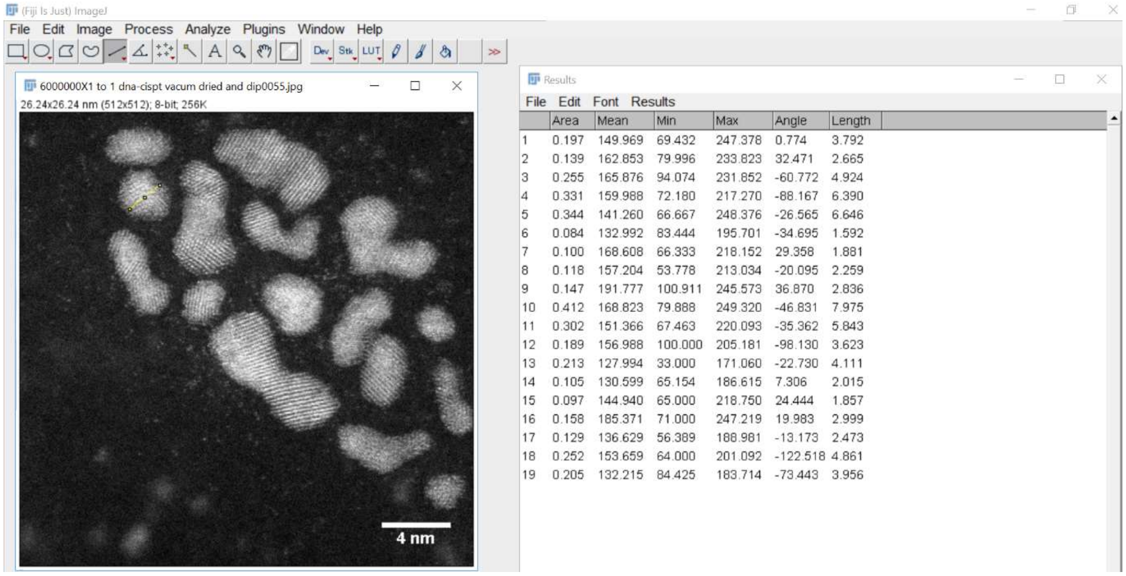

	Area	Mean	Min	Max	Angle	Length
1	0.197	149.969	69.432	247.378	0.774	3.792
2	0.139	162.853	79.996	233.823	32.471	2.665
3	0.255	165.876	94.074	231.852	-60.772	4.924
4	0.331	159.988	72.180	217.270	-88.167	6.390
5	0.344	141.260	66.667	248.376	-26.565	6.646
6	0.084	132.992	83.444	195.701	-34.695	1.592
7	0.100	168.608	66.333	218.152	29.358	1.881
8	0.118	157.204	53.778	213.034	-20.095	2.259
9	0.147	191.777	100.911	245.573	36.870	2.836
10	0.412	168.823	79.888	249.320	-46.831	7.975
11	0.302	151.366	67.463	220.093	-35.362	5.843
12	0.189	156.988	100.000	205.181	-98.130	3.623
13	0.213	127.994	33.000	171.060	-22.730	4.111
14	0.105	130.599	65.154	186.615	7.306	2.015
15	0.097	144.940	65.000	218.750	24.444	1.857
16	0.158	185.371	71.000	247.219	19.983	2.999
17	0.129	136.629	56.389	188.981	-13.173	2.473
18	0.252	153.659	64.000	201.092	-122.518	4.861
19	0.205	132.215	84.425	183.714	-73.443	3.956

***Figure A1.9-** Diameter Measurements of platinum of 1 to 1 DNA-cisPt solution casted on TEM grid and characterised via STEM imaging.*

Appendix 2- Chapter 5: Functionalisation of DNA-cisplatin with Single Walled Carbon Nanotubes (SWCNT)

Nanocluster size measurements with sonication time

Table A2.1*: Data measurements of the nanocluster size at 15 minutes sonication of the 2 to 1 SWCNTS –DNA-cisPt based on STEM Images in figures 5 (A) to (C).*

Measurement number	Particle size / nm
1	58.073
2	48.646
3	19.231
4	61.059
5	105.212
6	73.517
7	41.268
8	45.395
9	35.071
10	45.973
11	22.133
Average ± Standard deviation error	50.1 ± 24.2 nm

Table A2.2*- Data measurements of the nanocluster size at 90 minutes sonication of the 2 to 1 SWCNTS –DNA-cisPt based on STEM Images in figures 5 (D) to (F).*

Measurement number	Particle size / nm	Measurement number	Particle size / nm	Measurement number	Particle size / nm	Measurement number	Particle size / nm
1	12.258	12	28.95	23	16.769	34	7.225
2	19.549	13	7.471	24	8.078	35	9.501
3	8.502	14	5.709	25	6.342	36	11.17
4	17.394	15	17.246	26	5.381	37	8.716
5	10.51	16	6.383	27	10.696	38	8.393
6	10.452	17	15.172	28	8.675	39	9.642
7	11.4	18	31.173	29	19.288	40	10.596
8	11.13	19	7.895	30	11.936	41	10.218
9	8.285	20	14.173	31	7.622	42	11.377
10	12.52	21	16.706	32	10.086	43	7.225
11	12.258	22	8.682	33	9.651	44	9.501
Average ± Standard deviation error	12.3 ± 2.73 nm						

***Nanocluster size measurements with sonication time at* higher resolution**

Table A2.3- *Data measurements of the nanocluster size at 45 minutes sonication of the 2 to 1 SWCNTS –DNA-cisPt from STEM images.*

Measurement number	**Particle size / nm**	**Measurement number**	**Particle size / nm**
1	1.639	16	0.827
2	2.398	17	1.433
3	2.213	18	1.123
4	0.986	19	0.728
5	1.56	20	0.852
6	1.36	21	1.203
7	1.886	22	0.771
8	0.713	23	1.837
9	1.07	24	1.521
10	2.262	25	1.577
11	2.103	26	2.166
12	1.702	27	0.993
13	0.775	28	0.82
14	1.076	29	0.793
15	1.036	30	1.705
Average ± Standard deviation error	1.26 ± 0.57 nm		

Table A2.4- *Data measurements of the nanocluster size at 90 minutes sonication of the 2 to 1 SWCNTS –DNA-cisPt from STEM images.*

Measurement number	Particle size / nm	Measurement number	Particle size / nm	Measurement number	Particle size / nm	Measurement number	Particle size / nm
1	1.628	43	0.832	83	1.344	122	1.174
2	1.601	44	2.366	84	1.058	123	1.193
3	1.69	45	2.288	85	1.079	124	0.675
4	1.508	46	1.765	86	1.404	125	1.068
5	0.721	47	1.285	87	0.904	126	1.14
6	1.039	48	1.183	88	1.706	127	1.767
7	1.324	49	1.747	89	0.883	128	1.233
8	0.849	50	1.196	90	1.026	129	1.603
9	0.789	51	1.018	91	2.118	130	1.604
10	2.164	52	0.656	92	0.774	131	1.628
11	1.69	53	0.676	93	1.033	132	0.65
12	1.198	54	0.765	94	0.962	133	1.179
13	1.694	55	1.102	95	1.083	134	0.581
14	1.426	56	1.422	96	1.854	135	0.757
15	0.877	57	1.681	97	0.993	136	0.97
16	0.592	58	2.029	98	1.646	137	1.273
17	1.439	59	2.457	99	0.871	138	0.74
18	0.594	60	2.288	100	0.599	139	1.217
19	0.553	61	0.98	101	1.174	140	1.075
20	0.704	62	0.973	102	1.455	141	0.839
21	0.902	63	0.741	103	1.713	142	1.25
22	0.864	64	1.468	104	1.217	143	1.32
23	1.916	65	1.408	105	1.564	144	1.95
24	1.973	66	1.267	106	1.291	145	1.205
25	1.297	67	1.05	107	1.885	146	1.973
26	1.577	68	0.978	108	1.922	147	1.36
27	0.826	69	1.081	109	0.943	148	1.209
28	0.951	70	0.86	110	1.586	149	1.465
29	0.869	71	1.118	111	0.914	150	1.084
30	0.888	72	0.99	112	0.774	151	0.999
31	1.916	73	1.205	113	0.914	152	1.268
32	1.403	74	1.548	114	1.034	153	1.034
34	1.352	75	1.678	115	1.894	154	2.008
35	0.761	76	1.478	116	1.104	155	1.36
36	1.521	77	1.036	117	1.432	156	1.142
37	1.118	78	1.935	118	1.199	157	1.061
38	1.296	79	1.248	119	1.088	158	0.691
39	0.758	80	1.763	120	1.147	159	1.046
40	1	81	1.232	121	1.125	160	1.193
41	1.016	82	2.1	122	1.174	161	1.316
Average particle size ± standard deviation error	1.26 ± 0.37 nm						

Table A2.5- *Data measurements of the nanocluster size at 30 minutes sonication of the 2 to 1 SWCNTS –DNA-cisPt from STEM.*

Measurement number	**Particle size / nm**	**Measurement number**	**Particle size / nm**	**Measurement number**	**Particle size / nm**
1	1.704	33	2.422	65	2.331
2	2.826	34	1.994	66	1.207
3	1.587	35	0.661	67	1.457
4	1.481	36	1.871	68	1.43
5	1.798	37	1.632	69	2.376
6	1.761	38	1.781	70	0.935
7	2.175	39	1.566	71	1.618
8	0.915	40	1.107	72	1.112
9	1.023	41	1.558	73	0.682
10	0.675	42	1.628	74	0.969
11	0.784	43	1.086	75	0.862
12	1.019	44	1.168	76	0.915
13	0.925	45	1.381	77	1.389
14	0.791	46	1.329	78	0.685
15	1.275	47	1.142	79	1.092
16	1.832	48	1.617	80	0.755
17	0.592	49	1.674	81	0.769
18	0.921	50	1.282	82	0.955
19	0.967	51	0.846	83	0.859
20	0.755	52	1.813	84	0.652
21	0.806	53	1.368	85	0.852
22	2.015	54	1.258	86	0.643
23	1.545	55	1.646	87	1.257
24	2.04	56	1.836	88	1.119
25	2.846	57	1.504	89	0.925
26	0.638	58	1.708	90	0.61
27	1.099	59	1.751	91	0.415
28	0.754	60	1.225	92	1.073
29	0.927	61	1.07	93	1.436
30	2.36	62	1.804	94	1.047
31	2.159	63	1.692	95	1.15
32	1.808	64	1.012	96	1.232
Average particle size ± standard deviation error	1.321 ± 0.52 nm				

Table A2. 6- *Data measurements of the nanocluster size at 15 minutes sonication of the 2 to 1 SWCNTS –DNA-cisPt from STEM.*

Measurement number	**Particle size / nm**	**Measurement number**	**Particle size / nm**	**Measurement number**	**Particle size / nm**
1	2.086	33	0.73	65	2.189
2	2.181	34	0.801	66	2.55
3	3.085	35	0.773	67	2.513
4	3.085	36	0.733	68	1.586
5	2.989	37	0.74	69	0.614
6	2.506	38	1.043	70	2.189
7	2.061	39	0.859	71	2.55
8	1.814	40	0.816	72	1.888
9	1.81	41	0.978	73	1.69
10	2.367	42	0.952	74	1.27
11	2.372	43	0.734	75	0.943
12	1.807	44	1.024	76	1.439
13	2.133	45	2.162	77	1.003
14	1.853	46	1.573	78	1.018
15	2.172	47	2.276	79	1.146
16	1.172	48	3.034	80	0.59
17	2.45	49	3.123	81	0.85
18	1.755	50	2.584	82	0.788
19	1.485	51	3.286	83	0.908
20	1.541	52	2.752	84	0.792
21	1.408	53	2.274	85	1.089
22	1.332	54	2.551	86	1.092
23	1.373	55	3.503		
24	1.396	56	1.831		
25	1.085	57	1.526		
26	0.884	58	2.202		
27	0.959	59	2.889		
28	0.916	60	1.942		
29	1.373	61	1.206		
30	0.819	62	0.957		
31	1.079	63	1.625		
32	0.734	64	1.878		
Average particle size ± standard deviation error	1.57 ± 0.64 nm				

Nanocluster size measurements with ratio of the SWCNTS to DNA-cisPt

Table A2.7: *Platinum nanocluster size data of the measurements of the STEM images in figure 9 (A, B) at the 0.5:1 SWCNT –DNA-cisPt material.*

Measurement number	**Particle size / nm**
1	2.436
2	2.395
3	1.552
4	2.03
5	1.544
6	2.065
7	1.14
8	1.207
9	1.577
10	1.604
11	1.744
Average ± Standard deviation error	1.51 ± 0.67 nm

Table A2.8: *Platinum nanocluster size data of the measurements of the STEM images in figure 9 (C-F) at the 1:1 SWCNT –DNA-cisPt material.*

Measurement number	**Particle size / nm**	**Measurement number**	**Particle size / nm**	**Measurement number**	**Particle size / nm**
1	2.569	18	2.109	35	1.563
2	1.906	19	2.215	36	2.221
3	2.312	20	1.802	37	2.181
4	1.075	21	1.875	38	2.161
5	2.159	22	1.508	39	1.134
6	1.856	23	1.768	40	1.369
7	1.196	24	1.563	41	0.833
8	2.597	25	2.221	42	1.006
9	2.105	26	2.181	43	2.274
10	2.063	27	2.161	44	1.515
11	1.582	28	1.134	45	1.525
12	1.309	29	1.369	46	1.164
13	0.95	30	0.833	47	0.946
14	1.301	31	1.006	48	1.245
15	0.954	32	2.274	49	0.862
16	0.596	33	1.515	50	0.839
17	1.197	34	1.768	51	0.595
Average ± Standard deviation error	1.57 ± 0.55 nm				

Table A2.9: *Platinum nanocluster size data of the measurements of the STEM images in figure 9 (G-H) at the 2:1 SWCNT –DNA-cisPt material.*

Measurement number	**Particle size / nm**	**Measurement number**	**Particle size / nm**
1	1.639	16	0.827
2	2.398	17	1.433
3	2.213	18	1.123
4	0.986	19	0.728
5	1.56	20	0.852
6	1.36	21	1.203
7	1.886	22	0.771
8	0.713	23	1.837
9	1.07	24	1.521
10	2.262	25	1.577
11	2.103	26	2.166
12	1.702	27	0.993
13	0.775	28	0.82
14	1.076	29	0.793
15	1.036	30	1.705
Average ± Standard deviation error	1.26 ± 0.55 nm		

Theoretical Area: Scan rate study and R-S plots

2 to 1 SWCNT to DNA-Cisplatin

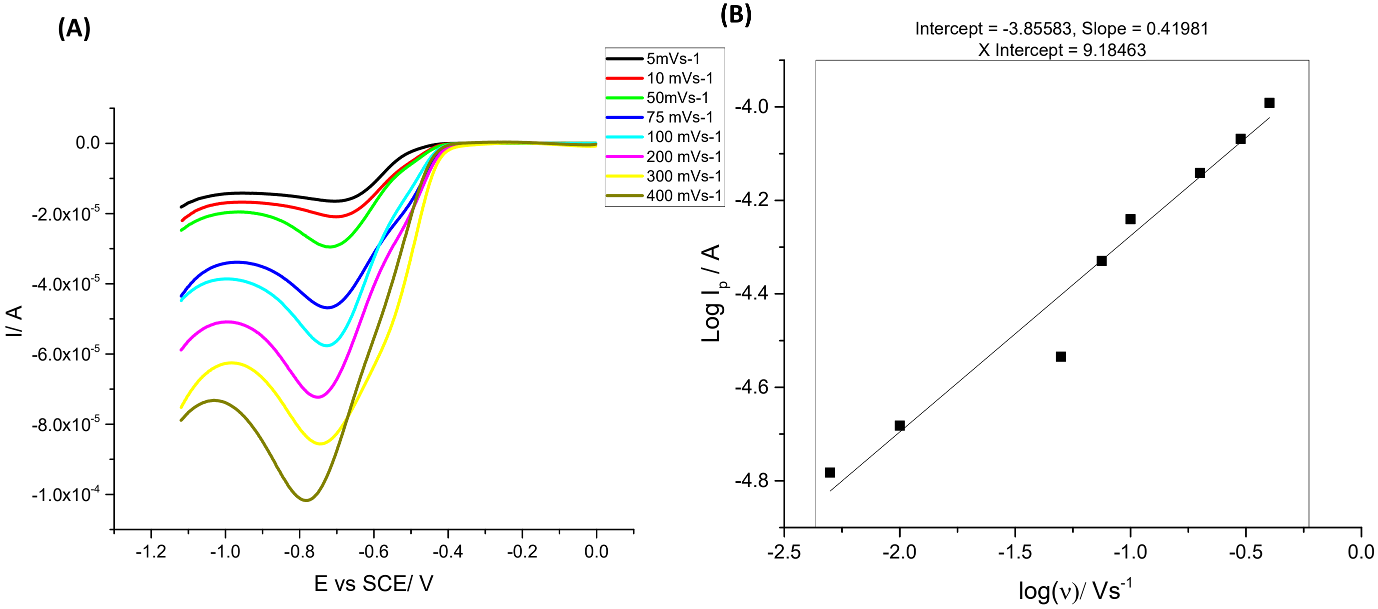

Figure A2.1- *Voltammetry response for the HER at 2:1 SWCNT-DNA-cisPt/GC in 1.04 mM $HClO_4$ and 0.1 M $NaClO_4$ at different scan rates (B) log R-S plot.*

1 to 1 SWCNT-DNA functionalized with cisplatin

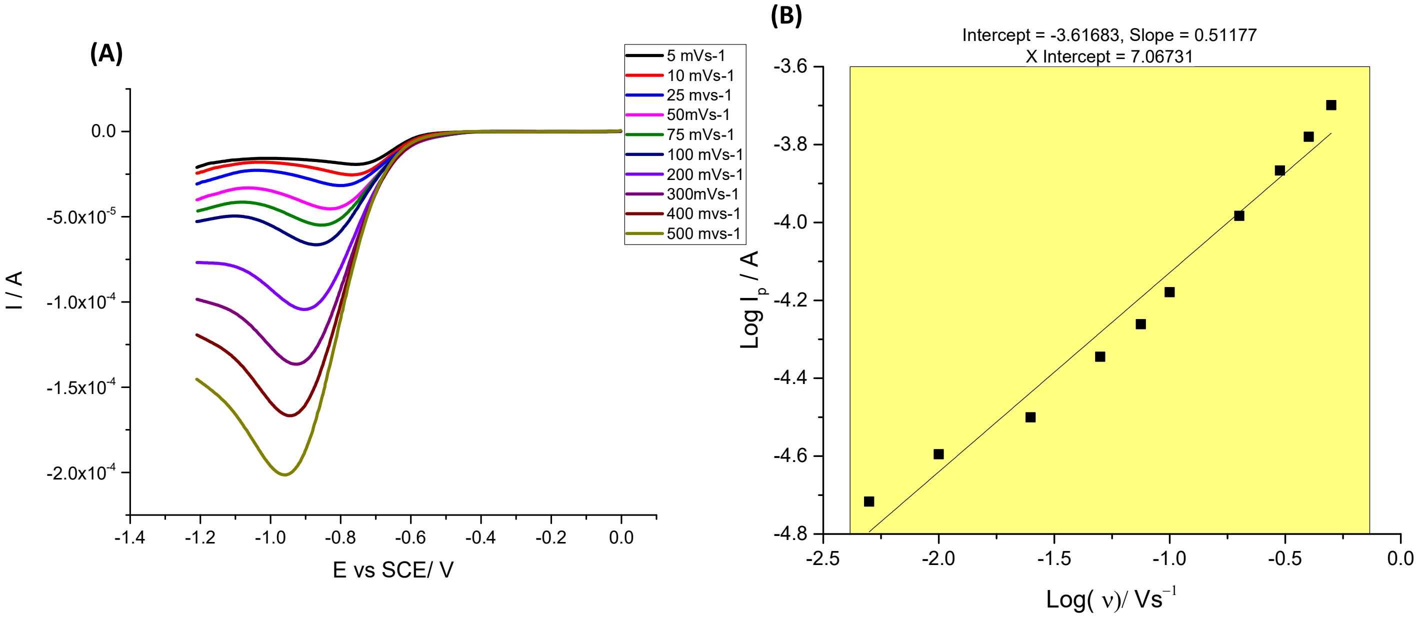

Figure A2.2- *Voltammetry response for the HER at 1:1 SWCNT-DNA functionalised with cisPt/GC in 1.04 mM HClO$_4$ and 0.1 M NaClO$_4$ at different scan rates (B) log R-S plot.*

Glassy Carbon (GC)

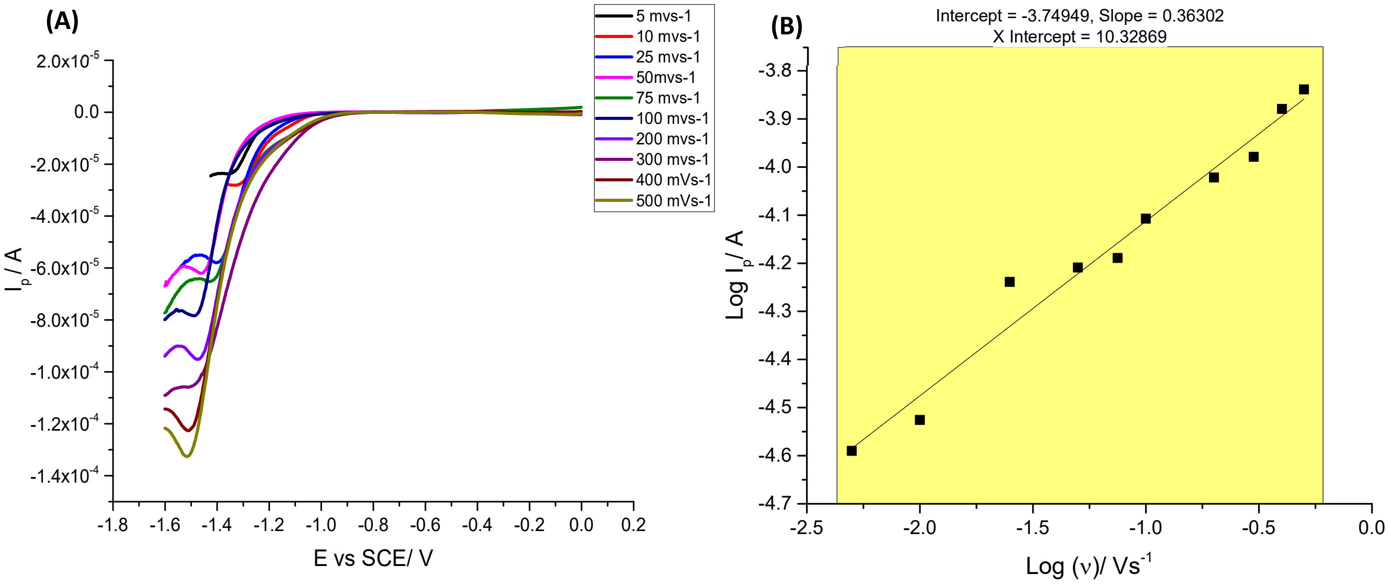

Figure A2.3- *Voltammetry response for the HER at bare GC (d= 3 mm) in 1.04 mM HClO$_4$ and 0.1 M NaClO$_4$ at different scan rates (B) log R-S plots.*

1 to 1 DNA-cisPt

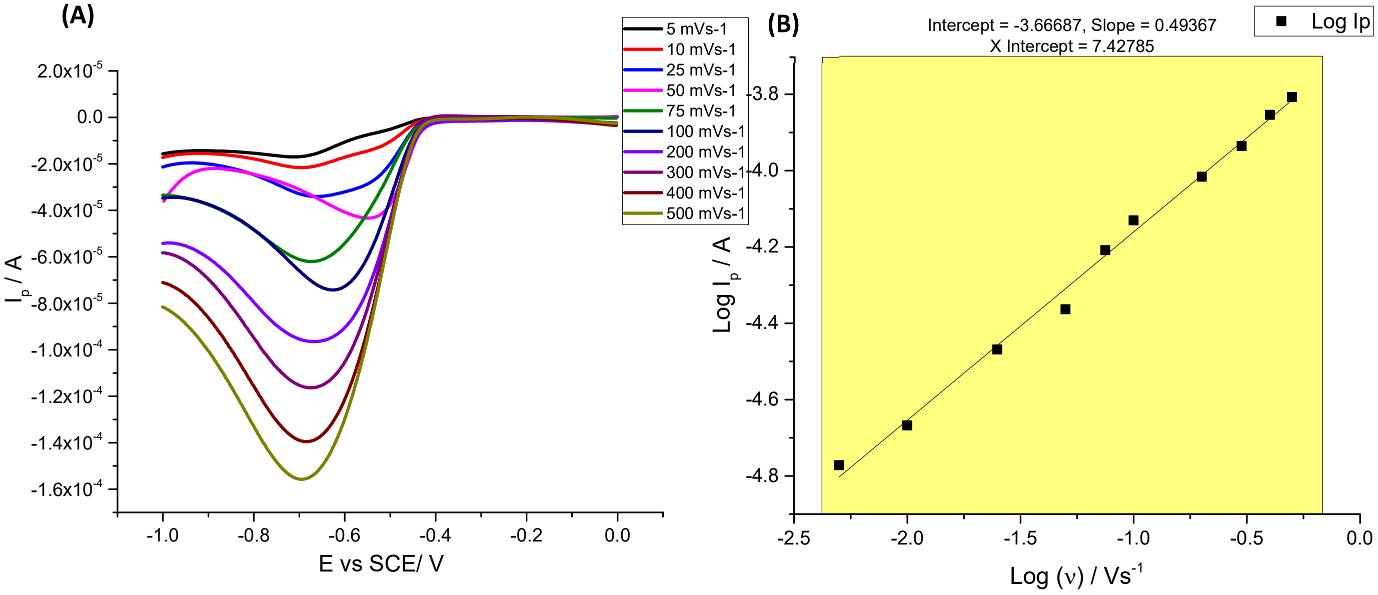

Figure A2.4- *Voltammetry response for the HER at 1 to 1 DNA-cisPt/GC in 1.04 mM $HClO_4$ and 0.1 M $NaClO_4$ at different scan rates (B) log R-S plots.*

4 to 1 SWCNT-DNA-cisPt

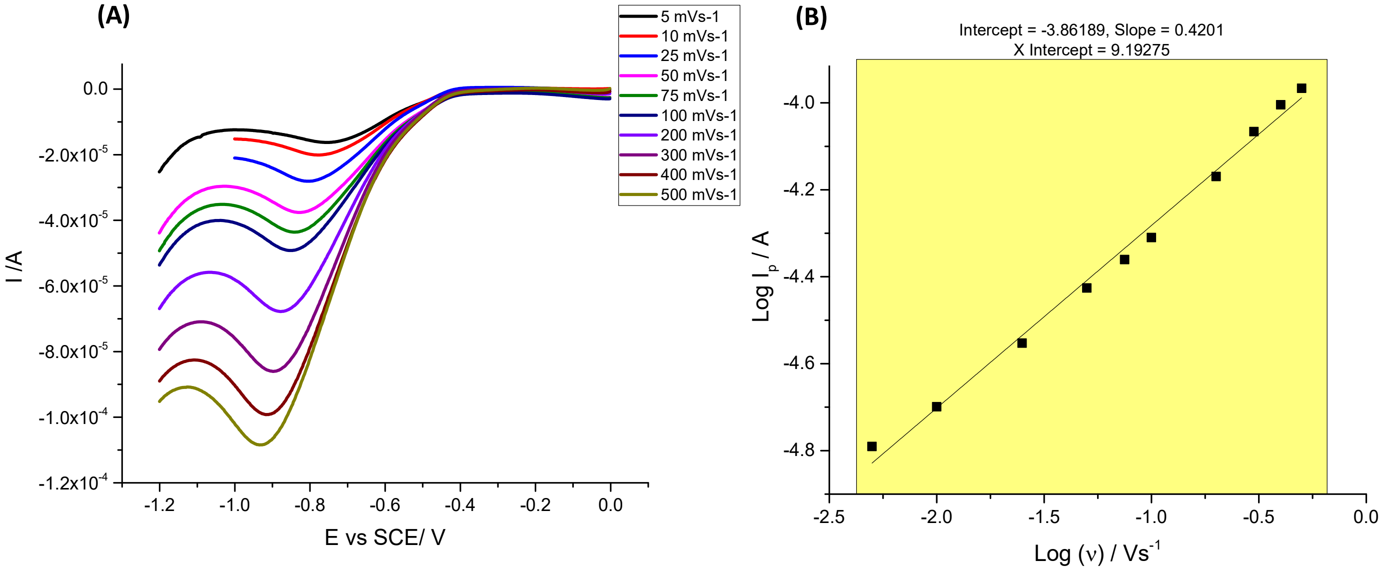

Figure A2.5- *Voltammetry response for the HER at 4 to 1 SWCNT-DNA-cisPt/GC in 1.04 mM $HClO_4$ and 0.1 M $NaClO_4$ at different scan rates (B) log R-S plots.*

SWCNT's-Cisplatin

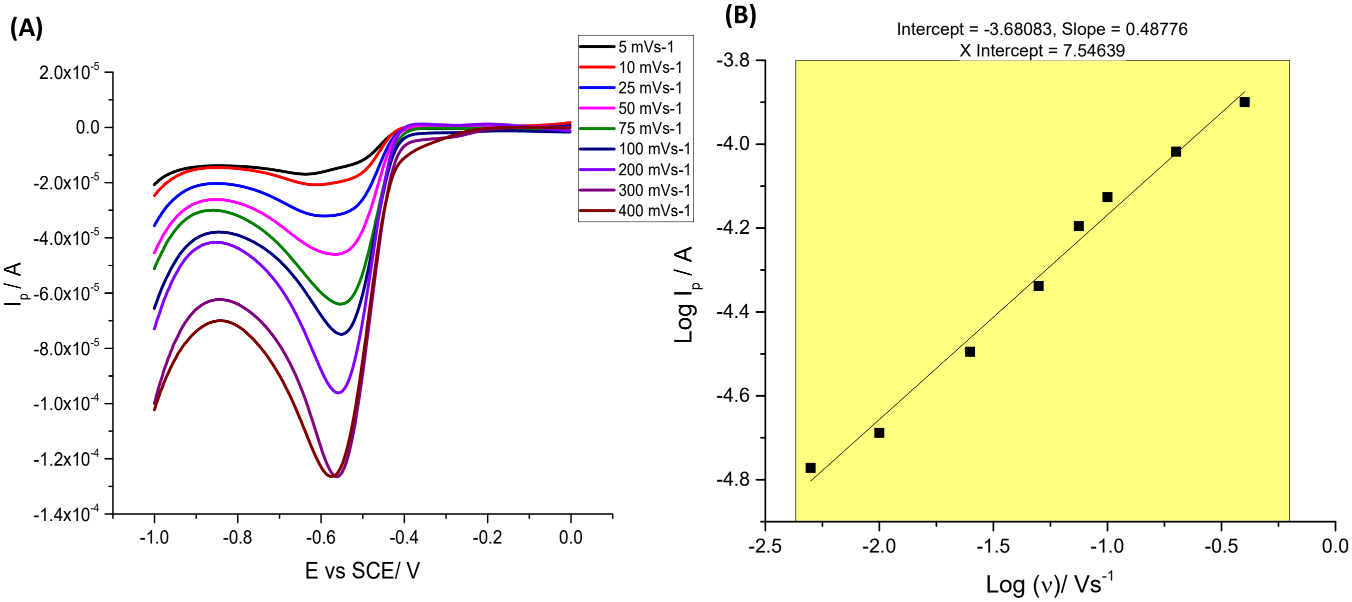

Figure A2.6-: *Voltammetry response for the HER at SWCNT- cisPt/GC in 1.04 mM HClO$_4$ and 0.1 M NaClO$_4$ at different scan rates (B) Log R-S plots.*

SWCNT's

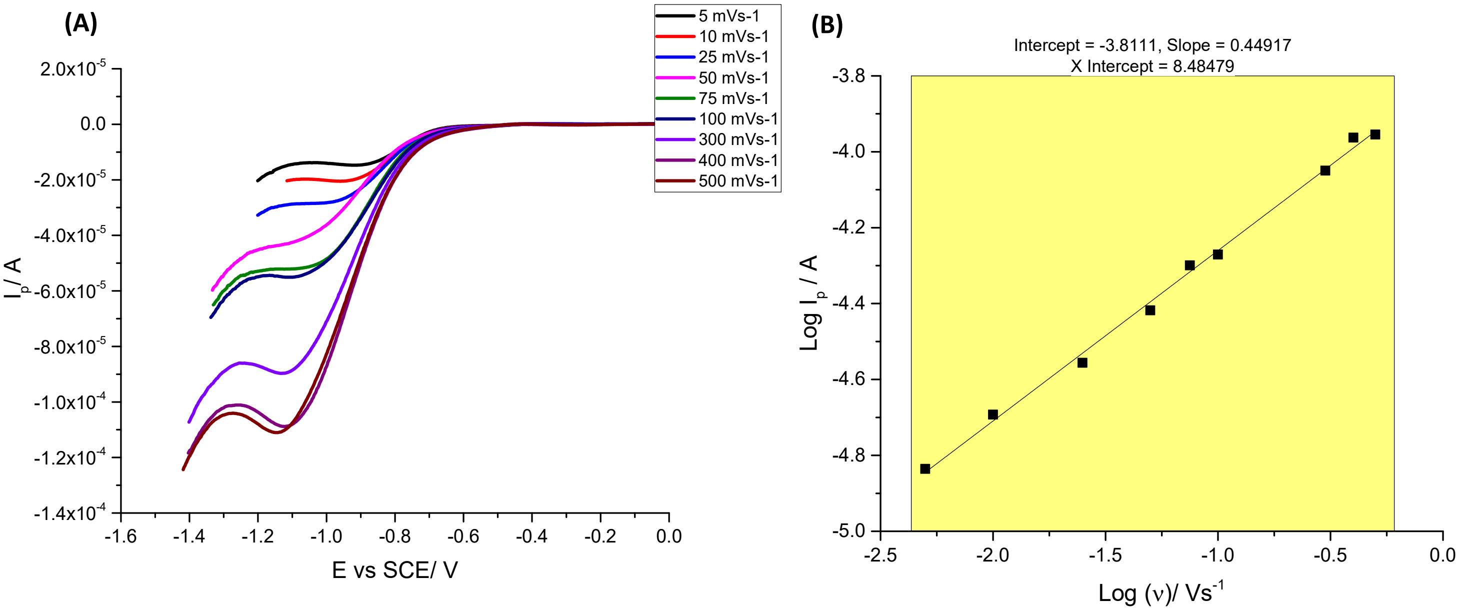

Figure A2.7*- Voltammetry response for the HER at 1000 μM SWCNT/GC in 1.04 mM HClO$_4$ and 0.1 M NaClO$_4$ at different scan rates (B) R-S plots.*

The log scan rate$^{0.5}$ vs log Peak current (I_P) plot for all the casted materials explored, the slope of the logarithmic of I_p vs scan rate ranged from 0.40 to 0.52, which is reflective of that of a diffusion controlled process.

Tafel slopes and alpha estimation

Tafel Plots

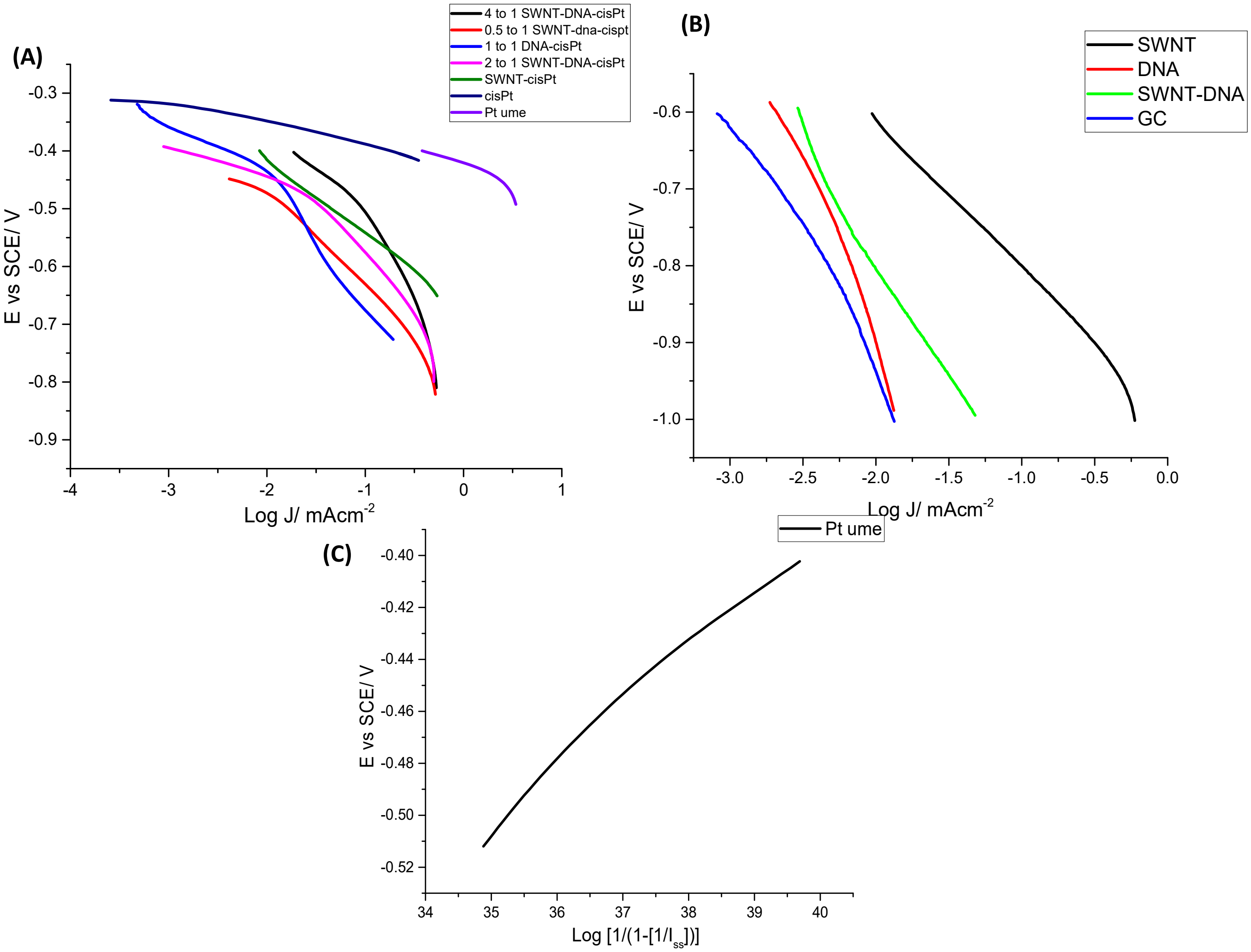

Figure A2.8 *-Tafel plot for (A) DNA-Cisplatin functionalized material (B) DNA functionalized material (C) Pt UME mass transport corrected at 50 mVs^{-1}, linear fit of y= 0. 0227x -1.296.*

Alpha calculations

Tafel slope for the HER at cisPt/GC is found to be 49.7 mVdec^{-1}.

$$\alpha = \frac{RT}{F(Tafel\ slope)} = \frac{(8.314\ \times 298)}{\left(96485\ \times \left(\frac{49.7}{1000}\right)\right)} = 0.516 = 0.52$$

Influence of Sonication time on Platinum cluster size measurements in image J

15 minutes

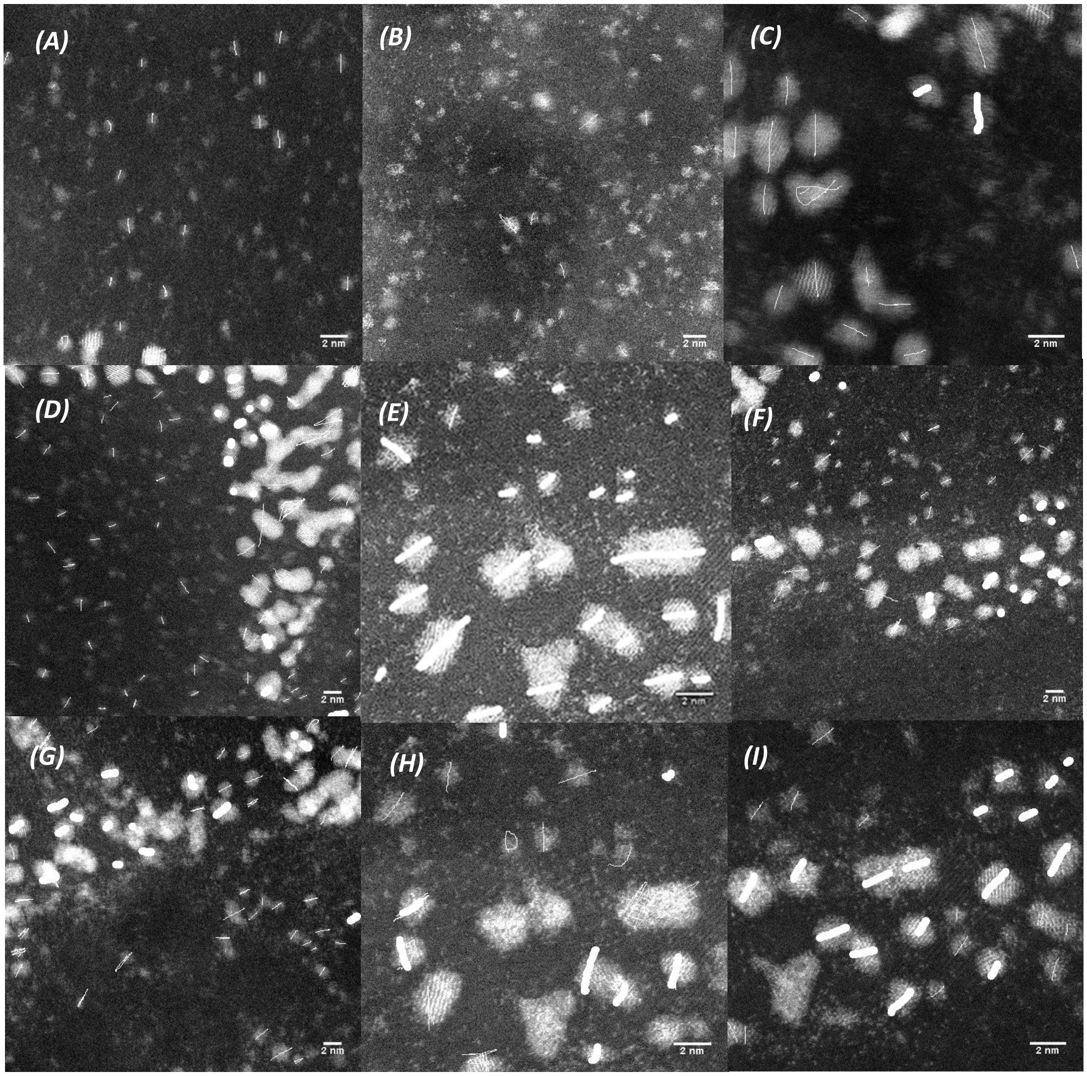

Figure A2.9- *(A- C) Measurements of the influence of sonication time employed on the functionalisation of a ratio of 2 to 1 DNA-cisPt with SWCNTs (A-C) 15 minutes in image J (D) 30 minutes (E) 45 minutes (F-I) 90 minutes in a 9-10 °C ice water bath.*

Appendix 3- Chapter 6: Graphitization of the DNA-cisPt via electron beam irradiation for the electrocatalysis of the hydrogen evolution reaction (HER)

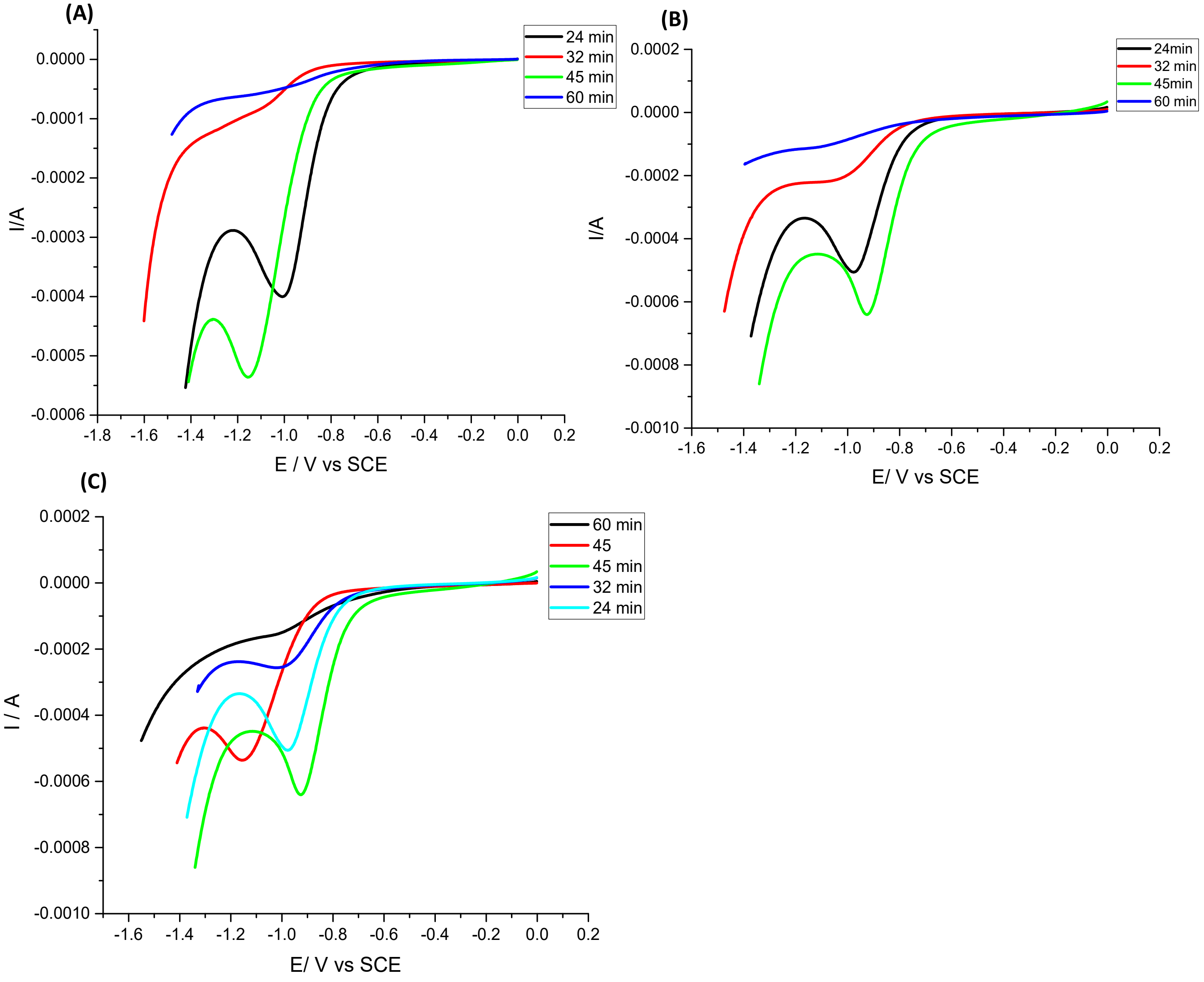

Figure A3.1- *Voltammetry response for HER (1 mM $HClO_4$ 0.1 M $NaClO_4$) 50 mV s^{-1}, 41.7 μL of 1 to 10^{-3} DNA-cisPt drop-cast on 5 mm GC at different exposure times of a 5 Kev electron beam error bars based on a standard deviation error (A) (1st scan) first set of data (B) (1^{st} scan) second set of data (C) 3^{rd} scan (first set of data).*

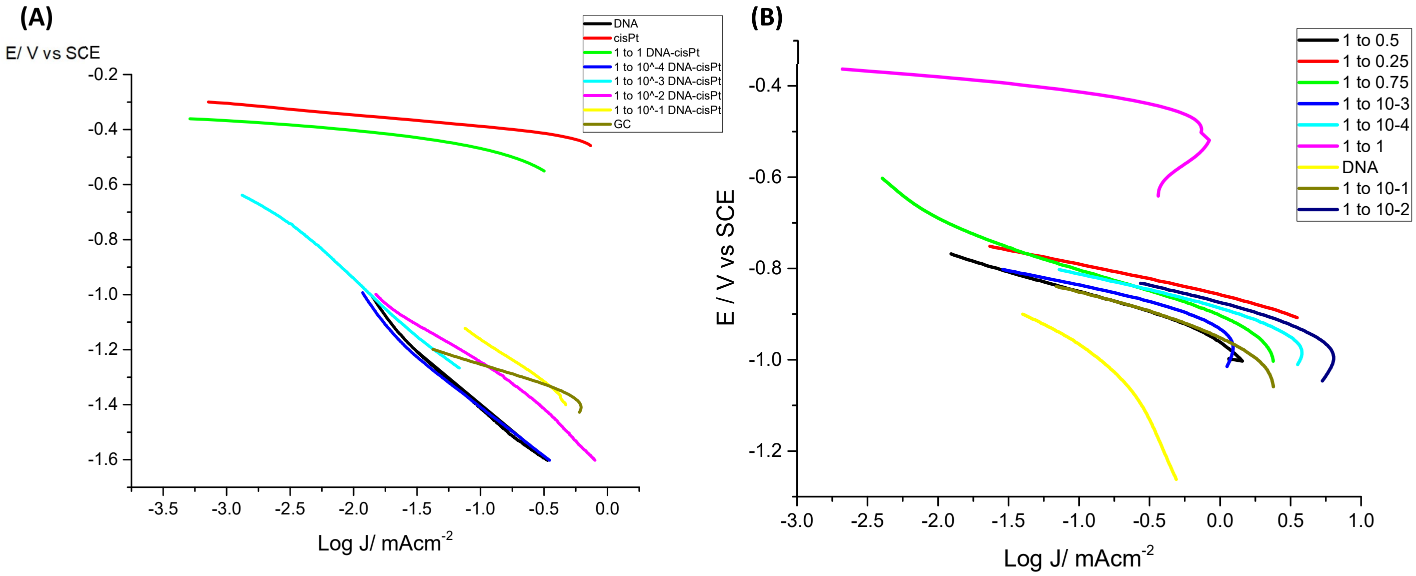

***Figure A3.2**- Tafel plots for the different DNA-cisPt loadings pre-irradiation (A) Different DNA-cisPt untreated (B) Different DNA-cisPt material following e-beam irradiation (5 keV, 24 min).*

E-beam irradiated DNA vs DNA-cisplatin

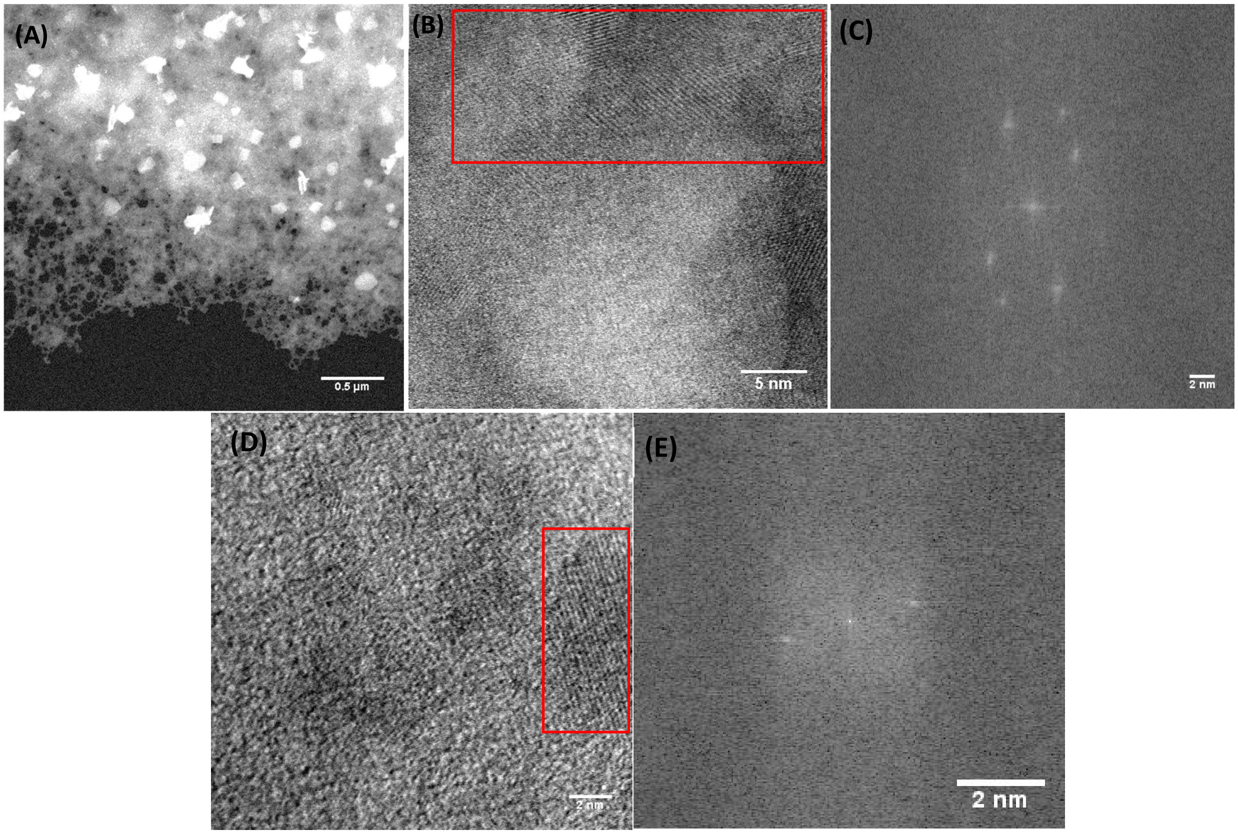

Figure A3.3- *HAADFF STEM imaging of Electron beam exposed (5 Kev, 24 minutes) (A) 1 to 1 DNA-cisPt (HADFF DF imaging) (B) 1000 µM DNA (HADFF BF imaging) (C) corresponding FFT measurements of outlined area in figure A3.3 (B) (D) 1 to 10^{-3} DNA-cisPt 5keV, 24 minutes (HAADFF BF imaging) (E) corresponding FFT measurements of outlined area in figure A3.3 (D).*

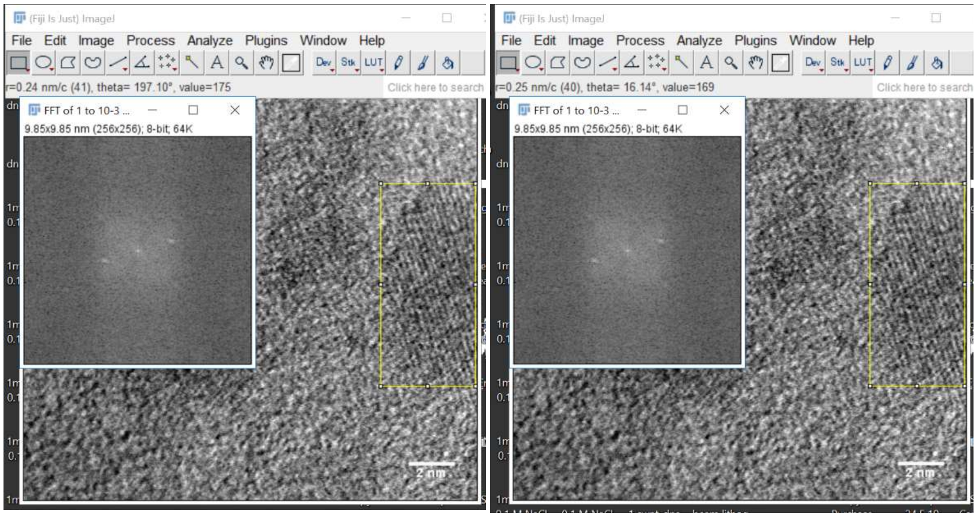

```
r=0.24 nm/c (41), theta= 197.10°, value=175
9.85x9.85 nm (256x256); 8-bit; 64K
```

```
r=0.25 nm/c (40), theta= 16.14°, value=169
9.85x9.85 nm (256x256); 8-bit; 64K
```

Figure A3.4- *FFT measurements for made for the selected region of the 1 to 10^{-3} DNA-cisPt.*

Average lattice spacing of 0.23 ± 0.015 nm* is found for 1 to 10^{-3} DNA-cisplatin, using the FFT function. * Based on a standard deviation error.

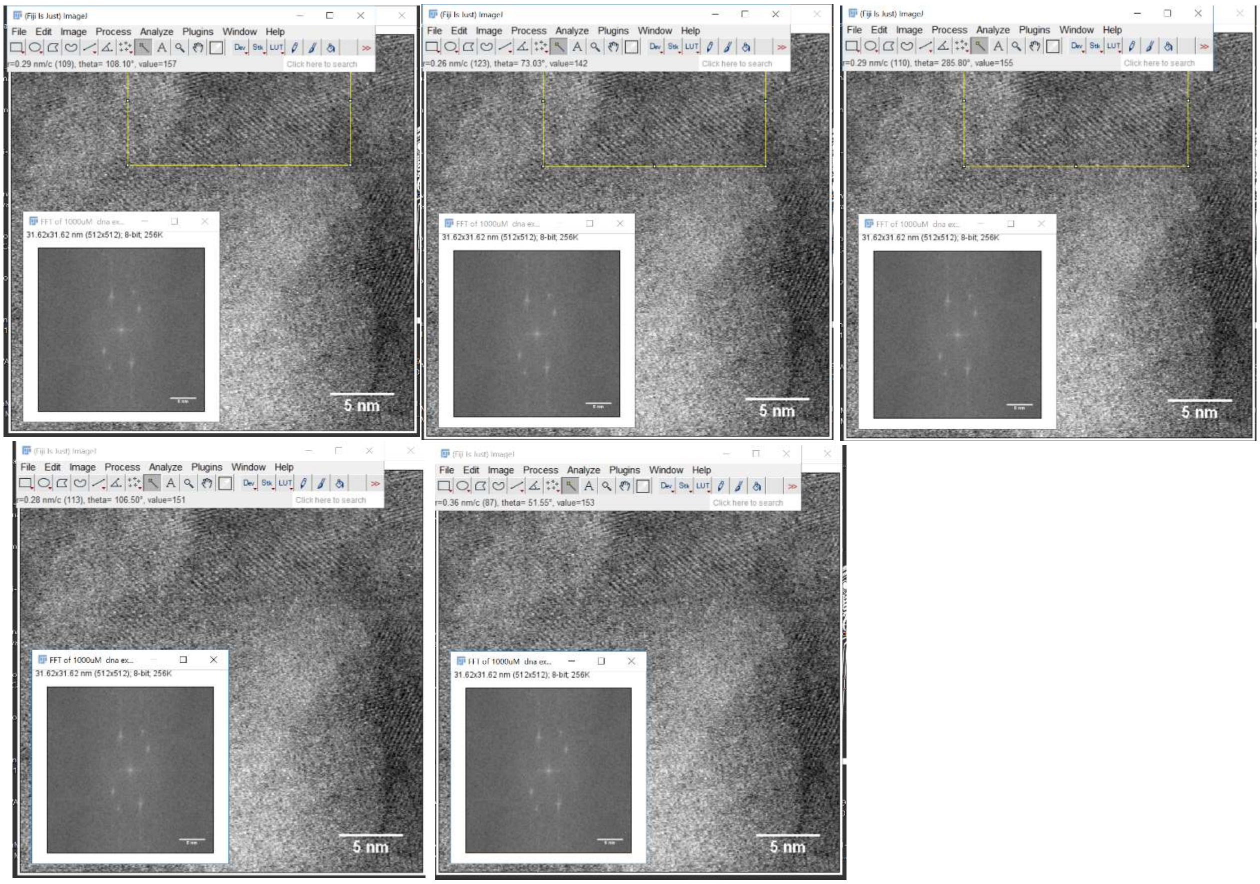

```
r=0.29 nm/c (109), theta= 108.10°, value=157
r=0.26 nm/c (123), theta= 73.03°, value=142
r=0.29 nm/c (110), theta= 285.80°, value=155
r=0.28 nm/c (113), theta= 106.50°, value=151
r=0.36 nm/c (87), theta= 51.55°, value=153
```

***Figure A3.5**- FFT measurements for made for the selected region of the 1000 µM DNA.*

Based on the FFT images generated, average of 0.29 ± 0.0512nm* found for 1000 µM DNA.

*based on a standard deviation error. Lattice measurement found reflective of carbon based material not platinum, given that for platinum 0.34 nm is reported for platinum metal lattice compared with 0.26nm (pure DNA) and an average lattice spacing of 0.23 nm for 1 to 10^{-3} DNA-cisplatin, using the FFT function.

Appendix 4- Chapter 7: Carbonisation of the DNA-cisplatin via a pseudo pyrolysis process for the electrocatalysis of the Hydrogen Evolution Reaction (HER)

Heat flow rate and heating rate calculations

The following expression can simply be used to attain the heat flow rate for the heat treatment process of the DNA-cisPt material, under an inert nitrogen atmosphere:

$$Q = \dot{m}c_p\Delta T \; Eq. (1)$$

Where Q is the heat flow rate (Js^{-1}), $\dot{m}$ is the mass flow rate (kgs^{-1}), c_p is the specific heat capacity ($Jkg^{-1}K^{-1}$) and ΔT is the temperature difference in K.

Given a volumetric flowrate of nitrogen gas of 50 $Lmin^{-1}$, we can convert this to mass flowrate using:

$$\dot{m} = \rho q \; Eq. (2)$$

Where $\dot{m}$ the mass flow rate (kgs^{-1}), ρ is the density ($kgcm^{-3}$) and q is the volumetric flowrate (cm^3s^{-1}).

Table A4.1: *Physical properties of Nitrogen at the relevant temperature condition [1].*

Temperature / °C	Density of Nitrogen/ $kgcm^{-3}$	Specific heat capacity of Nitrogen/ $kJkg^{-1}K^{-1}$
160	0.779	1.044
255	0.638	1.0605
350	0.542	1.0805

At room temperature and pressure conditions, the density of nitrogen is 1.132 kgm^{-3}. For the range of temperature conditions used for the heat treatment i.e. 160 to 350 °C, the density changes as presented in Table 1.

A volumetric flowrate of 50 $mLmin^{-1}$ is equivalent to 0.83 cm^3s^{-1}. Thus we can find the mass flowrate using equation (2) for the temperature range used in this work as shown:

$$At\ 160\ °C, \dot{m} = 0.779\ Kgcm^{-3} \times 0.83\ cm^3s^{-1} = 0.649\ kgs^{-1}\ Eq. (2a)$$
$$At\ 255\ °C, \dot{m} = 0.638\ Kgcm^{-3} \times 0.83\ cm^3s^{-1} = 0.532\ kgs^{-1}\ Eq. (2b)$$
$$At\ 350\ °C, \dot{m} = 0.542\ Kgcm^{-3} \times 0.83\ cm^3s^{-1} = 0.452\ kgs^{-1}\ Eq. (2c)$$

Therefore we calculate the heat flowrate (Q) (Js^{-1}) using equation (1) by substituting the relevant mass flowrate (equations 2(a-c)), temperature and the relevant specific heat capacity of nitrogen (see Table 1), we can find the heat flowrate as shown:

At 160 °C

$$Q = 0.649\ kgs^{-1} \times 1.044\ kJkg^{-1}K^{-1} \times (433 - 298)\ K = 91.5\ kJs^{-1}\ Eq. (3)$$

At 250 °C

$$Q = 0.532\ kgs^{-1} \times 1.0605\ kJkg^{-1}K^{-1} \times (528 - 298)\ K = 129.8\ kJs^{-1}\ Eq. (4)$$

At 350 °C

$$Q = 0.452\ kgs^{-1} \times 1.0805\ kJkg^{-1}K^{-1} \times (623 - 298)\ K = 158.7\ kJs^{-1}\ Eq. (5)$$

The heating rate of the process can be deduced simply from the following expression:

$$Heating\ rate = \frac{T_2 - T_1}{t_2 - t_1}\ Eq.(6)$$

Were T_2, t2 are the outlet temperature and time respectively and T_1, t1 are the inlet temperature and time conditions respectively. Therefore using expression (6) we can calculate the heating rate for the temperature range over a process duration of 30 minutes as shown:

At 160 °C

$$Heating\ rate = \frac{(160 - 25)\ °C}{(30 - 0)min} = \ 4.5\ °C\ min^{-1}$$

At 255 °C

$$Heating\ rate = \frac{(255 - 25)\ °C}{(30 - 0)min} = \ 7.7\ °C\ min^{-1}$$

At 350 °C

$$Heating\ rate = \frac{(350 - 25)\ °C}{(30 - 0)min} = \ 10.8\ °C\ min^{-1}$$

References

[1] Engineering Toolbox, (2005). *Nitrogen - Specific Heat*. [Online] Available at: https://www.engineeringtoolbox.com/nitrogen-d_977.html [Accessed 05/01/2021].

Heat treatment studies of the 1 to 10^{-3} DNA-cisPt material

Temperature effect

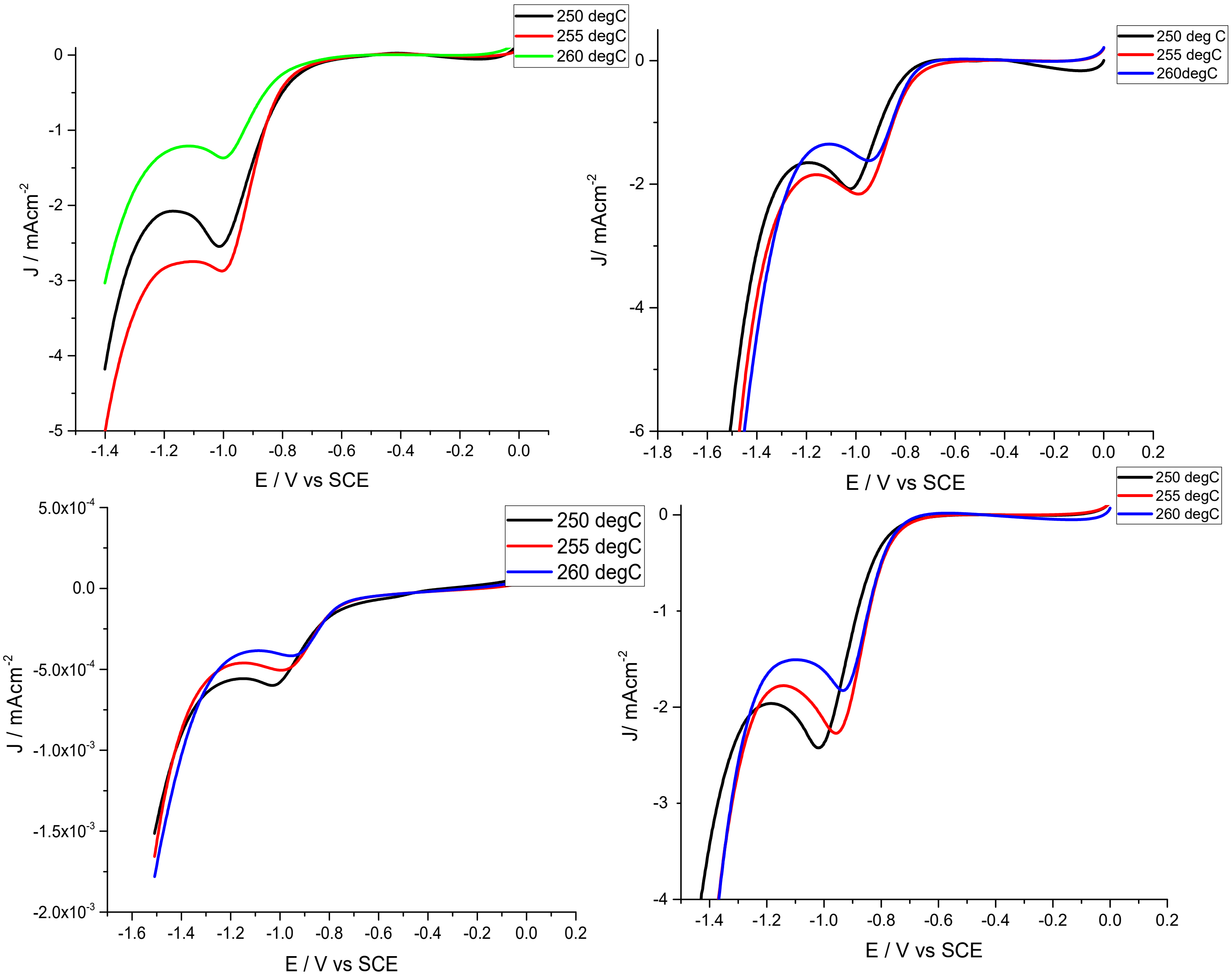

Figure A4.1- *Repeated testing for the effect of pseudo pyrolysis temperature in the range of 250-260 °C on the electrochemical response of 1 to 10^{-3} DNA-cisPt for the HER, 1 mM $HClO_4$ and 0. 1M $NaClO_4$ at 50 mVs^{-1}.*

The variation in the results obtained is accounted for by taking an average value of the E_p and J_p and observing the correlation between these parameters and pseudo pyrolysis temperature.

Time effect

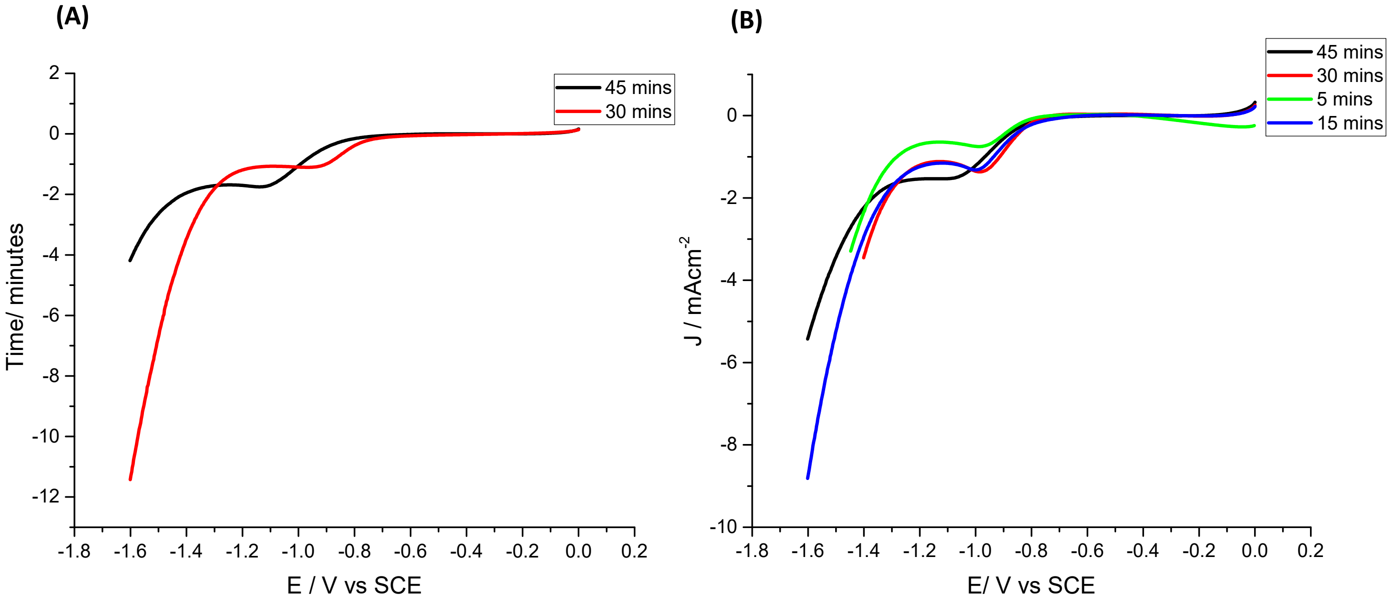

Figure A4.2 *Effect of 'duration time' of the pseudo pyrolysis process on the electrochemical response for the HER (1 mM $HClO_4$, 0.1 M $NaClO_4$, 50 mVs^{-1}) at (A) 255 °C and (B) 260°C on the electrochemical response of 1 to 10^{-3} DNA-cisPt/GC modified working electrode surface.*

Both figures A4.2 (A) & (B) suggest that 30 minutes is an ideal time for achieving pseudo pyrolysis of the material in terms of current density i.e. catalytic activity and peak potential.

Influence of duration time of the pseudo pyrolysis process at 255 °C on the electrochemical response for the Hydrogen evolution reaction (HER) at the surface of 1 to 10^{-4} DNA-cisPt

The influence of the duration of pseudo pyrolysis was explored for the 1 to 10^{-4} DNA-cisplatin loading. A new saturated Glassy Carbon electrode is employed to the previous section, hence the variation in peak potential, $E_{p.}$

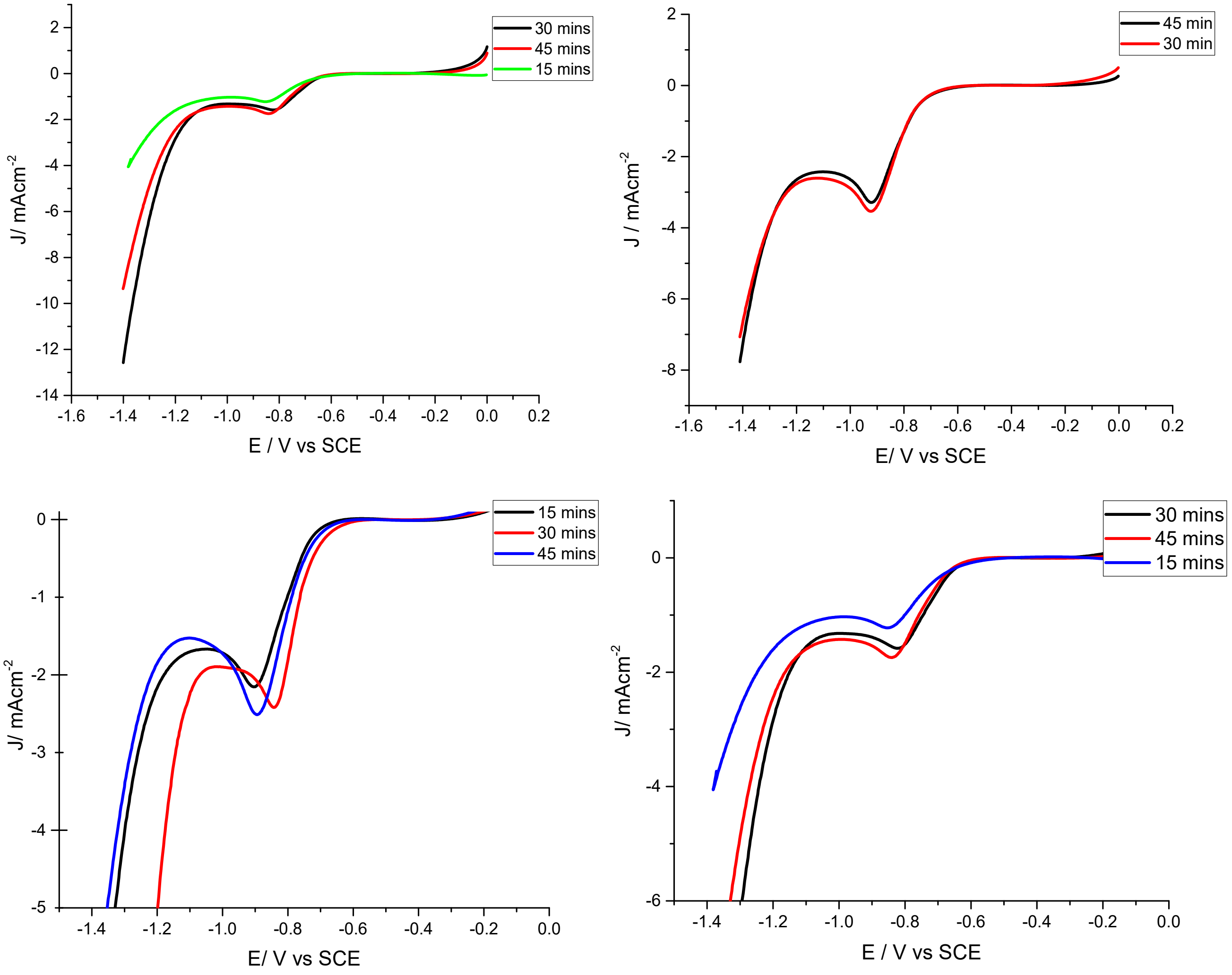

Figure A4.3 *Effect of 'duration time' of the pseudo pyrolysis process on the electrochemical response for the HER (1 mM $HClO_4$, 0.1 M $NaClO_4$, 50 mVs^{-1}) at (A) 255 °C on the electrochemical response of 1 to 10^{-4} DNA-cisPt/GC modified working electrode surface.*

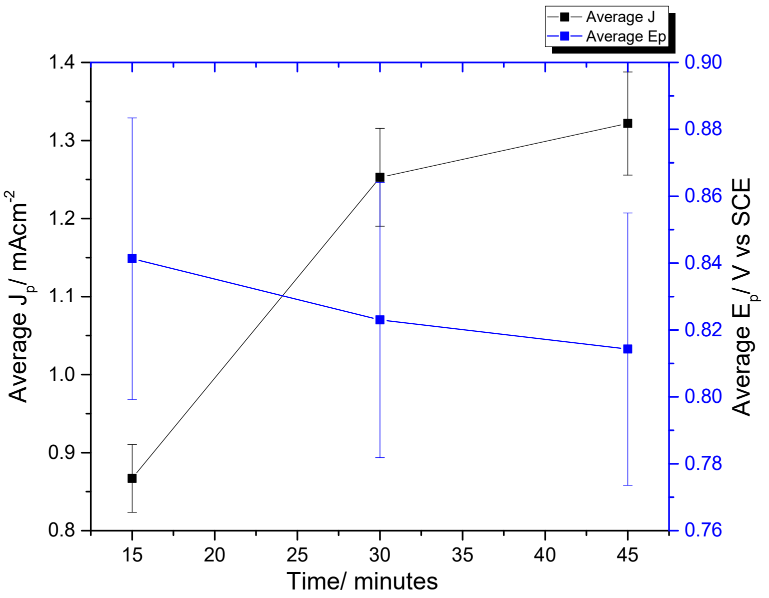

***Figure A4.4** Effect of 'duration time' of the pseudo pyrolysis process on the electrochemical response for the HER (1 mM $HClO_4$, 0.1 M $NaClO_4$, 50 mVs^{-1}) at (A) 255 °C on the electrochemical response of 1 to 10^{-4} DNA-cisPt/GC modified working electrode surface.*

STEM imaging characterisation of heat treated material

In order to characterize the influence of pseudo pyrolysis on the surface morphology of the DNA-Cisplatin well, imaging of a heat treated blank GC TEM substrate was conducted to enable effective distinguishes to be made between the support surface and the casted material of interest.

Imaging of the substrate: Bare Cu holey carbon TEM grid

A blank holey carbon TEM grid was inserted into the furnace purged with N_2 set at 255 °C for 30 minutes. The changes to the surface morphology of the grid as a result of this were explored.

From figure A4.5, it is evident that the transfer process between the furnace and STEM instrument, there is accumulation of dirt deposit onto the surface of the TEM grid. However there are no significant features associated with the material morphology i.e. lattice fringes corresponding to that of the lattice plane.

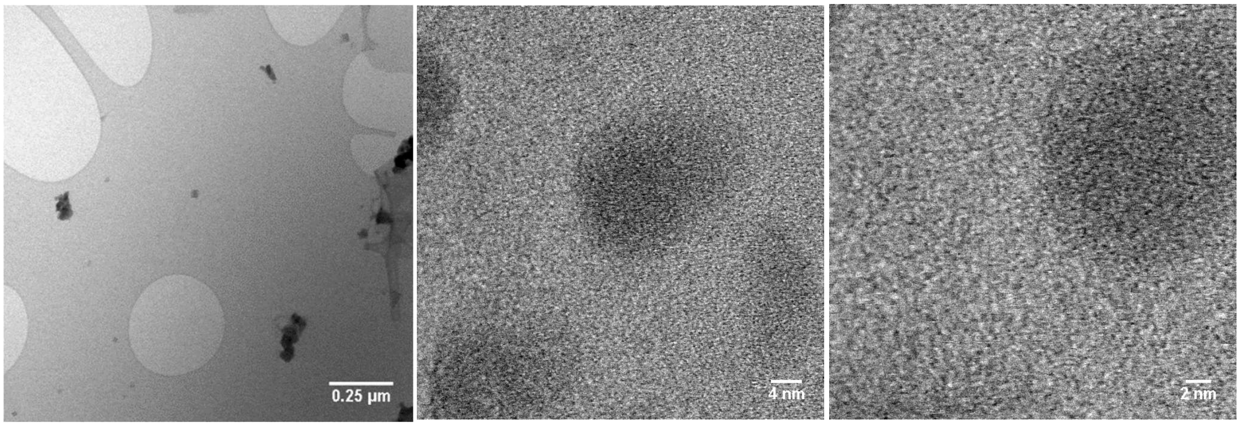

Figure A4.5 *-HAADF-BF STEM imaging of Blank holey carbon Cu TEM grid heat treated in a furnace at 255 °C for 30 minutes, 200 keV acceleration voltage.*

Influence of heat on a bare GC

In order to more closely assess the effect of heat treatment on the DNA-Cisplatin material, a polished bare GC stub was placed at 280 °C for 10 minutes in a furnace purged with N_2 gas. The GC surface was then polished using alumina slurry and immersed into the same Perchloric acid solution. From figure A4.6, it is evident that the polished GC surface produces a higher catalytic activity and a shift from -0.89 V to -0.87 V vs SCE. This is very much likely due to the sensitive nature of the heterogeneous surface of glassy carbon, hence also the changes that rise from surface treatments.

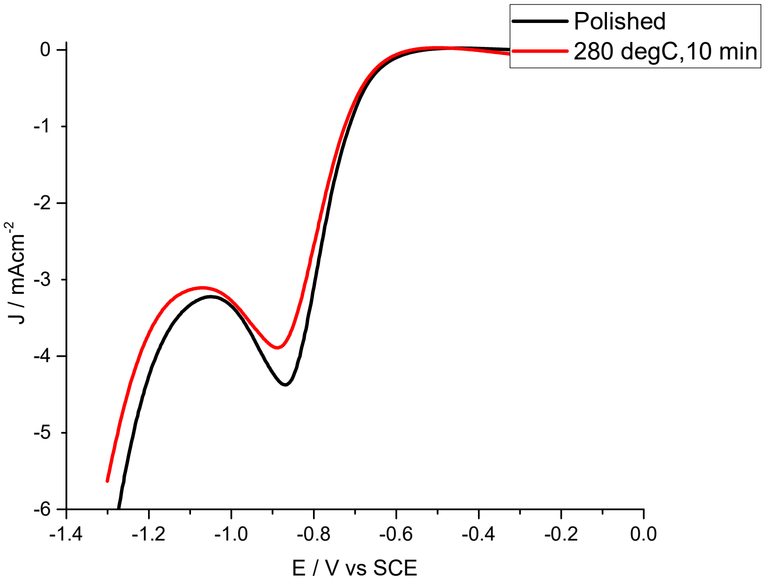

Figure A4.6 *The influence of the heat exposure of a bare GC on the electrochemical response of a HER, (1 mM $HClO_4$, 0.1 M $NaClO_4$) at 50 mV s^{-1}.*

STEM imaging characterization of carbonised DNA and DNA-cisPt solutions

Sample preparation

An aliquot of 3 µL of fabricated samples e.g. 1000 µM virgin DNA solution was casted onto a 3mm Carbon film on a Cu TEM grid and dried under a lamp. This was then transferred into ceramic crucible which was placed in a tubular furnace set at 255 °C under a nitrogen atmosphere (50 mL/min) for 30 minutes. The TEM grid was then removed and imaged using Scanning Transmission Electron Microscopy (STEM).

STEM-HAADF

The surface morphology of the material was attained using Scanning Transmission Electron Microscopy (*STEM*) operated in both Dark field and Bright field imaging using a JEOL2100F instrument. The STEM was operated in Z-contrast mode using a HAADF detector at 200 keV acceleration voltage.

Virgin DNA solution (1000 µM)

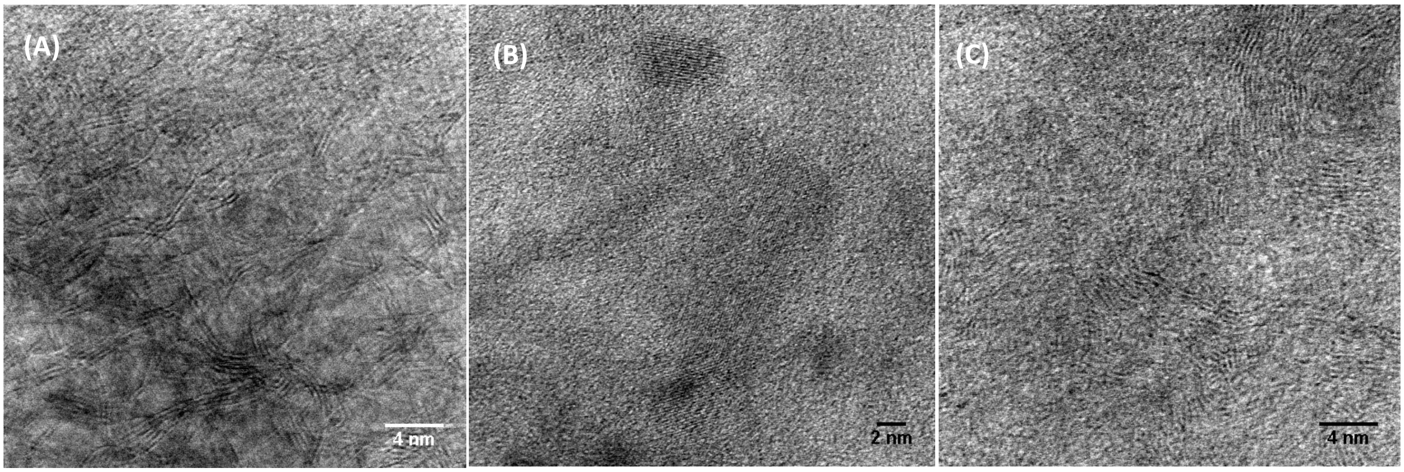

Figure A4.7- *1000 µM virgin DNA solution on carbon TEM, heated at 255°C, 30 minutes at a magnification of (A-C) 5 million.*

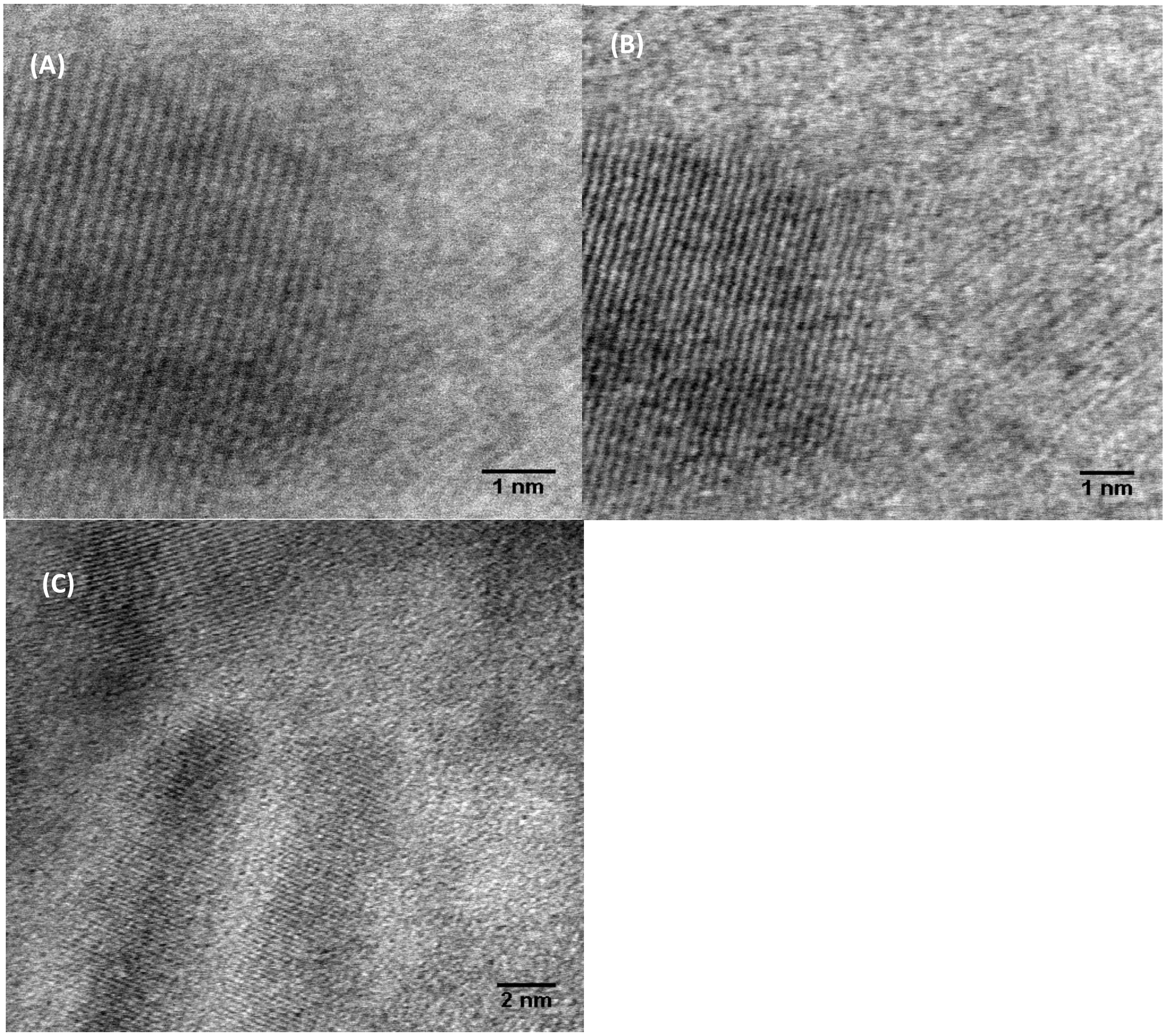

Figure A4.8- *1000 µM virgin DNA solution on carbon TEM , heated at 255°C, 30 minutes at a magnification of (A) 20* million *(B) 15 million (C) 8 million.*

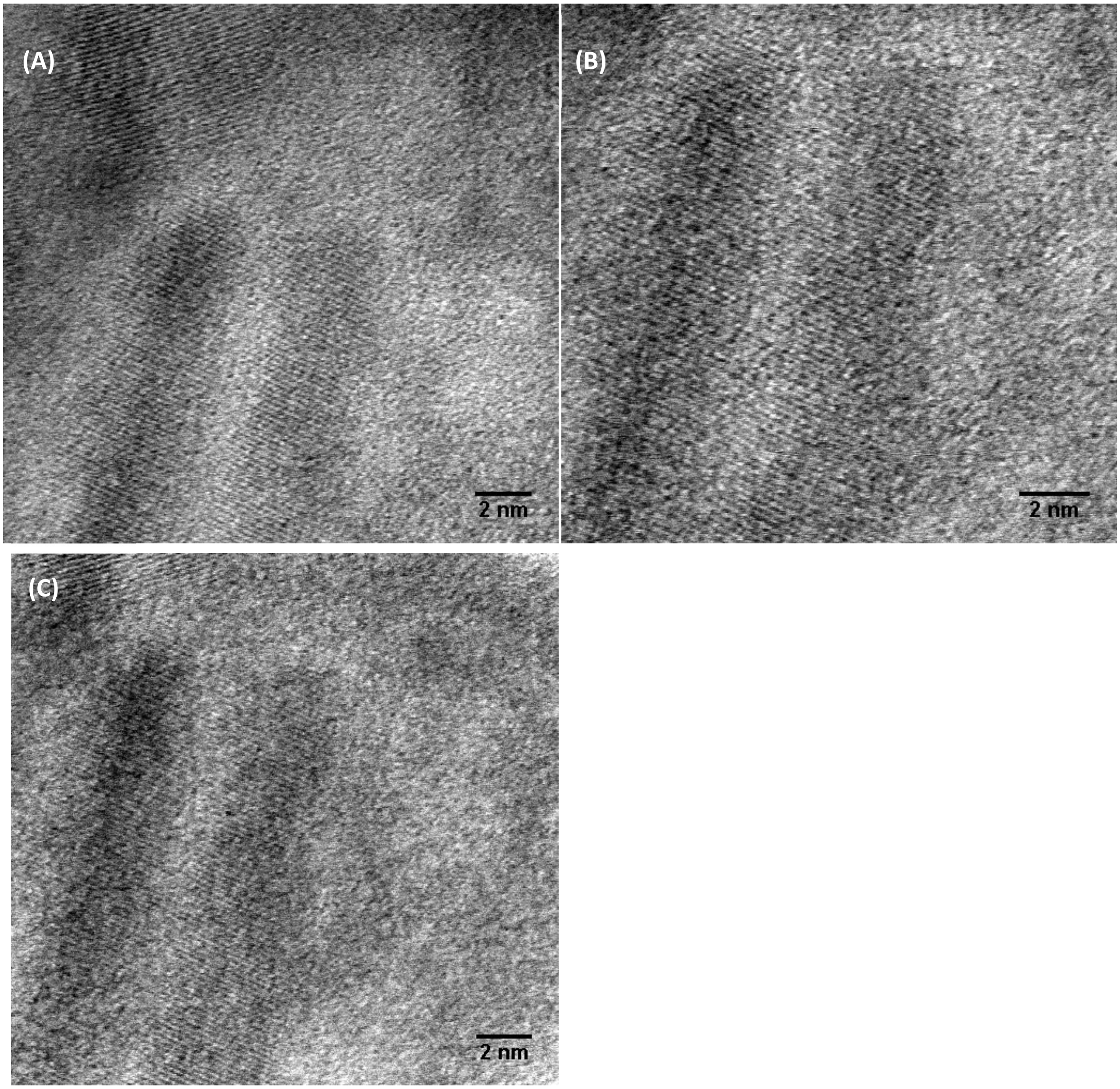

Figure A4.9- *1000 µM virgin DNA solution on carbon TEM , heated at 255°C, 30 minutes at different magnifications of (A) 8 million (B) 10 million (C) 8 million.*

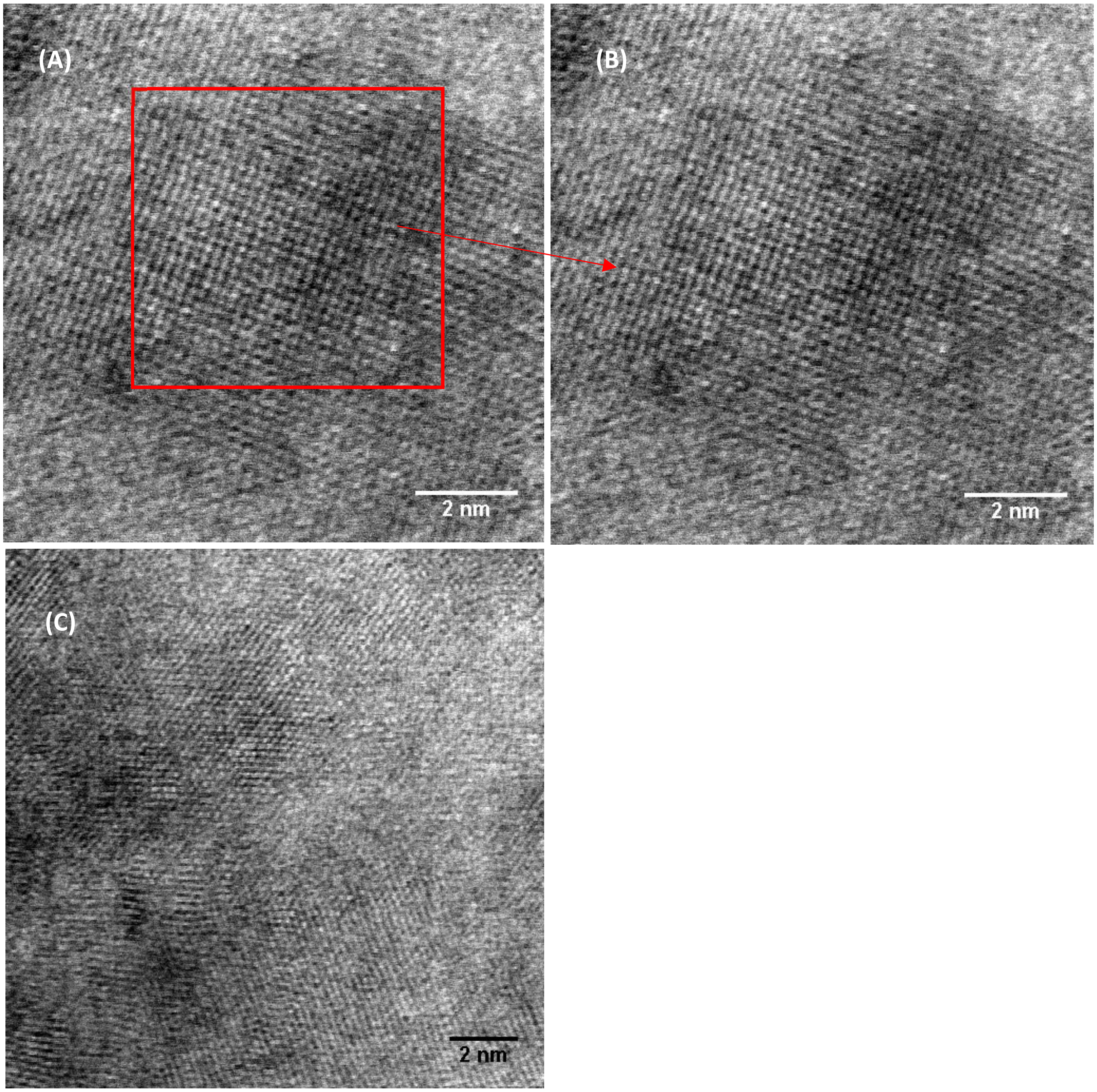

Figure A4.10 - *1000 μM virgin DNA solution on carbon TEM , heated at 255°C, 30 minutes at different magnifications of (A) 8 million (B) 15 million (C) 10 million.*

Lattice space measurements of carbonised DNA using the FFT function in image J

Using the FFT function in image J, the lattice space measurement of the carbonised virgin DNA material can be achieved. This measurement appears, as circled in the first figure, and corresponds to the analysis of the section highlighted (yellow rectangle) in the STEM image. This is found to range between 0.2-0.22nm for the carbonised DNA.

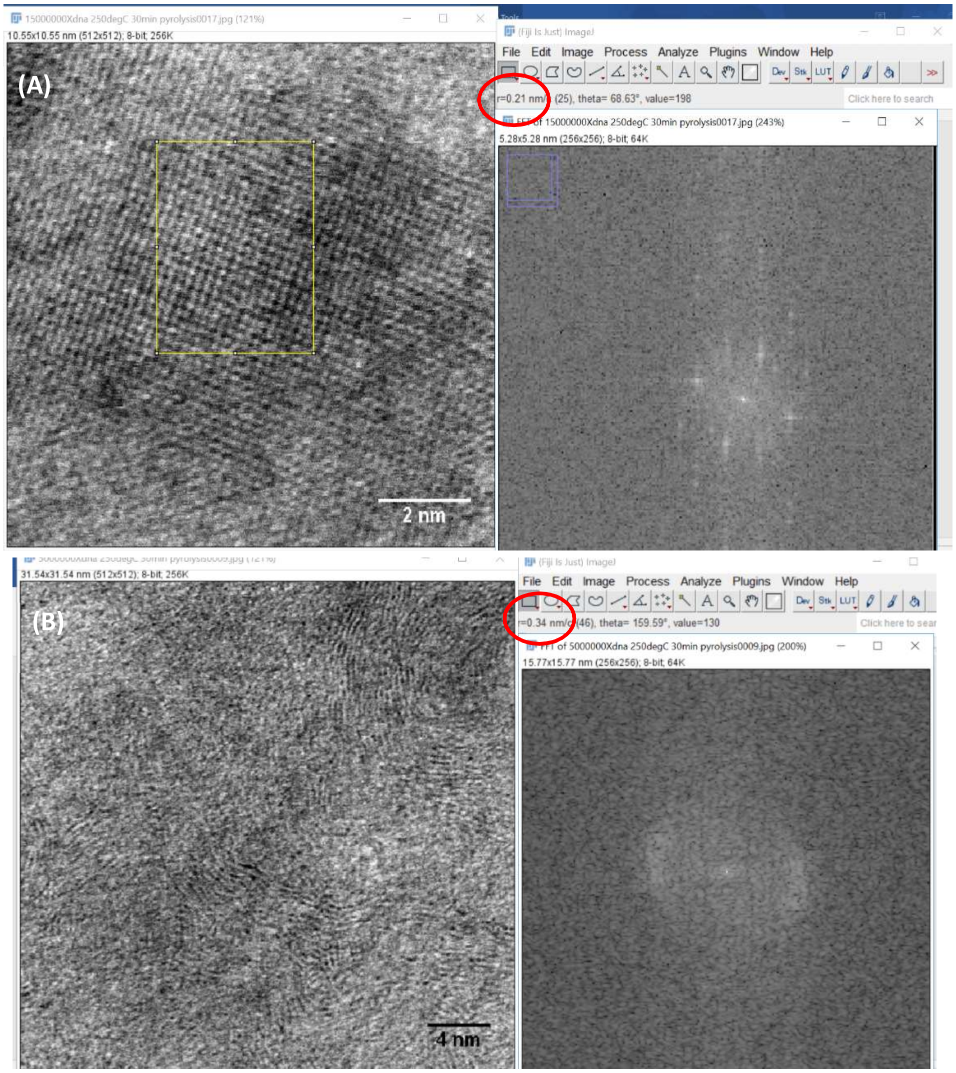

r=0.21 nm/ (25), theta= 68.63°, value=198

=0.34 nm/c (46), theta= 159.59°, value=130

Figure A4.11- *1000 μM virgin DNA solution on carbon TEM , heated at 255°C, 30 minutes at different magnifications of (A) 10 million (B) 8 million and their corresponding FFT measurements.*

The images displayed in Figure A4.11, show the appearance of more graphitic like material (nano rings) and this is reflected in the FFT measurements.

STEM characterization of carbonised DNA-cisPt (255 °C, 30 minutes) of different cisPt loadings

The lattice measurement using the FFT function in image J is repeated for the carbonised DNA-cisPt adducts synthesized at different loadings of the platinum metal i.e. different ratio of cisPt. The findings are summarized in Table 1 and measurements are displayed below.

Table A4.2- *Lattice Space measurements found using FFT function in Image J.*

Sample	***Lattice spacing measurement using FFT function (image J) different regions on TEM grid /nm***
Carbonised 1 to 10^{-3} DNA-cisPt	0.21
Carbonised 1 to 1 DNA-cisPt	0.225 , 0.24
Carbonised CisPt (1000 µM)	0.24 , 0.25, 0.23, 0.14
Untreated CisPt (1000 µM)	0.24

STEM characterization of carbonised DNA-cisPt (255 °C, 30 minutes) of different cisPt loadings

1 to 10^{-3} DNA-cisPt

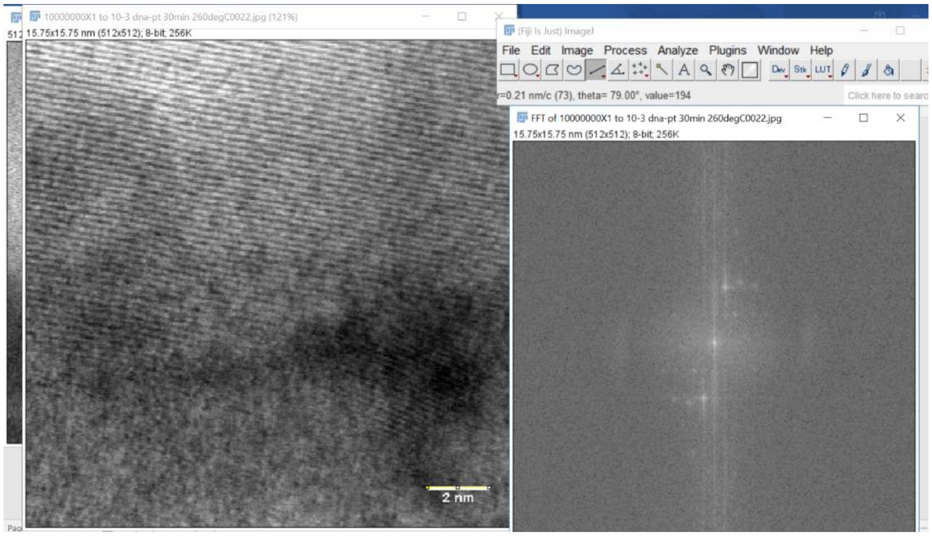

```
r=0.21 nm/c (73), theta= 79.00°, value=194
```

Figure A4.12- *1 to 10^{-3} DNA-cisPt solution on carbon TEM, heated at 255°C, 30 and the corresponding FFT measurement.*

1 to 1 DNA-cisPt carbonised

Inner and outer regions measure at 0.3 and 0.15 nm respectively. Thus an average spacing of 0.225 nm is found.

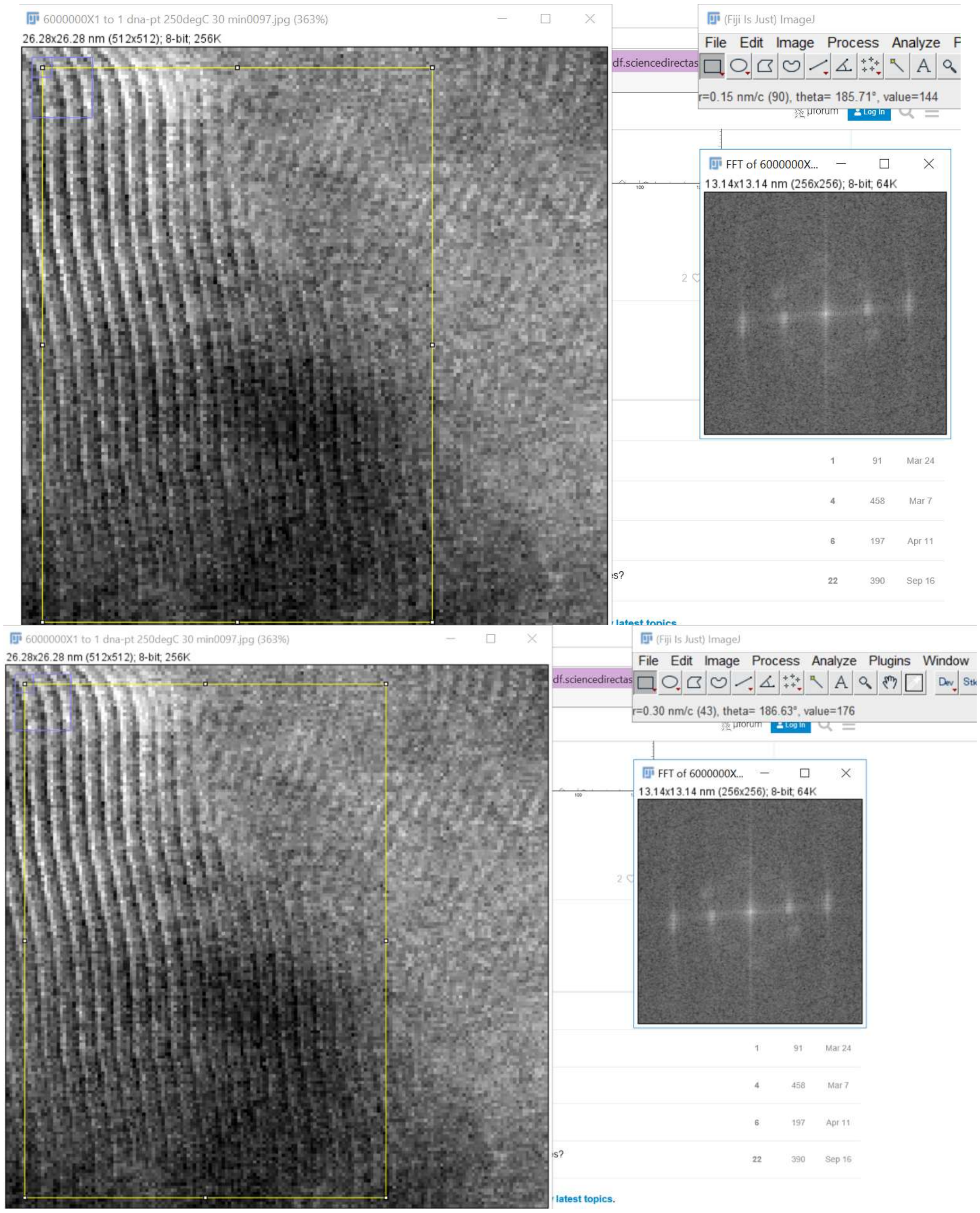

r=0.15 nm/c (90), theta= 185.71°, value=144

r=0.30 nm/c (43), theta= 186.63°, value=176

__Figure A4.13-__ 1 to 1 DNA-cisPt solution on carbon TEM, heated at 255 °C, 30 minutes and the corresponding FFT measurement.

A different region on the TEM grid for the carbonised 1 to 1 DNA-cisPt (255 °C, 30 minutes) is shown:

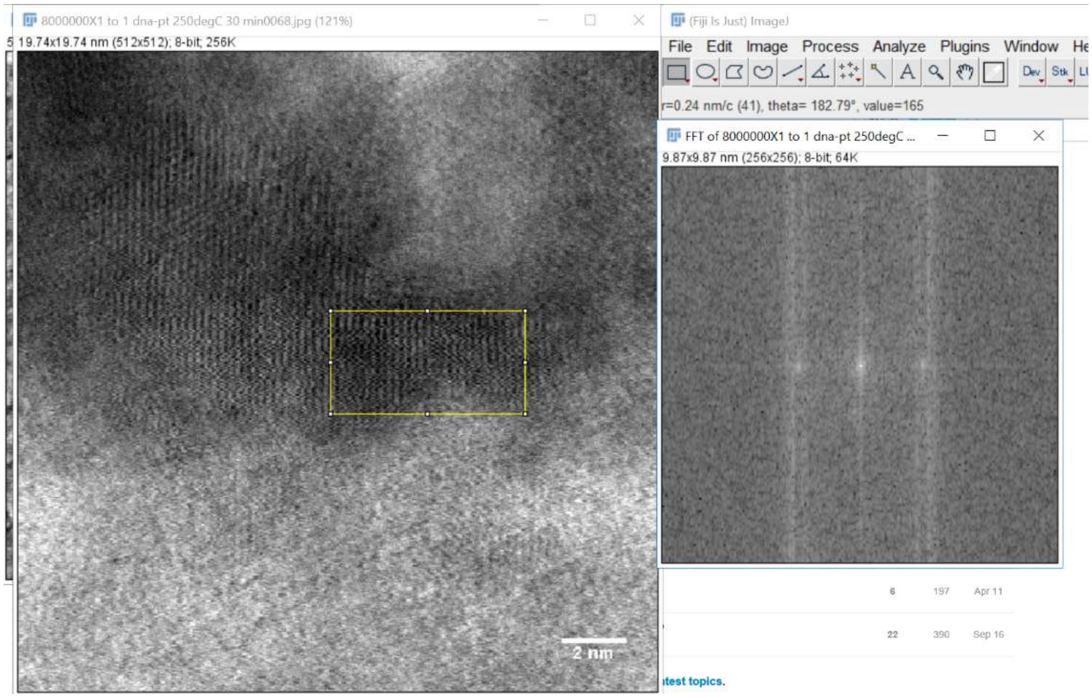

r=0.24 nm/c (41), theta= 182.79°, value=165

Figure A4.14 - *1 to 1 DNA-cisPt solution on carbon TEM, heated at 255 °C, 30 and the corresponding FFT measurement.*

STEM characterization of carbonised cisPt solution 1000 µM (255 °C, 30 minutes) vs untreated cisPt

1000 µM CisPt carbonised (255 °C, 30 minutes)

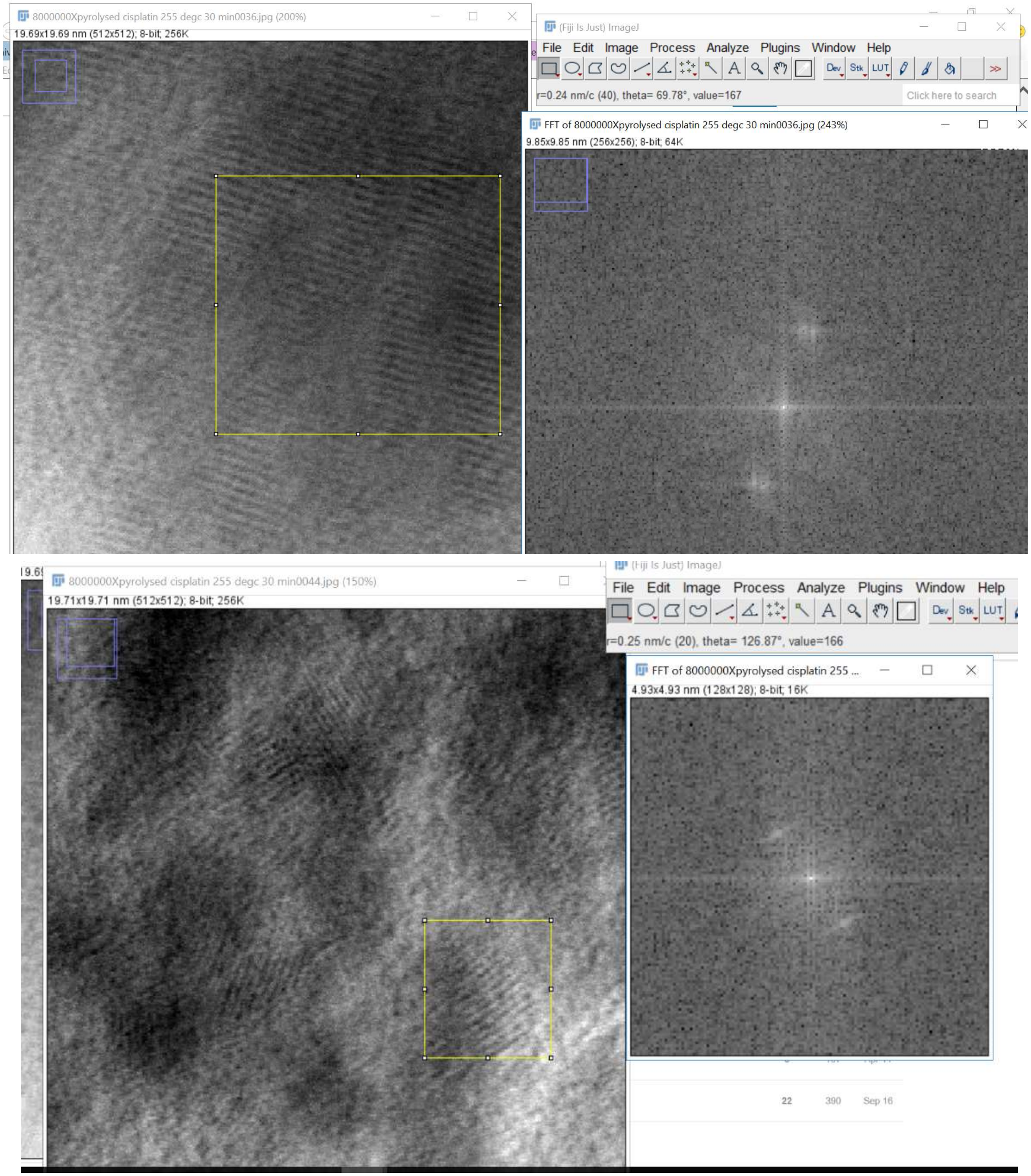

r=0.24 nm/c (40), theta= 69.78°, value=167

r=0.25 nm/c (20), theta= 126.87°, value=166

Figure A4.15 *– 1000 µM cisPt solution on carbon TEM, heated at 255°C, 30 and the corresponding FFT measurement.*

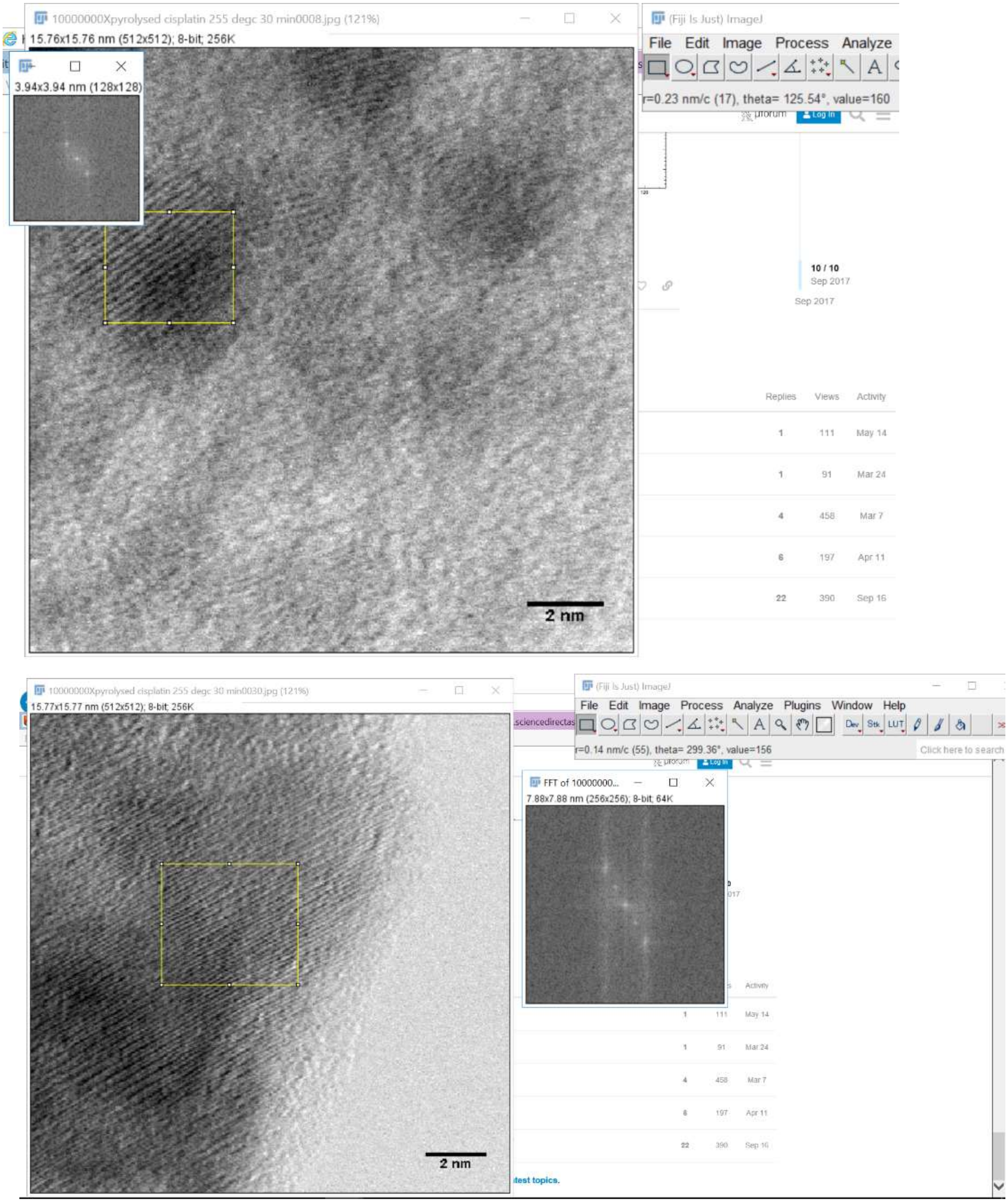

10000000Xpyrolysed cisplatin 255 degc 30 min0008.jpg (121%)

15.76x15.76 nm (512x512); 8-bit; 256K

3.94x3.94 nm (128x128)

r=0.23 nm/c (17), theta= 125.54°, value=160

10000000Xpyrolysed cisplatin 255 degc 30 min0030.jpg (121%)

15.77x15.77 nm (512x512); 8-bit; 256K

r=0.14 nm/c (55), theta= 299.36°, value=156

FFT of 10000000...

7.88x7.88 nm (256x256); 8-bit; 64K

Figure A4.16 - *1000 µM -cisPt solution on carbon TEM, heated at 255°C, 30 minutes and the corresponding FFT measurement.*

1000 µM untreated cisPt

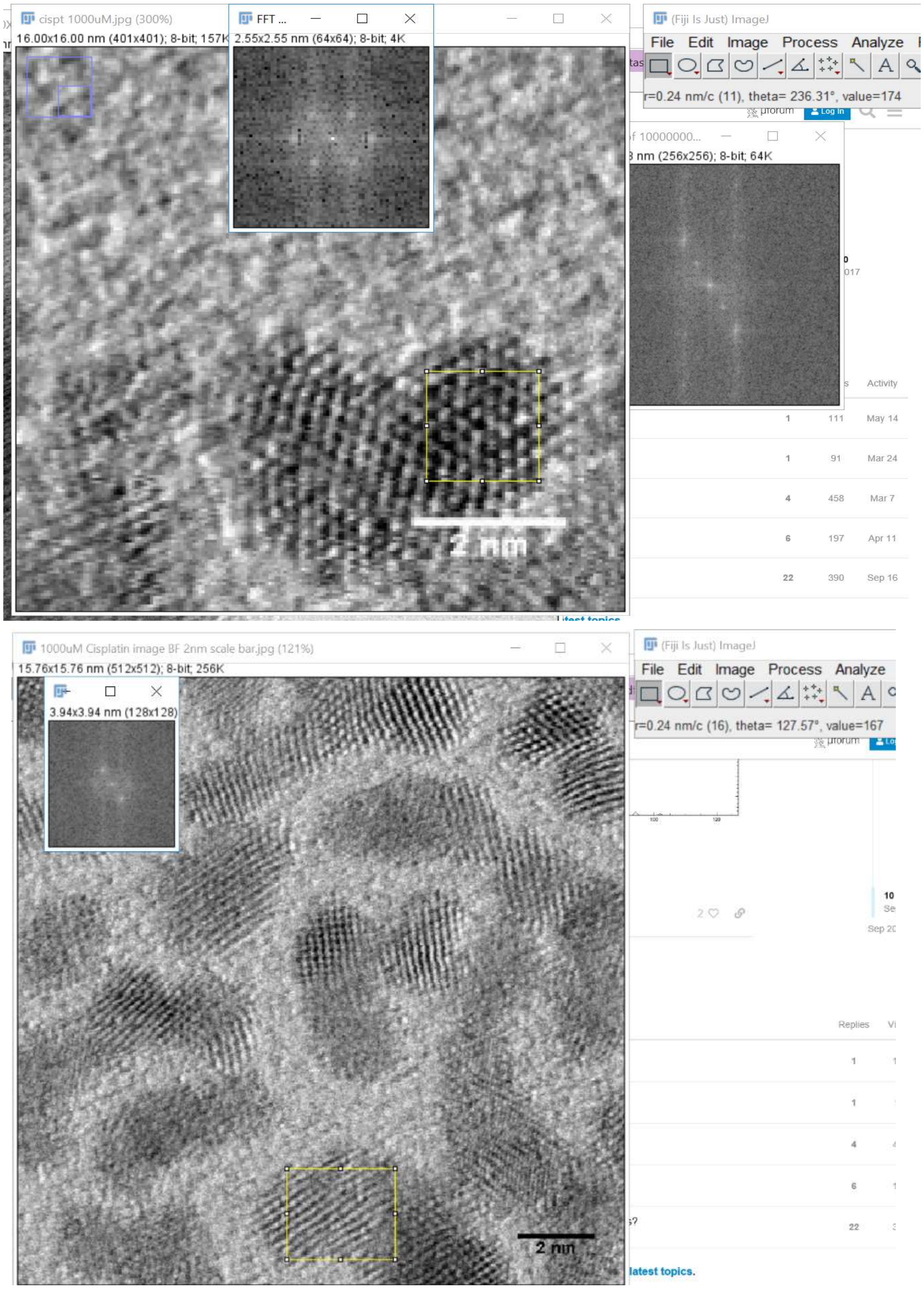

16.00x16.00 nm (401x401); 8-bit; 157K

2.55x2.55 nm (64x64); 8-bit; 4K

r=0.24 nm/c (11), theta= 236.31°, value=174

3 nm (256x256); 8-bit; 64K

15.76x15.76 nm (512x512); 8-bit; 256K

3.94x3.94 nm (128x128)

r=0.24 nm/c (16), theta= 127.57°, value=167

Figure A4.17 - *1000 µM cisPt solution on carbon TEM and the corresponding FFT measurement.*

D-Plot function in image J for Lattice space measurement

1 to 1 DNA-cisPt heat treated

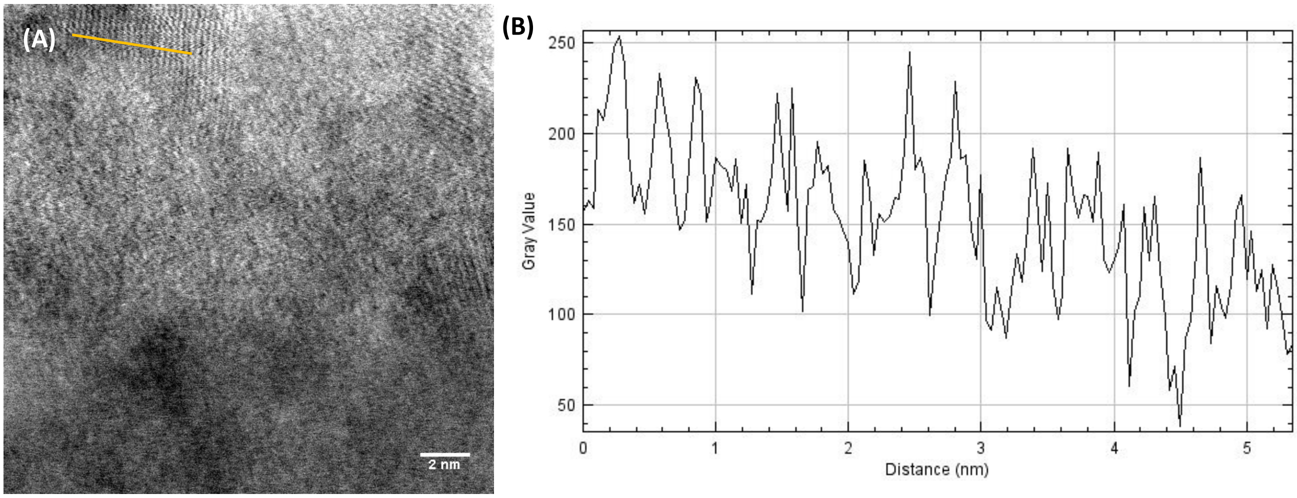

Figure A4.18*- STEM HAADF BF imaging of 3 µL of (A) 1 to 1 DNA –cisPt solution carbonised (255 °C, 30 minutes) (B) Corresponding D-plot for lattice spacing via d-spacing tool in Image J.*

These measurements were confirmed using the d-spacing tool in Image J, to further consolidate the findings above. An example of the produced d-plot produced from the line drawn across the area of interest on the STEM image is shown above. The d spacing (distance/number of points) is found from figure A4.18, where figure A4.18 (B) corresponds to a lattice spacing of 0.206 nm. This is in line with the measurement found using the FFT function.

Carbonised DNA

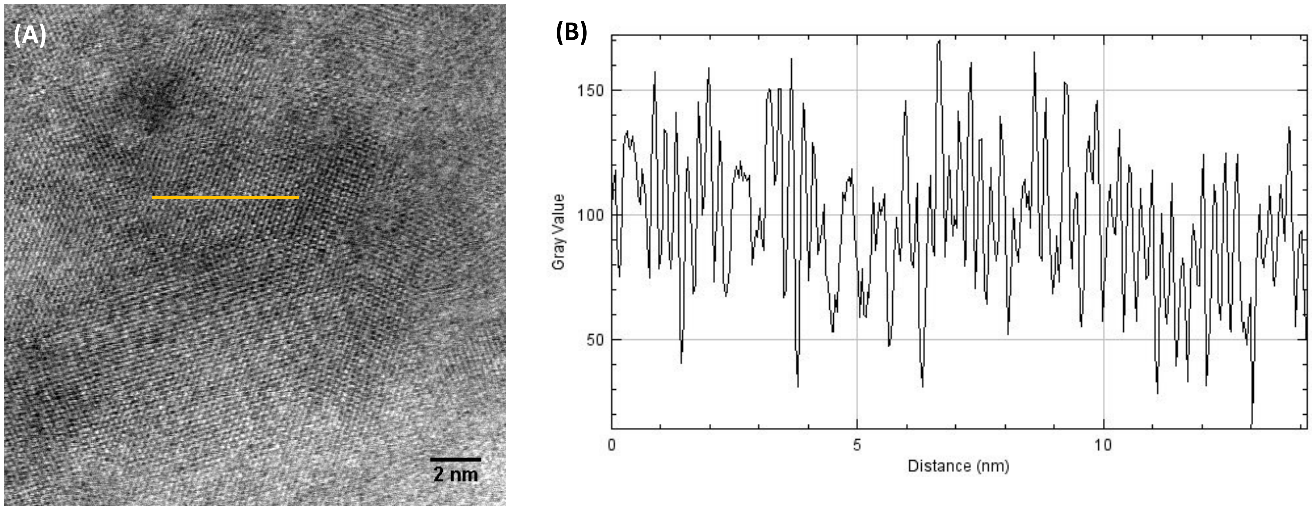

Figure A4.19*- STEM HAABF imaging of 3 µL of (A) 1 mM virgin untreated DNA solution carbonised (255 °C, 30 minutes) (x 8 million) (B) Corresponding D-plot for lattice spacing via d-spacing tool in Image J.*

The d spacing (distance/number of points) is found from figure A4.18, where figure A4.18 (B) corresponds to a lattice spacing of 0.248 nm. This is in line with the measurement found using the FFT function.

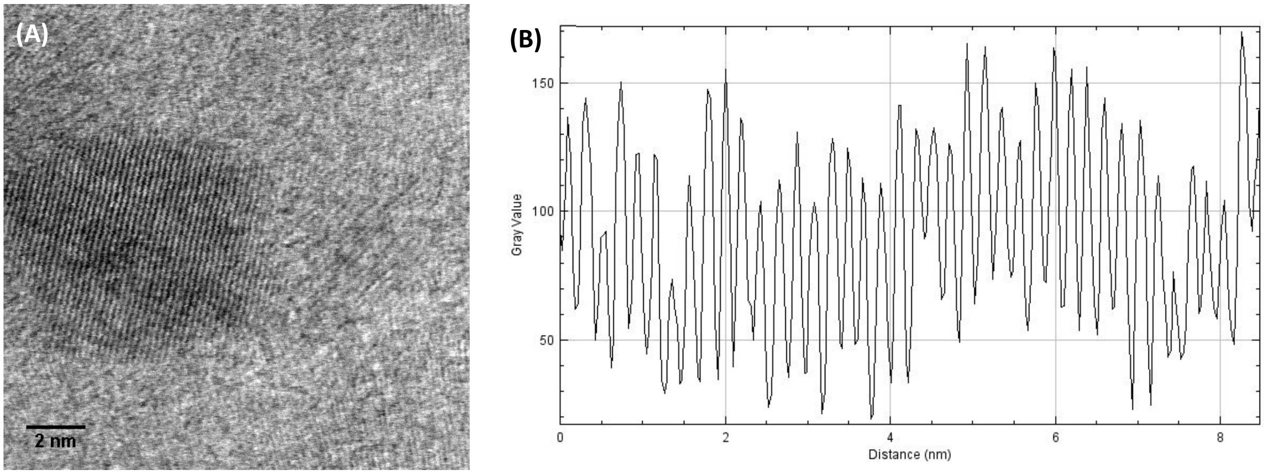

Figure A4.20- *STEM HAABF imaging of 3 µL of (A) 1 mM virgin untreated DNA solution carbonised (255 °C, 30 minutes) (x 10 million) (B) Corresponding D-plot for lattice spacing via d-spacing tool in Image J.*

The d spacing (distance/number of points) is found from figure A4.20, where figure A4.20 (B) corresponds to a lattice spacing of 0.213 nm. This is in line with the measurement found using the FFT function.

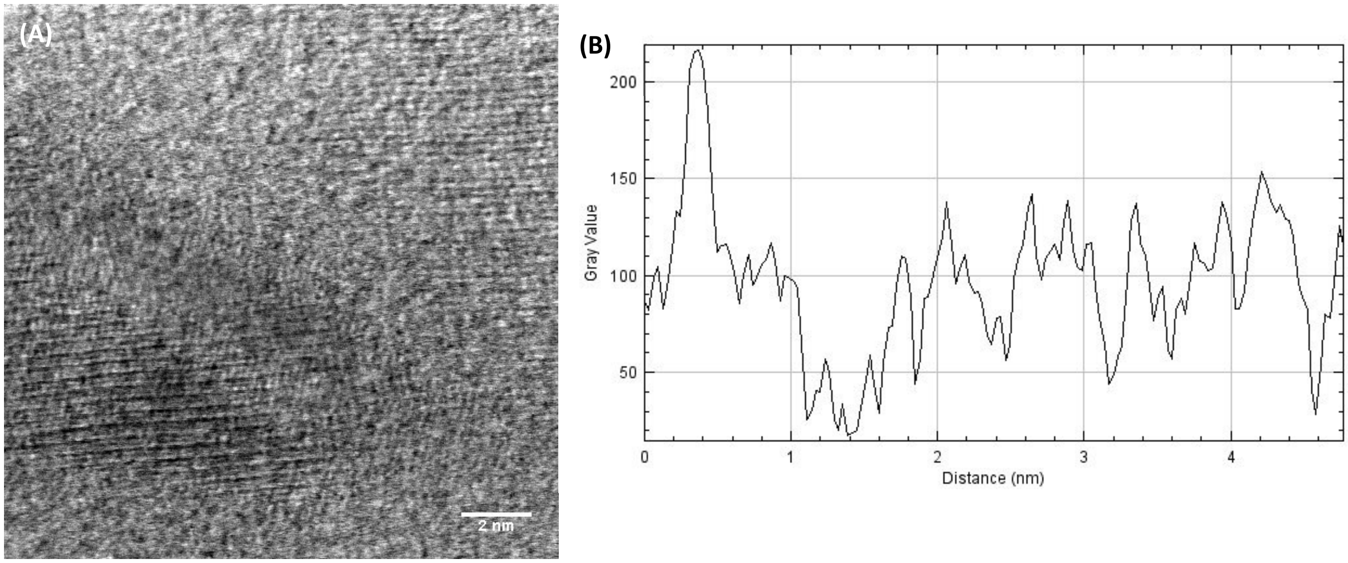

Figure A4.21- *STEM HAABF imaging of 3 µL of (A) 1 mM virgin untreated DNA solution carbonised (255 °C, 30 minutes) (x 10 million) (B) Corresponding D-plot for lattice spacing via d-spacing tool in Image J.*

The d spacing (distance/number of points) is found from figure A4.21, where figure A4.21 (B) corresponds to a lattice spacing of 0.1987 nm. This is in line with the measurement found using the FFT function.

Appendix 5- Chapter 8: Cisplatin DNA nanostructures for the electrocatalysis of the hydrogen evolution reaction (HER)

Materials and experiments

Material Synthesis

All the material processed and characterised in this work was synthesised and provided by Klaudia Englert, School of Chemistry, University of Birmingham [1]. An overview of the experimental methods used by Englert [1] to achieve this is outlined.

1 to 10^{-3} sm-DNA-cisPt

Deoxyribonucleic Acid (DNA), sodium salt from salmon testes, cisplatin (99.99 % purity, based on trace metal analysis) were purchased from Sigma Aldrich. DNA-cisPt adducts were synthesized by dissolving the salmon milt DNA (sm-DNA) in Milli-Q water (resistivity ≥ 18.2 MΩ.cm) and sonicating to prepare a stock solution. Cisplatin in aqueous form was mixed with the sm-DNA and incubated at 37 °C overnight for 10 hours. Confirmation of the adduct formation was achieved using spectrophotometric techniques using Shimadzu UV-1800 spectrophotometer, Jasco J-810 spectropolarimeter and Cary 5000 UV-Vis-NIR Spectrophotometer [1].

For the 1 to 10^{-3} sm-DNA-cisPt, this involves incubation of a 1 mM DNA solution with a 1 µM cisPt solution. This is chosen as the representative material of the different DNA-cisPt loadings explored in the previous work (see chapter 4), since it uses an intermediate loading of the platinum metal.

Holliday Junction arrays

To maximize the structural order of the three-layer logpile (3LL) design, the assembly of discrete Holliday junction units is achieved to form an array by hybridization of ‘sticky ends’ (46). Each unit is composed of four DNA oligonucleotides which forms the assembly upon annealing. Each of the four oligonucleotides terminate in a sticky end made up of six unpaired bases, see Table 1. The DNA strands, each of a 5 µM concentration, are left to anneal in a buffer for 72 hours from 90 °C to 20 °C. The annealing buffer employed is a made up of a 10 mM $MgCl_2$, 5 mM Tris-HCl , 20 mM Tris acetate and 1 mM EDTA/ 2 % Triton X-100 of pH of 8.3. A more detailed procedure is provided by Englert [1].

Holliday Junction cisPt arrays (Platinated)

The assembly of the cisPt Holliday Junction arrays, see figure 1, involves the reactions of a single strand of DNA, containing only two adjacent guanines, with an equimolar quantity of cisPt solution in Milli-Q water (resistivity ≥ 18.2 MΩ.cm). This ensures the cisPt binding occurs specifically at the two available guanine bases in the sequence, see Table 1. The cisPt compatible strands refer to the sequence containing the GG bases (marked in red in Table 1), the site where the Pt is expected to coordinate.

The desired cisPt DNA adduct is then purified by high performance liquid chromatography (HPLC) (performed by Klaudia Englert) to remove the unreacted DNA. The cisPt modified Holliday Junction strand along with the three remaining unmodified Holliday Junction strands (Table A5.1) are then annealed following the same method described above for the HJ array fabrication. There is one cisPt molecule per HJ structure, which is equivalent to one cisPt per 79 DNA base pairs.

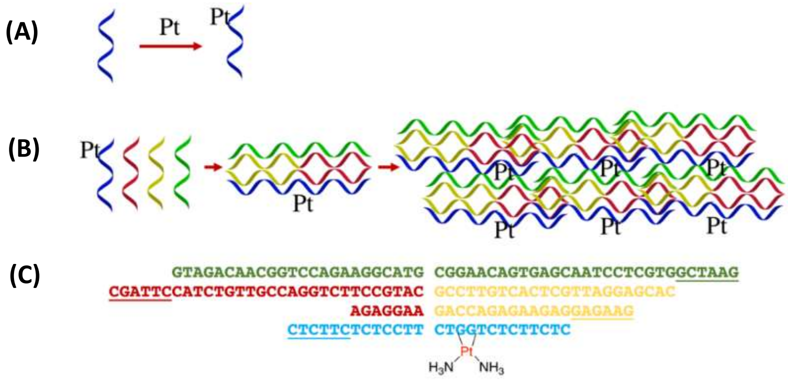

Figure A5. 1- Schematic representation of the design of cisPt modified Holliday Junction (HJ) assembly (A) Platination of the oligonucleotide (B) Assembly of the platinated HJ array (C) cisPt HJ monomer with its sequences – Reproduced with permission of Englert [1].

Table A5.1- *Sequence of the Holliday Junction used to synthesize the Arrays with and without cisPt, Englert [1].*

Holliday junction with sticky ends	*Holliday junction cisPt compatible sequence*
5' CTA ACT ACA TGC CTT CTG GAC CGT TGT CTA C CTT AGC3'	5'GTAGACAACGGTCCAGAA**GG**CATGCGGAACAGT GAGCAATCCTCGTGGCTAAG 3'
5' GCG ATG AGC AGG ATA GTT AG AGT ATC 3'	5' AGA GGA ACA TGC CTT CTG GAC CGT TGT CTA CCT TAG C 3'
5' CAC GAG GAT TGC TCA CTG TTC CGT CCT GCT CAT CGC GAT ACT3'	5' CAC GAG GAT TGC TCA CTG TTC CGG ACC AGA GAA GAG GAG AAG 3'
5' GTA GAC AAC GGT CCA GAA GGC ATG CGG AAC AGT GAG CAA TCC TCG TG GCT AAG3'	5' CTC TTC TCT GGT CTT CCT CTC TTC TC 3'

The four-armed junctions can be described as being two quasi continuous duplexes connected by the exchange of two strands where they meet. They are stacked upon each other and are bent at 60° relative to one another. The design of the helices is straight to avoid distortions that can reduce the crystalline order [1].

cisPt DNA origami (40 nM of phage origami)

Discrete DNA origami nanostructures, based on a triangular template were created from an M13mp18 genomic DNA and assembled using 200 oligonucleotide staples. 15 out of the 200 staples have a polyA extension, which allows docking of a complementary polyT sequence in 15 positions of the DNA origami triangle. The polyT strand, having two additional guanine bases at its 3’ end, would allow cisPt adduct formation such that the DNA origami triangle would be loaded with platinum at specific locations, as demonstrated in figure 2(B) [1]. It is important to note that the cisPt containing docking strands do not take part in the DNA origami triangle formation, but are merely attached onto the origami via its staple extensions [1].

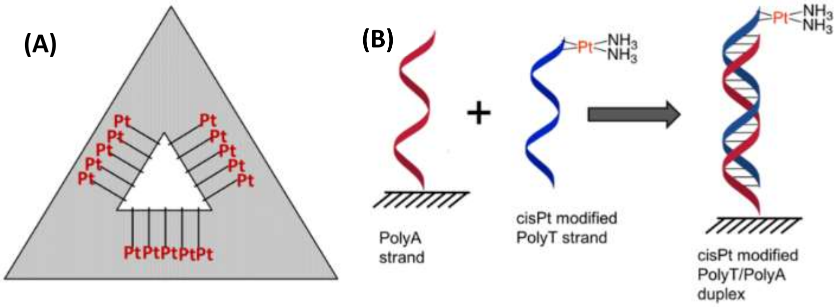

Figure A5.2- *Schematic representation of the design of cisPt modified DNA Origami Triangle: (A) cisPt DNA Origami Triangle, (B) hybridization of the polyA strand, anchored within the DNA origami via staples, with a cisPt modified polyT strand, copied from Englert [1].*

Sharp triangle designs are favoured due to their structural rigidity and low tendency to aggregate. The material synthesis entailed the mixing of staple strands (100 nM) and scaffold strands (40 nM single stranded M13mp18) in 10 mM Tris base, 1 mM EDTA buffer and 12.5 mM $MgCl_2$. The 2.5:1 staple: scaffold mixture was then incubated at 90 °C for 5 minutes and then cooled to 20 °C at a rate of 0.2 °C per minute using Bio-Rad Thermocycler [1]. The purification of the DNA origami triangle was accomplished by mixing the folded reaction mixture with PEG purification buffer [1]. The base sequences used for each strand is outlined in Table A5.2.

Table A5.2- *Sequence of the strands used for the synthesis of the DNA Origami triangle, Englert [1].*

Strand sequence for synthesis of the origami scaffold
TCA TAT GTG TAA TCG TAA AAC TAG TCA TTT TC
GGG TCA TAT GTG TAA TCG TAA AAC TAG TCA TTT TC
TCG GGA GAT ATA CAG TAA CAG TAC AAA TAA TT
CGG GGT TTC CTC AAG AGA AGG ATT TTG AAT TA
TCA TAT GTG TAA TCG TAA AAC TAG TCA TTT TC

The DNA origami triangle consists of 15 cisPt molecules per 7500 DNA base pairs (including the staple extensions) (15 cisPt per DNA origami triangle). This is equivalent to one cisPt per 500 DNA base pairs compared to one cisPt per 79 DNA base pairs in the HJ arrays. A more detailed method for fabricating the DNA nanostructures is provided by Englert [1].

EDX elemental mapping

In order to determine whether we have single platinum atoms or clusters on a DNA based scaffold and EDX mapping was produced to provide an insight into the distribution of the elements. The results are shown in the figure below:

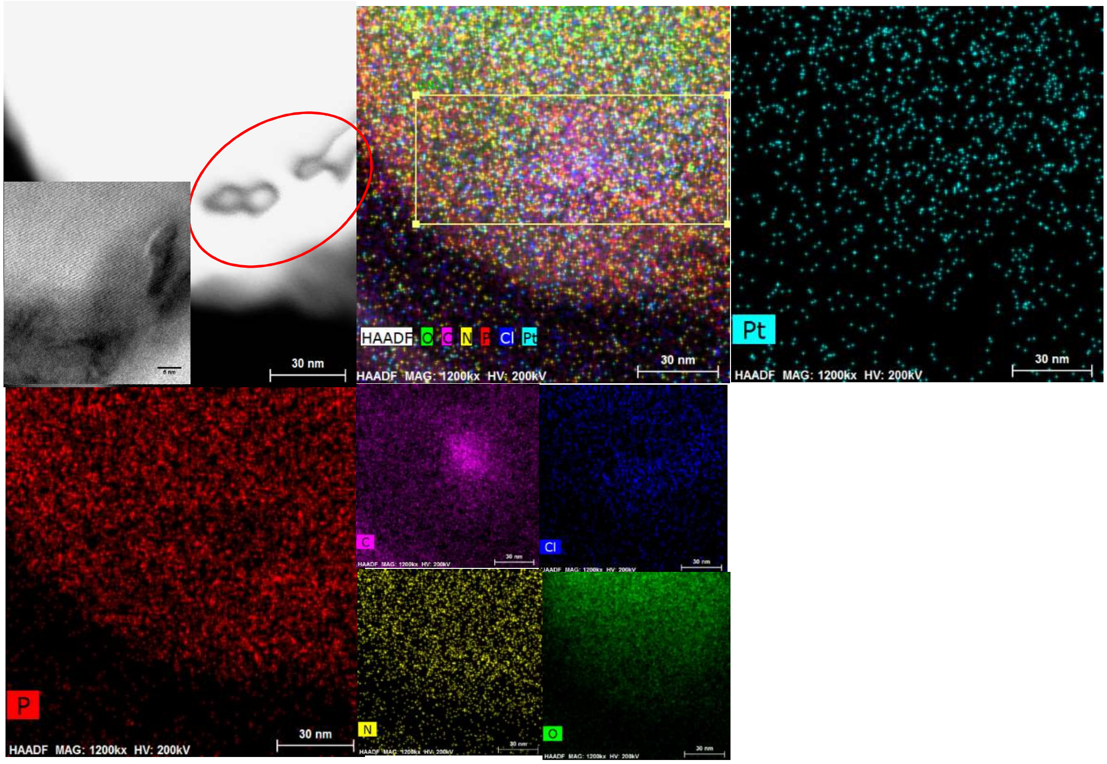

Figure A5.3 *- STEM EDX elemental mapping of 1 to 10^{-3} DNA-cisPt carbonised 255 °C for 30 minutes.*

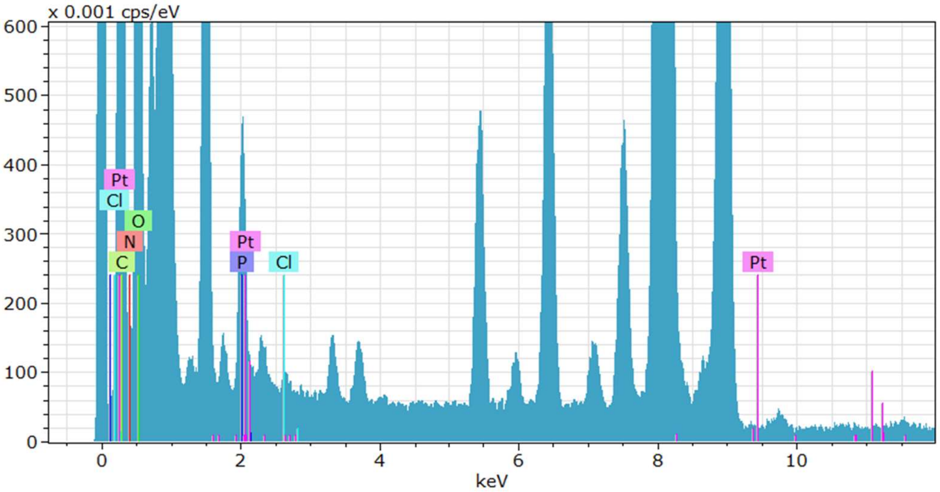

Figure A5.4- *EDX spectrum of STEM EDX mapping (figure A9.1) of carbonised 1 to 10^{-3} DNA-cisPt.*

References

[1] Englert K. DNA Origami Catalysts. [PhD thesis]. Birmingham (UK): University of Birmingham; 2019.

Appendix 6- Study of the stability of the Saturated Calomel Reference (SCE) electrode

Ruthenium Hexamine (II) chloride, is the employed redox couple for assessing the stability of a range of reference electrodes. The Ru^{3+}/Ru^{2+} redox couple is well known and reported in the literature (240,241) and (242). For this complex molecule, this can be summarised by equation (1).

$$[Ru(NH_3)_6]^{3+} + e^- \rightleftharpoons [Ru(NH_3)_6]^{2+}\ Eq.(1)$$

Experimental

Chemical reagents

All reagents were used as provided by Sigma Aldrich. This includes Hexaamineruthenium (III) chloride and Potassium Chloride at amounts equivalent to 5 mM and 0.1 M concentrations respectively, using a 100 mL of water of a resistivity not less than 18.2 $\mathrm{M\Omega.cm}$ (Millipore, UK).

Equipment and Experimental set-up

50 mL of the prepared solution of ruthenium hexamine in potassium chloride is transferred into a three electrode electrochemical cell. An autolab potentiostat is used to perform cyclic voltammetry across this cell for the assessment of the ruthenium hexamine chloride III/II redox couple.

A 3 electrode cell was employed, using a glassy carbon electrode (GC, d=3mm, BASi) as the working electrode and a bright platinum mesh counter electrode. The reference electrode of interest was employed for the testing, ranging from Saturated Calomel Electrode, Ag/AgCl, Mercurous sulphate and leakless Ag/AgCl.

The cell was controlled by an Autolab 128N potentiostat running Nova 2.1 software (Metrohm-Autolab BV, Netherlands). All potentials are reported against the reference electrode of interest, in a supporting electrolyte of 0.1 M. The GC electrodes were polished on microcloth pads with decreasing size alumina slurries (1.0, 0.3, 0.05 µm, Buehler IL), followed by rinsing with de-ionised water and drying under a gentle flow of nitrogen between each measurement. All experimental testing took place at room temperature conditions.

Results

Table A6.1- SCE electrode stability and drifting test results.

Electrode number	electrode type	adjustment to NHE	Peak (ox)	Peak (red)	$E_{1/2}$	$E_{1/2}$ adjusted	deviation	Peak to peak
Glassy Carbon Electrode 1 (d =3 mm)								
1	standard calomel	0.244	-0.14526	-0.23071	-0.187985	-0.431985	0.020504	-0.08545
2	standard calomel	0.244	-0.1426	-0.22995	-0.186275	-0.430275	0.022214	-0.08735
3	standard calomel	0.244	-0.14526	-0.23315	-0.189205	-0.433205	0.019284	-0.08789
Glassy Carbon Electrode 2 (d =3 mm)								
1	standard calomel	0.244	-0.14282	-0.23315	-0.18799	-0.43199	0.020504	-0.09033
2	standard calomel	0.244			0	-0.244	0.208489	0
2	Standard calomel	0.244	-0.1445	-0.23483	-0.18967	-0.43367		-0.09033
3	standard calomel	0.244	-0.14282	-0.23315	-0.18799	-0.43199	0.020504	-0.09033

Appendix 7- Optical Microscopy imaging of the DNA-cisPt films

Figure A7.1- *42 µL of 1 to 10^{-4} DNA-cisPt hot plate 255 °C, 30 minutes.*

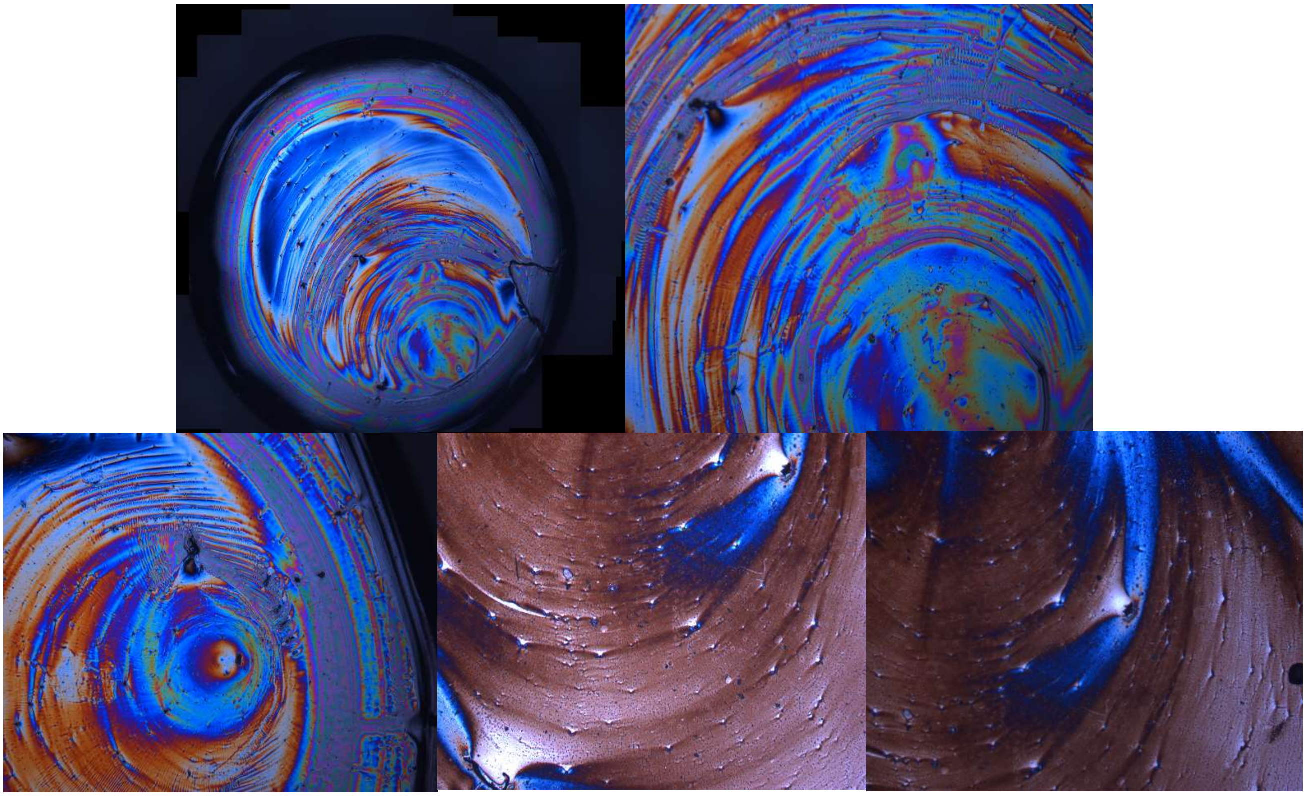

Figure A7.2 - *42 µL of (A, B) DNA 5 keV, 24 minutes e-beam irradiated. (C) Untreated DNA (D, E) Hot plate 255 °C, 30 minutes.*

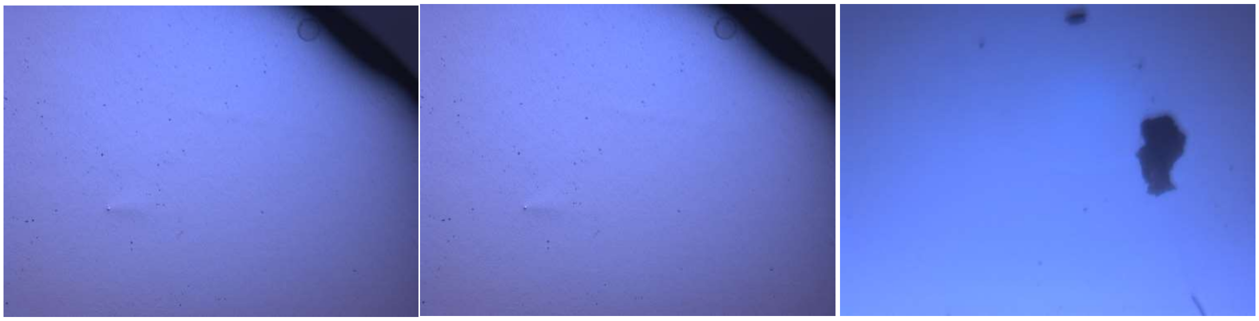

Figure A7.3- *Bare GC 5 mm electrode surface.*

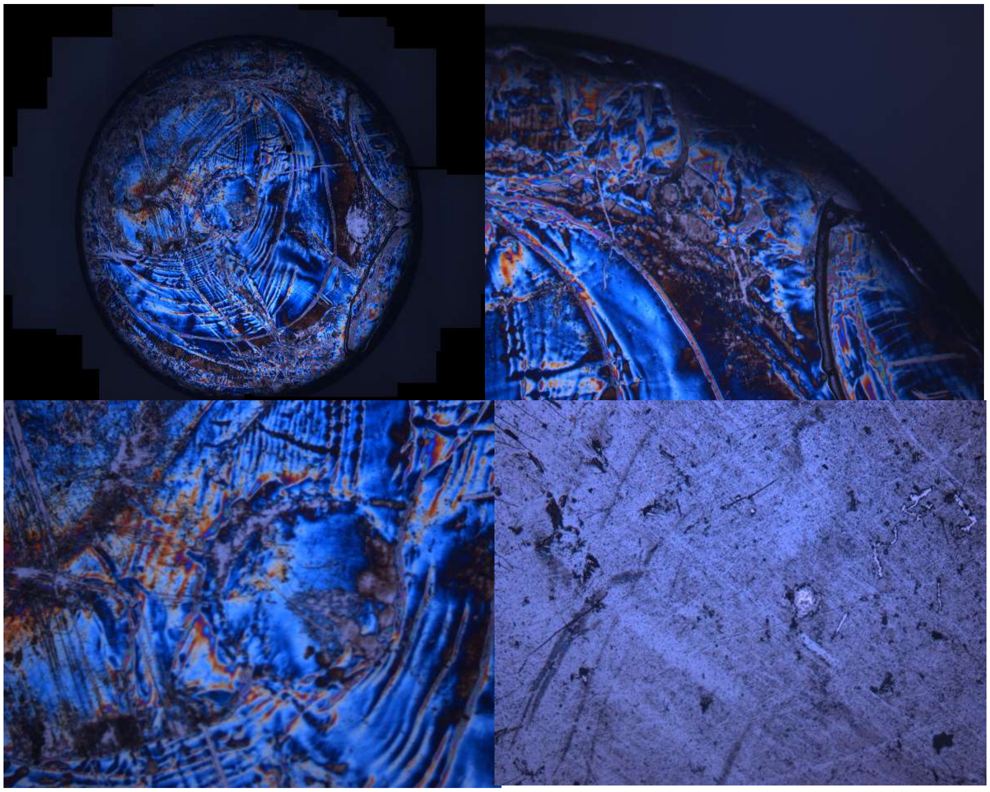

Figure A7.4 - *(A,B,C) 42 µL of DNA film pseudo pyrolysed, and cycled in acid on GC surface (D) 1 to 1 DNA-cisPt pseudo pyrolysed, and cycled in acid on GC surface.*